

**EXPERIMENTAL AND NUMERICAL
INVESTIGATION OF THE IMPACT RESISTANCE
AND IMPACT DAMAGE TOLERANCE OF A
CARBON FIBER REINFORCED
THERMOPLASTIC POLYPHENYLENE SULFIDE
(PPS) MATRIX COMPOSITE**

**A Thesis Submitted to
The Graduate School of
İzmir Institute of Technology
in Partial Fulfillment of the Requirements for the Degree of**

DOCTOR OF PHILOSOPHY

in Mechanical Engineering

**by
Semih Berk SEVEN**

June 2024

İZMİR

We approve the thesis of **Semih Berk SEVEN**

Examining Committee Members:

Prof. Dr. Mustafa GÜDEN

Department of Mechanical Engineering, İzmir Institute of Technology

Assist. Prof. Dr. Muhammet Fatih TOKSOY

Department of Mechanical Engineering, İzmir Institute of Technology

Assist. Prof. Dr. Halil TETİK

Department of Mechanical Engineering, İzmir Institute of Technology

Prof. Dr. Ramazan KARAKUZU

Department of Mechanical Engineering, Dokuz Eylül University

Prof. Dr. Hasan YILDIZ

Department of Mechanical Engineering, Ege University

12 June 2024

Prof. Dr. Mustafa GÜDEN

Supervisor, Department of
Mechanical Engineering
İzmir Institute of Technology

Prof. Dr. Alper TAŞDEMİRÇİ

Co-Supervisor, Department of
Mechanical Engineering
İzmir Institute of Technology

Prof. Dr. M. İ. Can DEDE

Head of the Department of
Mechanical Engineering

Prof. Dr. Mehtap EANES

Dean of the Graduate School

ACKNOWLEDGMENTS

I would like to express my deepest gratitude to my supervisor Prof. Dr. Mustafa GÜDEN for his invaluable support and guidance throughout this thesis study. I am also grateful to my thesis progress committee Prof. Dr. Ramazan KARAKUZU, Assist. Prof. Dr. M. Fatih TOKSOY and my co-supervisor Prof. Dr. Alper TAŞDEMİRÇİ for their inspiring comments and contributions during the thesis progress.

Special thanks to TAI (Turkish Aerospace Company) for letting me to manufacture composites and using facilities I need to complete my study. I also thank my colleagues who work in TAI. I would like to extend my sincere thanks to people who took part in the manufacturing of composite test specimens and inspection procedures.

I would like to express many thanks to my friends Mesut BAYHAN for his efforts and help.

Finally, I am also grateful to my wife Pınar KESKİN SEVEN for her patience, endless support and encouragement during my thesis study. Our son, Cesur SEVEN who was just born during the thesis study has always inspired me and given me strength to continue.

ABSTRACT

EXPERIMENTAL AND NUMERICAL INVESTIGATION OF THE IMPACT RESISTANCE AND IMPACT DAMAGE TOLERANCE OF A CARBON FIBER REINFORCED THERMOPLASTIC POLYPHENYLENE SULFIDE (PPS) MATRIX COMPOSITE

The impact resistance and impact damage tolerance of an aerospace grade high performance 5 Harness Satin woven fabric carbon fiber reinforced/polyphenylene sulfide matrix (CF/PPS) thermoplastic composite were investigated experimentally and numerically. The numerical modeling was performed using the experimentally determined parameters of material model MAT-58 and Hashin failure criteria in LS-DYNA using the single shell and stacked shell models. The numerical models of the low velocity impact (LVI) tests showed good correlations with the experimental tests while the stacked shell model showed nearer results with the experimental tests. The stacked shell model also estimated the LVI test delamination areas, which were comparable with the experimental damage areas. The LVI tested coupons were further subjected to compression after impact (CAI) tests to determine the damage tolerance of CF/PPS composite. The CAI tests were modeled using the single shell model. The numerical models of the CAI tests showed very similar trends with the experimental CAI tests. The trends were shown to be more converging in the specimens tested at 3 m/s and above in the LVI tests. Lastly, three high velocity impact (HVI) tests were performed at around 100 m/s. The failure mode of the HVI tests was shown to be very different from that of the LVI tests. The long longitudinal and transverse cracks were formed in the HVI tests. The delamination damage in the HVI tests determined using the stacked shell model was found to be more comparable with the experimental delamination damage determined by the C-Scan.

ÖZET

KARBON FİBER TAKVİYELİ TERMOPLASTİK POLİFENİLEN SÜLFİT (PPS) MATRİS KOMPOZİTİN DARBE DİRENCİNİN VE DARBE HASAR TOLERANSININ DENEYSEL VE NÜMERİK ARAŞTIRILMASI

Havacılık sınıfı yüksek performanslı 5 Harness Satin (5 HS) örgülü kumaş karbon fiber takviyeli/polifenilen sülfid matrisli (CF/PPS) termoplastik kompozitlerin çarpma direnci ve çarpma hasar toleransı deneysel ve nümerik olarak incelenmiştir. Nümerik modelleme çalışmaları deneysel testler sonucu parametreleri belirlenen MAT-58 malzeme modeli ve Hashin kırılma kriterleri kullanılarak LS-DYNA'da tek katman ve çoklu katman modelleri ile gerçekleştirilmiştir. Düşük hızlı çarpma testlerinin nümerik modelleri deneysel testlerle iyi korelasyon göstermesine karşın çoklu katman modeli ile daha yakın sonuçlar elde edilmiştir. Ayrıca, çoklu katman modeli kullanarak düşük hızlı çarpma testlerindeki delaminasyon alanlarını hesaplanabilmiş, elde edilen sonuçlar deneysel testlerdeki delaminasyon hasar alanlarıyla benzer bulunmuştur. LVI testine tabi tutulan CF/PPS kompozit numuneler sonrasında hasar sonrası oluşan dayanım toleransını belirlemek için çarpma sonrası basma (CAI) testlerine tabi tutulmuştur. CAI testlerinin nümerik modeli tek katmanlı modelleme tekniği kullanılarak modellenmiştir. CAI testlerinin nümerik modelleri, deneysel CAI testleriyle çok benzer eğilimler göstermiştir. Bu eğilimler, LVI testlerinde 3 m/s ve üzeri hızlarda test edilen numunelerde daha yakınsamış olarak görülmüştür. Son olarak, yaklaşık 100 m/s hızda üç adet yüksek hızlı çarpma (HVI) testi gerçekleştirilmiştir. HVI testlerinin kırılma ve hasar modları, LVI testlerinininkinden çok farklı olarak gözlemlenmiştir. Boyuna ve enine olmak üzere uzun ana çatlaklar HVI testleri sonucu oluşmuştur. HVI testleri hem tekli katman hem de çoklu katman modelleme teknikleri ile modellenmiştir. Çoklu katman modeli kullanılarak belirlenen HVI testlerindeki delaminasyon hasarı, C-Tarama hasarsız muayene ile belirlenen deneysel delaminasyon hasarıyla tutarlı bulunmuştur.

TABLE OF CONTENTS

| | |
|---|------|
| TABLE OF CONTENTS..... | vi |
| LIST OF FIGURES | ix |
| LIST OF TABLES..... | xvii |
| CHAPTER 1. INTRODUCTION | 1 |
| 1.1. Introduction | 1 |
| 1.2. Thermoplastic Composites | 4 |
| 1.2.1. Advantages of Thermoplastic Composites..... | 4 |
| 1.2.2. Application of Thermoplastic Composites..... | 6 |
| 1.3. Research Objectives | 9 |
| 1.4. Scope of the Study..... | 10 |
| CHAPTER 2. LITERATURE REVIEW | 12 |
| 2.1. Introduction | 12 |
| 2.2. Mechanical Properties of Thermoplastic Composites..... | 12 |
| 2.3. Impact Resistance and Damage Tolerance of Fiber-Reinforced Composites | 19 |
| 2.3.1. Impact Behavior of Thermoplastic Composites..... | 25 |
| 2.3.2. Compression After Impact Behavior of Thermoplastic Composites | 32 |
| 2.4. Finite Element Modeling of Impact Damage and Damage Tolerance of Composites..... | 34 |
| 2.4.1. Numerical Constitutive Material Modelling Studies..... | 37 |
| 2.4.2. Cohesive Zone Modeling of the Composite Laminates | 39 |
| 2.4.3. Impact Modelling and Damage Tolerance Prediction of Fiber Reinforced Composites | 41 |
| CHAPTER 3. EXPERIMENTAL METHODOLOGY | 46 |
| 3.1. Introduction | 46 |

| | |
|--|-----|
| 3.2. Laminate and Test Specimen Preparation | 46 |
| 3.3. Strain Measurements in the Tests..... | 50 |
| 3.4. Quasi-Static Material Characterization Tests..... | 52 |
| 3.4.1. Tensile Tests | 52 |
| 3.4.2. Compression Tests | 54 |
| 3.4.3. In-plane Shear Tests | 56 |
| 3.5. Low Velocity Impact Tests | 58 |
| 3.6. Compression After Impact Tests..... | 61 |
| 3.7. Gas Gun Impact Tests | 64 |
| | |
| CHAPTER 4. EXPERIMENTAL TEST RESULTS..... | 67 |
| 4.1. Mechanical Testing | 67 |
| 4.1.1. Tension Tests..... | 67 |
| 4.1.2. Compression Tests | 70 |
| 4.1.3. In-plane Shear Tests | 75 |
| 4.2. Low Velocity Impact Tests | 76 |
| 4.2.1. The Effect of Impact Velocity..... | 77 |
| 4.2.2. The Effect of Impactor Geometry | 84 |
| 4.3. Compression After Impact Tests..... | 88 |
| 4.4. Gas Gun Impact Tests | 95 |
| | |
| CHAPTER 5. NUMERICAL ANALYSIS METHODOLOGY..... | 99 |
| 5.1. Introduction | 99 |
| 5.2. Material Model Selection and Parameter Identification | 99 |
| 5.3. Material Model Theory and Parameter Identification..... | 101 |
| 5.4. Modeling Composite Laminates using Tiebreak Contacts | 107 |
| 5.5. Material Characterization Modeling Studies..... | 112 |
| 5.5.1. Single Element Level Analysis | 113 |
| 5.5.2. Coupon-level Material Characterization Analysis | 113 |
| 5.5.2.1. Standard Tensile Test Numerical Model..... | 114 |
| 5.5.2.2. Standard Compression Test Numerical Model | 115 |
| 5.5.2.3. Standard In-plane Shear Test Numerical Model..... | 115 |
| 5.6. Drop-Weight Impact Test Modeling | 116 |

| | |
|--|-----|
| 5.6.1. Single Shell Technique of the Low Velocity Impact Modeling | 117 |
| 5.6.2. Stacked Shell Technique of Low Velocity Impact Modeling | 118 |
| 5.7. Compression After Impact Modeling..... | 120 |
| 5.8. High Velocity Impact Tests and Modeling Studies | 121 |
| 5.8.1. Single Shell Technique Gas Gun Impact Analysis | 121 |
| 5.8.2. Stacked Shell Element Technique Gas Gun Impact Analysis..... | 122 |
| | |
| CHAPTER 6. NUMERICAL ANALYSIS RESULTS AND DISCUSSION | 124 |
| 6.1. Introduction | 124 |
| 6.2. Material Model and Tiebreak Contact Parameters..... | 124 |
| 6.3. Mechanical Characterization Analysis Results | 126 |
| 6.3.1. Tensile Analysis | 126 |
| 6.3.2. Compression Analysis | 129 |
| 6.3.3. In-plane Shear Analysis..... | 132 |
| 6.4. Mesh Sensitivity Analysis..... | 135 |
| 6.5. Low Velocity Impact Analysis Results | 138 |
| 6.5.1. Numerical Investigation of the Effect of Impactor Velocity..... | 138 |
| 6.5.2. Numerical Investigation of the Effect of Impactor Geometry..... | 148 |
| 6.6. Compression After Impact Analysis Results | 152 |
| 6.7. Gas Gun Impact Analysis Results | 157 |
| | |
| CHAPTER 7. CONCLUSIONS | 162 |
| | |
| REFERENCES | 164 |

LIST OF FIGURES

| <u>Figure</u> | <u>Page</u> |
|--|--------------------|
| Figure 1.1. Global CFRP demand in the Year 2018 classified by (a) application, (b) sales, (c) region, and (d) manufacturing process. The global carbon fiber demand in 2020 (e) by application, and (f) estimated Global CFRP waste in 2050 from the aeronautical sector by region | 7 |
| Figure 2.1. The effect of temperature on the compressive stress-strain curves of notched specimen | 14 |
| Figure 2.2. (a) modulus and (b) ultimate stress and properties of CF/PPS with different cooling rates and types of loading..... | 16 |
| Figure 2.3. Interlaminar strength comparison of different thermoplastic resins at different testing temperatures | 17 |
| Figure 2.4. In-plane direction CF/PPS composite dynamic properties at various strain rates | 19 |
| Figure 2.5. Diagram of factors that may influence impact resistance and damage tolerance of fiber reinforced composites | 22 |
| Figure 2.6. Schematic diagrams for generic low velocity impact test; a) Force-Energy-Deflection-Time plot, b) Force-Deflection plot and c) Force- Deflection and Energy-Deflection plots | 23 |
| Figure 2.7. An example of Load versus Time curve and important points. | 24 |
| Figure 2.8. Load versus displacement curves for the low-velocity drop-weight tests for the CF/PEEK and CF/Epoxy specimens at impact energies of a) 4.5 J, b) 7.5 J and c) 10.5 J | 27 |
| Figure 2.9. Microscopic image of impacted C/PPS specimen at 17 J | 28 |
| Figure 2.10. Impact energy versus damage projection area of different composite systems with different lay-ups..... | 29 |
| Figure 2.11. Damage area of CF/PPS versus impact energy after LVI..... | 30 |
| Figure 2.12. Low velocity impact tests of CF/PPS composites having 3 mm thickness; rebound (T30), onset of back face penetration (T50), and perforation (T70) | 30 |

| <u>Figure</u> | <u>Page</u> |
|--|--------------------|
| Figure 2.13. Impact energy versus KEA and damaged area of the CF/PEEK and CF/epoxy comparison | 31 |
| Figure 2.14. Impact energy versus CAI strength for CF/PEEK thermoplastic composite laminates | 32 |
| Figure 2.15. Impact energy versus CAI strength of different composite systems | 33 |
| Figure 2.16. Normalized impact energy versus CAI strength and delamination area of three composite systems..... | 33 |
| Figure 2.17. Experiment and simulation comparison of damage area and load versus time curves for CF/PEEK composites a) 4.5, b) 7.5 and c) 10.5 J | 36 |
| Figure 2.18. Different methods for impact analysis | 37 |
| Figure 2.19. Traction separation law for interlaminar damage modeling of composite laminates | 41 |
| Figure 2.20. Experimental and numerical comparison of normalized CAI strength for a) 2.1 mm lay-up, b) 4.2 mm lay-up..... | 43 |
| Figure 2.21. Compression after impact results for low and HVI tests..... | 43 |
| Figure 2.22. Impact and CAI numerical models..... | 44 |
| Figure 2.23. Comparison of CAI experimental and numerical results; a) complete model, b) simplified model | 45 |
| Figure 3.1. Ply cutting from a pre-preg roll | 47 |
| Figure 3.2. Composite laminate before consolidation process | 47 |
| Figure 3.3. Automated press machine for manufacturing composite plates..... | 47 |
| Figure 3.4. Water jet test specimen cutting | 48 |
| Figure 3.5. Weave pattern for 5 harness satin weave | 49 |
| Figure 3.6. Warp and weft direction alignment of the composite laminate..... | 49 |
| Figure 3.7. Coupon extraction from a large composite laminate after thermoforming | 50 |
| Figure 3.8. Implementation of strain gauge and video extensometer..... | 51 |
| Figure 3.9. Specimen Surface Preparation for DIC Application | 51 |
| Figure 3.10. Standard quasi-static tensile test setup | 53 |
| Figure 3.11. A typical CLC test fixture for compression testing..... | 54 |
| Figure 3.12. Standard quasi-static compression test setup | 54 |

| <u>Figure</u> | <u>Page</u> |
|--|--------------------|
| Figure 3.13. Three-part failure mode codes according to the ASTM for compression test specimen..... | 55 |
| Figure 3.14. Definition and material axis for shear test coupon..... | 56 |
| Figure 3.15. Standard in-plane shear test of $\pm 45^\circ$ specimen test setup | 57 |
| Figure 3.16. Illustration of modulus and offset strength determination | 58 |
| Figure 3.17. Drop weight impact test apparatus | 59 |
| Figure 3.18. Drop weight impact specimen and its dimensions | 59 |
| Figure 3.19. Impact support fixture for drop weight test specimen..... | 59 |
| Figure 3.20. Frequently observed damage modes from drop-weight impact tests..... | 60 |
| Figure 3.21. Drop weight impact test projectiles..... | 60 |
| Figure 3.22. Schematic of ASTM CAI test apparatus with specimen | 62 |
| Figure 3.23. CAI test apparatus | 62 |
| Figure 3.24. Commonly observed acceptable residual strength failure modes | 63 |
| Figure 3.25. Gas gun impact testing | 64 |
| Figure 3.26. Manufacturing of sabot process | 65 |
| Figure 3.27. Gas gun impact test boundary condition and specimen | 65 |
| Figure 3.28. Steel ball projectile and sabot..... | 65 |
| Figure 3.29. Gas gun impact test video recording system | 66 |
| Figure 4.1. Standard quasi-static tension stress-strain curves in a) the warp and b) weft direction | 67 |
| Figure 4.2. Failed tension test specimens in warp direction a) front face and b) back face | 68 |
| Figure 4.3. Failed tension test specimens in weft direction a) front face and b) back face | 68 |
| Figure 4.4. Tensile stress-strain curves at 0.01 1/s in a) warp and b) weft direction | 70 |
| Figure 4.5. Standard quasi-static compression stress-strain curves in a) warp and b) weft direction | 71 |
| Figure 4.6. Compression stress-strain curve using strain gauge..... | 71 |
| Figure 4.7. Failed compression test sample in the warp direction..... | 73 |
| Figure 4.8. Failed compression test specimens in warp direction a) front face and b) back face..... | 73 |

| <u>Figure</u> | <u>Page</u> |
|---|--------------------|
| Figure 4.9. A picture of failed compression test sample in the weft direction | 73 |
| Figure 4.10. Failed compression test specimens in weft direction a) front face and b) back face..... | 73 |
| Figure 4.11. Compressive stress vs. strain for higher strain rate tests; a) warp and b) weft direction | 74 |
| Figure 4.12. Standard quasi-static in-plane shear test curves | 75 |
| Figure 4.13. Failed shear test specimens a) front face and b) back face | 76 |
| Figure 4.14. Force-Energy vs a) time and b) displacement curves at 1.37J impact energy (1 m/s) | 78 |
| Figure 4.15. Force-Energy vs a) time and b) displacement curves at 5.60J impact energy (2 m/s) | 78 |
| Figure 4.16. Force-Energy vs a) time and b) displacement curves at 12.51J impact energy (3 m/s) | 79 |
| Figure 4.17. Force-Energy vs a) time and b) displacement curves at 14.97J impact energy (CAI m/s)..... | 79 |
| Figure 4.18. Force-Energy vs a) time and b) displacement curves at 22.23J impact energy (4 m/s) | 79 |
| Figure 4.19. Force-Energy vs a) time and b) displacement curves at 31.65J impact energy (5 m/s) | 80 |
| Figure 4.20. Force-Energy vs a) time and b) displacement curves at 45.48J impact energy (6 m/s) | 80 |
| Figure 4.21. Impact velocity versus a) Contact time, b) Peak Force, c) Absorbed energy, d) Maximum displacement, e) Dent depth and f) Damaged Area | 82 |
| Figure 4.22. NDI and impacted specimen images at different impact velocities | 83 |
| Figure 4.23. Force-Energy vs a) time (31.14J), b) displacement (31.14J) c) time (44.18J) and d) displacement (44.18J) curves for the 38 mm impactor | 85 |
| Figure 4.24. NDI images and impacted specimen images at two different impact energies and impactor | 86 |

| <u>Figure</u> | <u>Page</u> |
|--|--------------------|
| Figure 4.25. Impact Energy versus a) Contact time, b) Peak Force, c) Absorbed energy, d) Maximum displacement and e) Damaged Area for the 38 mm impactor | 87 |
| Figure 4.26. Stress-strain curve for CAI tests | 89 |
| Figure 4.27. Impact Energy versus a) Ultimate strength, b) Failure strain, c) Effective modulus and d) Damaged Area | 90 |
| Figure 4.28. Full-field strain measurement just before failure for test specimen; a) CAI Test-1, b) CAI Test-2, c) CAI Test-3, d) CAI Test-4, e) CAI Test-5 and f) CAI Test-6..... | 91 |
| Figure 4.29. CAI test specimen-1 after failure a) front face, b) back face, c) DIC image, and d) C-Scan image | 92 |
| Figure 4.30. CAI test specimen-2 after failure a) front face, b) back face, c) DIC image, and d) C-Scan image | 92 |
| Figure 4.31. CAI test specimen-3 after failure a) front face, b) back face, c) DIC image, and d) C-Scan image | 93 |
| Figure 4.32. CAI test specimen-4 after failure a) front face, b) back face, c) DIC image, and d) C-Scan image | 93 |
| Figure 4.33. CAI test specimen-5 after failure a) front face, b) back face, c) DIC image, and d) C-Scan image | 94 |
| Figure 4.34. CAI test specimen-6 after failure a) front face, b) back face, c) DIC image, and d) C-Scan image | 94 |
| Figure 4.35. High-speed video camera images during impact | 96 |
| Figure 4.36. Gas gun impact test specimen-1 after impact; a) front face, b) back face, and c) C-scan image for damage assessment..... | 97 |
| Figure 4.37. Gas gun impact test specimen-2 after impact; a) front face, b) back face, and c) C-scan image for damage assessment..... | 97 |
| Figure 4.38. Gas gun impact test specimen-3 after impact; a) front face, b) back face, and c) C-scan image for damage assessment..... | 98 |
| Figure 5.1. Shear stress-strain curve when the value of FS is set to -1 | 104 |
| Figure 5.2. Failure modes of MAT_58 according to the failure surface | 105 |
| Figure 5.3. Failure modes of matrix | 108 |
| Figure 5.4. Bilinear constitutive law..... | 109 |
| Figure 5.5. Mixed-mode traction-separation law..... | 111 |

| <u>Figure</u> | <u>Page</u> |
|---|--------------------|
| Figure 5.6. Single element analysis loading and boundary conditions..... | 113 |
| Figure 5.7. Numerical Model of Standard Tensile Test | 114 |
| Figure 5.8. Numerical Model of Standard Compression Test | 115 |
| Figure 5.9. Numerical Model of Standard In-plane Shear Test..... | 116 |
| Figure 5.10. Finite Element Model of Drop Weight Impact Test..... | 117 |
| Figure 5.11. Finite element model of single shell drop weight impact testing..... | 118 |
| Figure 5.12. Finite element representation of the composite laminate using single shell layer technique | 118 |
| Figure 5.13. Finite element representation of the composite laminate using stacked shell technique..... | 119 |
| Figure 5.14. Finite element model of stacked shell drop weight impact testing | 120 |
| Figure 5.15. Finite element model of the compression after impact analysis | 121 |
| Figure 5.16. High velocity impact test model using single shell technique | 122 |
| Figure 5.17. Finite element model of the stacked shell element gas gun impact test | 123 |
| Figure 6.1. Experimental and numerical standard quasi-static tension test stress-strain curves of the a) warp and b) weft direction | 129 |
| Figure 6.2. Tension -x strain FEA results and experimental failure..... | 129 |
| Figure 6.3. Experimental and numerical standard quasi-static compression test stress-strain curves of the a) warp and b) weft direction..... | 132 |
| Figure 6.4. Compression -x strain FEA results and experimental failure..... | 132 |
| Figure 6.5. Shear stress-strain test-analysis comparison | 134 |
| Figure 6.6. In-plane shear -x strain FEA results and experimental failure..... | 134 |
| Figure 6.7. Experimental and numerical force-time comparisons for different mesh sizes; a) 0.5 mm, b) 1 mm, c) 2 mm and d) 4 mm | 136 |
| Figure 6.8. Experimental and numerical after impact images with different mesh sizes; a) 0.5 mm, b) 1 mm, c) 2 mm and d) 4 mm..... | 137 |
| Figure 6.9. Experimental and numerical force-time curve comparison for different velocities; a) 1 m/s, b) 2 m/s, c) 3 m/s, d) 4 m/s, e) 5 m/s, f) 6 m/s | 140 |

| <u>Figure</u> | <u>Page</u> |
|---|--------------------|
| Figure 6.10. Experimental and numerical force-displacement curve comparison for different velocities; a) 1 m/s, b) 2 m/s, c) 3 m/s, d) 4 m/s, e) 5 m/s and f) 6 m/s | 142 |
| Figure 6.11. Experimental and numerical energy-time curve comparison for different velocities; a) 1 m/s, b) 2 m/s, c) 3 m/s, d) 4 m/s, e) 5 m/s and f) 6 m/s..... | 143 |
| Figure 6.12. Experimental and numerical energy-displacement curve comparison for different velocities; a) 1 m/s, b) 2 m/s, c) 3 m/s, d) 4 m/s, e) 5 m/s and f) 6 m/s | 144 |
| Figure 6.13. Experimental NDI images and numerical delamination parameter results at different impact velocities; a) 1 m/s, b) 2 m/s, c) 3 m/s, d) 4 m/s, e) 5 m/s and f) 6 m/s..... | 146 |
| Figure 6.14. Damage history variable mapping for single shell and stacked shell method at different impact velocities, a) 1 m/s, b) 2 m/s, c) 3 m/s, d) 4 m/s, e) 5 m/s and f) 6 m/s..... | 147 |
| Figure 6.15. Experimental and numerical comparison for 31 J impact energy; a) Force-time, b) Force-displacement, c) Energy-time and d) Energy-displacement curves | 149 |
| Figure 6.16. Comparison of two different impactor LVI tests results at 31 J impact energy | 150 |
| Figure 6.17. Experimental and numerical comparison for 44 J impact energy; a) Force-time, b) Force-displacement, c) Energy-time and d) Energy-displacement curves | 151 |
| Figure 6.18. Comparison of two different impactor LVI tests results at 44 Joule impact energy | 152 |
| Figure 6.19. Time-Stress curve experimental and numerical results comparison; a) CAI Test-1, b) CAI Test-2, c) CAI Test-3, d) CAI Test-4, e) CAI Test-5 and f) CAI Test-6..... | 154 |
| Figure 6.20. Experimental and numerical CAI test results comparison | 156 |
| Figure 6.21. Numerical comparison curves; a) Force-time, b) Velocity-time, c) Kinetic energy-time and d) Displacement-time | 158 |
| Figure 6.22. Longitudinal and transverse failure dimensions at the impact zone; a) Experiment, b) Single shell and c) Stacked shell | 159 |

| <u>Figure</u> | <u>Page</u> |
|--|--------------------|
| Figure 6.23. Failure modes; a) Stacked shell model and b) Experimental test..... | 160 |
| Figure 6.24. Delamination area comparison a) Stacked shell model CGAP, b) The resultant delamination area and c) C-Scan | 161 |

LIST OF TABLES

| <u>Table</u> | <u>Page</u> |
|---|-------------|
| Table 1.1. Physical properties of the woven prepreg..... | 3 |
| Table 1.2. Physical and thermal properties of PPS resin | 3 |
| Table 3.1. The stacking sequence and dimensions of the manufactured composite plates | 48 |
| Table 3.2. Summary of the quasi-static test campaign | 52 |
| Table 3.3. Test matrix for low-velocity impact tests | 61 |
| Table 3.4. Failure modes according to ASTM D7137 standard | 63 |
| Table 3.5. Summary of the gas gun impact tests | 66 |
| Table 4.1. Standard quasi-static tensile test results in the warp direction | 69 |
| Table 4.2. Standard quasi-static tensile test results in the weft direction | 69 |
| Table 4.3. Tensile test results at 0.01 1/s in the warp direction..... | 70 |
| Table 4.4. Tensile test results at 0.01 1/s in the weft direction..... | 70 |
| Table 4.5. Standard quasi-static compression test results in the warp direction | 72 |
| Table 4.6. Standard quasi-static compression test results in the weft direction | 72 |
| Table 4.7. Compression test results at 0.01 1/s in the warp direction | 74 |
| Table 4.8. Compression test results at 0.01 1/s in the weft direction | 75 |
| Table 4.9. Standard in-plane shear test results..... | 76 |
| Table 4.10. Summary of drop weight impact tests | 77 |
| Table 4.11. Impact energy levels for comparison of impactor geometry | 84 |
| Table 4.12. Compression after impact test specimens and their impact scenario | 88 |
| Table 4.13. Compression after impact test results | 89 |
| Table 4.14. Gas gun impact test results | 95 |
| Table 5.1. MAT_58 material model parameter set..... | 101 |
| Table 5.2. Material model parameter definitions..... | 102 |
| Table 5.3. Tiebreak contact parameters used to model CF/PPS thermoplastic composite | 111 |

| <u>Table</u> | <u>Page</u> |
|---|--------------------|
| Table 5.4. Delamination damage model input parameters | 112 |
| Table 6.1. Material model parameter set for MAT-58 | 125 |
| Table 6.2. Delamination damage model input parameters | 126 |
| Table 6.3. Experimental tests and numerical analyses results for tension..... | 128 |
| Table 6.4. Experimental tests and numerical analyses results for compression | 131 |
| Table 6.5. Experimental tests and numerical analyses results for shear tests..... | 133 |
| Table 6.6. Mesh sensitivity analysis results..... | 136 |
| Table 6.7. Experimental and numerical LVI results summary | 139 |
| Table 6.8. CAI Experimental and numerical results comparison | 153 |
| Table 6.9. Experimental and numerical gas gun test results comparison | 157 |

CHAPTER 1

INTRODUCTION

1.1. Introduction

The use of thermoplastic composites in the aerospace industry has significantly increased in the last decade. The use of composites in the aerospace structures has already surpassed the use of traditional materials such as aluminum. The extensive research and development in the field of composites have also led to an evolution in aerospace engineering. Thermoset composites such as carbon-epoxy have been, for many years, successfully employed in the industry while their limitations have been brought the thermoplastic composites as a viable solution. High-performance thermoplastic composites offer several advantages over thermoset composites including,

- Indefinite shelf life
- High strength and toughness
- Higher strain to failure
- Post-formability
- Ease of joining and repair by welding and solvent bonding
- Reprocessibility and recyclability
- Faster manufacturing and shorter fabrication time

On the other side, manufacturing thermoplastic composites has few challenges to be overcome. Relatively higher processing temperatures require very special equipment. Also, the manufacturing and processing methodologies of thermoplastic composites have not yet been fully standardized. Furthermore, the mechanical behavior, damage resistance, and damage tolerance of thermoplastic composites particularly under dynamic loading are not thoroughly understood. The same further applies to the numerical models. There is a lack of comprehensive research on the test-analysis validation and material modeling for the impact loading. As the aerospace industry continues to explore these materials, further research and development are essential to harness the full potential of thermoplastic composites.

In the aerospace industry, the impacts of the foreign bodies expose a significant threat to the structural integrity of the aircraft parts. Typical examples include the bird strikes, hail strikes, runway debris and tool drops and ground crashes which cause Foreign Object Damage (FOD) on the aircraft. Hence, the impact resistance of the composites used in aviation is very critical in order to decrease the extent of the FOD. Impact damage can be visible through the inspection with naked eye. The damage, on the other side, is not readily detectable by visual inspection in the case of low velocity impact (LVI). This type of damage is called Barely Visible Impact Damage (BVID) which requires special techniques to detect, including ultrasonic scan or X-ray tomography.

The impact damage might greatly affect the residual strength of composites, which determines the ability to withstand further loading. Correspondingly, damage tolerance is a crucial property, ensuring that composites can continue to function safely, even in the presence of minor damage or defects. The research is directed to enhance the impact resistance and damage tolerance of composites by understanding the damage and energy absorption mechanisms. In this context, thermoplastic composites, with their exceptional mechanical properties, show promises as a solution to improve damage tolerance and to decline the maintenance and manufacturing costs in the aerospace applications, marking a notable advancement in this aspect. However, there have been a limited number of studies on the impact resistance and damage tolerance properties of thermoplastic composites.

This thesis is on the experimental and numerical investigation of the impact damage resistance and damage tolerance of a 5 Harness Satin (5-HS) woven fabric carbon fiber reinforced Polyphenylene Sulfide matrix (CF/PPS) thermoplastic composite laminate. The trade name of the composite is known as Toray Cetex TC1100 PPS. The resin is a semi-crystalline polymer, and the reinforcement is a standard modulus T300JB 3K Carbon fiber 5-HS woven fabric with an areal density of 281 g/m². In the study, the composite laminate was mechanically characterized in order to establish a numerical material model of the composite, followed by a test-analysis validation procedure. The physical properties of the used woven prepreg are tabulated in Table 1.1. Typical physical and thermal properties of PPS thermoplastic resin are given in Table 1.2.

Lastly, the featured properties of the thermoplastic composites can be summarized as:

- Qualified and certified to aerospace OEM specifications
- Outstanding performance-to-cost ratio

- Service temperature can exceed T_g depending on part design
- Lightning strike material as well as galvanic corrosion protection can be incorporated into laminates
- Inherently flame retardant
- Outstanding chemical and solvent resistance
- Indefinite shelf life at ambient temperature storage

Typical application areas for this composite system according to the product data sheet include,

- Primary and secondary aircraft structures: wing leading edges, engine pylon structures, clips, and cleats for fuselage structure
- Aircraft interiors: acoustic structures, structural components of seats, galleys, storage boxes
- High-end industrial applications where corrosive environments, dimensional stability, or vibration dampening play a role.

High-performance thermoplastic composites seem to play an important role and start replacing thermoset composites in the aerospace industry. CF/PPS thermoplastic composites are one of the advanced high-performance thermoplastic composites. This study investigated the impact resistance and impact damage tolerance of CF/PPS thermoplastic composite both experimentally and numerically.

Table 1.1. Physical properties of the woven prepreg (Source: Toray-Cetex¹)

| Property | 5-HS (T300JB Carbon Woven Prepreg) |
|----------------------------------|------------------------------------|
| Fiber areal weight (FAW) | 281 g/m ² |
| Weight per ply (PAW) | 496 g/m ² |
| Resin content by weight (RC) | 43% |
| Consolidated ply thickness (CPT) | 0.31 mm |
| Density | 1.55 g/cm ³ |
| Width | 1270 mm |

Table 1.2. Physical and thermal properties of PPS resin (Source: Toray-Cetex¹)

| | |
|--------------------------|------------------------|
| Density | 1.35 g/cm ³ |
| T_g (glass transition) | 90°C |
| T_m (melting) | 280°C |
| T_p (processing) | 300-330°C |

1.2. Thermoplastic Composites

Fiber-reinforced polymer (FRP) composites, including thermoset and thermoplastic matrices, are widely used in structural applications. Thermoplastic polymer matrices are usually classified as standard, engineering, and high-standard.² More expensive high standard thermoplastic matrices have higher mechanical and heat resistance properties, and they are highly demanded by the automotive and aerospace industries. Examples of this category include PPS, polysulfones (PSU), and polyetherketones (PEK). Carbon, glass, aramid, and even metal alloy² fibers have been investigated as the reinforcement in thermoplastic composites. The thermal, mechanical, and electrical properties of thermoplastic resins with the carbon fiber reinforcement have also been investigated along with the discussions on the effect of fiber surface treatments and manufacturing methods.³

As a group of matrices in thermoplastic composites, amorphous thermoplastic polymers exhibit disordered polymer chains in a random coil configuration, lacking any discernible local order. In contrast, semi-crystalline thermoplastic polymers display some level of polymer chain ordering. The chains in thermoplastic polymers are interlocked and, due to their non-fixed nature, can slide past one another. In contrast, when a thermoset resin experience localized stress, it tends to break in a brittle manner. The chain slippage capability of the thermoplastic matrices gives toughness to composite. Semi-crystalline thermoplastic materials exhibit a higher level of efficiency when reinforced with carbon fibers compared to amorphous thermoplastics. This enhanced performance is attributed to the fibers serving as nucleation sites, promoting the crystallization process. Consequently, the fibers become encapsulated within a finely dispersed microcrystalline structure, further enhancing properties like modulus, particularly the flexural modulus. The extent of reinforcement is directly proportional to the increase in crystallinity.⁴

1.2.1. Advantages of Thermoplastic Composites

Thermoplastic composites do not need a curing cycle to harden as opposite to thermoset composites. This leads to a shorter production cycle and cost efficiency. The automated manufacturing processes can also be more easily implemented to thermoplastic composites, promoting a cost-effective mass production. Gong et al.⁵ have

recently reviewed the thermo-stamping process of 2D woven fabric thermoplastic composites. It was stated in the same study that woven fiber-reinforced thermoplastic composites are highly suitable for thermo-stamping, providing flexibility of design, cost-effectiveness, and extremely low manufacturing times.

Thermoplastic composites can be recycled, reshaped, and reused multiple times by applying heating and cooling. This is one of the biggest advantages of thermoplastic composites over thermoset composites. The recycling is possible due to the chemical structure of thermoplastics and reduces the waste generation and promotes sustainability in the aerospace industry. It also contributes to energy savings in production and brings out environmental benefits thanks to no need for special storage. Recycled carbon fiber-reinforced PPS composites was further shown to have equivalent mechanical properties to those produced using industrial grades of virgin CF.⁶

Aerospace grade thermoset composites require a clean room environment in order to prevent any contamination from the atmospheric. This naturally increases the processing cost and reduces the production speed of thermoset composites. On the contrary, thermoplastic composites does not require a clean room, making the production more cost-effective and faster.

Thermoset composites have shorter shelf life. The unused material at the end of its shelf life is wasted. Thermoplastic composites have however a longer shelf life, reducing the risk of wasting materials. Thermoset composites further stored in more expensive special environment. The absence of special storage conditions also contributes to energy savings in environmental inspections.

Thermoplastic resins improve the impact resistance of thermoplastic composites.⁷ High-performance aerospace grade thermoplastic composites are tougher than thermoset composites. Thermoplastic resins also exhibit superior resistance to chemical agents and have much higher corrosion resistances.⁸ Composite materials are known to undergo chemical and mechanical property degradation under moisture, which is particularly more pronounced for the aerospace components. However, thermoplastic materials also have an advantage in this domain, given their relatively higher resistance to water absorption.

Thermoplastic composites can furthermore be weldable as opposite to thermoset ones because the bonding is easier and faster in thermoplastic composites. The repair and joining of thermoplastic composites have been reviewed by Reis et al.⁷ The performance of the repaired (compression molding) thermoplastic three layers woven glass fiber-polypropylene resin composites with two different fiber volume configurations after LVI

damage were investigated was investigated by Reyes and Sharma.⁹ Repaired specimens showed significant recovery in the flexural strength and modulus for both configurations.⁹ Zhao et al.¹⁰ compared the mechanical behavior of spot-welded and mechanically welded CF/PEEK thermoplastic composites. It was concluded there is a certain advantage for the welded structural components that provides ease of repair and reusability. The comparable load carrying capacity and exceptional rigidity of spot-welded connections under shear loading present potential to serve as an alternative to traditional mechanical fasteners.

There are also a few disadvantages of thermoplastic composites over conventional thermoset composites. Thermoplastic composites require higher processing temperatures and pressures for manufacturing. Manufacturing complex geometrical shape products using thermoforming may also require autoclaving. The current price of raw materials is also higher for thermoplastic composites. However, it is expected to decrease over time and the higher raw price is balanced by the cost-effectiveness of manufacturing as stated above. Lastly, repairing procedures are not mature enough to be used in service aircraft.⁸

1.2.2. Application of Thermoplastic Composites

Thermoplastic composites have already started to replace metals and thermoset composites in industrial applications. Xavier¹¹ stated that there is a great possibility that thermoplastic composites can replace thermoset composites for the next-generation fighter aircraft. Carbon fiber reinforced polymer composites are gaining a globally increasing demand from a variety of sectors and applications. Zhang et al.¹² presented pie charts on the global demands of CFRP as shown in Figure 1.1(a-f). The global demands are presented in terms of a) application, b) sales, c) region, d) manufacturing process, and global demand in 2020, e) application and f) estimated global CFRP waste in 2050 from the aeronautical sector by region. As seen in the same figure, CFRP usage and market share will increase over the years. However, increasing the use of FRP increases the amount of scrap material for several reasons. One of the major reasons is the definite shelf life of thermoset composites, causing scrap formation before production. Rybicka et al.¹³ reported that 30-50 % of polymer composites are manufacturing scrap in the aerospace industry. Thermoplastic composites can overcome the scrap issue of composites and reduce manufacturing costs in the aerospace industry.

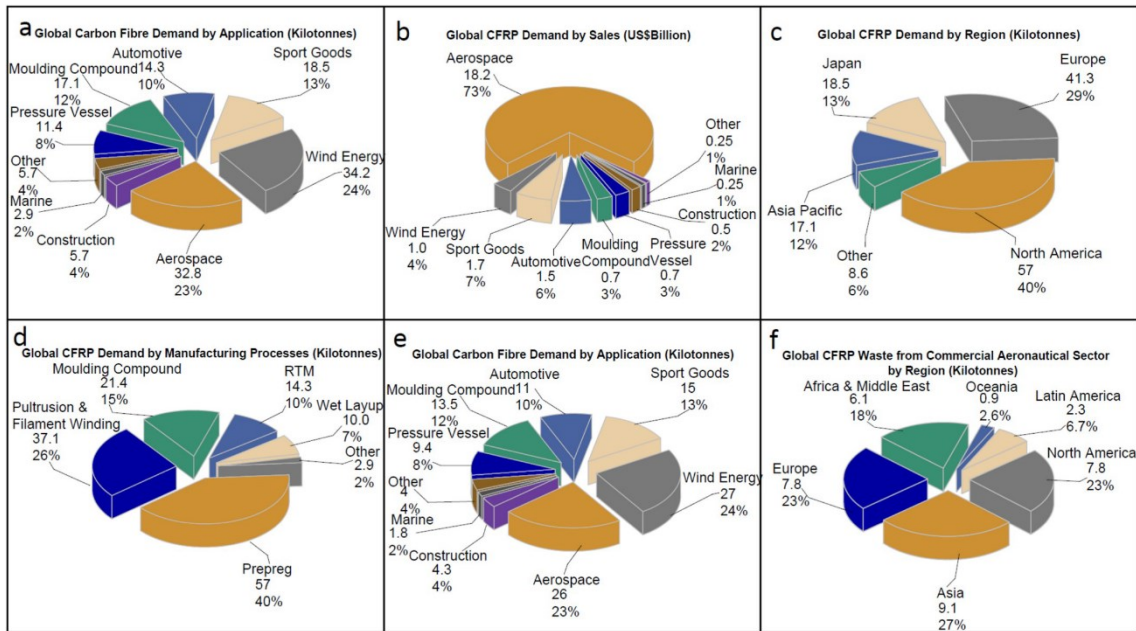


Figure 1.1. Global CFRP demand in the Year 2018 classified by (a) application, (b) sales, (c) region, and (d) manufacturing process. The global carbon fiber demand in 2020 (e) by application, and (f) estimated Global CFRP waste in 2050 from the aeronautical sector by region (Source: Zhang et al.¹²)

Thanks to the excellent properties and several advantages of thermoplastic composites, including recyclability, no shelf life and weldability, the usage of thermoplastic composites gains increasing demand in several industries such as aerospace, automotive, energy, sports, etc. as stated by Ning.¹⁴

The application areas, processing, and recycling of PPS-based materials have been reviewed by Montagna et al.¹⁵ It was reported in the same study that the recycling properties of the PPS-based composite materials have a great impact on the demand for these materials because of their economic and environmental effects. On the application side, CF/PPS composites have been used in the aerospace industry to manufacture structural parts of the Boeing 787 and Airbus A350. Structural parts including fuselage, doors, wings, stabilizers, flaps, and many more parts have been manufactured using carbon fiber-reinforced thermoplastic composites. Besides, there is an increasing demand for PPS-based materials in the automotive sector as well. Currently, manufacturers have been using PPS in structural parts such as housings, electronic components, and exterior and interior parts. One of the advantages of the PPS thermoplastic composites is the ease of manufacturing compared to other thermoplastic composites since they require relatively lower processing temperatures (300-350°C).

Thermoplastic composites have found applications in both structural and non-structural components of aircraft. Thermoplastic composites were started to be used during the 1990s, in the ribs and spars of undercarriage doors, followed by floor panels. Airbus, a major consumer, incorporated thermoplastic skins, panels, and leading edges in their A340-600 and A380 aircraft. The consumption of thermoplastic composites has grown to include small-sized parts, such as clips, cleats, brackets, and floor panels for commercial aircraft, jets, and military helicopters. The Gulfstream G650 provides an important example for the thermoplastic composite use in its rudder and tail. The commonly used interior thermoplastic composite parts include pans, backs, trays, and seat frames. An important example of cabin applications is the production of sidewall and ceiling attachment rails for Airbus A330 and A340.¹⁶

Airbuses including A320, A340, and A380 incorporate composites. The A320 and A340 airplanes utilize 15% composite while the A380 has 25% composite use, predominantly consisting of CF/PPS. These polymeric composites are strategically employed in various aircraft components, such as ailerons, rudders, flaps, spoilers, elevators, vertical and horizontal stabilizers, wing panels, landing gear doors, nacelles, flap rail fairing, and wing boxes. Remarkably, the A380 is the first aircraft equipped with a composite central wing box. The use of PPS in the composition of both aircraft is widespread, as it is currently utilized in a myriad of aircraft components, including interior parts, passenger seats, overhead cabinets, aerodynamic stabilizers, and wing trailing edge panels. The Fokker 50 and Gulfstream G650 are additional examples to the use of PPS/CF composites that includes the critical control surfaces, namely the rear rudder and elevator. These examples illustrate the growing implementation of composites in aircraft structures.¹⁵ Lockheed Aeronautical Systems Company has implemented thermoplastics to manufacture an aircraft door. Also, the same company used AS4/PEEK thermoplastic pre-pregs to manufacture a section of the composite fuselage of a fighter aircraft.⁸

The key factors that make thermoplastic composites distinguished from traditional thermoset composites are; the enhanced fracture toughness, recycling, short production cycle times, and superior Fire/Smoke/Toxicity properties as stated by Valverde et al.¹⁷ These properties coupled with the fast-processing techniques make thermoplastic composites cost-effective for structural applications in the aerospace industry.

Wind turbine blades are generally made of polymeric composites. However, the blades suffer from erosion which causes a loss of efficiency in aerodynamics and a

reduction in performance. The potential of utilizing thermoplastics in wind turbine blades has been demonstrated to be significant and accompanied by several advantages. Thermoplastics possess superior ductility, which reduces degradation and thus prevents erosion compared to thermosets. In the event of damage, welding can be performed, eliminating the need for adhesive bonds between blade components and enhancing the overall strength.¹⁵

Thermoplastic composites are getting greater attention, and the market size has been increased over the years for several industries. Especially, high-performance thermoplastic composites with PEEK, PAEK, and PPS thermoplastic resins are the most promising materials. It is very important to characterize the mechanical behavior of these materials in every aspect since the aerospace industry has strict regulations and standards.

1.3. Research Objectives

Composite structures in the aerospace industry may face several types of external damage during their service. Damage can be caused by the tool drops, runway debris, crashes, accidents, bird strikes, hail strikes, and lightning strikes. Impact damage is one of the main mechanisms for the reduction in the strength and strain-to-failure of the composite parts. Composites behave differently under different loading conditions and even at different impact speeds. The main objective of this thesis is to investigate both experimentally and numerically the impact characteristics and damage tolerances of a CF/PPS thermoplastic composite. The composite test specimens were exposed to impact tests in order to quantify its damage tolerance at varying impact energies. The specific damage mechanisms and failure modes during the impact tests were identified and characterized. The energy-absorbing mechanisms and failure modes are critical issues for understanding the impact performance of the tested composites. It is important to determine how composite material absorbs energy and dissipates impact energy under different impact speeds to assess its performance in practical applications. The post-impact damage tolerances and structural integrity of the composite, including its ability to withstand subsequent loads following an impact event were further investigated in the thesis. This aspect of the study explored the material's ability to maintain its integrity and functionality even after experiencing impact-induced damage. The tests were further validated by the numerical models and simulations. Numerical models were developed to

predict the response of the composite material at varying impact velocities and in the post-impact tests. These models are critical in enhancing the accuracy of impact predictions and can provide insights into optimizing composite designs. Correspondingly, it is important to establish correlations between the experimental and numerical simulation results, which further contribute to the validation of the developed models and a more comprehensive understanding of impact behavior.

Lastly, it is hoped that the outcomes of this study will contribute to the understanding of the impact phenomenon on fiber-reinforced composites. A numerical modeling pathway for the thermoplastic composite in this study would be applicable to any fiber-reinforced composite system. Also, correlated finite element models for CF/PPS composite and modeling methodologies would be used for further studies.

1.4. Scope of the Study

This study focused on the experimental and numerical investigation of impact resistance and damage tolerances of a high-performance aerospace-grade 5-HS weave woven fabric CF/PPS thermoplastic composite. The experimental test campaign was categorized into four sections as,

- 1) Material characterization tests: These tests in accordance with the ASTM standards were performed to obtain the mechanical properties. The results provided inputs for the constitutive material model used in the numerical analysis. Several different ex-situ displacement measurement techniques were used, including a video extensometer, strain gauges, and a digital image correlation (DIC) system.
- 2) Low-velocity impact tests: These tests aimed to investigate impact damage that could potentially degrade the strength of the composite materials. For this purpose, LVI tests were conducted using a drop-weight impact test apparatus. A great range of impact velocities was chosen to reveal the effect of impact kinetic energy on the impact resistance and damage mechanisms. Also, the effect of projectile diameter was investigated.
- 3) Compression after impact tests: The damage tolerance of impacted composite laminates was assessed through compression after impact (CAI) tests. Residual

strength, strain to failure, and damage areas were determined for every impacted test specimen at different impact velocities.

- 4) High-velocity impact tests: These tests were performed using a gas gun apparatus to examine the high-speed impact behavior of the CF/PPS thermoplastic composite.

The tested coupons in the impact and CAI tests were inspected using the non-destructive inspection (NDI) technique. The NDI allowed to determine the extent of the damage on the composite laminates. Finite element modeling studies were performed for each type of experimental test to explore numerical modeling capabilities. Constitutive material model parameters were set using experimental data and then optimized by benchmarking analysis with impact tests. A full set of material model parameters was created and used in numerical analyses. Different finite element modeling techniques were employed in this thesis study. Single-element and coupon-level modeling were implemented for material characterization test simulations. The stacked shell method with contact definition for the cohesive zone modeling was implemented to model composite laminate under impact loading. The main purpose of using different FE modeling techniques was to predict the impact behavior of thermoplastic composites under different loading conditions efficiently and accurately. The purpose of using different numerical methodologies was also to compare the advantages and disadvantages of these different modeling techniques.

CHAPTER 2

LITERATURE REVIEW

2.1. Introduction

This chapter presents a literature survey on mechanical behavior, impact resistance and damage tolerance, and finite element modeling studies on thermoplastic composites. Both experimental and numerical studies in the literature are included in the survey. Although the material system used in this study is a 5-HS weave carbon fiber fabric reinforced PPS thermoplastic composite, the results of the research on the thermoplastic composites of other resins are also considered due to the limited number of studies on the PPS thermoplastic composites. The mechanical behavior and properties of thermoplastic composites under different loadings and conditions draw general perspectives for thermoplastic composites. The background and implementation of impact resistance and damage tolerance of fiber-reinforced composites are also summarized. Available literature on the impact and CAI behavior of thermoplastic composites is also considered. Finite element modeling studies for impact damage and damage tolerance of fiber-reinforced composites are presented. Numerical constitutive material modeling approaches and different techniques for cohesive zone modeling of fiber-reinforced composites are also given. The literature on the impact modeling and damage tolerances of thermoplastic composites is further reviewed.

2.2. Mechanical Properties of Thermoplastic Composites

A wide range of thermoplastic composite matrix materials, including polypropylene (PP), polyethylene (PE), PEEK, polyetherimide (PEI), and polyamide (PA) offer distinct advantages in terms of temperature resistance, chemical compatibility, and processing easiness. These resins demonstrate a greater ability to withstand tensile strains than thermoset resins.¹⁸ Fracture toughness is also superior characteristic of thermoplastic composites as compared with thermoset epoxy composites.¹⁸

Although the research on thermoplastic composites is not as extensive or mature as that on thermoset composites, there is a continuing focus on thermoplastic composites. In a study¹⁹, the effect of thermoplastic resin type, PPS and PEEK, on the fracture and strength of carbon fiber reinforced composites was investigated. A higher mode I and mode II interlaminar fracture toughness of CF/PEEK composite than CF/PPS composite was shown in the same study. It was also stated that the smaller damage area yielded higher CAI strength and hence CF/PEEK laminate exhibited higher strength than CF/PPS

The failure and damage behavior of woven CF/ PPS thermoplastic composite with notched and unnotched specimens were investigated both experimentally and numerically.²⁰ The uniaxial tensile tests for both warp and weft direction were performed to obtain elastic properties for the numerical study. The tensile tests with samples oriented 45° to the loading direction were also conducted. A good correlation between the experimental and numerical results was obtained for both notched and unnotched specimens with different orientations. Stress concentration regions, fiber failure and delamination behavior observed in the experimental tests were all well represented by the numerical analysis tools.

The effect of temperature on the compression behavior of notched and unnotched woven CF/PPS thermoplastic laminates was investigated by Fang et al.²¹ The effect of temperature on the mechanical response of the compression specimens, on the matrix state, failure modes and local damage of notched and unnotched specimens were determined. The stress-strain curves of the compression tests at 25, 95, 125, and 200°C showed that there was a gradual decrease in the strength values as the temperature increased (Figure 2.1). A linear relationship at the initial portion of stress-strain curves at all temperatures was shown while there was a slight nonlinearity at the end of the stress-strain curves which might be attributed to the matrix damage and interlaminar strength reduction. In the case of unnotched specimens, a parallel stress-strain behavior with the notched specimen was found. It was stated that the notched specimen had special failure modes at 125 and 200°C because there was a load bearing capacity of the composite after the failure. The microscopic inspections of the failed specimens revealed that the failure mode highly depended on the test temperature. Correspondingly, a brittle failure was observed for the unnotched specimen at room temperature where there was a matrix and interface crack dominancy. An increase in the test temperature also increased the matrix flowability, but the interface bonding was affected negatively. This phenomenon yielded a change of the failure mode from brooming to kink-band and to wedge shear for the

unnotched specimens. Finally, it was stated that the existence of a hole increased the effect of temperature.

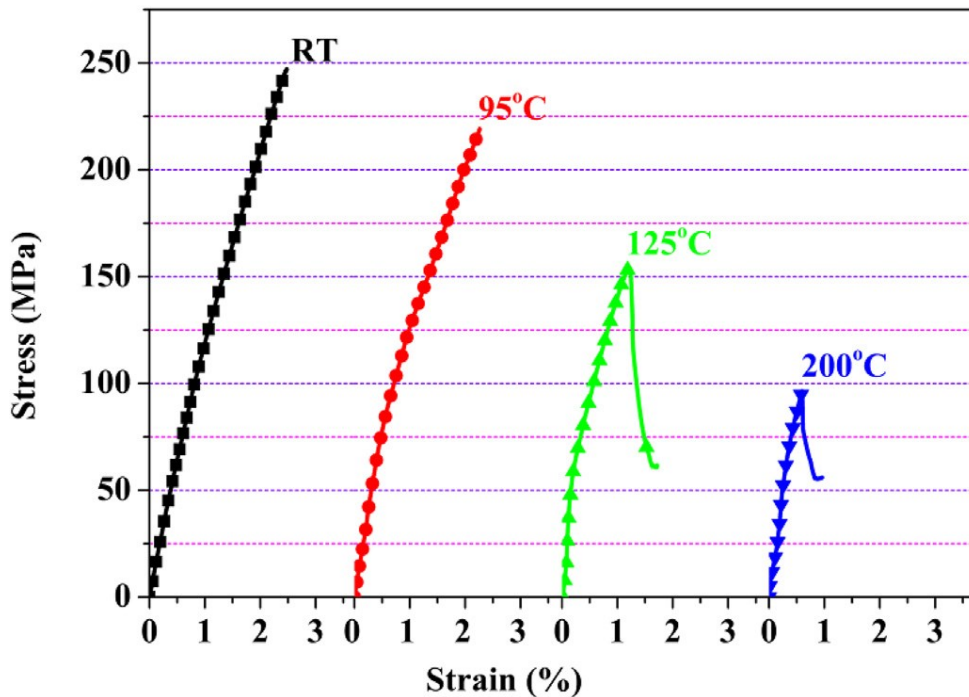


Figure 2.1. The effect of temperature on the compressive stress-strain curves of notched specimen (Source: Fang et al.²¹)

The mechanical performance of notched and unnotched specimens of CF/PPS and CF/Epoxy polymer composites were investigated under static loading at room temperature and at 120°C. It was found that the stress concentration on the notched region decreased at 120°C due to an increase in the matrix ductility of thermoplastic composite. This indicated that thermoplastic based composites have an inherent specification on matrix ductility at high temperatures.²²

Kouka et al.²³ investigated the tensile loading behavior of woven-ply PPS thermoplastic laminate specimens having circular holes. A DIC system was used to observe the stress concentration regions and damage evolution on the specimen at increasing deformations. The effect of woven ply orientation of fibers on the mechanical behavior of the composite was also shown in the same study.

Brown²⁴ studied E-glass/polypropylene commingled woven fabric thermoplastic composite and sandwiches with a crushable thermoplastic foam material. Both static and dynamic mechanical tests were performed and the developed numerical model was validated to predict the damage in the composite and the impact failure behavior of the

sandwich. LS-DYNA MAT-162 constitutive material model was used to predict the damage propagation and the deformation behavior of thermoplastic composites.

Ionescu²⁵ simulated mixed mode bending tests to investigate the delamination failure behavior of an AS4/PEEK thermoplastic composite. The Benzeggagh and Kenane mixed mode failure criterion was used to predict the delamination. It was shown in the same study that the delamination failure was caused by mainly fiber breakage or matrix cracking.

Few studies focused on the manufacturing techniques and their effects on the material properties of fiber reinforced thermoplastic composites. The mechanical properties, morphology, and flammability of an unidirectional pre-preg CF/PPS thermoplastic composite manufactured via induction heating molding were investigated by Kang et al.²⁶ It was concluded that the induction heating molding technique was suitable for the fabrication of thermoplastic composites. Alshammari et al.²⁷ studied CF reinforced thermoplastic polymers and their future improvements through processing modification techniques. They reviewed the current literature on the chemical and physical treatments of carbon fibers to improve mechanical, thermal, and electrical properties.

Abbasi et al.²⁸ investigated the thermo-stamping of a woven carbon fiber reinforced thermoplastic composite using an experimental forming set-up operating at 320°C. The effects of cooling rates on the crystallinity and interlaminar fracture toughness of a CF/PPS thermoplastic composite were investigated by Sacchetti et al.²⁹ A lower degree of crystallinity was detected at lower mold temperatures. Correspondingly, the interlaminar fracture toughness increased as the degree of crystallinity decreased from 33% to 12%. The microscopic analyses of the fracture surfaces revealed that a larger local plastic deformation at lower degree of crystallinity was the main mechanism for the increased fracture toughness.

The cooling rate dependent properties of a neat PPS and a CF/PPS thermoplastic composite were determined by Oshima et al.³⁰ The results showed that an increase in the cooling rate slightly decreased the elastic moduli as shown in Figure 2.2(a) while it increased the strength as shown in Figure 2.2(b). The fracture toughness of CF/PPS samples was shown less affected by the cooling rate than that of neat PPS. This is because of the relatively weak bonding between carbon fiber and PPS resin. It is concluded that the interface properties of fiber/matrix have great influence on the mechanical properties of CF/PPS composite.

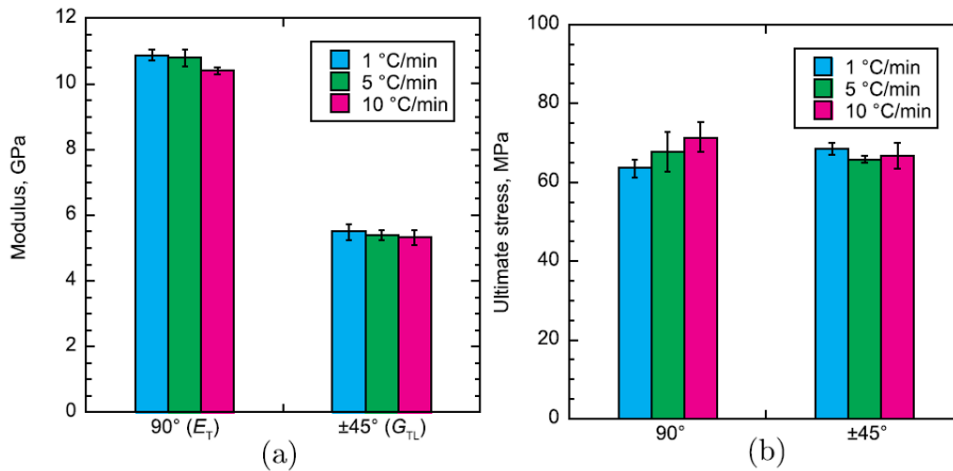


Figure 2.2. (a) modulus and (b) ultimate stress and properties of CF/PPS with different cooling rates and types of loading (Source: Oshima et al.³⁰)

The tensile loading damage mechanisms of thermoset and thermoplastic carbon fiber reinforced polymer composites were further compared in a study.³¹ The compared thermoset epoxy composite was manufactured in an autoclave while IM7/PEEK and AS4/PA thermoplastic composites were manufactured by a laser-automated tape placement. It was found that mechanical performances of thermoplastic composites manufactured by laser-automated tape placement was higher than those of the thermoset composites manufactured using autoclave.

The mechanical performances of T700 carbon fiber reinforced PA 6.6 and PPS thermoplastic composites used in automotive industry were investigated both experimentally and numerically through in-plane and out-of-plane directions by Mohsin.³² The tensile, compressive, in-plane shear, fracture toughness, dynamic tension using split Hopkinson bar and low velocity and high velocity impact (HVI) tests were conducted experimentally. Correspondingly, the numerical models of the compact tension, LVI and HVI tests were developed using the energy based finite element method in LS-DYNA.

Tan and Falzon³³ studied the experimental and numerical quasi-static crushing behavior of unidirectional CF/AS4 and PEEK thermoplastic composite corrugated panels. The implemented finite element model predicted well the experimental results both qualitatively and quantitatively. The numerical model captured the experimental matrix cracking and delamination as well as the crushing behavior. The results were also compared with those of epoxy based thermoset composite specimens and it was found that thermoplastic composites had higher specific energy absorption than thermoset composites.

The effect of test procedure on the curved beam strengths of three 5-HS carbon fiber reinforced thermoplastic composites with different resin types (PPS, PAEK and PEEK) were investigated by Hron et al.³⁴ Interlaminar strengths were measured at room temperature and at -55°C . The interlaminar strengths of three different thermoplastic composites at room temperature and at -55°C are shown in Figure 2.3. As seen in the same figure, the interlaminar strength of PAEK is superior to both PEEK and PPS composites at both temperatures. No visible distinction was also found between PPS and PEEK composites. In comparison to room temperature conditions, cold temperature resulted in an augmentation of interlaminar strength in all analyzed scenarios.

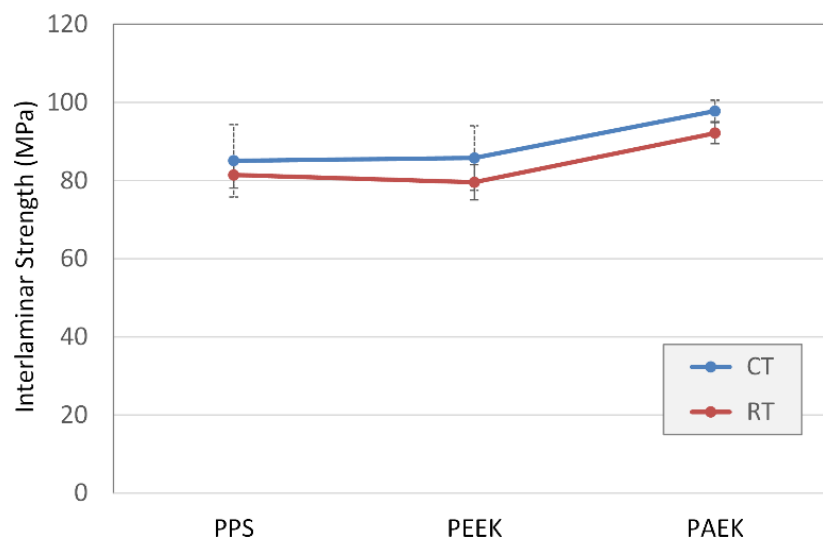


Figure 2.3. Interlaminar strength comparison of different thermoplastic resins at different testing temperatures (Source: Hron et al.³⁴)

There have been few studies on the strain rate dependent strengths of fiber reinforced thermoplastic composites. Strain rate sensitivity of an AS4/PEEK thermoplastic composite was investigated in the out-of-plane using compression split Hopkinson pressure bar by Zou et al.³⁵ It was shown that low incident pulse amplitude caused an incomplete failure at around 1500 1/s. Although, the pulse was not enough to establish complete failure and the specimen remained intact, a certain damage was formed on the test specimen. Increasing the strain rate in the elastic region did not yield a change in the elastic modulus while there was an increase in both failure stress and strain at higher strain rates. As the strain rate increased, the specimen completely failed and both failure strength, failure strain and dynamic compression modulus of the specimen increased. Microscopic observations revealed the failure modes and damage mechanisms at different

strain rates. Increasing strain rate changed the material failure mode and mechanism significantly.

High strain rate compression behavior of a 5-HS carbon fabric and a 8-HS glass fabric PPS thermoplastic composite were investigated by Ramirez et al.³⁶ The rectangular specimens having an area of 9x10 mm² were cut from the original laminates. The quasi-static compression tests at the strain rates of 0.001, 0.01 and 0.1 1/s were performed using a servo-mechanic universal testing machine. High strain rate tests were conducted using a split Hopkinson pressure bar test apparatus. Results showed that the strength and maximum strain of glass/PPS composites increased at increasing strain rates. On the other hand, the strength was shown to have no dependency on the strain rate for the CF/PPS composite specimens while the ultimate strain increased, and the elastic moduli decreased with increasing strain rate.

High strain rate and high temperature dynamic compression behavior of a 5-HS weave CF/PPS matrix thermoplastic composite was investigated by Wang et al.³⁷ The CF/PPS composites exhibited a linear strain rate dependency in the in-plane direction in which the compressive strength and modulus increased as the strain rate increased and decreased drastically at increasing temperatures. The out of plane compressive modulus increased at high temperatures while the compressive strength was not sensitive to the temperature. Also, the failure mechanisms of CF/PPS composites were affected by high strain rates and temperatures. At high temperatures and high strain rates, delamination was the main mode of failure.

Mohsin et al.³⁸ investigated the high strain rate impact behavior of the non-crimp fabric T700 CF/PA 6.6 thermoplastic rectangular composite specimens using a tensile Split Hopkinson Pressure Bar set-up. There was only a limited (3.5%) strength increase up to 700 1/s strain rate.

Wang et al.³⁹ examined two different thermoplastic composites with the same PPS matrix but with two different fabric reinforcements, 5-HS glass and carbon fiber. The study showed that there was a greater temperature dependence of the CF/PPS composite. The strength, elastic modulus and absorbed energy increased while failure strain decreased at increasing strain rates above a threshold strain rate for both materials (Figure 2.4(a-d)). Again, CF/PPS exhibited a linear relationship with the strain rate, as the strain rate increased above the threshold strain rate while GF/PPS composite show a gradual increase in the properties.

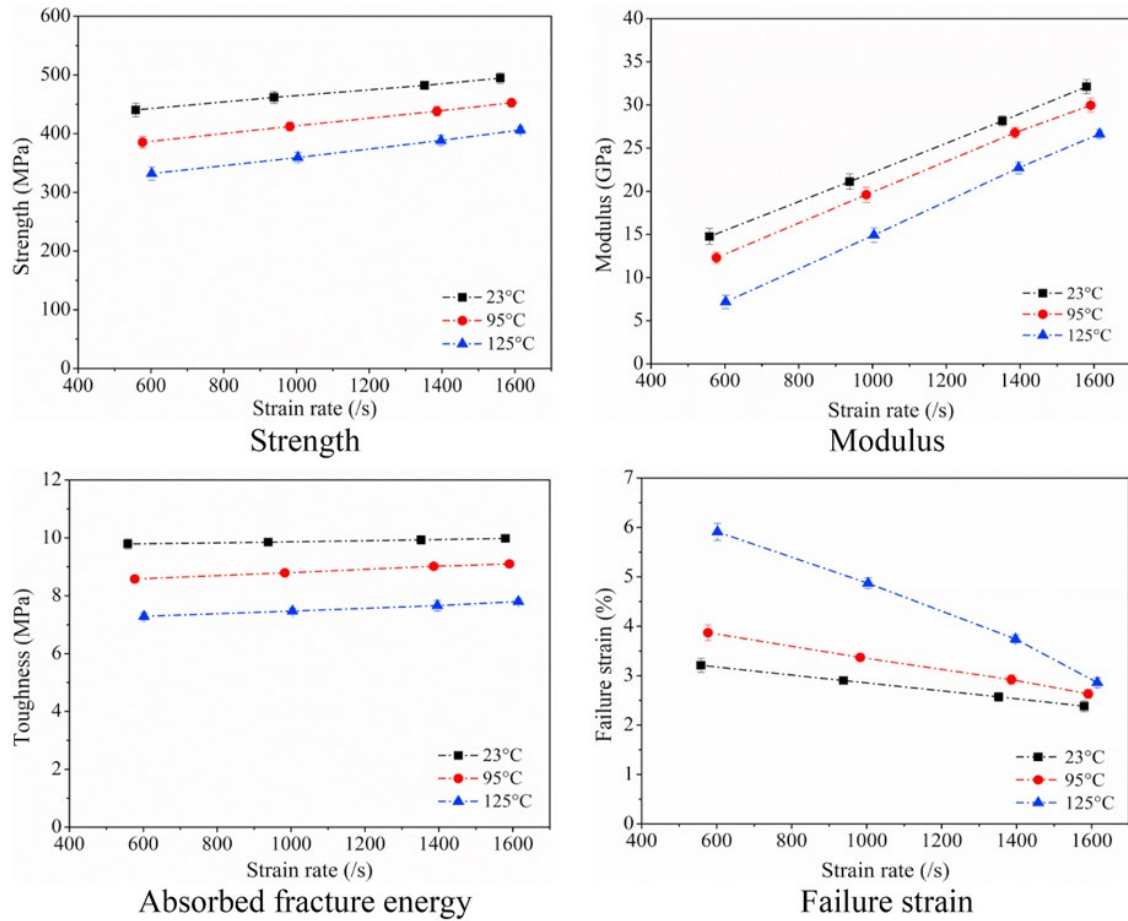


Figure 2.4. In-plane direction CF/PPS composite dynamic properties at various strain rates (Source: Wang et al.³⁹)

2.3. Impact Resistance and Damage Tolerance of Fiber-Reinforced Composites

In fiber-reinforced composites, the impact resistance is primarily influenced by factors such as fiber type, matrix material, fiber orientation, and the interfacial bonding between fibers and the matrix. High-strength fibers like carbon or aramid provide excellent impact resistance when properly oriented and embedded within a matrix material. Additionally, the design of composite structures, such as laminates or sandwich panels, can enhance impact resistance by distributing and dissipating impact energy efficiently. Effective impact resistance is crucial in applications where composite components may experience dynamic loads, such as aircraft fuselages, vehicle body panels, and sporting equipment, as it ensures the structural integrity and safety of the product under sudden stress.

Damage tolerance is closely related to impact resistance and involves the ability of a composite material to maintain its structural integrity and functionality even after sustaining damage. This property is of paramount importance in applications where composites are exposed to potential damage sources, such as impacts, micro-cracks, or fatigue loading. Damage tolerance is achieved through careful material selection, structural design, and the incorporation of toughening mechanisms within the composite. For example, the use of toughening agents like thermoplastic particles or interlaminar veils can help arrest crack propagation and prevent catastrophic failure. Furthermore, advanced non-destructive testing methods, such as ultrasonic inspections and thermography, are employed to detect and monitor damage within composites, allowing for timely repairs or replacements to ensure the continued safe operation of composite components. Overall, the combination of impact resistance and damage tolerance is essential for ensuring the reliability and longevity of fiber-reinforced composites in demanding applications.

During their service life, FRP composites may be subjected to both LVI and HVI damages. Especially, the composite aircraft structures are more susceptible to impact damage in their operational environment and maintenance condition. Foreign object damage such as tool drop, and low velocity crash runway debris can be classified as LVI. Cantwell and Morton⁴⁰ characterized LVI up to 10 m/s. Sjoblom et al. defined the LVI range between 1 and 10 m/s.⁴¹ Impact velocities above 10 m/s are generally accepted as intermediate or HVI.⁴² Jogur et al.⁴³ classified impact phenomena according to impact velocity. Low velocity impact is defined as the impact velocities lower than 11 m/s. High velocity impact was described as velocities over 11 m/s. Ballistic impact covers the impact velocities higher than 500 m/s. And, impact velocities higher than 2000 m/s were considered hypervelocity impact. The hail strike, bird strike, runway debris and ballistic impact are classified as HVI, which are above 100 m/s.

Composites can experience a variety of failures and may involve BVID, which can significantly reduce the structural integrity of the component. Richardson and Wisheart⁴⁴ stated that BVID may cause up to 50% strength reduction in composites. Since most composites are brittle, they can only absorb energy through damage mechanisms and elastic deformation, lacking the ability to do so via plastic deformation. Damage resistance pertains to the amount of impact damage incurred by a composite system. While the majority of impacts on a composite plate will be transverse, the lack of through-thickness reinforcement results in poor transverse damage resistance. Interlaminar

stresses, such as shear and tension, are often the cause of first failure due to low interlaminar strengths. Consequently, design failure strains of 0.5% are utilized to guard against impact failure, failing to fully capitalize on the superior in-plane strength and stiffness properties of composites.

According to Feraboli⁴⁵ damage resistance (or impact resistance) is defined as an evaluation of relationship between the force, energy, and the other parameters in the consequence of event or several events causing damage size and type. Damage tolerance on the other hand is defined as the relationship between an inherent damage size and type in the structure and the capability of maintaining structural functionality such as ability to sustain applied forces without failure. Drop weight impact tests are generally used for investigation of the dynamic response of composite structures and it is also referred to LVI test to measure damage resistance tolerance studies.

Ahmad et al.⁴⁶ investigated the impact responses of CFRP composite plates with different stacking sequences including quasi-isotropic, unidirectional, and cross-ply. The study evaluated the impact resistance of the composite plates by analyzing parameters such as peak impact force and absorbed energy. The results showed that the stacking sequence significantly affected the impact resistance of the CFRP composite plates. The cross-ply composite plate exhibited the best resistance to LVI load while the unidirectional composite plate showed the worst.

Shah et al.⁴⁷ proposed the factors that may influence impact resistance and damage tolerance of fiber reinforced composites explicitly as shown in Figure 2.5. The factors are considered as the primary and secondary. The primary factors that affects the impact resistance and damage tolerance of FRP composites include resin toughness and fabric architecture while secondary factors include for example the fracture toughness, test environment, the fiber and matrix response to the environment, fabric and matrix hybridization, and the properties of the impactor.

The effect of fiber and resin type, geometry and the bonding interphase between matrix and fiber on the impact resistance and after impact residual strength properties were investigated by Cantwell and Morton.⁴⁰ Thus, several parameters affect the results of LVI properties, not only one parameter is responsible for the whole damage characteristics. For example, it is stated that even if the impact kinetic energies are the same, an impact test with a large mass at a low velocity might not cause the same damage with a smaller mass at a higher velocity impact.

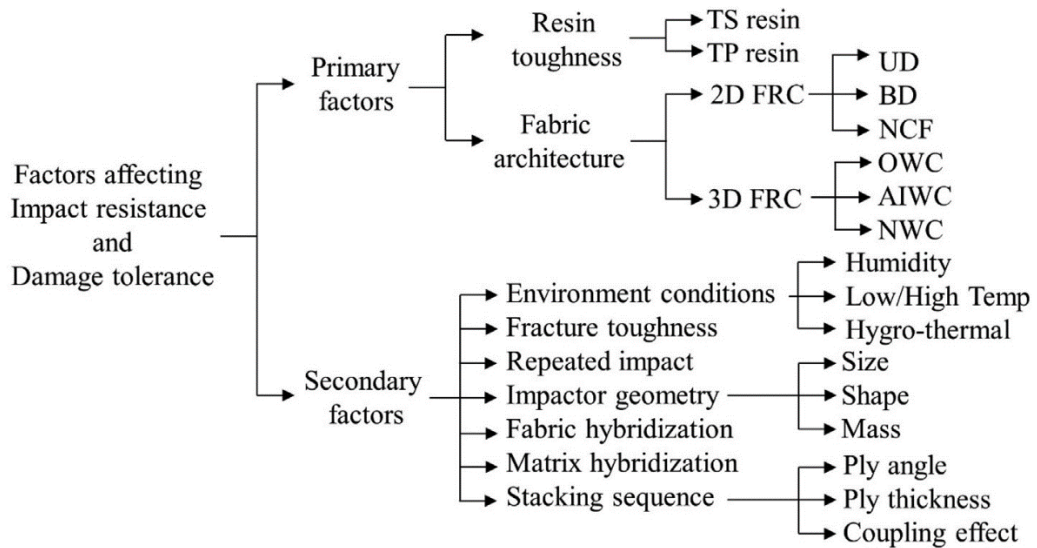


Figure 2.5. Diagram of factors that may influence impact resistance and damage tolerance of fiber reinforced composites (Source: Shah et al.⁴⁷)

Strait et al.⁴⁸ evaluated the effects of stacking sequence on the impact resistance of carbon fiber reinforced thermoplastic composites. Drop weight impact tests were performed on the samples with different lay-ups. The impact in the same study was characterized by the following parameters: energy required for incipient damage, peak load, absorbed energy at peak load, energy required for penetration and energy after peak load. Shah et al.⁴⁷ presented and described the typical examples of plots obtained during a LVI test, depicted in Figure 2.6 (a-c). Figure 2.6(a) shows the schematics of force-time, energy-time, and deflection-time plots of a typical LVI test. The oscillations are observed in the force-time plot due to transient stress waves in the transverse direction. The maximum peak force in the same figure is denoted as " F_{max} ," while the maximum contact time between the FRC material and impactor is represented as "OA." The area under the force-deflection curve corresponds to the composite's energy absorption. The bending stiffness of the composites is determined from the slope of the force-deflection diagram, depicted in Figure 2.6(b). Furthermore, the diagram offers valuable insights into the composite's permanent deflection (indentation), which is denoted as "G" and "H". Figure 2.6(b) also illustrates various damage scenarios resulting from LVI, such as the rebounding of the impactor, the maximum deflection of the composite without perforation, the perforation of the impactor, and the penetration of the impactor, which are represented by the points "G," "H," "I," and "J," respectively. In the event of a rebound, the point "E" corresponds to the maximum deflection. Figure 2.6(c) illustrates the comparison between the force-deflection plot denoted by " $F(\delta)$ " and the energy-

deflection plot indicated by " $E(\delta)$ ". In the " $E(\delta)$ " plot, the point "B" represents the energy at the damage initiation, specifically matrix cracking. On the other hand, the "BA" line signifies the energy absorption during damage propagation, which encompasses matrix crack, plasticization, and fiber failure. Once the fiber failure occurs at point "A," the impactor undergoes perforation. Consequently, the energy remains constant thereafter. The perforation energy, termed as " E_{perf} ", results from the combination of both damage initiation energy, referred to as " E_{ini} ," and damage propagation energy, denoted by " E_{prop} " in the " $F(\delta)$ " diagram, point "D" indicates the location where the impactor stops due to friction. Consequently, the force becomes zero.

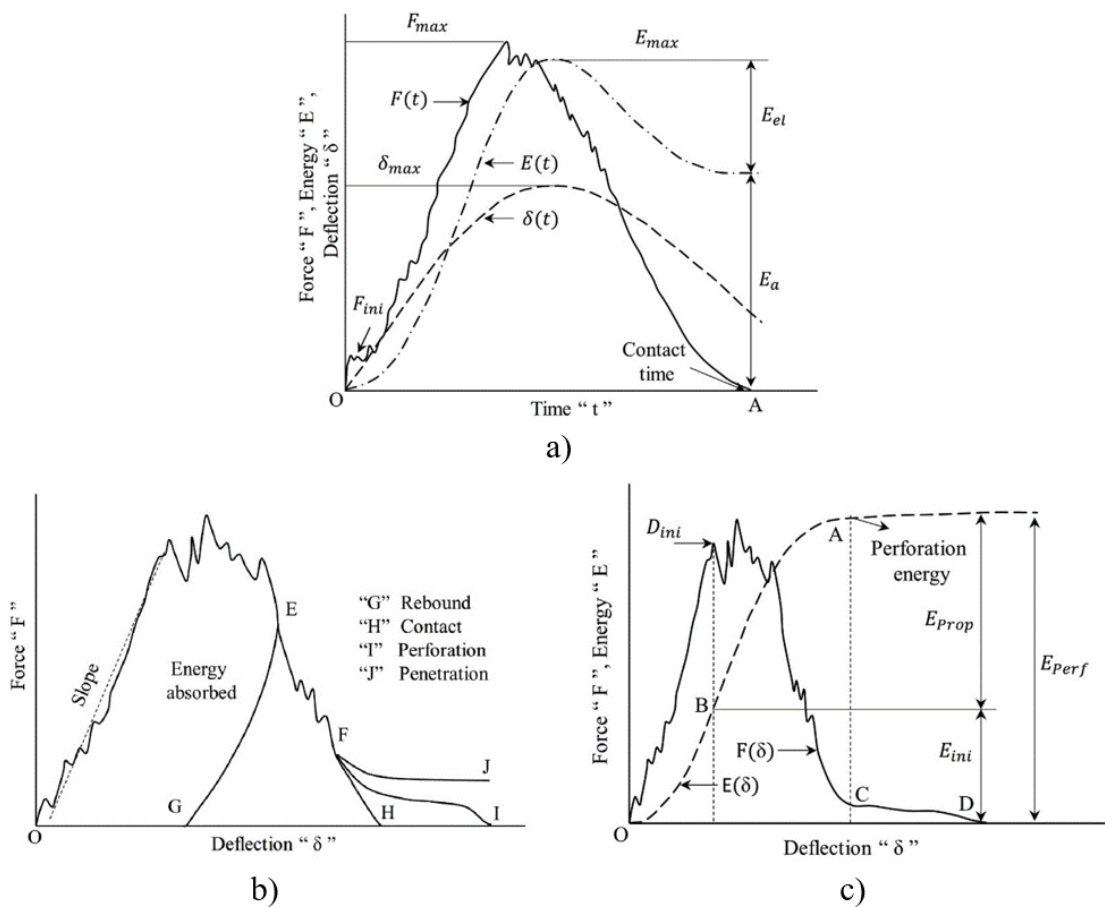


Figure 2.6. Schematic diagrams for generic low velocity impact test; a) Force-Energy-Deflection-Time plot, b) Force-Deflection plot and c) Force-Deflection and Energy-Deflection plots (Source: Shah et al.⁴⁷)

In a LVI test, several parameters are crucial to determine the impact resistance. Vaidya⁴⁹ described these parameters as the incident impact energy, impact velocity, incipient energy (E_i), total energy absorbed (E_t), total deflection (l_t), incipient damage point (P_i), maximum load (P_{max}), failure load point (P_f), total load point (P_t), energy at

maximum load (E_m), deflection at maximum load (l_m), and energy ($E_p = E_t - E_m$) and deflection ($l_p = l_t - l_m$) after maximum load (Figure 2.7). The point of incipient damage (P_i and E_i) is characterized by distinguished matrix microcracking, fiber damage, or onset of debonding. This point is the first significant deviation or break from the initial portion of the load-time curve. In many cases, the incipient damage point corresponds to the maximum load point (P_m). The maximum load point (P_m) and energy (E_m) signify the maximum penetration of the impactor and beginning of its rebound. The failure load (P_f) and energy (E_t) points represent the specimen response to the end of the rebound phase of the impactor, and subsequently the end of event is represented by P_t and E_t respectively. The determination of each of these parameters is influenced by several factors, including material thickness and geometry, boundary conditions, damage accumulation, fiber orientation, interface variations, geometry of the projectile (sharp, blunt, spherical).

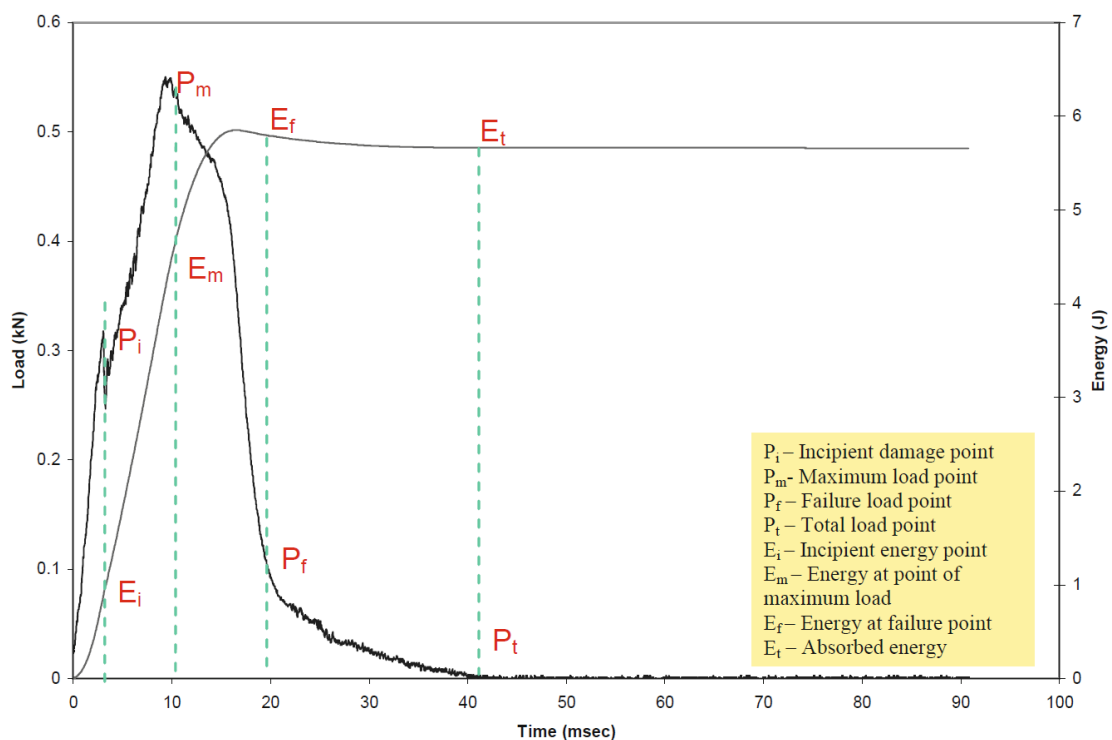


Figure 2.7. An example of Load versus Time curve and important points.
(Source: Vaidya⁴⁹)

In the same work of Vaidya, failure modes of fiber reinforced plastic composite laminates under LVI are described. It is stated that several failure modes occur due to the non-homogeneous and orthotropic behavior of composites. These are matrix cracking, delamination, fiber failure and buckling, and penetration.⁴⁹

The compression after impact test is a vital tool for evaluating the post-impact performance of polymer matrix composites. The roots of CAI tests on the polymer matrix composites can be traced back to the aerospace sector where these materials are extensively used. Early research in this domain was primarily driven by a need to assess the structural integrity of composite components following LVI. The compression after impact test methods tailored to polymer matrix composites have been developed, which may include adaptations of standardized tests like ASTM D7136 and Boeing CAI tests. Specialized test apparatus and load frames have been designed to accommodate the unique properties and configurations of polymer matrix composite specimens. Polymer matrix composites often exhibit a range of damage types of post-impact, including delamination, matrix cracking, and fiber damage. Researchers employ non-destructive evaluation techniques such as ultrasonic testing, X-ray computed tomography, and thermography to assess the extent of internal damage in polymer matrix composites. Extensive research focuses on understanding the behavior of polymer matrix composites in CAI tests, taking into account factors such as resin type, fiber reinforcement, and layup configuration.^{50, 51} The aim is to optimize polymer matrix composite designs to enhance impact resistance and post-impact structural performance.

Environmental factors including temperature and humidity can significantly influence the CAI behavior in polymer matrix composites. Studies investigated how these factors affected the polymer matrix composite performance in CAI tests, particularly in aerospace applications. Aktas et al.⁵¹ investigated the CAI performance of E-glass fabric epoxy composite plates which are subjected to LVI at high temperatures. The CAI strength of E-glass composite plates was shown in the same study to be greatly affected by the impact tests at different temperatures.

Emerging technologies like DIC, FEA, and machine learning are being integrated into the CAI test research on polymer matrix composites. These innovations hold the potential to enhance our understanding and prediction of the post-impact behavior of polymer matrix composites.

2.3.1. Impact Behavior of Thermoplastic Composites

The impact behavior of fiber-reinforced polymer matrix composites was subjected to several studies.^{40, 44, 45, 47, 52, 53} However, there are very few studies on the LVI of

thermoplastic composites.⁴⁹ A comparison between the impact damage resistance and CAI response of thermoset and thermoplastic carbon fiber-reinforced composites was performed by Bajurko.⁵⁴ It was shown that thermoplastic laminates exhibited higher compressive strength than thermoset laminates at low impact energies. The impact properties of thermoplastic composites has been reviewed by Jogur et al.⁴³ Thermoplastic PPS, PES, PEI and PEEK resins are classified as high temperature thermoplastics as they are processed at elevated temperatures. These resins also offer better mechanical properties than other thermoplastic resins.

Polymer matrix composites are recognized for their vulnerability to internal damage due to transverse loads, even during LVI. Both surface and internal damage can occur in these composites even at LVI and is hardly noticeable upon visual examination of the surface. In an LVI event, several damage modes can occur on the composite such as delamination, fiber breakage, matrix cracking and debonding at the fiber-matrix interface. All these failure modes have greatly influenced the energy absorption capability and the residual strength properties of the composites. Several parameters may influence the impact resistance and failure modes of the composites, including fiber type, matrix type, lay-up, thickness, loading velocity, projectile and specimen geometry.⁵²

The effect of temperature on the mechanical behavior of thermoplastic laminates was investigated in several studies.^{21, 39, 55} Sorrentino et al.⁵⁶ investigated the effect of temperature on the static and LVI properties of various thermoplastic composites. Dubary et al.⁵⁵ examined the impact behavior and damage tolerance of woven ply thermoplastic laminates at elevated temperatures. It was shown that PEEK laminates had very good properties regarding high permanent indentation, impact detectability, and reduced delamination as well as damage tolerance properties even at elevated temperatures. The impact energy to impose BVID was decreased by 24% when the temperature increased from room temperature to glass transition temperature. In parallel to this, visible damage area decreased nearly 3 times at 150°C compared to room temperature. Additionally, it was stated that impact induced damage did not affect the CAI strength of the laminates.

Liu et al.⁵⁷ compared impact damage behavior of thermoplastic and thermoset composites at low and high velocities, between 4.5 and 10.5 J (Figure 2.8(a-c)). Less damage area and fewer oscillations in load versus time curves were captured at LVI tests in the CF/PEEK thermoplastic composites. It was further concluded that the impact damage resistance of CF/PEEK composite was better than that of CF/Epoxy composite. C-scan images revealed that there was no damage zone for the 4.5 J impact test in the

CF/PEEK specimen while damage existed in the CF/Epoxy specimen at the same impact energy. Also, C-Scan images revealed that all CF/PEEK specimens had lower damage areas than CF/Epoxy specimens. Higher delamination and damage areas were observed in the HVI tests than the LVI tests. The reason behind this might be localized impact damage on the impact side which caused delamination and crack growth through the ply interfaces. It was also reported that high strain rate effect might be another reason for the higher damage in the HVI tests since interlaminar and matrix fracture energies decreased for both CF/PEEK and CF/Epoxy composites.

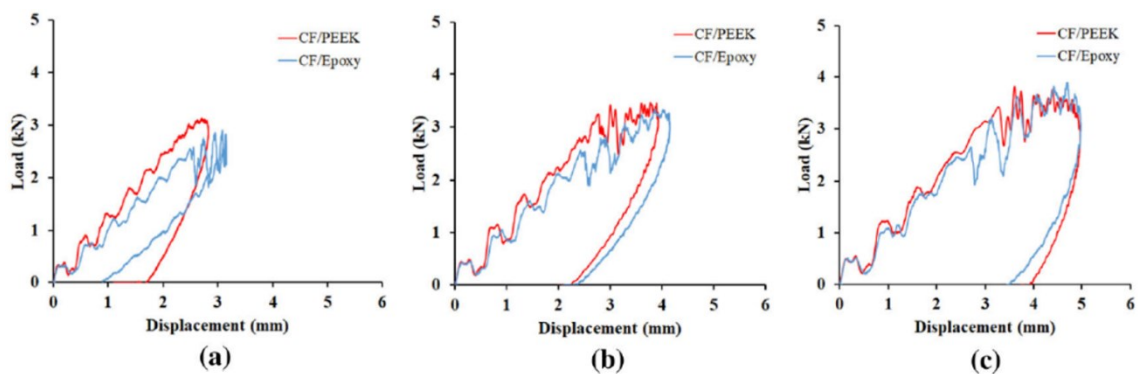


Figure 2.8. Load versus displacement curves for the low-velocity drop-weight tests for the CF/PEEK and CF/Epoxy specimens at impact energies of a) 4.5 J, b) 7.5 J and c) 10.5 J (Source: Liu et al.⁵⁷)

The LVI performance of non-crimp fabric T700 CF/PA and T700 CF/PPS thermoplastic composites were investigated experimentally and numerically by Mohsin et al.⁵⁸ Drop weight impact tests were performed at 40, 100 and 160 J impact energy levels. The delamination mode was affected by the interlaminar properties in which weaker interlaminar shear properties of T700/PPS resulted in more delamination damage than the T700/PA. Consequently, T700/PPS composite absorbed more energy per areal weight under the same impact energy level. The numerical results represented good correlations with the experimental results at 40 J. However, the discrepancies occurred at higher impact energies. The numerical model was not able to capture extensive delamination and shear plugging at high energy levels.

Nejhad and Majidi⁵⁹ performed drop weight and CAI tests on CF/PEEK and CF/PPS. Three different impact energy levels were chosen to investigate the effect of impact energy. After the impact tests, the specimens were subjected to the CAI tests. The perforation energy of the CF/PPS was found to be significantly higher than that of CF/PEEK. The dynamic response curves increased with increasing impact energy. The

failure modes were more dominant in CF/PPS and the failure modes included delamination, fiber breakage, matrix cracking, fiber matrix debonding and pull-out for both materials. The larger damage area of the CF/PPS specimens led to lower residual compressive strengths and strains. An improved CAI strength of CF/PEEK composite indicated a higher matrix failure strain, leading to a higher interlaminar fracture toughness.

Vielle et al.⁶⁰ showed that the matrix toughness had a great influence on the impact performance of fiber reinforced polymer composites. They performed LVI tests on CF/Epoxy, CF/PPS and CF/PEEK composites at five different impact energy levels: 2, 6, 10.5, 17, and 25 J. Microscopic, macroscopic, and C-scan inspections were performed on the impacted specimens to determine the damage patterns and failure modes. CF/PPS exhibited mainly fiber/matrix debonding as well as interlaminar cracking and delamination, fiber breakage and fiber bridging (Figure 2.9). It was found that CF/Epoxy laminates were subjected to larger damage area than the thermoplastic composite laminates meaning tougher matrix have a great influence on the impact performance of FRP composites.

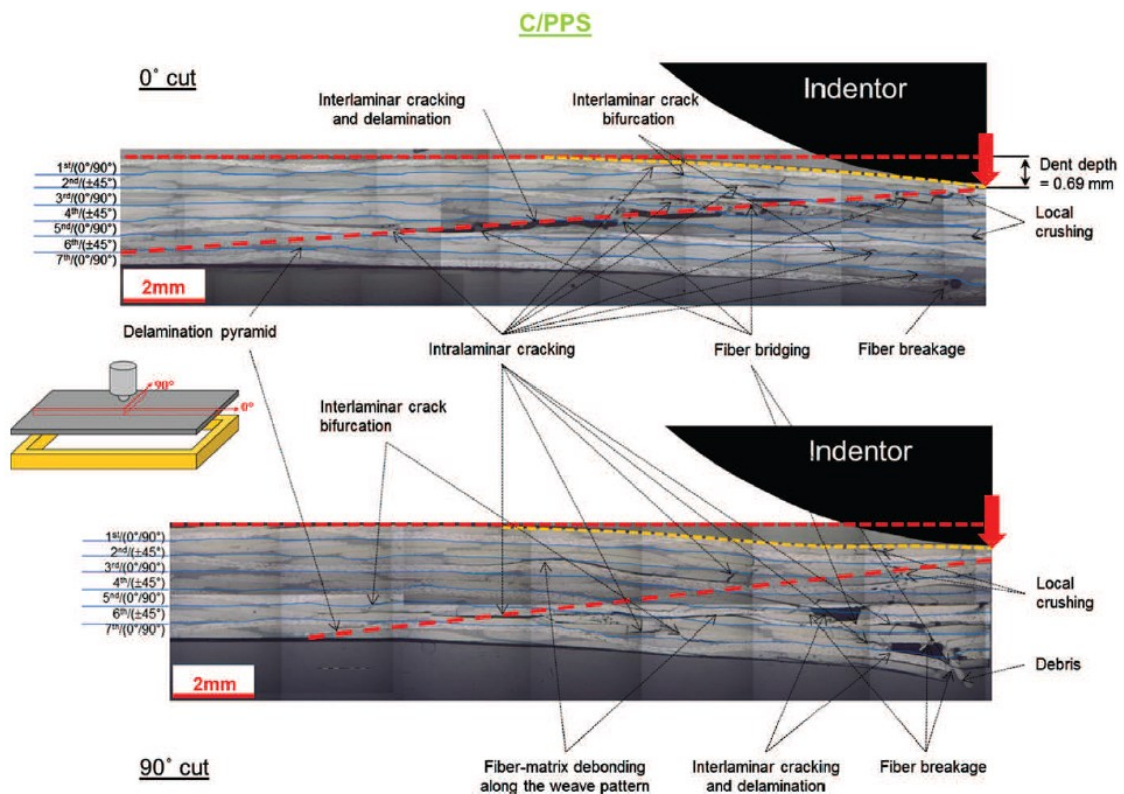


Figure 2.9. Microscopic image of impacted C/PPS specimen at 17 J (Source: Vielle et al.⁶⁰)

The effect of resin on the LVI behavior of thermoplastic and thermoset composites having the same carbon fiber reinforcement was investigated by Schimmer et al.⁶¹ CF reinforced epoxy thermoset composite and PEEK thermoplastic composites were subjected to LVI tests having two different lay-ups; cross-ply and quasi-isotropic stacking sequence. They showed that the C-Scan images of the damage projection area of the impacted specimens with respect to impact energy. Results showed that thermoplastic composite exhibited higher damage tolerance and lower damage area than the thermoset composite (Figure 2.10). Also, quasi-isotropic lay-up showed larger damage area than the cross-ply laminates. This outcome is more dominant in epoxy thermoset composite system.

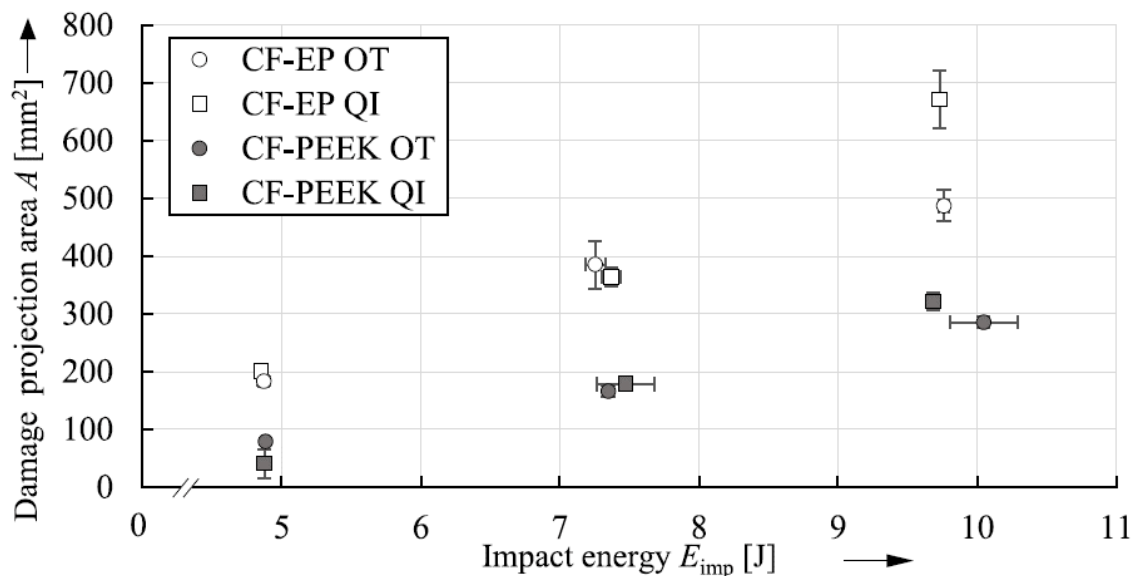


Figure 2.10. Impact energy versus damage projection area of different composite systems with different lay-ups (Source: Schimmer et al.⁶¹)

The LVI response of CF/PPS composite under 30, 50 and 70 J was investigated by Vaidya.⁴⁹ There was an exponential increase in the damage area with increasing impact energy levels as shown in Figure 2.11. It was concluded that fiber fracture was the main mechanism for the failure at low impact energy levels. When the energy level was sufficient to propagate damage and perforate through the panel, there was up to 50% abrupt reduce in the load bearing capacity and the panel failed gradually until it was unable to carry no more loads as shown in Figure 2.12. It was also seen that as the impact energy is increased the failure mechanism is changed from onset of back face penetration to perforation.

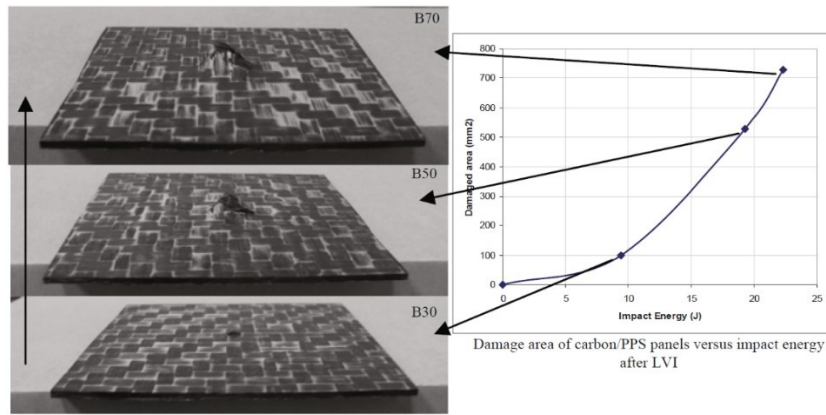


Figure 2.11. Damage area of CF/PPS versus impact energy after LVI (Source: Vaidya⁴⁹)

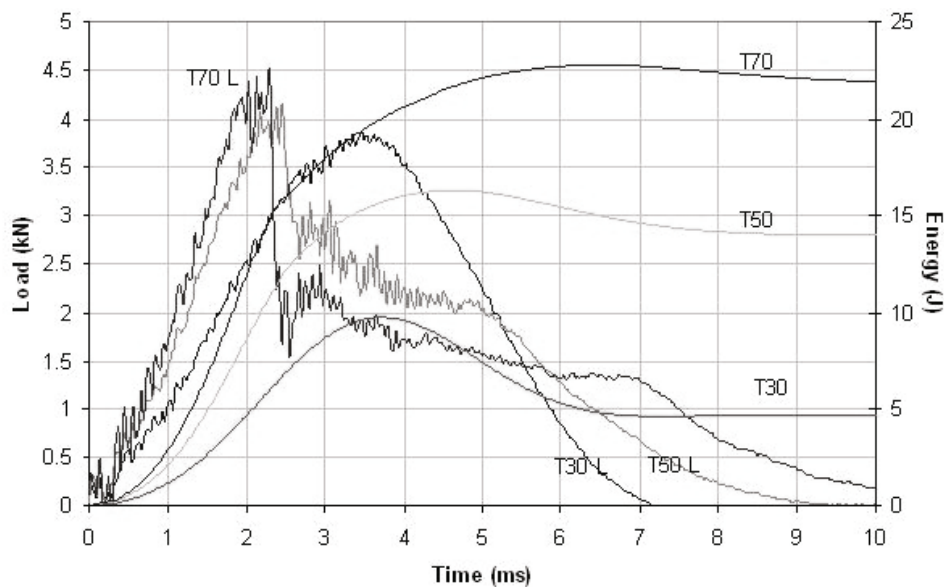


Figure 2.12. Low velocity impact tests of CF/PPS composites having 3 mm thickness; rebound (T30), onset of back face penetration (T50), and perforation (T70) (Source: Vaidya⁴⁹)

A comparison was also made between the LVI and HVI behavior of thermoplastic and thermoset composites laminates having cross-ply layups by Liu et al.⁶² A drop weight impact test setup was used for the LVI tests and a gas gun was used for the HVI tests. The out-of-displacement of the specimens were measured using 3D DIC. C-scan inspection was used to observe damaged areas on the specimens. The impact energy levels of 4.5, 7.5 and 10.5 J were employed for the LVI tests. Peak loads of the CF/PEEK composites were higher than those of CF/Epoxy composites at all impact energy levels. CF/PEEK composite also exhibited lower damage areas in the C-scan images, proving a higher

impact resistance. Also, the HVI gas gun tests resulted in higher damage than the low velocity drop-weight tests.

During the process of aircraft takeoff and landing, the presence of debris on the runway may result in damage. This impact scenario with small mass and high velocity objects can be best simulated at the laboratory using a gas gun impact test setup.⁵² The HVI behavior of CF/PPS thermoplastic composites was investigated by experimentally and numerically to determine the ballistic limit.⁶³ Numerical predictions were shown in a good agreement with those experimental tests.

Dear et al.⁶⁴ conducted HVI tests on CF/Epoxy and CF/PEEK composites. A gelatine body was used as a soft projectile to represent a bird strike and a hard aluminum alloy projectile was used to represent the foreign body impact. The HVI tests up to 100 m/s were carried out using a gas gun set-up utilizing a 3D DIC system to visualize out of plane displacements of the composite specimens at different impact velocities. The variation of the damage area and kinetic energy absorption as function of impact energy for the tested composites are shown in Figure 2.13. The CF/PEEK composite specimens demonstrated lower maximum out-of-plane displacements than CF/Epoxy composite specimens. No delamination was observed for the 100 m/s soft body gelatine impact on CF/PEEK thermoplastic composite whereas delamination type damage mode was found in the CF/Epoxy composite specimen which shows the superior damage resistance characteristics of thermoplastic composites. In addition to that, CF/PEEK composite exhibited better damage resistance and lower damage area when it was subjected to the high velocity a hard aluminum alloy projectile impact.

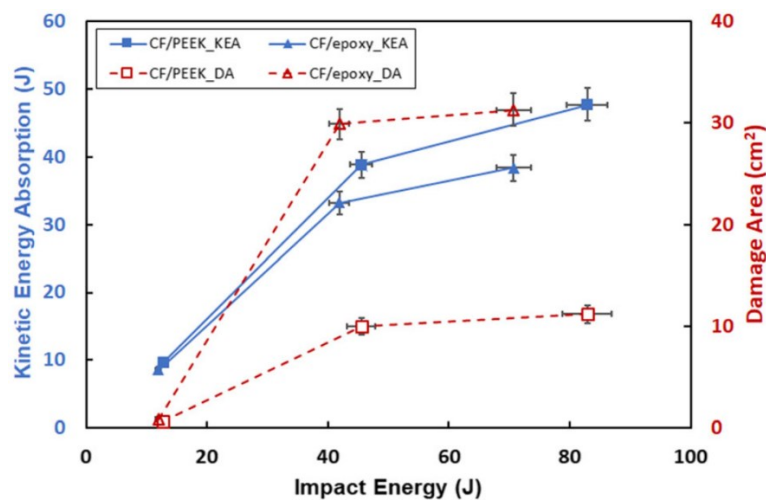


Figure 2.13. Impact energy versus KEA and damaged area of the CF/PEEK and CF/epoxy comparison (Source: Dear et al.⁶⁴)

2.3.2. Compression After Impact Behavior of Thermoplastic Composites

The C-Scan inspections showed that thermoplastic composites had less damage area as compared with epoxy-based composites.¹⁸ The LVI damage and CAI behavior of CF/PEEK thermoplastic composite laminates was studied by Liu et al.⁶⁵ An ultrasonic C-scan inspection was employed to explore structural damage and a DIC technique was used to measure the full-field displacement measurements in the CAI tests. The LVI and CAI response were further predicted numerically. The experimental results of the CAI strength and normalized strength versus impact energy are shown in Figure 2.14(a) and (b), respectively.

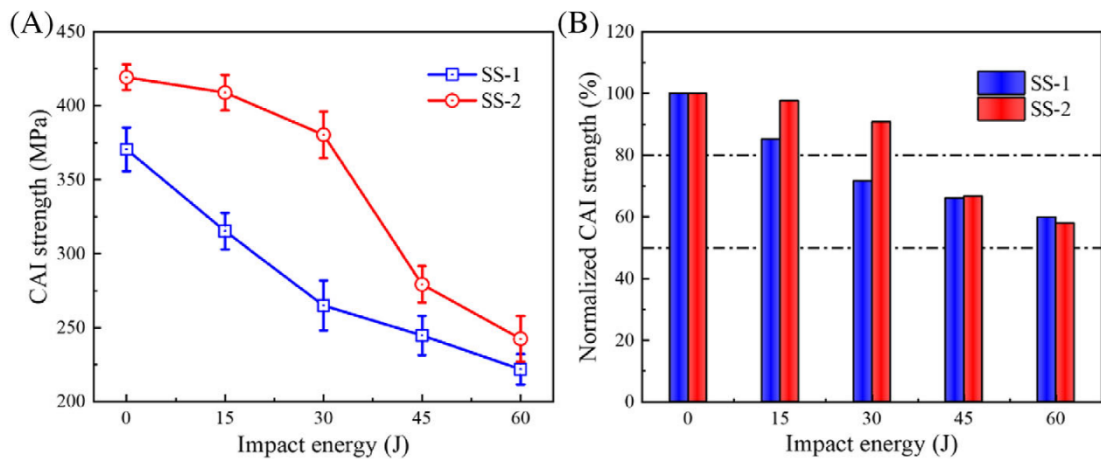


Figure 2.14. Impact energy versus CAI strength for CF/PEEK thermoplastic composite laminates (Source: Liu et al.⁶⁵)

The residual compressive strength and LVI behavior of woven thermoset and thermoplastic composites were compared by Vieille et al.⁶⁶ Woven ply 5-HS weave CF/PPS and CF/PEEK and CF/Epoxy laminates, sequentially having the thicknesses of 2.31, 2.24 and 2.4 mm were subjected to LVI tests at 2, 6, 10.5, 17, and 25 J. The impacted specimens were compressed at a constant velocity of 0.2 mm/min. A 3D-DIC technique was employed to observe the strain field and crack propagation on the specimen surface. It was concluded that the residual strength of PEEK-based thermoplastic laminates was 40% higher than that of PPS-based thermoplastic laminates and 10% higher than the CF/Epoxy laminates for those specimens impacted at low energies as shown in Figure

2.15. For the high-impact energy levels, the three-material system exhibited similar strength behavior.

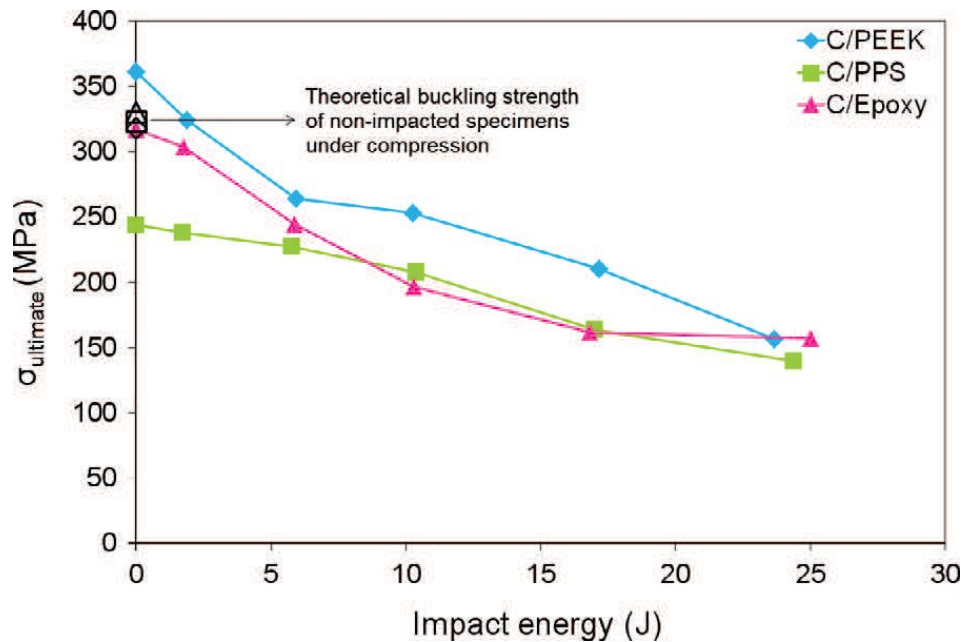


Figure 2.15. Impact energy versus CAI strength of different composite systems (Source: Vieille et al.⁶⁶)

The CAI behavior of three composites, T300/976/Epoxy, AS4, and IM-7 fiber thermoplastic PEEK APC-2 were experimentally investigated.⁶⁷ The CAI strength and delamination area versus normalized impact energy of the composites are shown in Figure 2.16(a) and (b), respectively. It is seen in Figure 2.16(a) that the CAI strength reduction is more obvious in the thermoset composite. Also, as the impact energy increases, the delamination increases for all composites as noted in Figure 2.16(b).

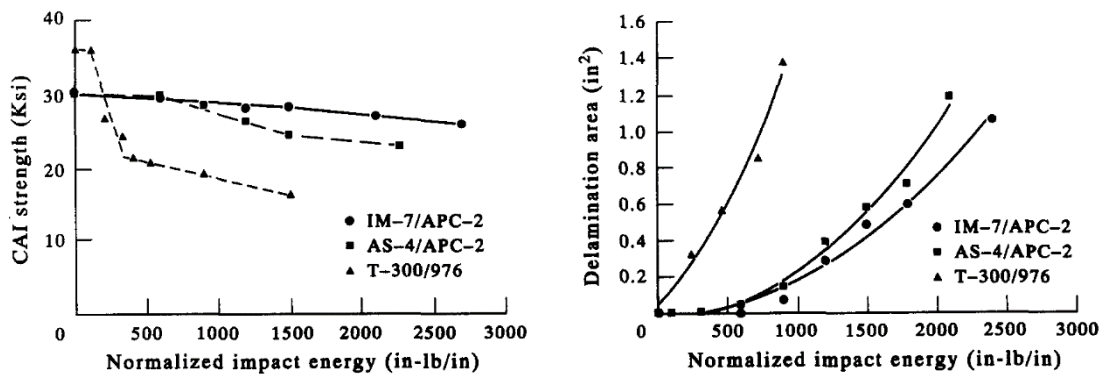


Figure 2.16. Normalized impact energy versus CAI strength and delamination area of three composite systems (Source: Ong and Liou⁶⁷)

2.4. Finite Element Modeling of Impact Damage and Damage Tolerance of Composites

The timeline of the design and manufacturing phase of a composite structural component of an aircraft are relatively long because many experimental tests may be needed in the development phase. Thus, predictive models of the composite structures have gained importance in the aerospace industry. Finite element modeling is a powerful method to investigate the structural response of a component under specified loadings, boundary conditions and etc. After validating the numerical modeling methodology, the same methodology can be used safely for further investigation, reducing the number of experimental tests; hence, the corresponding manufacturing time in the design phase. To obtain robust and accurate numerical simulation results, several factors must be satisfied. These factors include material model, cohesive zone, boundary conditions, and contacts. The constituted model should also be computationally cost-effective to reduce solution time.

Modeling composite laminates is not straightforward as with metallic materials since composite laminates are generally made of several plies, stacked in different angles, and exhibit orthotropic behavior. Modeling damage is also a challenge in fiber reinforced composites because there are different failure modes and damage mechanisms operating simultaneously like fiber failure, matrix cracking, delamination and etc. Capturing failure and damage in numerical analysis using finite element modeling techniques require careful selection of constitutive material modeling.

Delamination is a dominant failure mode for the composites under transverse impact loading. Explicit numerical analysis methods are generally used to solve impact loading cases which include contact, material, and damage non-linearity. In numerical analysis, cohesive zone modeling between composite plies is used to predict delamination failure. There are two most common methods used by researchers which are cohesive interface elements between plies and cohesive interface contact definition between each ply.

Olsson⁶⁸ emphasized the importance of computational methods for evaluating the impact damage and impact response of polymer matrix composites. Limaye et al.⁶⁹ performed a series of experiments and numerical analysis to obtain the optimal manufacturing-to-response pathway of carbon fiber-reinforced thermoplastic-based

composites manufactured using a thermoforming process. The study was dedicated to the manufacturing-to-response pathway of thermoplastic composites in which the relationship between the manufacturing process and mechanical performances was established. To obtain the effect of manufacturing processes, thermoforming analyses were performed. Experimental studies including coupon level material characterization, quasi-static three-point bending tests, and dynamic impact tests were also accomplished to measure the mechanical performance of manufacturing-induced effects of the thermoforming process and used in the finite element modeling of experimental validation studies. The material used in this study was twill weave CF/PA thermoplastic composite laminates. LS-DYNA was used for numerical analysis studies. MAT_58 material model was used for the static and quasi-static three-point bending tests and MAT_54 material model was used for the dynamic impact tests. A good agreement was achieved between the experimental and numerical results. Thermoforming process-induced effects such as thickness changes, fiber orientations, and residual stresses were also investigated numerically.

The crashworthiness behavior of twill weave glass fabric reinforced PA6 thermoplastic composite was investigated by Striewe et al.⁷⁰ The numerical simulations of the crush tests were performed in LS-DYNA. Shell elements with interlaminar contact definitions were set for the composite modelling and MAT-54 material model was selected as the constitutive model. Force-displacement curves and specific energy absorption characteristics were compared experimentally and numerically. The results showed that there was a good correlation between the experimental and numerical results. It was also stated that the thermoplastic composite made of bidirectional glass fabric was a promising material for automotive industry.

Liu et al.⁵⁷ developed numerical analysis simulations to predict the LVI and HVI behavior of thermoplastic CF/PEEK and thermoset CF/Epoxy composites. The Hashin failure criteria was used as the failure and interlaminar damage model for the cohesive zone modeling. There was a good agreement between experimental test and FE analyses in terms of load versus time curves and damage areas for both LVI and HVI cases. The LVI comparison results for damage area and load versus time curves for CF/PEEK composites are shown in Figure 2.17(a-c). The discrepancy between the experimental results and the simulation is increasing with increasing impact velocity. Also, with increasing impact velocity the fluctuations in both experimental and numerical load-time curves are increasing.

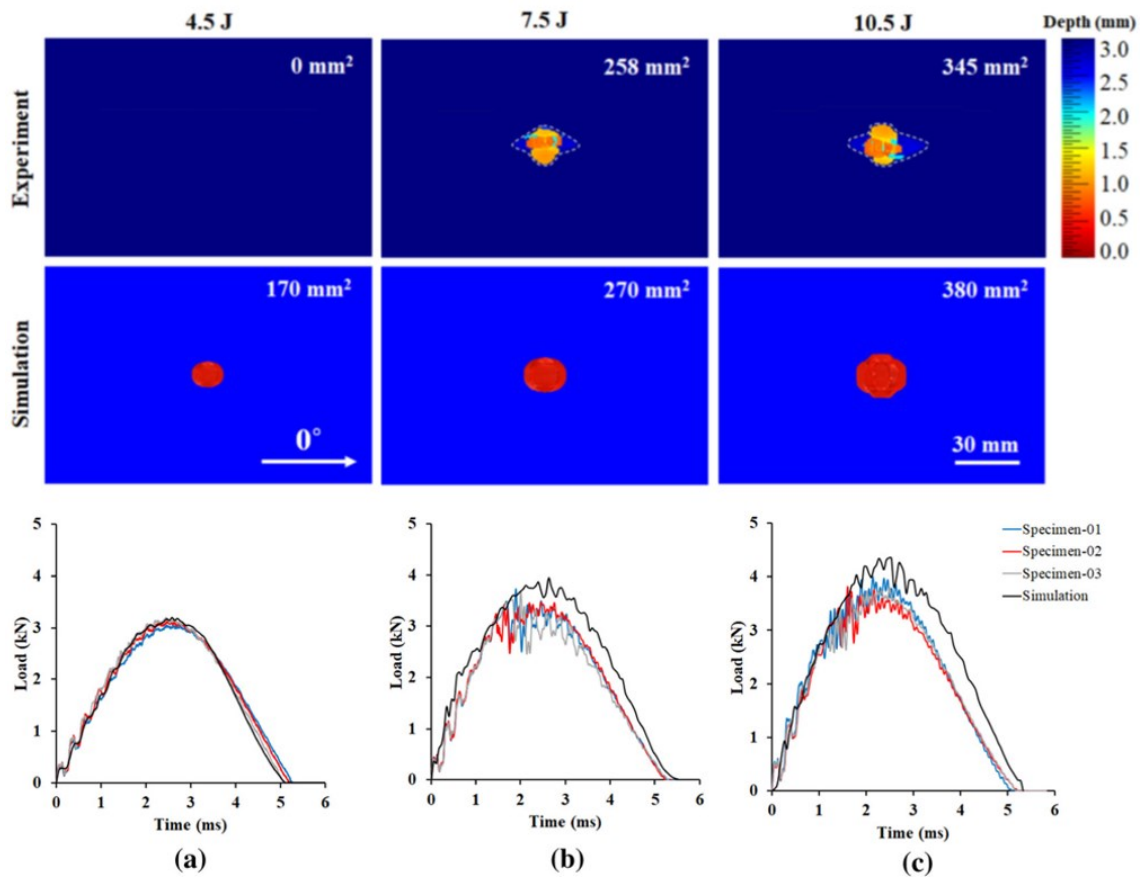


Figure 2.17. Experiment and simulation comparison of damage area and load versus time curves for CF/PEEK composites a) 4.5, b) 7.5 and c) 10.5 J (Source: Liu et al.⁵⁷)

Bogenfeld et al.⁷¹ reviewed the LVI analysis techniques of the composite laminates and made a benchmark study. Six representative modeling approaches in different scales were derived and considered for a qualitative and quantitative benchmark study. These approaches include high-fidelity models on mesoscale, macro-scale shell models, and analytical estimations. Analysis methods from simple analytical approach to complex finite element modelling are shown in Figure 2.18. The authors suggested the use of a layered-shell model for the impact analysis on the structural level. This modeling approach involves the use of solid or shell elements to represent the specimen layup, with interfaces for delamination and cohesive zone approaches for capturing damage. The used modeling approach was considered suitable for structural level composite analysis due to its balance between accuracy and computation effort. However, the study also acknowledged that the computation effort of an accurate mesoscale model was too large for direct application on the structural level. Therefore, the layered-shell model was recommended as a practical alternative for impact analysis. Raajeneesh and Bruyneel⁷²

developed a modified mesoscale finite element model to predict LVI and CAI behavior of composites. The intraply behavior of the laminates was described using a modified mesoscale model, while the interply behavior was captured using cohesive elements. They concluded that the developed model accurately predicted the behavior of composite laminates under LVI and CAI conditions.

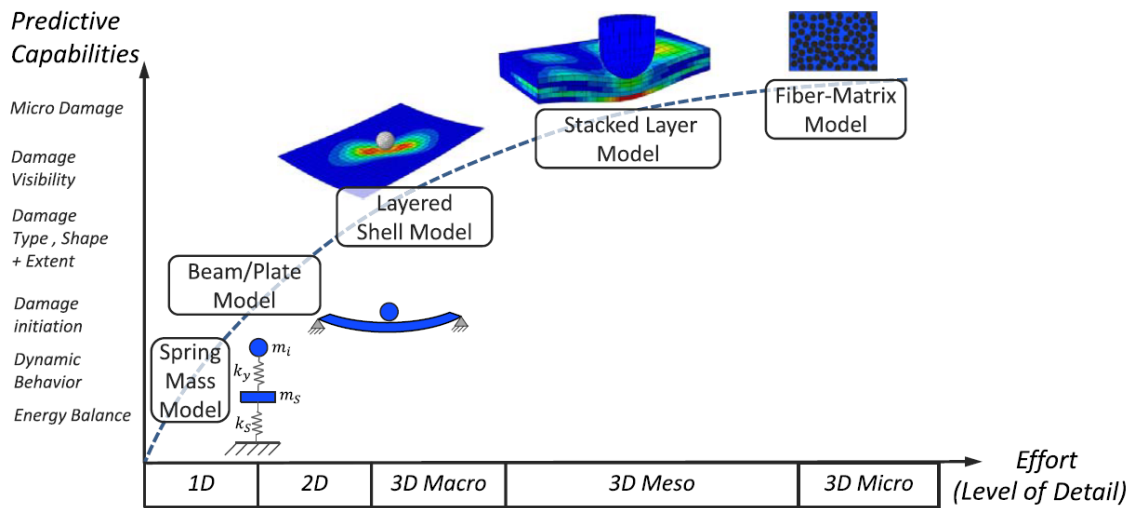


Figure 2.18. Different methods for impact analysis (Source: Bogenfeld et al.⁷¹)

2.4.1. Numerical Constitutive Material Modelling Studies

Constitutive material modeling is a crucial issue in numerical modeling to predict actual phenomenon within good accuracy and reliability. There are many material models in finite element modeling of composites according to their complexity and limitations. Choosing a proper material model depends on element type (shell, thick shell, solid), model scale (micro, macro, and mesoscale), and complexity (delamination, strain rate, orthotropic properties etc.). Rabiee and Ghasemnejad⁷³ discussed various material models to simulate the crushing behavior of glass/epoxy tubes, including Composite Damage Models (MAT055055), Enhanced Composite Damage Models (MAT054-055), Laminated Composite Fabric Model (MAT058), and Shell-Solid Composite Failure Model (MAT059). They compared the performance of these material models in terms of their ability to predict energy absorption capability and computational cost. They suggested the material model MAT54-55 which could predict material behavior with

respect to energy absorption capability and has a reasonable computational cost compared to other models.

Zeleniakiene et al.⁷⁴ investigated the impact behavior of CF/ PMMA thermoplastic composites in LS-DYNA . The study used material models MAT58 and MAT54, which are based on the Matzenmiller damage mechanics⁷⁵ with four Hashin failure criteria and four Chang-Chang failure criteria, respectively. The numerical analyses showed good agreement with the experimental results in terms of contact force histories, peak forces, absorbed energy, and projected damage area.

Single stage gas gun was used to accelerate plate shaped projectile to the velocities in the range of 80-130 m/s to investigate the impact resistance of laminated and textile composites.⁷⁶ Numerical models of the experimental tests were built using LS-DYNA and MAT54 material model with the Chang-Chang failure criterion. To extract mechanical constants, quasi-static compression and tension tests were conducted. The authors concluded that finite element models accurately predicted the impact threshold and failure behavior of composite panels, and the numerical studies revealed the different impact resistances of the laminated and textile composites.

A detailed material model calibration and finite element analysis study was performed by Giannaro et al.⁷⁷ for aerospace grade CFRP composite laminate. Quasi-static tensile, compression, in-plane shear, short beam shear, and fracture toughness tests were conducted. LS-DYNA implicit code has been used to perform numerical analyses of the quasi-static mechanical tests. Ply-based stacked-solid elements method was used for the simulation of laminated composite specimens. MAT54 material model with the Hashin failure criterion was implemented since it included tensile and compressive failure in matrix and fiber mode. MAT_186 cohesive material model was used to model cohesive zone between plies. The study proposed a calibration routine to optimize material model parameters for virtual simulation of impact tests on composite materials, improving the accuracy of numerical predictions. The calibration process was divided into two parts: in-plane loading tests for the calibration of orthotropic damage material model, and interlaminar fracture tests for the adjustment of cohesive model parameters. After calibration, the numerical simulations showed a significant reduction in the difference between the numerical and experimental delamination area for both low and high-velocity impact. The computational error in terms of maximum compressive load during compression loading was close to 1% for both impact conditions, indicating the accuracy of the calibrated material models.

Gonzalez et al.⁷⁸ used a finite element modeling strategy in ABAQUS/Explicit software to simulate LVI and CAI behavior of composite laminates. Conventional shell elements and cohesive surfaces were used with surface elements on the top and bottom faces of the layers to solve the out-of-plane structural response. The modeling strategy was validated by simulating monolithic and rectangular laboratory coupons. The modelling results showed good agreements with the experimental results.

Chatla⁷⁹ investigated several material models available in LS-DYNA for modelling composite laminates. These material models included MAT22, MAT54-55, MAT58, and MAT59. Among those investigated material models, MAT58 was selected as the best choice regarding accuracy and complexity.

2.4.2. Cohesive Zone Modeling of the Composite Laminates

Cohesive zone modeling techniques are integral for simulating and understanding the behavior of composite materials, particularly in the scenarios where delamination or debonding between layers is concerned. These techniques focus on representing the adhesive forces between adjacent layers, offering a means to predict and analyze the initiation and propagation of delamination. The approach involves defining cohesive zones along the interface between layers, with each element modeling the cohesive behavior, typically characterized by traction-separation laws. These laws describe how the cohesive forces between the layers evolve as separation or sliding between them occurs. By incorporating cohesive zone models into numerical analyses, engineers and researchers can gain valuable insights into the delamination process, its location, extent, and the energy required for crack propagation. This information is essential for predicting damage tolerance and structural integrity, enabling the development of strategies to mitigate delamination in composite structures. Cohesive zone modeling techniques for simulating delamination and debonding in composite materials can be implemented through different numerical methods, including the use of contact elements and cohesive elements or layers of elements. Contact elements represent cohesive forces through contact interactions between surfaces and are often used for modeling the initial stages of delamination. In contrast, cohesive elements or layers of elements are designed to provide a more detailed and accurate representation of cohesive behavior, incorporating cohesive zone models that describe how cohesive forces evolve with separation or sliding between

layers. The choice between these methods depends on the specific analysis objectives and the level of detail required, with both approaches serving as valuable tools for comprehensively understanding and simulating delamination phenomena in composite structures.

Modeling cohesive elements between each ply requires additional elements and correspondingly more computational cost. The tiebreak contact algorithm is also an efficient method to simulate delamination damage in composite laminates. It does not require additional elements between each ply. Instead, a unique tiebreak contact algorithm shall be defined as adhesives between each ply. Tiebreak contact exists for the adjacent ply nodes which are initially in contact with each other. When the failure criteria satisfied for the tiebreak contact, the tied surface will be broken. One way contact algorithm in LS-DYNA code ties slave and master nodes of two adjacent plies that are initially in contact. A linear spring is created between the nodes, and it carries the load until maximum failure stress is met. After maximum stress is reached, the stress is decreased by a linear damage curve until the critical opening is reached. Then the spring is removed, and delamination occurs.⁸⁰

There are three main failure modes for delamination growth in composites namely Mode I, Mode II and Mode III. However, composites used in structural applications are usually subjected to mixed-mode loading.⁸¹ This means the damage onset can occur before any traction component reaches their allowable value. Thus, coupling interaction between different modes of energy release rate is needed to satisfy the mixed-mode failure criterion. Interlaminar damage in composite laminates is commonly created using bilinear traction separation constitutive law as shown in Figure 2.19.⁸² The Benzeggagh and Kenane (B-K) propagation criterion is a fracture mechanics-based model used to predict the onset and subsequent propagation of delamination or interface cracks in composite materials. It specifically addresses the interlaminar cracks, which occur between layers (plies) of composite. The B-K criterion is a widely accepted and practical tool in the field of composite materials and is particularly useful for understanding the delamination behavior in laminated composite structures.

Dogan et al.⁸³ used both tiebreak contacts and cohesive elements to model the delamination of impacted composites. The influence of tiebreak contact parameters was also studied. More realistic results were found with thin shell elements than solid or thick shell elements. It was also found that element size, contact parameters, simulation parameters and number of shell sub-laminates greatly affected the results.

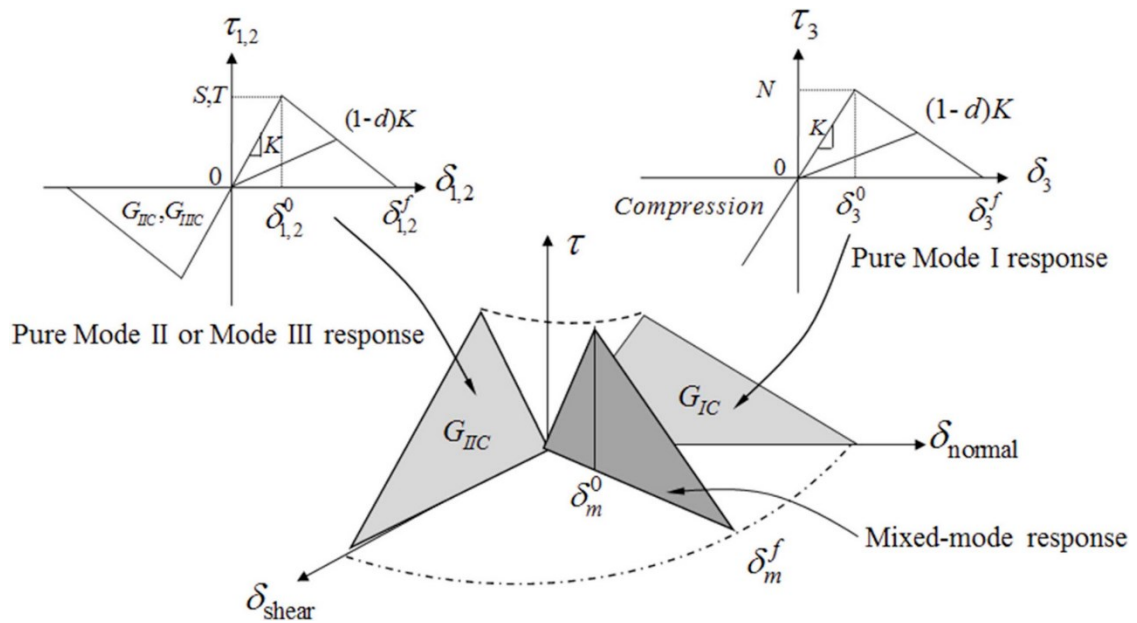


Figure 2.19. Traction separation law for interlaminar damage modeling of composite laminates (Source: Tuo et al.⁸²)

Ahmad et al.⁸⁴ used one way tiebreak contacts to model LVI delamination . They used solid elements to model composite laminate and utilized option 6 failure law for the separation of solid element layers. In option 6, nodal normal and shear stresses are implemented as failure criterion for interface strength to control delamination. It was stated that geometric shape and dimensions of the delaminated area was well predicted by the constituted numerical model.

The two adhesive modeling techniques; tiebreak contact, and cohesive zone method were used in a crash analysis study conducted by Kim et al.⁸⁵ They concluded that both adhesive modeling methods predicted similar results for the crash simulation.

2.4.3. Impact Modelling and Damage Tolerance Prediction of Fiber Reinforced Composites

The study of impact modeling and damage tolerance prediction in fiber reinforced composites have advanced significantly. Researchers employed a range of analytical, numerical, and experimental methods to enhance our understanding of impact damage mechanisms and improve the longevity and safety of composite structures. Among the methods developed so far, FEA is widely adopted to simulate and analyze the impact response of composites. It allows researchers to predict the evolution of damage, including delamination, matrix cracking, and fiber breakage, under diverse impact

conditions. Finite Element Analysis offers a range of powerful methods for predicting impact damage and assessing damage tolerance in composite materials. Explicit dynamic analysis, a fundamental FEA approach, is particularly well-suited for simulating HVI events. It considers the transient nature of dynamic loading conditions, allowing for the prediction of impact damage progression and the structural response during and after an impact. Finite Element Analysis incorporates advanced material models specific to composites, which consider their anisotropic nature. Common failure criteria, such as the Hashin-Rotem, Puck, and Tsai-Wu, are employed to account for the complex behavior of fibers, matrices, and interfaces under impact loading.

Maamar and Ramdane⁸⁶ investigated the LVI behavior of a CF/Epoxy laminate, both experimentally and numerically. Increasing impact velocity resulted in an increase in the contact load, delamination area, and displacement. A good agreement was found between the experimental and numerical results, quantitatively.

Borrelli et al.⁸⁷ proposed a two-step numerical analysis methodology for the CAI analysis of composite laminates. In the first step, they performed explicit finite element analysis to investigate impact damage resistance and determine damage extent after the impact. In the second step, they transferred the damaged specimen to CAI analysis which is simulated in LS-DYNA implicit finite element code. MAT54 material model was used to represent composite laminate. Both stacked shell models with contact definitions and single layer shell model were used for the evaluation. It was reported that the proposed numerical techniques provided good estimations with the experimental results.

Mendes and Donadon⁸⁸ presented a numerical and experimental study on the CAI strength of woven composite laminates. Two different modeling approaches, Single Shell Model and Split Shell Model were proposed to model the CAI event using ABAQUS. The numerical predictions showed good correlation with experimental results for the impact response. The CAI strength comparison between experimental and numerical results for 2.1 mm and 4.2 mm lay-ups are shown in Figure 2.20(a) and (b). The Split Shell Model approach showed better correlation than the Single Shell Model for 2.1 mm and 4.2 mm laminates. For 2.1 mm laminates, a good agreement between experimental and numerical results was observed for low and medium impact energy levels, but total plate perforation was experimentally observed for high impact energy levels. The proposed damage models and modeling approaches have proven to be capable of reproducing experimental results with good accuracy for the impact tests and CAI tests. Both CAI models predicted very similar results in terms of normalized CAI strength.

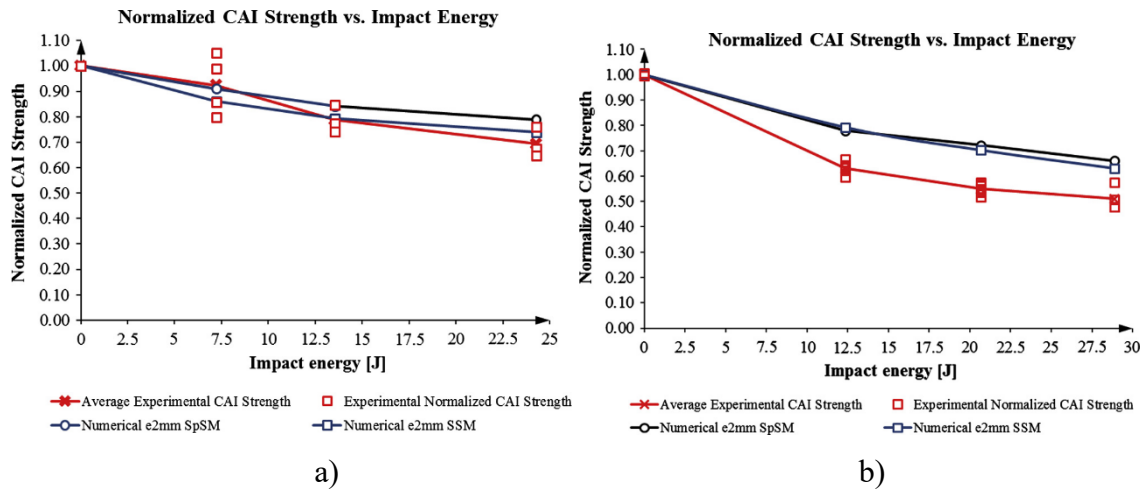


Figure 2.20. Experimental and numerical comparison of normalized CAI strength for a) 2.1 mm lay-up, b) 4.2 mm lay-up. (Source: Mendes and Donadon⁸⁸)

Experimental and numerical comparison for CAI tests for the tests performed both low velocity and high velocity are shown in Figure 2.21. Numerical results estimated maximum load in the range of 1% error margin. Both experimental and numerical results exhibited compressive fiber failure at the impact point area which is valid according to the AITM standard.⁷⁷ Giannaros et al.⁷⁷ proposed multi-stage material model calibration procedure for a carbon fiber reinforced polymer composite material using LS-DYNA. Their work included LVI, HVI and CAI tests. Numerical model setups for these tests are shown in Figure 2.22

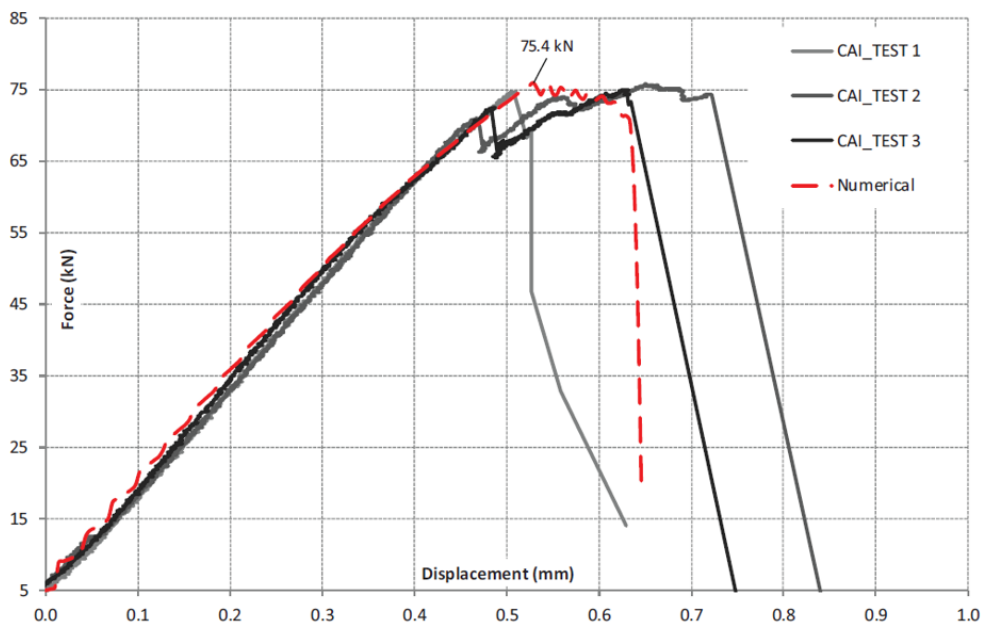


Figure 2.21. Compression after impact results for low and HVI tests (Source: Giannaros et al.⁷⁷)

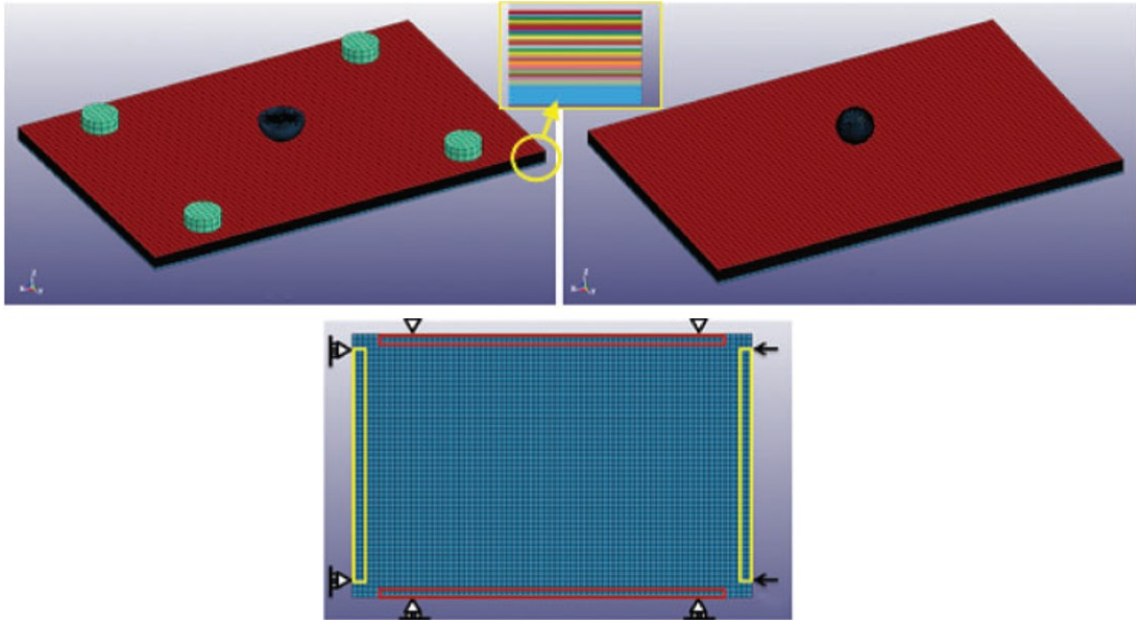


Figure 2.22. Impact and CAI numerical models
(Source: Giannaros et al.⁷⁷)

A finite element modeling methodology to model composite laminates using conventional shell elements was proposed by Gonzales et al.⁷⁸ ABAQUS numerical explicit FE code was used in the simulations. The CAI strength was over-predicted by the model by 7%. The reason for the discrepancy between experimental and numerical results was attributed to the boundary conditions, loading alignment, and the material property heterogeneity.

Rozylo et al.⁸⁹ proposed a simplified model of the damage on the composite plates subjected to LVI tests, considering a decrease in laminate ply thickness based on impact energy, and verified through CAI tests. The proposed damage model was based on a gradient decrease in the thickness of individual plies and was verified by the CAI tests, with adequacy verified based on the results reported in the literature. The numerical analysis was performed using ABAQUS, with composite plates made of CFRP laminate subjected to uniform compression. The analysis considered the regions of damage caused by different impact energies and evaluated the damage process using a progressive damage criterion. The CAI results confirmed a significant decrease in the stiffness of the composite plates subjected to the LVI tests, supporting the validity of the proposed damage model. It was reported that the model can be applied to assess the decrease in stiffness of composite plates which are damaged by the LVI, which is important for evaluating the structural integrity and performance of composite structures in various industries. The model can aid in predicting the damage initiation and evolution in

composite materials, allowing for better design and optimization of composite structures to withstand the LVI events (Figure 2.23(a) and (b)).⁸⁹

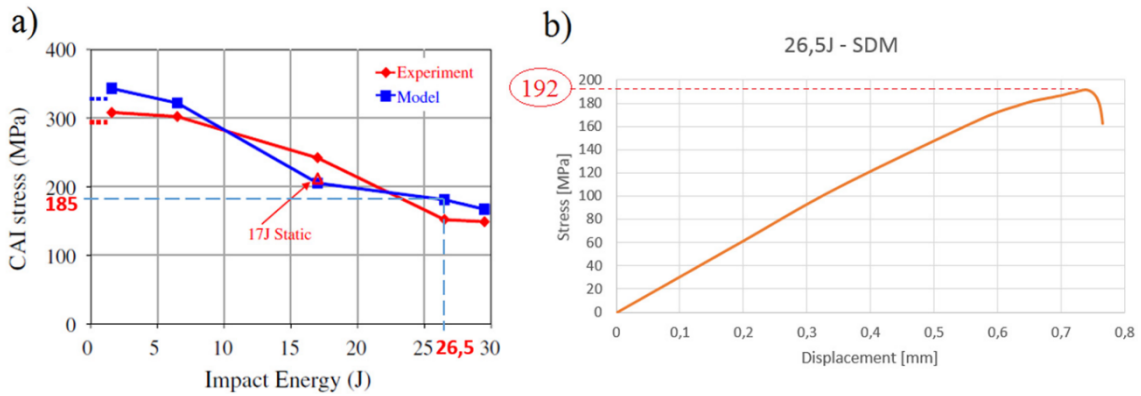


Figure 2.23. Comparison of CAI experimental and numerical results; a) complete model, b) simplified model (Source: Rozylo)

Specific failure criteria and models have been developed to predict the CAI performance of polymer matrix composites. Analytical and numerical methods have been developed and used extensively for the prediction of the CAI response. Researchers proposed fracture mechanics based analytical methods to evaluate the CAI strength of impacted laminates.⁹⁰

Numerical methods have been effectively adopted for the investigation of the CAI tests. Reiner et al.⁹¹ presented a finite element modelling approach for simulating the CAI residual strength of carbon fiber reinforced composite laminates. The approach was validated by the transverse impact tests and predicted the residual strength with reasonable accuracy. The approach has been previously validated for transverse impact test simulations with impact energies ranging from 6 J up to 20 J. The modelling strategy involved the use of sub-laminates and scaled laminates to analyze residual strength, damage patterns, and prediction errors caused by transverse impact simulations. The authors compared the accuracy of predicting residual strength in different types of laminates, such as $[45_0/90_{-45}]_{4s}$ sub-laminates and $[45_2/0_2/90_2/-45_2]_{2s}$ ply scaled laminate. They found that the approach could predict residual strength in certain sub-laminate scaled laminates with a maximum error of 10% while other laminates yield errors of up to 30%.

CHAPTER 3

EXPERIMENTAL METHODOLOGY

3.1. Introduction

The experimental methodology used in the thesis included the fabrication of 5-HS weave fabric CF/PPS thermoplastic composite laminates, the preparation of the test coupons from the fabricated composite laminates, coupon level testing, and the inspection of the damage and failure mechanisms of the tested coupons. Four types of mechanical tests were conducted: quasi-static strain rate, LVI, CAI and HVI. Quasi-static strain rate tests included the standard tensile, compression and shear tests. The LVI tests were performed using a drop weight tester while the HVI tests were performed using a single-stage gas gun setup.

3.2. Laminate and Test Specimen Preparation

The laminates and test coupons cut from the laminates were fabricated in Turkish Aerospace Industry (TAI). As a first step, the pre-preg plies were cut from the same roll of fabric (see Figure 3.1). The used pre-preg, commercially known as Toray Cetex TC1100 PPS, was a 5-HS T300JB carbon fiber woven fabric impregnated in a PPS thermoplastic resin. Each ply was cut into the dimensions of 1000x420 mm. The cut-plyes were then carefully stacked together using a Kapton tape at the four corners and then placed between grease film as shown in Figure 3.2. The grease film covered the stacked plies from the bottom to the top to ensure no leakage formation during the consolidation stage. Each laminate fabricated consisted of 8 plies. The consolidation was performed in an automated servo-hydraulic thermoforming press machine as shown in Figure 3.3. The press platforms were then heated up to 315°C and a 350 kN pressure was applied to the stacked plies. Afterwards, the pressure was increased to 550 kN and the temperature was decreased to 160°C in 10 minutes. The whole consolidation process took placed 2 hours to complete.

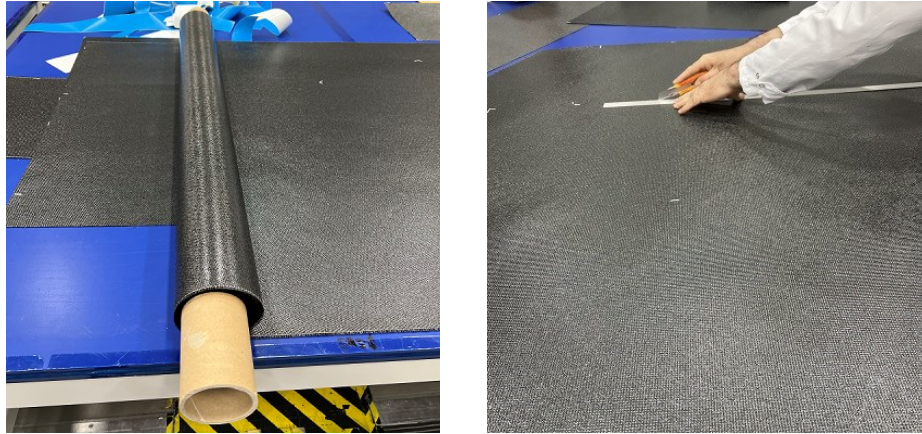


Figure 3.1. Ply cutting from a pre-preg roll



Figure 3.2. Composite laminate before consolidation process

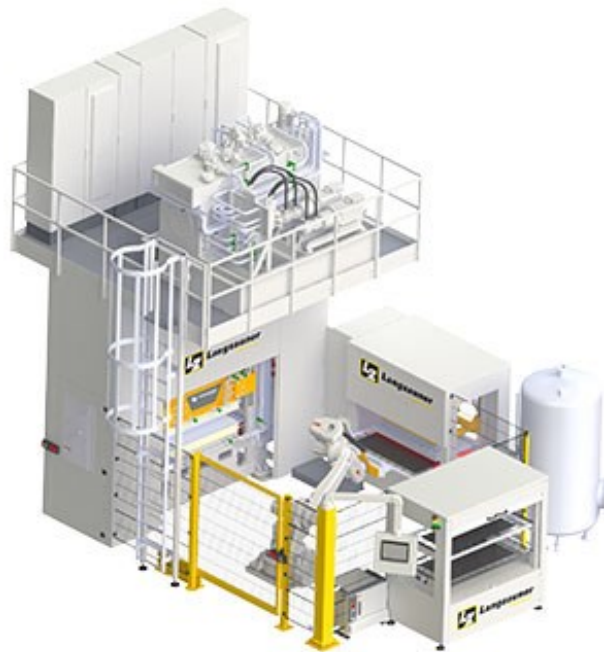


Figure 3.3. Automated press machine for manufacturing composite plates

Three composite plates having a thickness of 2.25 ± 0.02 mm were fabricated through a thermoforming process. The stacking sequence and dimensions of the fabricated plates are tabulated in Table 3.1. Two 8-ply composite plates had 0° ply sequence and the third plate was a symmetric quasi-isotropic laminate. The consolidated thickness of one-ply is 0.31 mm according to the technical datasheet.¹ The final thicknesses of the laminates were measured as 2.25 ± 0.02 mm after the consolidation of 8 plies in the thermoforming press machine. The experimental test specimens were extracted/cut from these plates by water jet as shown in Figure 3.4.

Table 3.1. The stacking sequence and dimensions of the manufactured composite plates

| Total Ply Number | Stacking Sequence | Dimensions | Pieces |
|------------------|-------------------|------------------|--------|
| 8 ply | $[0]_8$ | 1000 mm x 420 mm | 2 |
| 8 ply | $[45/0/-45/90]_s$ | 1000 mm x 420 mm | 1 |

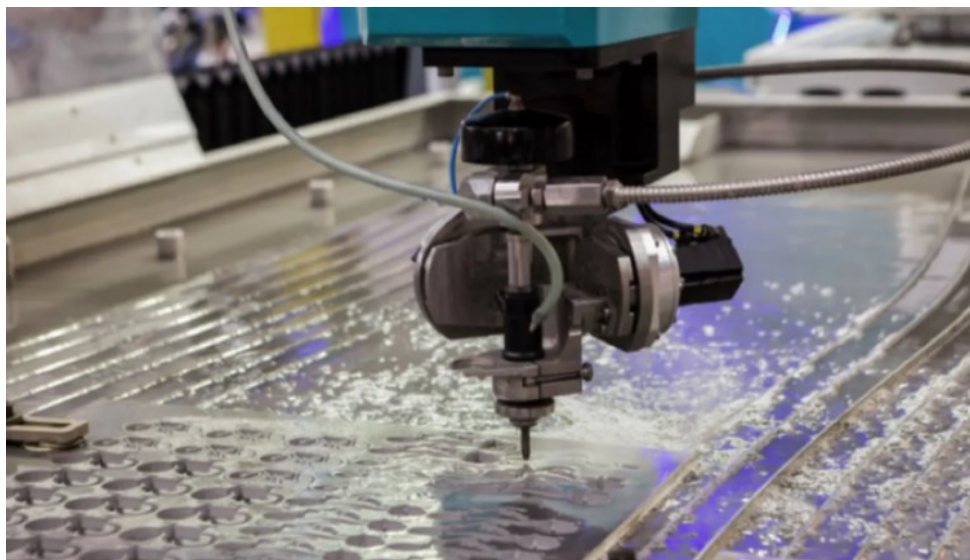


Figure 3.4. Water jet test specimen cutting

In the 5-HS weave fabric, the fibers are arranged by interlacing warp and weft fiber tows (Figure 3.5). The warp is called longitudinal fiber tow while the weft is transverse fiber tow which is interlaced over and under the warp. Due to the interlaced structure of fibers, woven fabric composite has more balanced mechanical properties in longitudinal and transverse directions compared to unidirectional composites. The warp and weft directions for determining the longitudinal and transverse direction properties as well as the general representations of the fiber and matrix alignment are shown in Figure 3.6.

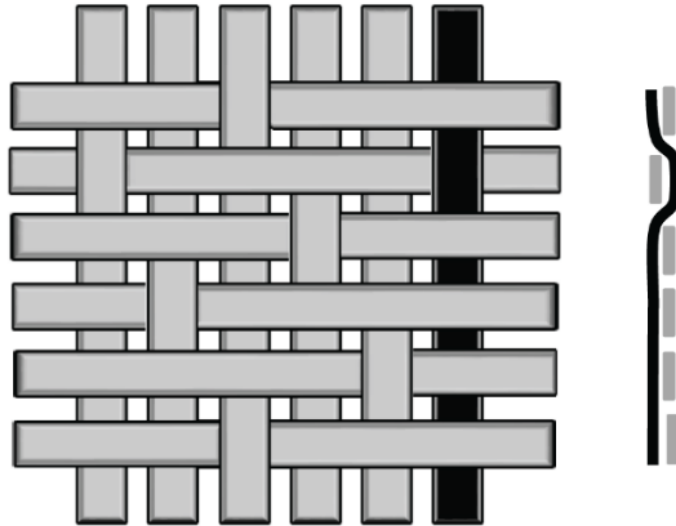


Figure 3.5. Weave pattern for 5 harness satin weave
(Source: Haibin Ning¹⁴)

Longitudinal Properties

Transverse Properties

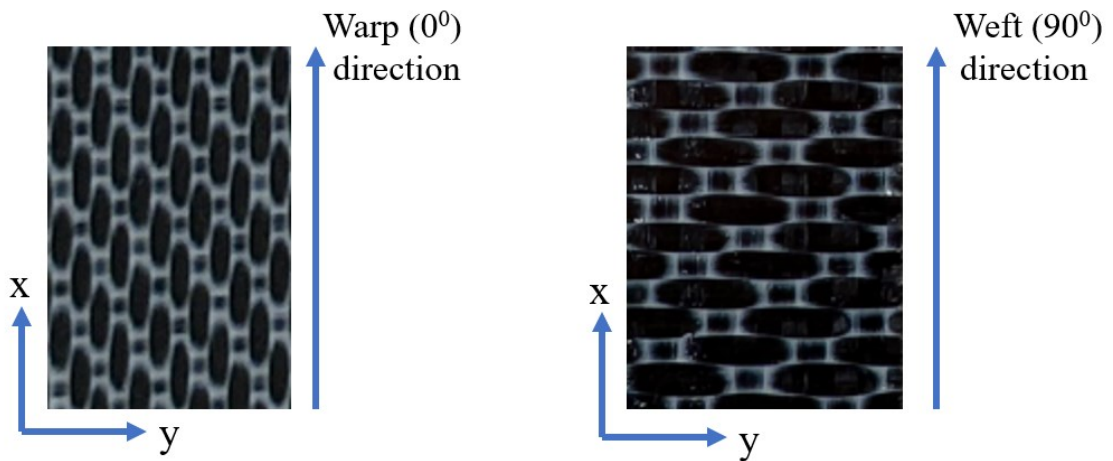


Figure 3.6. Warp and weft direction alignment of the composite laminate

Six different type test coupons were extracted from a 1000 mm x 420 mm x 2.25 mm large composite laminate with $[0^0]_8$ lay-up which were the tension and compression test coupons in the warp and weft direction and in-plane shear test coupons that were cut from the same laminate. The LVI test specimens were extracted from the $[45/0/-45/90]_s$ lay-up composite laminate. The HVI test specimens were cut from the second $[0^0]_8$ lay-up composite laminate. The schematic of the coupon extraction for experimental testing from a large composite laminate after thermoforming and consolidation process is shown in Figure 3.7.

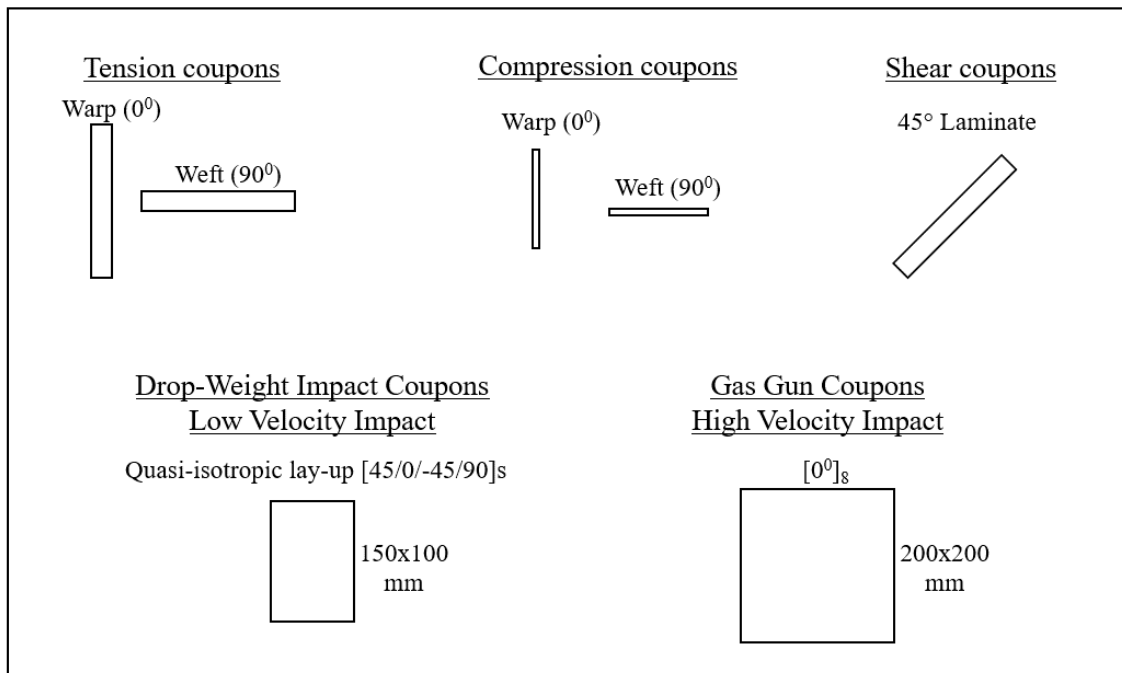


Figure 3.7. Coupon extraction from a large composite laminate after thermoforming

3.3. Strain Measurements in the Tests

The strain can be measured during a mechanical test by physical contact with the test specimen and the techniques that measure the strain without any contact with the specimen are called contactless. The contact extensometer and strain gauge are among the examples of the strain measurement with a contact with the specimen. On the other hand, video extensometers and DIC are classified as non-contact strain measurement methods. In this study, a non-contact video extensometer was used to measure the strains in all tests including CAI tests.

The used video extensometer system had two cameras which followed two gauge markers on the test specimen (Figure 3.8); hence they recorded the change in the distance between two markers. Then, the strain was calculated from the displacement change between markers. At least one tension, compression, and in-plane shear test specimen were strain gaged during the tests (see Figure 3.8 for a strain gaged test specimen). Strain gauges measure the displacement more precisely than video extensometers. However, the strain gauge cannot measure the strains after the failure. The strain gauges also may be detached from the surface of a specimen before the failure and hence cannot measure the strains before the failure.

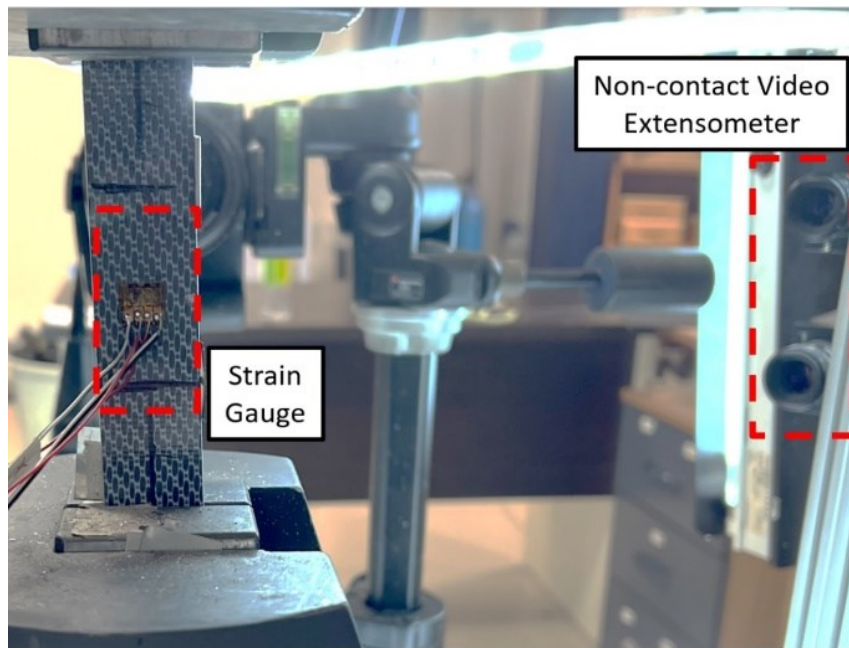


Figure 3.8. Implementation of strain gauge and video extensometer

The DIC was implemented for all quasi-static and CAI test specimens. The DIC is a novel and non-contact strain measurement technique. The DIC system consists of a video camera for recording the specimen deformation and an image processing software or algorithm that calculates the displacements and strains. Before the tests, the front or back surfaces of the test specimens were spray-coated with white paint and randomly positioned black specks (Figure 3.9). During a test, the video record was captured from the front side of the specimen. A MATLAB code was then calculated the displacements and strains on the specimen surface by using the frames of the video records. The DIC measurement allowed a full-field strain measurement and showed the deformations locally.



Figure 3.9. Specimen Surface Preparation for DIC Application

3.4. Quasi-Static Material Characterization Tests

The quasi-static standard tests and strain rate tests were performed in a Shimadzu 300 kN test machine. The test types and directions along with the following standards in the tests are listed in Table 3.2. Test types are divided into three types which are tension, compression and in plane shear tests. Quasi-static strain rate screening tests were performed for only tension and compression. Since the material is 5-harness satin weave fabric, tension and compression tests were performed in both warp (0°) and weft (0°) directions.

Table 3.2. Summary of the quasi-static test campaign

| Test Type | Description | Test Standard |
|----------------|-------------------------------------|--------------------------|
| Tension | Tension in warp (0°) direction | ASTM D3039 ⁹² |
| Tension | Tension in weft (90°) direction | ASTM D3039 ⁹² |
| Compression | Compression in warp (0°) direction | ASTM D6641 ⁹³ |
| Compression | Compression in weft (90°) direction | ASTM D6641 ⁹³ |
| In-plane Shear | Tensile Test of a ±45° Laminate | ASTM D3518 ⁹⁴ |

3.4.1. Tensile Tests

Tensile tests were accomplished in accord with the ASTM 3039.⁹² The test specimen dimensions were 250x25x2.25±0.02 mm and cut using a water jet. Tensile tests were performed at two different crosshead speeds. A reference crosshead speed of 2 mm/min was selected as the reference strain rate and the cross-head speed was increased 10 times, 20 mm/min, in the second group of test specimens. The Poisson's ratio was determined from the strain gauged test specimens. According to the ASTM D3039, the test specimens can be tested with end-tabs or without tabs. Preliminary tests showed the test specimens with end tabs exhibited premature failures at the tab ends. Hence, the tests were continued without end tabs. The tensile test specimen and test setup are shown in Figure 3.10. Wedge-type grips were used for gripping the test specimens with a grip length of 70 mm at both ends. It was ensured that grips were aligned parallel to each other in order to prevent bending moment that might result in premature failure at the grip. A folded medium-grade emery cloth was inserted between the specimen faces and grips (grit side facing towards the specimen). Five valid tests for both directions at the standard strain rate and three valid tests at the higher strain rate were acquired.

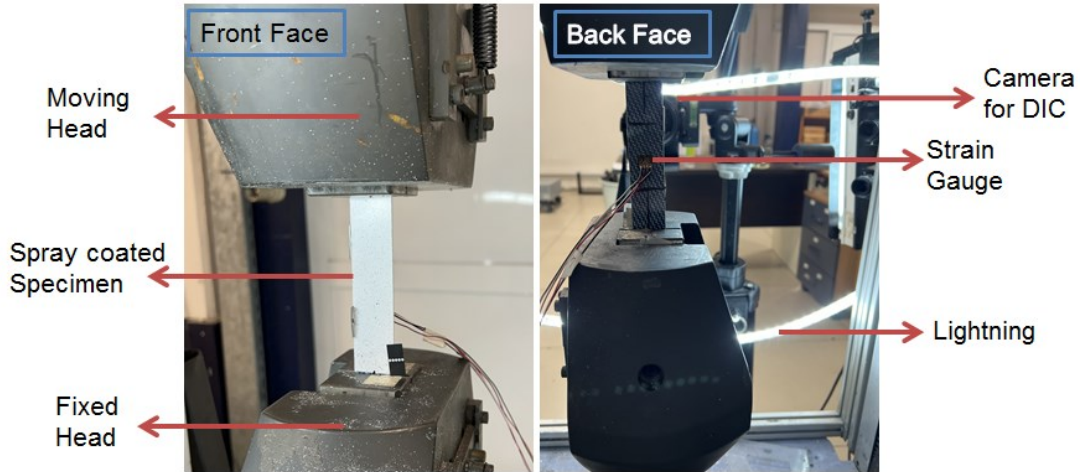


Figure 3.10. Standard quasi-static tensile test setup

Tensile strength, tensile strain, modulus of elasticity, and Poisson's ratio for both warp and weft directions were calculated using the equations stated in ASTM Standard D3039. The tensile strength (F^{tu}) was calculated as,

$$F^{tu} = P^{max} / A \quad (3-1)$$

where, P^{max} is the maximum force before failure and A is average cross-sectional area. Tensile strain at i -th data point (ε_i) was determined as

$$\varepsilon_i = \delta_i / L_g \quad (3-2)$$

where, δ_i is the extensometer displacement at i -th data point and L_g is the extensometer gauge length. Tensile chord modulus of elasticity (E^{chord}) was calculated as

$$E^{chord} = \Delta\sigma / \Delta\varepsilon \quad (3-3)$$

Poisson's ratio (ν) was determined as

$$\nu = -\Delta\varepsilon_t / \Delta\varepsilon_l \quad (3-4)$$

where, $\Delta\varepsilon_t$ is the difference in lateral strain between the two longitudinal strain points and $\Delta\varepsilon_l$ is the difference in longitudinal strain between the two longitudinal strain points.

3.4.2. Compression Tests

The compression tests were conducted in accordance with the ASTM 6641.⁹³ In this standard, a Combined Loading Compression (CLC) test fixture was used for the tests as shown in Figure 3.11. The specimens without end tabs had the dimensions of $140 \times 13 \times 2.25 \pm 0.02$ mm with a 13 mm gauge section. The specimens both in the warp and weft direction specimens were tested at a reference crosshead speed of 1.3 mm/min and at 13 mm/min. All compression tests were performed using the DIC and at least two specimens were tested using the strain gauges (Figure 3.12).

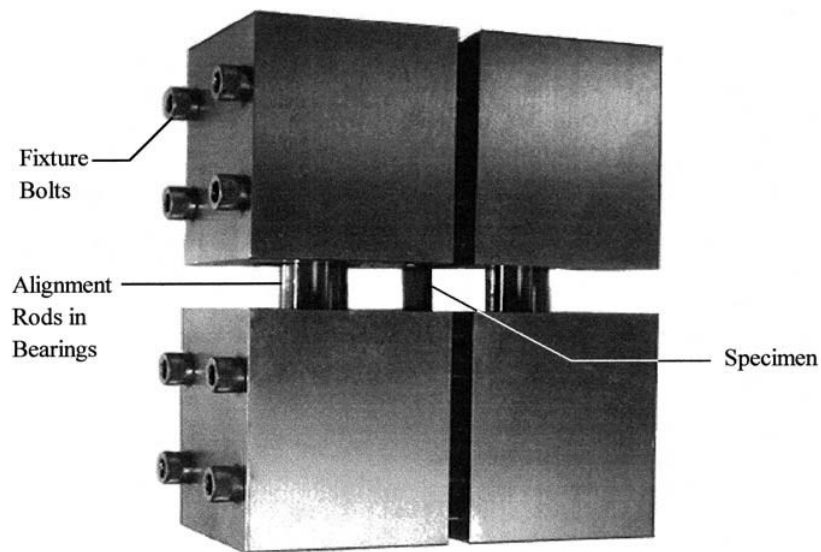


Figure 3.11. A typical CLC test fixture for compression testing (Source: ASTM D6641⁹³)

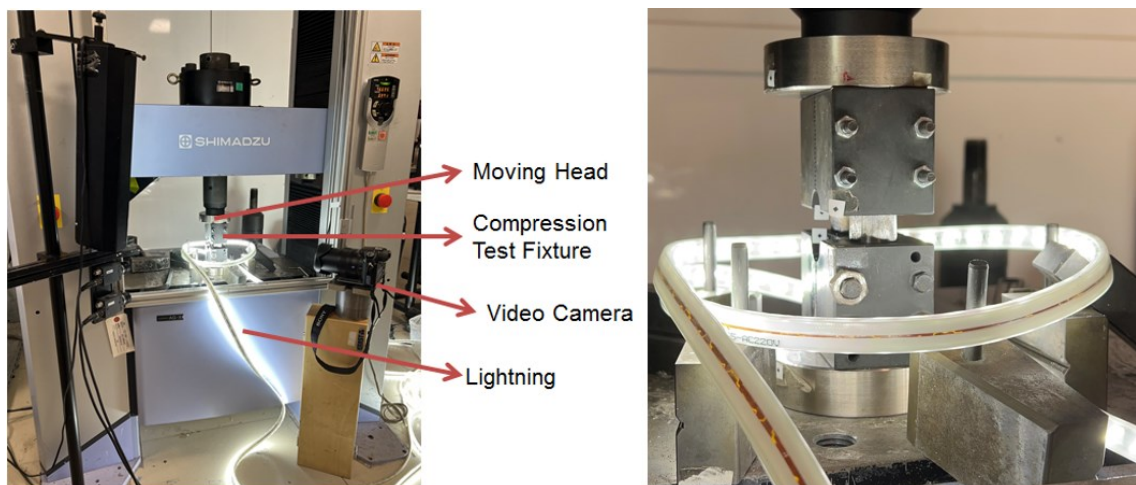


Figure 3.12. Standard quasi-static compression test setup

The compressive strength (F^{cu}) was calculated as

$$F^{cu} = \frac{P_f}{wh} \quad (3-5)$$

where, P_f = maximum load to failure

w = specimen gauge width

h = specimen gauge thickness

The compressive modulus (E^c) was determined as

$$E^c = \frac{P_2 - P_1}{(\varepsilon_{x2} - \varepsilon_{x1})wh} \quad (3-6)$$

where, P_1 = load at ε_{x1}

P_2 = load at ε_{x2}

ε_{x1} = actual strain nearest lower end of strain range used (1000 microstrain)

ε_{x2} = actual strain nearest upper end of strain range used (3000 microstrain)

w = specimen gauge width

h = specimen gauge thickness

The failure identification was based on a three-part failure code given by ASTM standard⁹³ and is shown in Figure 3.13. To accept a compression test as valid, the failure should be located in an acceptable area and should have an acceptable failure mode.

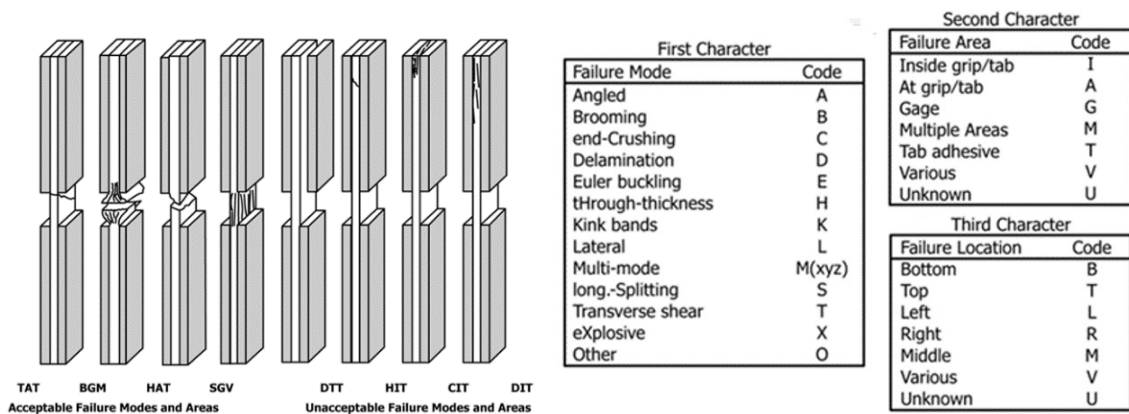


Figure 3.13. Three-part failure mode codes according to the ASTM for compression test specimen (Source: ASTM D6641⁹³)

3.4.3. In-plane Shear Tests

The shear modulus, shear strength, and failure strain were determined by following the ASTM D3518.⁹⁴ In this test method, tensile test coupons of carbon composites with a fiber orientation of ± 45 -degree were tested at a displacement rate of 2 mm/min. Six specimens were tested using a digital image correlation system to measure the shear strain while three of them were instrumented additionally with strain gauges. Fiber orientations and loading direction for the shear test coupon are shown in Figure 3.14. Indice-1 shows the longitudinal fiber direction (0°) while indice-2 demonstrates the transverse direction (90°) in the plane of a ply. The x- and y-axis represent the specimen axes in which the x-axis is the loading axis.

The used test setup for the standard in-plane shear test of $\pm 45^\circ$ specimen is shown in Figure 3.15. All specimens were spray-coated for the DIC measurements and a few of the test specimens were equipped with biaxial strain gauges (Figure 3.15). Longitudinal and transverse strains were measured using the strain gauges to calculate shear strain and compared with DIC results. The specimen dimensions were the same as the tensile test specimens. The strain gauge was mounted at the back surface of the test specimen (Figure 3.15).

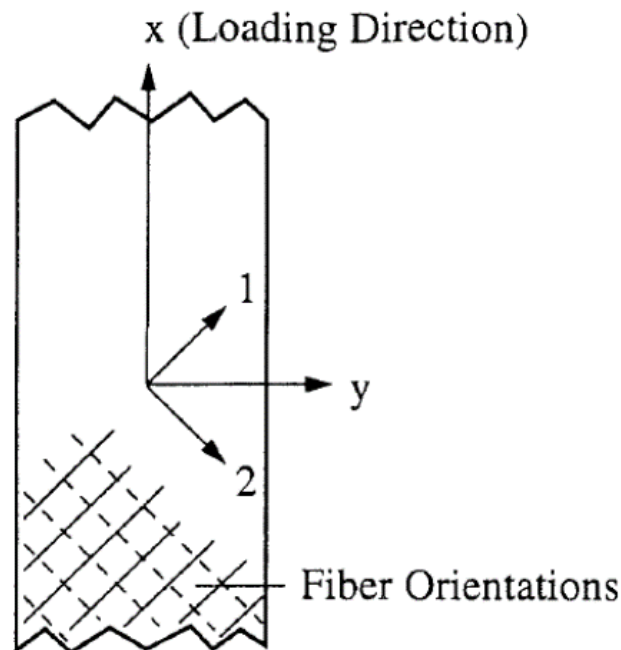


Figure 3.14. Definition and material axis for shear test coupon
(Source: ASTM D3518⁹⁴)



Figure 3.15. Standard in-plane shear test of $\pm 45^\circ$ specimen test setup

The uniaxial tensile load was applied to the test coupon and then shear stress and strain at failure were calculated using the following equations based on Mohr-Coulomb theory or by Mohr's circle.

$$\text{Shear strength; } \tau_{12} = \frac{P}{2A} \quad , \quad \sigma_a = \frac{P}{A} \quad (3-7)$$

P = maximum load A = cross-sectional area σ_a = axial stress

$$\text{Shear strain; } \gamma_{12} = \varepsilon_x - \varepsilon_y \quad \varepsilon_{12} = \frac{\gamma_{12}}{2} \quad (3-8)$$

γ_{12} = engineering shear strain ε_{12} = engineering strain
 ε_x = longitudinal normal strain ε_y = lateral normal strain

Shear modulus of elasticity and offset shear strength were determined according to Figure 3.16. The formulation is given by ASTM test standard⁹⁴ as follows;

$$\text{Shear modulus; } G_{12} = \frac{\Delta\tau_{12}}{\Delta\gamma_{12}} \quad (3-9)$$

G_{12} = shear chord modulus of elasticity

$\Delta\tau_{12}$ = difference in applied shear stress between the two shear strain points

$\Delta\gamma_{12}$ = difference between the two shear strain points (nominally 0.004).

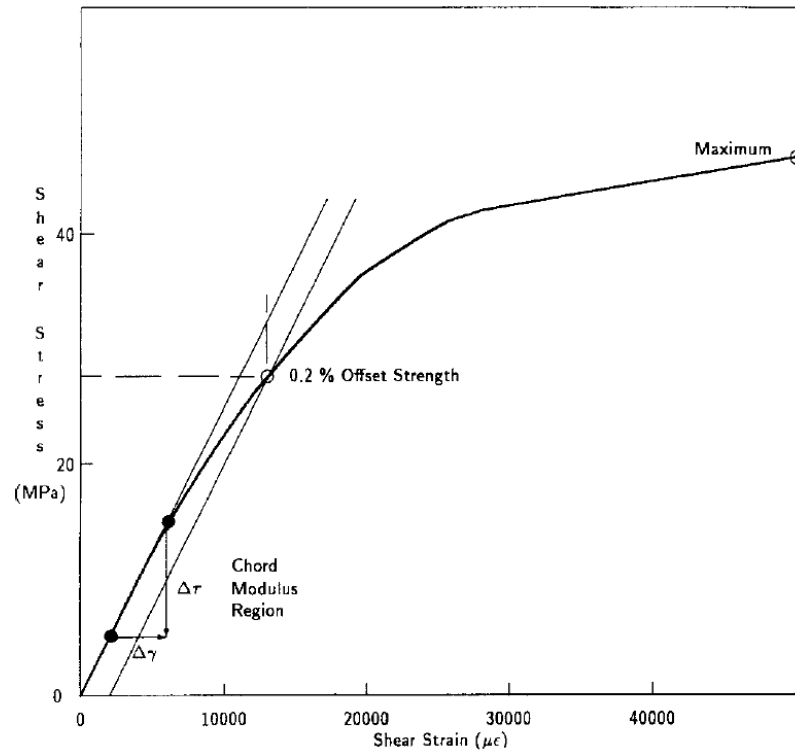


Figure 3.16. Illustration of modulus and offset strength determination (Source: ASTM D3518⁹⁴)

3.5. Low Velocity Impact Tests

The LVI tests were performed using a CEAST drop weight tester as shown in Figure 3.17. The tests were conducted in accordance with the ASTM D7136.⁹⁵ A high-speed camera, Fastcam SA1.1, together with a spotlight, Dedolight Daylight 400D, was used to record the test as seen in Figure 3.17. The speed camera was set to 20000 fps at a 512 mm x 512 mm frame; frames were taken 50 microseconds of interval. The dimensions of the test specimens were 150x100x2.25 mm (Figure 3.18) and the test specimens were clamped to the support fixture on its four sides. The schematic of the supporting fixture is shown in Figure 3.19. Four rubber tip clamps were used to fix the during the test. The fixture was made of steel, and it had 350x 350 mm dimensions and with a rectangular opening at the center, 75x125 mm. Commonly observed damage modes of the drop-weight impact tests are shown in Figure 3.20. Damage is categorized into externally visible damage and internal damage. Externally visible damage can be detected with the naked eye while internal damage can only be observed using NDI such as X-Ray, Ultrasonic Scan, etc. The damage caused by low velocity impact tests is assessed by both visual inspection and NDI methods.

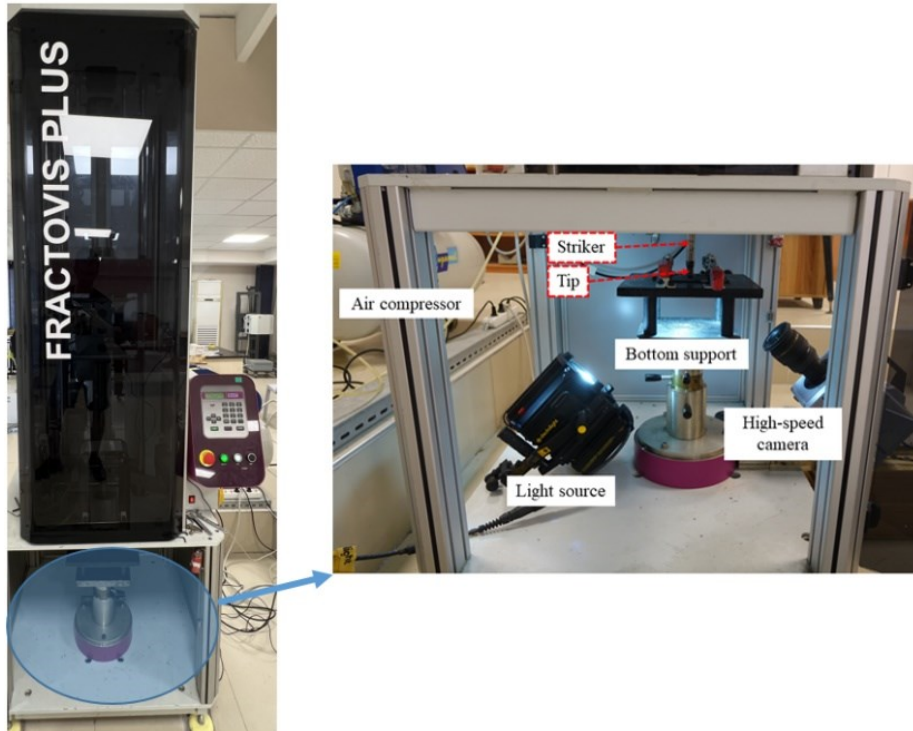


Figure 3.17. Drop weight impact test apparatus

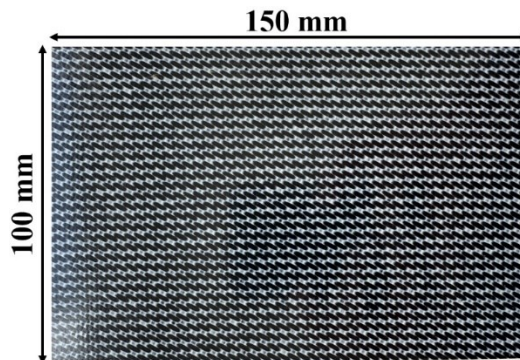


Figure 3.18. Drop weight impact specimen and its dimensions

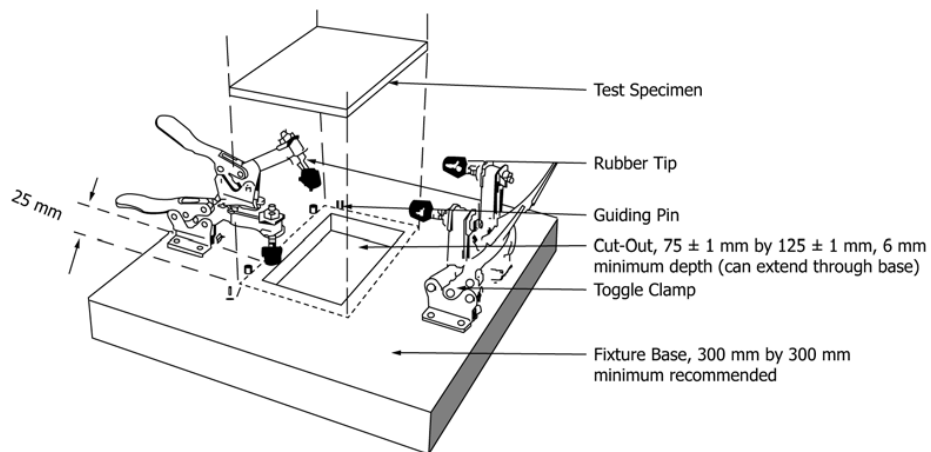


Figure 3.19. Impact support fixture for drop weight test specimen
(Source: ASTM D7136⁹⁵)

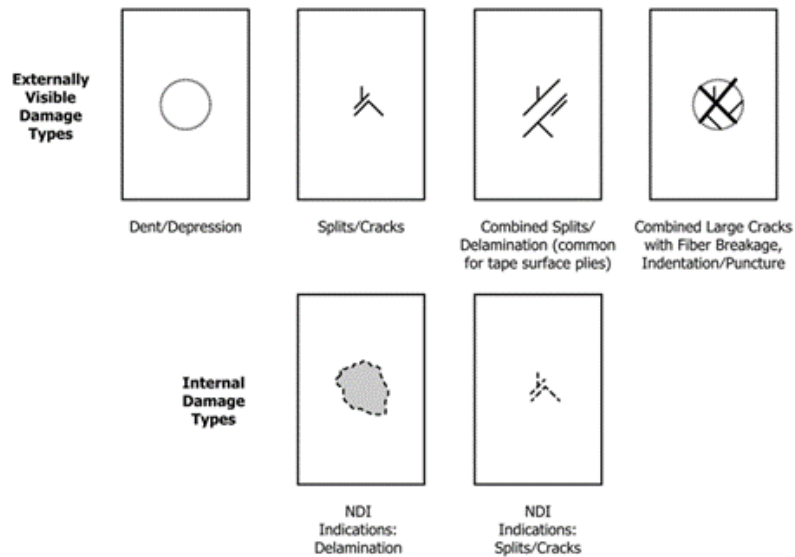


Figure 3.20. Frequently observed damage modes from drop-weight impact tests (Source: ASTM D7136⁹⁵)

A 16 mm-diameter hemispherical tip steel impactor was used to investigate the effect of impact velocity on the damage resistance and damage tolerance of the studies composite plates. One of the tested specimens for every impact velocity using the 16 mm impactor were further subjected to CAI tests. Additionally, the plates were tested with a 38 mm-diameter hemispherical tip steel impactor in order to investigate the effect of projectile geometry. The pictures of both impactors are shown in Figure 3.21.

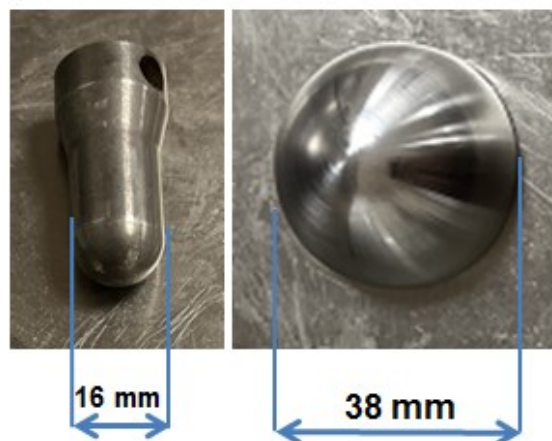


Figure 3.21. Drop weight impact test projectiles

The test campaign of the LVI tests is shown in Table 3.3. Six different impact velocities were chosen from 1 m/s to 6 m/s with a 1 m/s velocity increment. One additional impact energy is chosen according to the ASTM test standard suggestion. The impact energy level (E) is,

$$E = C_E h \quad (3-10)$$

C_E = specified ratio of impact energy to specimen thickness, 6.7 J/mm

h = nominal thickness of specimen

For a specimen thickness of 2.25 mm and 6.7 J/mm, the standard energy ratio yields 15 Joule impact energy according to the ASTM standard. The effect of impactor geometry was investigated with two impact energy levels. Those impact energy levels are approximately the same as the 5 m/s and 6 m/s targeted impact velocity tests.

Table 3.3. Test matrix for low-velocity impact tests

| Impact Case | Test No | Target Impact Velocity (m/s) | Measured Impact Velocity (m/s) | Measured Impact Kinetic Energy (J) |
|--|--|------------------------------|--------------------------------|------------------------------------|
| Effect of Impact Velocity -16 mm hemispherical impactor - 2.8 total impact weight | 1 | 1 | 0.99 | 1.372 |
| | 2 | 1 | 0.99 | 1.372 |
| | 1 | 2 | 2 | 5.600 |
| | 2 | 2 | 2 | 5.600 |
| | 1 | 3 | 2.99 | 12.516 |
| | 2 | 3 | 2.99 | 12.516 |
| | 1 | ASTM Standard | 3.27 | 14.970 |
| | 2 | ASTM Standard | 3.27 | 14.970 |
| | 3 | ASTM Standard | 3.27 | 14.970 |
| | 1 | 4 | 3.98 | 22.177 |
| | 2 | 4 | 3.99 | 22.288 |
| | 3 | 4 | 3.98 | 22.177 |
| | 1 | 5 | 4.76 | 31.721 |
| | 2 | 5 | 4.75 | 31.588 |
| | 1 | 6 | 5.68 | 45.167 |
| | 2 | 6 | 5.7 | 45.486 |
| | 3 | 6 | 5.7 | 45.486 |
| | Effect of Impactor Geometry - 38 mm hemispherical impactor - 1.986 kg impact weight | 1 | - | 5.6 |
| 1 | | - | 6.67 | 44.177 |

3.6. Compression After Impact Tests

The CAI tests were conducted based on the ASTM D7137.⁹⁶ The schematic of the CAI test apparatus assembly and test specimen positioning are shown in Figure 3.22. The Shimadzu servo-hydraulic test machine was used for these tests as shown in Figure 3.23. By making sure that the specimen was held perpendicular to the base plate, screws of the

side and slide plate were hand tightened with a 7 Nm torque. The fixture was then placed between the flat platens of the testing machine. The compressive force was applied at a suggested standard crosshead displacement rate of 1.25 mm/min. The specimen was loaded until a maximum force was reached and the force had dropped off about 30% from the maximum. The specimen face of the impacted side was spray-coated for DIC measurement, and the tests were recorded using a video camera.

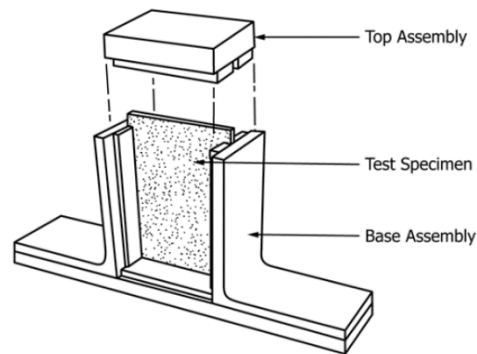


Figure 3.22. Schematic of ASTM CAI test apparatus with specimen (Source: ASTM D7137⁹⁶)

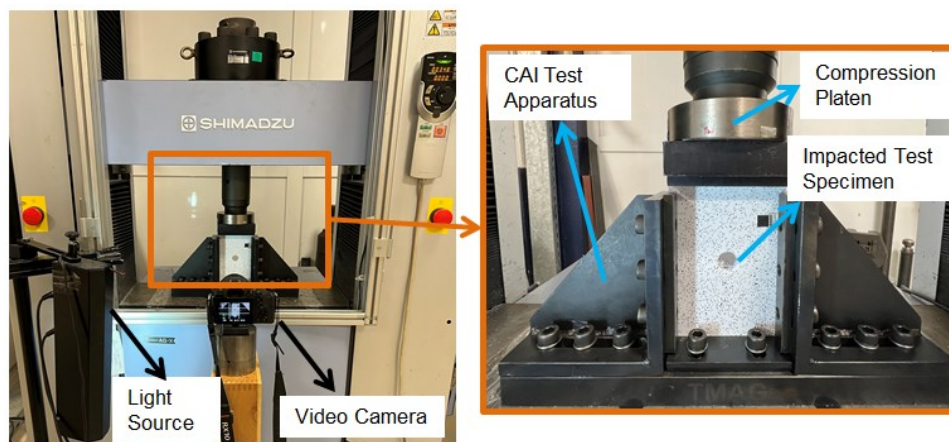


Figure 3.23. CAI test apparatus

The ultimate compressive residual strength (F_{CAI}) and effective compressive modulus (E^{CAI}) are calculated with the following equations;

$$F_{CAI} = P_{max}/A \quad (3-11)$$

P_{max} = maximum force before failure,

A = cross-sectional area

$$E^{CAI} = ((P_{3000} - P_{1000})/(\epsilon_{3000} - \epsilon_{1000})A) \quad (3-12)$$

(P_{3000}) = applied force corresponding to (ϵ_{3000})

(P_{1000}) = applied force corresponding to (ϵ_{1000})

(ϵ_{3000}) = recorded strain value closest to 3000 microstrain.

(ϵ_{1000}) = recorded strain value closest to 1000 microstrain.

The standard required to determine failure type, failure area and failure location for every specimen tested as described in Table 3.4. Commonly observed acceptable residual strength failure modes are further illustrated in Figure 3.24.

Table 3.4. Failure modes according to ASTM D7137 standard
(Source: ASTM D7137⁹⁶)

| First Character | | Second Character | | Third Character | |
|---|------|-------------------|------|------------------|------|
| Failure Type | Code | Failure Area | Code | Failure Location | Code |
| Angled | A | At end/edge | A | Bottom | B |
| Brooming | B | at/through Damage | D | Left | L |
| End-Crushing | C | Gage, away damage | G | Middle | M |
| Delamination growth to edge at final failure | D | Multiple areas | M | Right | R |
| Through-thickness | H | Various | V | Top | T |
| Panel Instability | I | Unknown | U | Various | V |
| Kink bands | K | | | Unknown | U |
| Lateral | L | | | | |
| Multimode | M | | | | |
| Delamination growth to edge prior to final failure | R | | | | |
| Long, Splitting | S | | | | |
| Delamination growth to edge at final failure, Widthwise | W | | | | |
| Explosive | X | | | | |
| Other | O | | | | |

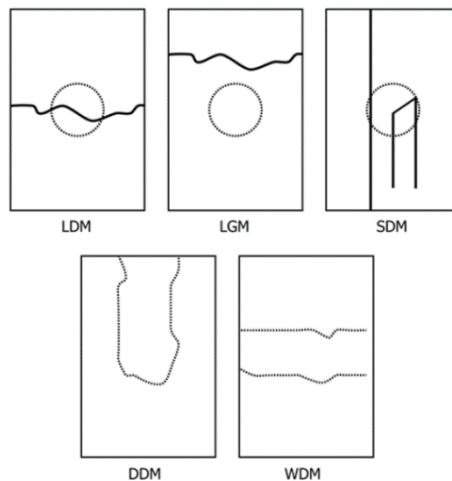


Figure 3.24. Commonly observed acceptable residual strength failure modes
(Source: ASTM D7137⁹⁶)

3.7. Gas Gun Impact Tests

The used gas gun impact test apparatus is shown in Figure 3.25. The gas gun, a single stage, worked with compressed air gas in the gas tank. In a typical test, the compressed air is released with a trigger mechanism and the projectile in the barrel is launched. The projectile is carried by a sabot to provide safe and linear movement of the projectile in the barrel. A lightweight foam sabot which was made of liquid foam mix was used in the gas gun impact tests. Since the sabot was stopped by the sabot trap, a new sabot was produced for each test. The sabot manufacturing process is shown in Figure 3.26. An equal mixture of 24-gram A and B liquids was stirred for one minute and then was poured into a steel sabot mold. Steel mold was greased up just before pouring the mixture to ease extraction of the cured sabot. Sabot mold was closed after pouring and left for curing for about 3 hours. The tests are instrumented with a high-speed video camera. The HVI tests were performed around 100 m/s. Test specimen and boundary condition are shown in Figure 3.27. Test specimens had dimensions of $200 \times 200 \times 2.25 \pm 0.02$ mm. The specimen was clamped within 25 mm width from its four sides using M12 bolts from every side. So, the observable area of the specimen was 150×150 mm. A sphere steel ball with a mass of 110 g and a diameter of 30 mm was used as a projectile in the gas gun impact tests. The projectile was inserted inside the manufactured sabot as shown in Figure 3.28. The gas gun impact tests were recorded with a high-speed camera (Fastcam SA1.1) at 675000 fps with the Dedolight Daylight 400D light (Figure 3.29). The damaged areas are measured using ultrasonic C-scan inspection.

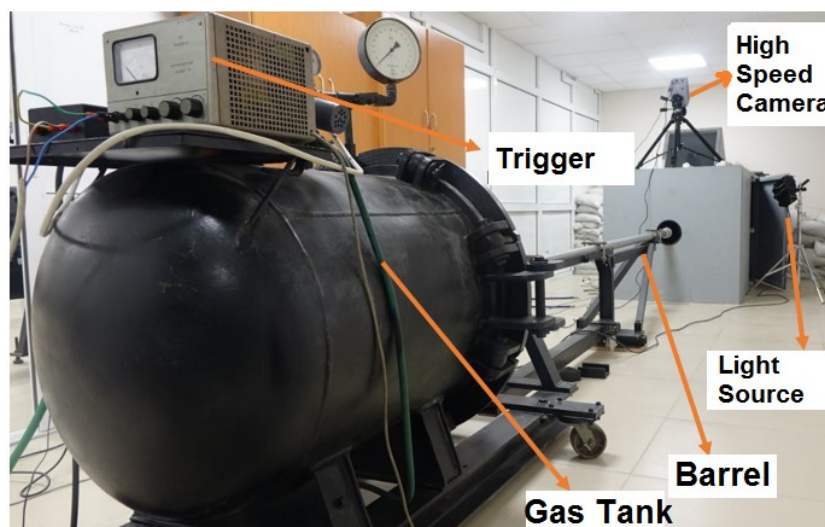


Figure 3.25. Gas gun impact testing



Figure 3.26. Manufacturing of sabot process

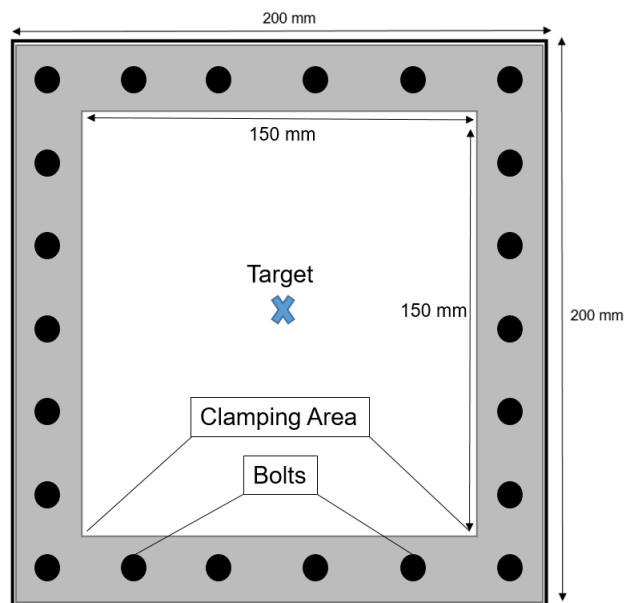


Figure 3.27. Gas gun impact test boundary condition and specimen

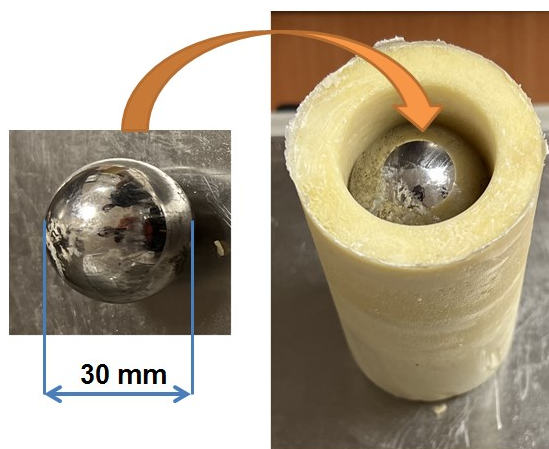


Figure 3.28. Steel ball projectile and sabot

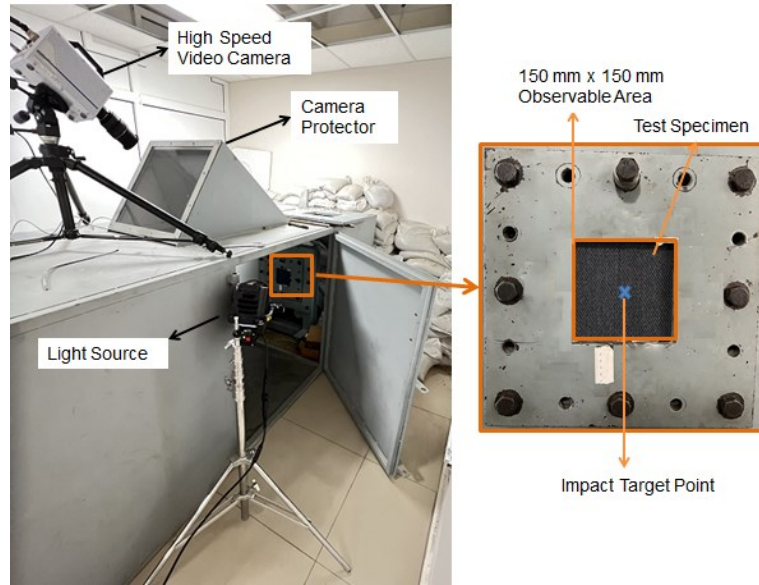


Figure 3.29. Gas gun impact test video recording system

The impact velocities and exit velocities of the ball were determined using a laser beam velocity measurement system. The corresponding impact energy, exit energy, and absorbed energy were calculated using the basic kinetic energy formulas given as;

$$\text{Impact Energy,} \quad IE = \frac{1}{2} mV_i^2 \quad (3-13)$$

$$\text{Exit Energy,} \quad EE = \frac{1}{2} mV_e^2 \quad (3-14)$$

$$\text{Absorbed Energy,} \quad AE = IE - EE \quad (3-15)$$

where, V_i is the impact velocity, V_e is the exit velocity, and “m” is the mass of the steel ball. The summary of the HVI tests is tabulated in Table 3.5.

Table 3.5. Summary of the gas gun impact tests

| Test Number | Impact Velocity (m/s) | Exit Velocity (m/s) | Impact energy (J) | Exit Energy (J) | Absorbed Energy (J) |
|--------------------|------------------------------|----------------------------|--------------------------|------------------------|----------------------------|
| Test 1 | 100 | 85 | 550 | 397 | 153 |
| Test 2 | 101 | 89 | 561 | 436 | 125 |
| Test 3 | 103 | 91 | 583 | 455 | 128 |

CHAPTER 4

EXPERIMENTAL TEST RESULTS

4.1. Mechanical Testing

Mechanical tests in the thesis study were performed under tension, compression and shear. The results of these tests were then used to construct the constitutive equations of the tested composite. The constitutive equations were finally implemented in the numerical simulations of the tests.

4.1.1. Tension Tests

The tensile stress-strain curves of five tests in both warp and weft directions at 2 mm/min cross-head speed (0.001 1/s) are shown in Figure 4.1(a) and (b), respectively. The specimens show almost a linear stress-strain behavior till fracture. It is clear from the same curves that the failures stresses are slightly higher in the weft than the warp direction.

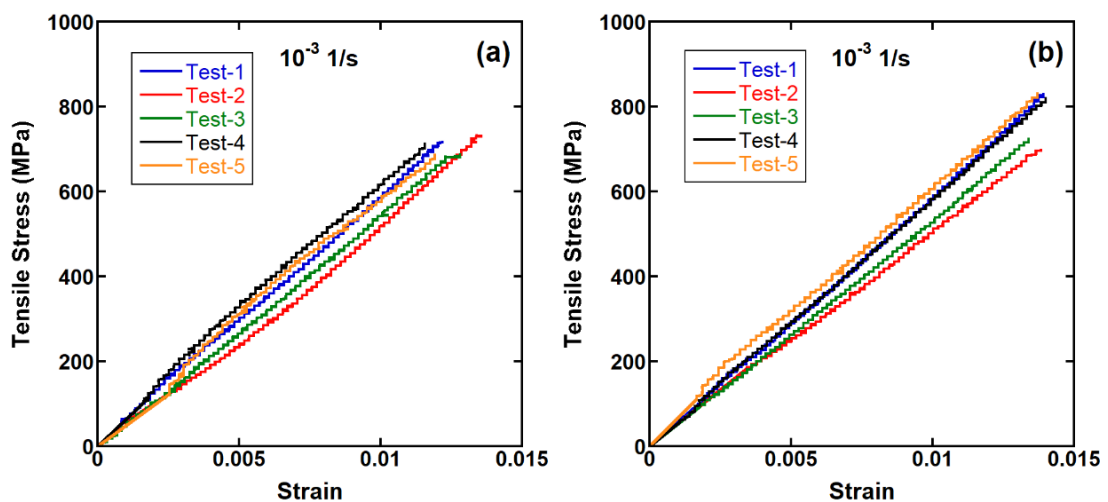


Figure 4.1. Standard quasi-static tension stress-strain curves in a) the warp and b) weft direction

The front and back pictures of the fractured test coupons tested in the warp direction are shown in Figure 4.2(a-b), respectively. As is seen in the same pictures all tested samples fracture laterally near the bottom grip. Similar to the warp direction specimens, the fracture of the weft direction specimens occur laterally near the bottom grip as depicted in Figure 4.3(a-b)

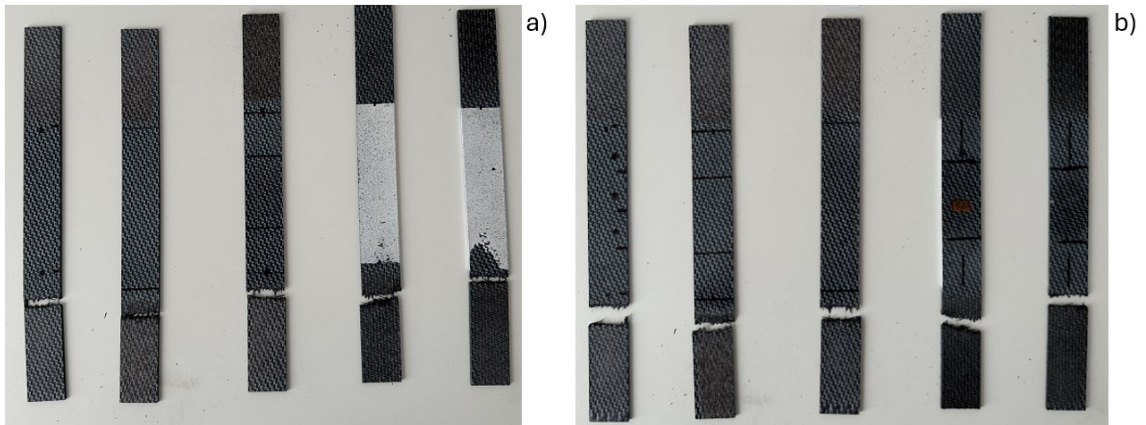


Figure 4.2. Failed tension test specimens in warp direction a) front face and b) back face

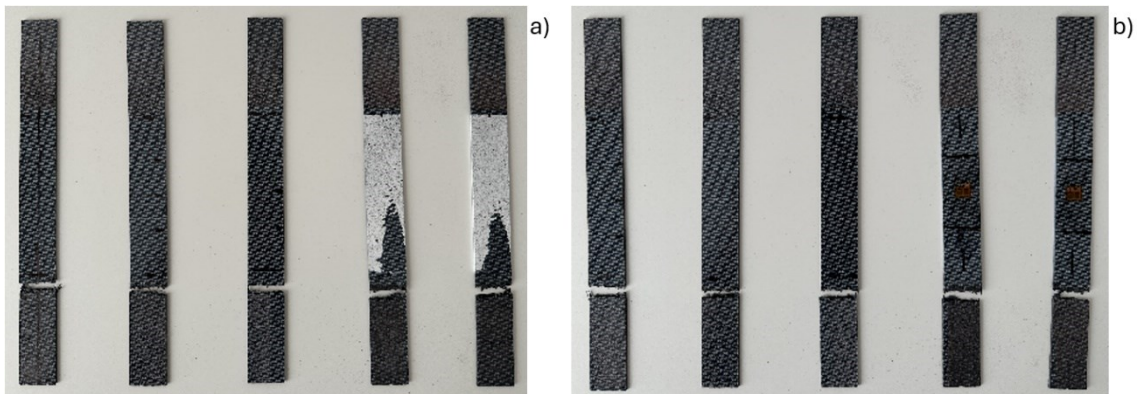


Figure 4.3. Failed tension test specimens in weft direction a) front face and b) back face

The quasi-static tension mechanical properties of the tested composite in the warp and weft directions (at 0.001 1/s) are tabulated in Table 4.1 and Table 4.2, respectively. The mean elastic modulus is slightly higher in the warp direction, 56029 MPa, than in the weft direction, 54943 MPa, as tabulated in the same tables. However, both mean failure strain and mean peak failure stress are higher in the weft direction (0.013 and 762 MPa) than the warp direction (0.0121 and 707 MPa). The standard deviations of the elastic modulus and peak stress are also higher in the weft direction (3694 MPa and 59 MPa) than in the warp direction (2052 MPa and 20 MPa). The Poisson's ratio is measured as 0.05 for both warp and weft directions.

Table 4.1. Standard quasi-static tensile test results in the warp direction

| Tensile test results in warp (0⁰) direction | | | | |
|---|------------------------------|-----------------------|------------------------|--------------------------|
| TEST_ID | Elastic Modulus (MPa) | Failure Strain | Poisson's Ratio | Peak Stress (MPa) |
| 1 | 55580 | 0.0111 | N/A | 716 |
| 2 | 53505 | 0.0142 | N/A | 731 |
| 3 | 54854 | 0.0128 | N/A | 688 |
| 4 | 58487 | 0.0116 | 0.05 | 712 |
| 5 | 57717 | 0.0109 | 0.05 | 686 |
| Mean | 56029 | 0.0121 | 0.05 | 707 |
| Std. Dev. | 2052 | 0.0014 | N/A | 20 |

Table 4.2. Standard quasi-static tensile test results in the weft direction

| Tensile test results in weft (90⁰) direction | | | | |
|--|------------------------------|-----------------------|------------------------|--------------------------|
| TEST_ID | Elastic Modulus (MPa) | Failure Strain | Poisson's Ratio | Peak Stress (MPa) |
| 1 | 58918 | 0.0129 | N/A | 830 |
| 2 | 49383 | 0.0119 | N/A | 698 |
| 3 | 53566 | 0.0128 | N/A | 724 |
| 4 | 57314 | 0.0151 | 0.05 | 820 |
| 5 | 55535 | 0.0122 | 0.05 | 740 |
| Mean | 54943 | 0.0130 | 0.05 | 762 |
| Std. Dev. | 3694 | 0.0013 | N/A | 59 |

The warp and weft direction tensile stress-strain curves of three specimens at 0.01 1/s are shown in Figure 4.4(a) and (b), respectively. The curves showed a good similarity between each others. The mechanical properties of the tested composite in the warp and weft directions at 0.01 1/s are tabulated in Table 4.3 and Table 4.4, respectively. For the warp direction, the mean peak stress, elastic modulus and failure strain are found as 691 MPa, 56448 MPa and 0.01, respectively. For the weft direction, the mean peak stress, elastic modulus and failure strain are sequentially 747 MPa, 51685 MPa and 0.0123. As with lower strain rate tests the weft direction exhibits higher failure strains and peak stresses than the warp direction while an opposite behavior is seen for the modulus values as tabulated in the same tables. Based on these results, one can interpret that the tested CF/PPS thermoplastic composite system show nearly no strain rate sensitivity within the studied strain rates.

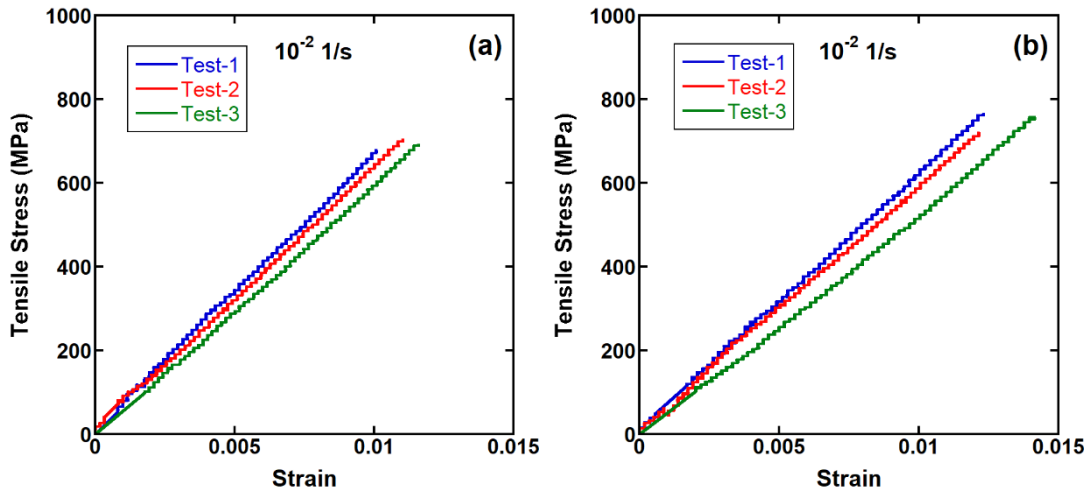


Figure 4.4. Tensile stress-strain curves at 0.01 1/s in a) warp and b) weft direction

Table 4.3. Tensile test results at 0.01 1/s in the warp direction

| Tensile test results in warp (0^0) direction at higher strain rate | | | |
|--|-----------------------|----------------|-------------------|
| TEST_ID | Elastic Modulus (MPa) | Failure Strain | Peak Stress (MPa) |
| 1 | 56245 | 0.0104 | 678 |
| 2 | 55614 | 0.0111 | 703 |
| 3 | 57485 | 0.0115 | 691 |
| Mean | 56448 | 0.0110 | 691 |
| Std. Dev. | 777 | 0.0005 | 10 |

Table 4.4. Tensile test results at 0.01 1/s in the weft direction

| Tensile test results in weft (90^0) direction at higher strain rate | | | |
|---|-----------------------|----------------|-------------------|
| TEST_ID | Elastic Modulus (MPa) | Failure Strain | Peak Stress (MPa) |
| 1 | 52905 | 0.0123 | 764 |
| 2 | 51887 | 0.0121 | 720 |
| 3 | 50262 | 0.0123 | 757 |
| Mean | 51685 | 0.0123 | 747 |
| Std. Dev. | 1088 | 0.0001 | 19 |

4.1.2. Compression Tests

The quasi-static strain rate (0.001 1/s) compression stress-strain curves of five warp and weft direction test specimens are shown in Figure 4.5. In both directions, almost a linear behavior is seen until the failure as seen in the same curves. An example of a compressive stress-strain curve of a specimen with a strain gage is illustrated in Figure

4.6. The slope of the curve between 3000-6000 micro-strain according to the ASTM standard was used to determine the elastic modulus. The results for compression tests in the warp and weft directions are listed in Table 4.5 and Table 4.6, respectively. The mean elastic modulus was found as 53000 MPa for both warp and weft directions. Failure strain and peak failure stress are 0.0111 and 588 MPa for the warp direction and 0.0113, and 598 MPa for the weft direction. The Poisson's ratio for both warp and weft directions are determined by the test with strain gauges. The calculated Poisson's ratio for both warp and weft directions is 0.05.

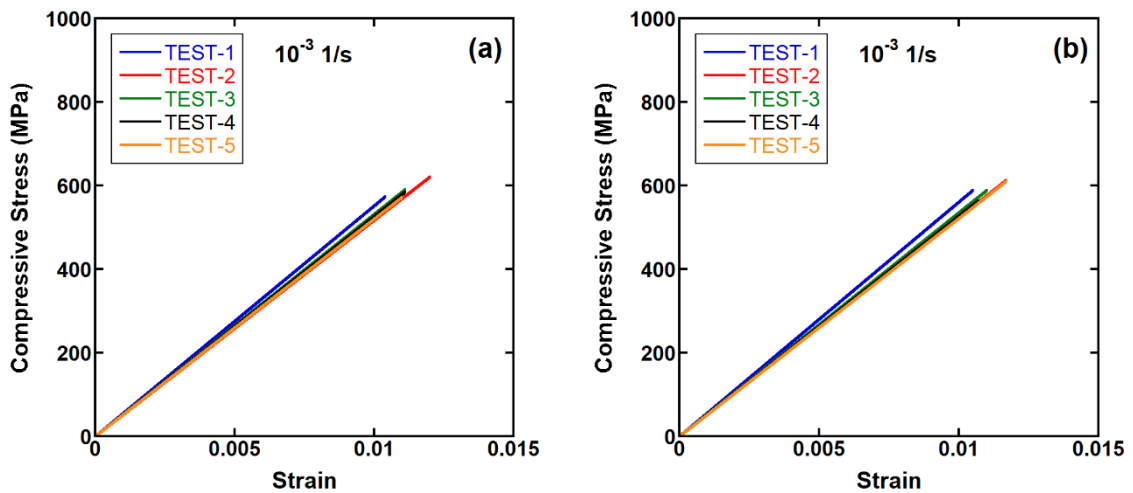


Figure 4.5. Standard quasi-static compression stress-strain curves in a) warp and b) weft direction

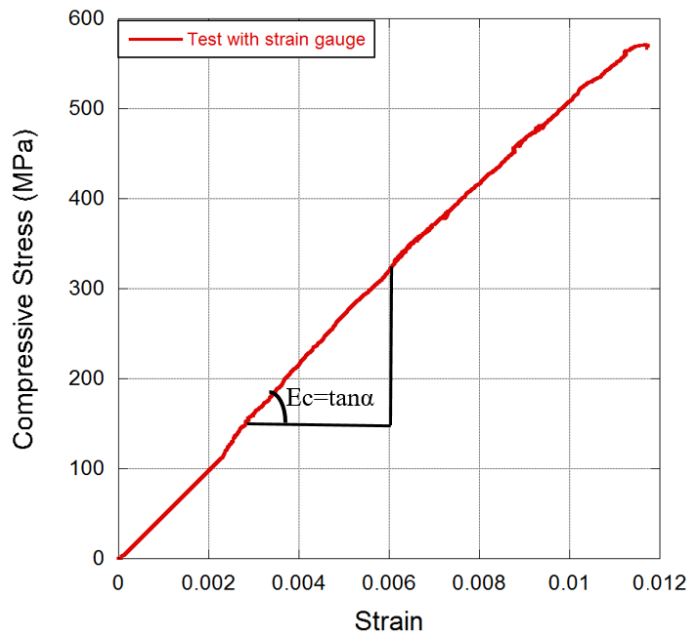


Figure 4.6. Compression stress-strain curve using strain gauge

Table 4.5. Standard quasi-static compression test results in the warp direction

| Compression test results in warp (0⁰) direction | | | | |
|---|------------------------------|-----------------------|------------------------|--------------------------|
| TEST_ID | Elastic Modulus (MPa) | Failure Strain | Poisson's Ratio | Peak Stress (MPa) |
| 1 | 55212 | 0.0104 | N/A | 574 |
| 2 | 51946 | 0.0120 | N/A | 621 |
| 3 | 53429 | 0.0111 | N/A | 590 |
| 4 | 52721 | 0.0111 | 0.05 | 585 |
| 5 | 51886 | 0.0110 | 0.05 | 572 |
| Mean | 53039 | 0.0111 | 0.05 | 588 |
| Std. Dev. | 1369 | 0.0006 | N/A | 20 |

Table 4.6. Standard quasi-static compression test results in the weft direction

| Compression test results in weft (90⁰) direction | | | | |
|--|------------------------------|-----------------------|------------------------|--------------------------|
| TEST_ID | Elastic Modulus (MPa) | Failure Strain | Poisson's Ratio | Peak Stress (MPa) |
| 1 | 54537 | 0.0113 | N/A | 617 |
| 2 | 52251 | 0.0117 | N/A | 613 |
| 3 | 53638 | 0.0110 | N/A | 589 |
| 4 | 52911 | 0.0107 | 0.05 | 564 |
| 5 | 51988 | 0.0117 | 0.05 | 610 |
| Mean | 53065 | 0.0113 | 0.05 | 598 |
| Std. Dev. | 1042 | 0.0005 | N/A | 22 |

A side view detailed image of the failure mode of the compression test sample tested in the warp direction is shown in Figure 4.7. The brooming and extensive splitting of the fibers can be clearly seen. This failure mode corresponds to the three-part failure code of “BGM” according to ASTM standards. “BGM” stands for the failure mode representing brooming at the middle gauge section of the specimen.

The pictures of the fractured warp direction test coupons at the front and back faces are shown in Figure 4.8. An example of the side view close-up failure mode of the compression test sample in the weft direction is shown in Figure 4.9. Similar to warp direction test specimen, overall failure mode for the weft direction test specimen is again brooming at the middle gauge section of the specimen resulting in a “BGM” three-part failure code according to ASTM standards. The pictures of the fractured weft direction test coupons at the front and back faces are further shown in Figure 4.10. There is a good consistency in the failure mode of every specimen for both warp and weft direction specimens.



Figure 4.7. Failed compression test sample in the warp direction

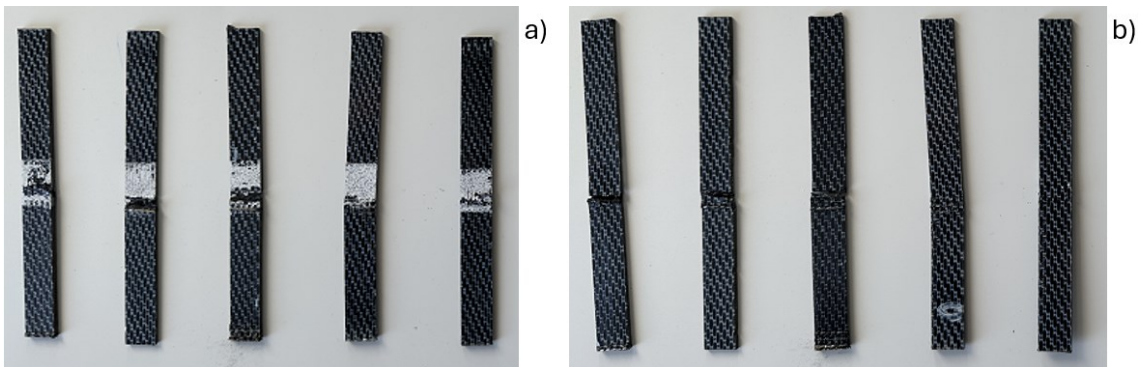


Figure 4.8. Failed compression test specimens in warp direction a) front face and b) back face



Figure 4.9. A picture of failed compression test sample in the weft direction

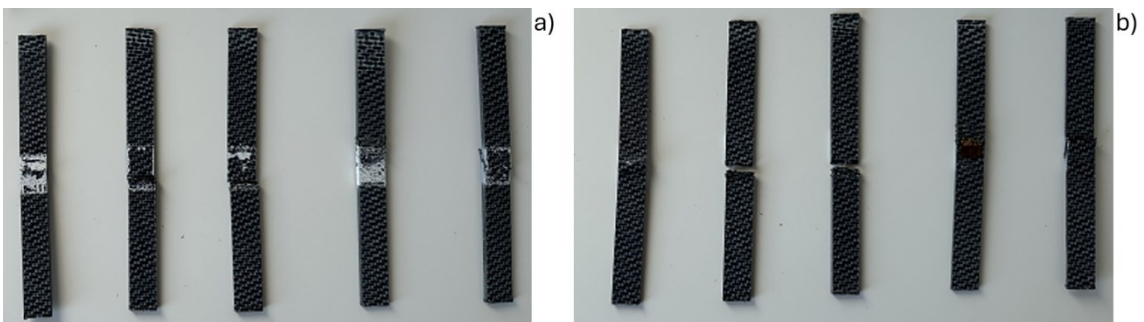


Figure 4.10. Failed compression test specimens in weft direction a) front face and b) back face

The compression stress-strain curves of three tests in the warp and weft direction at 0.01 1/s are depicted in Figure 4.11(a) and (b), respectively. In both directions, a similar compression stress-strain behavior is seen from the same figures. The results of the compression tests in the warp and weft directions at 0.01 1/s are listed in Table 4.7 and Table 4.8, respectively. The mean elastic modulus is 53658 MPa and 54516 MPa for the warp and weft directions, respectively. The failure strain and peak failure stress are 0.0108 and 575 MPa for the tests in the warp direction and 0.0106 and 579 MPa for the tests in the weft direction. The standard deviation in the weft direction is found lower than that in the warp direction. These results show that the tested composite show no change in the deformation mode with increasing strain rate and no strain rate sensitivity with the studied strain rates.

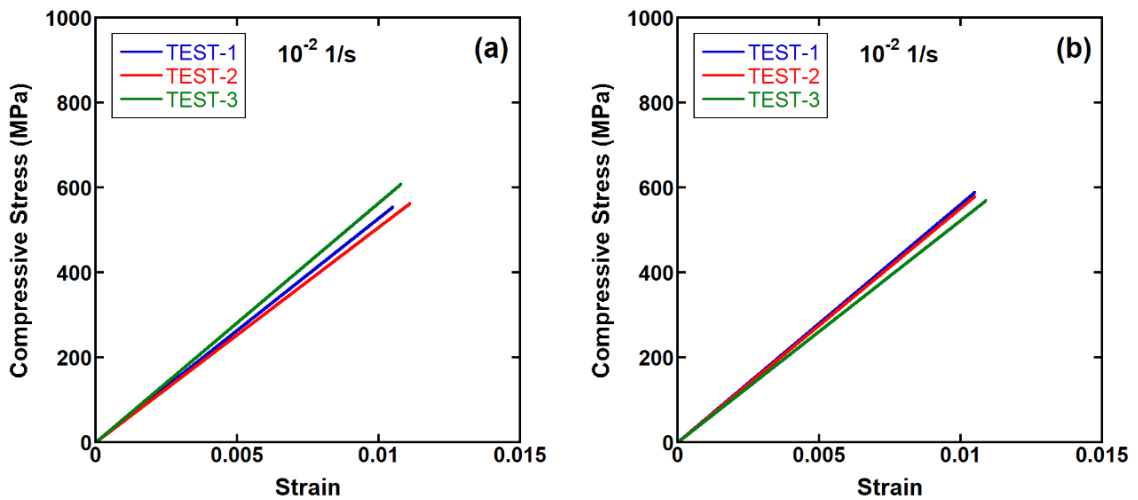


Figure 4.11. Compressive stress vs. strain for higher strain rate tests; a) warp and b) weft direction

Table 4.7. Compression test results at 0.01 1/s in the warp direction

| Compression test results in warp (0^0) direction at higher strain rate | | | |
|--|------------------------------|-----------------------|--------------------------|
| TEST_ID | Elastic Modulus (MPa) | Failure Strain | Peak Stress (MPa) |
| 1 | 52542 | 0.0105 | 554 |
| 2 | 53109 | 0.0111 | 563 |
| 3 | 55322 | 0.0107 | 609 |
| Mean | 53658 | 0.0108 | 575 |
| Std. Dev. | 1199 | 0.0002 | 24 |

Table 4.8. Compression test results at 0.01 1/s in the weft direction

| Compression test results in weft (90⁰) direction at higher strain rate | | | |
|--|------------------------------|-----------------------|--------------------------|
| TEST_ID | Elastic Modulus (MPa) | Failure Strain | Peak Stress (MPa) |
| 1 | 56047 | 0.0105 | 589 |
| 2 | 55313 | 0.0105 | 579 |
| 3 | 52188 | 0.0109 | 569 |
| Mean | 54516 | 0.0106 | 579 |
| Std. Dev. | 1673 | 0.0002 | 8 |

4.1.3. In-plane Shear Tests

The shear stress – shear strain curves for all tested specimens are presented in Figure 4.12. In these curves, shear stress values were calculated from the force measurement by the load cell, and the shear strain was derived from the video extensometers.

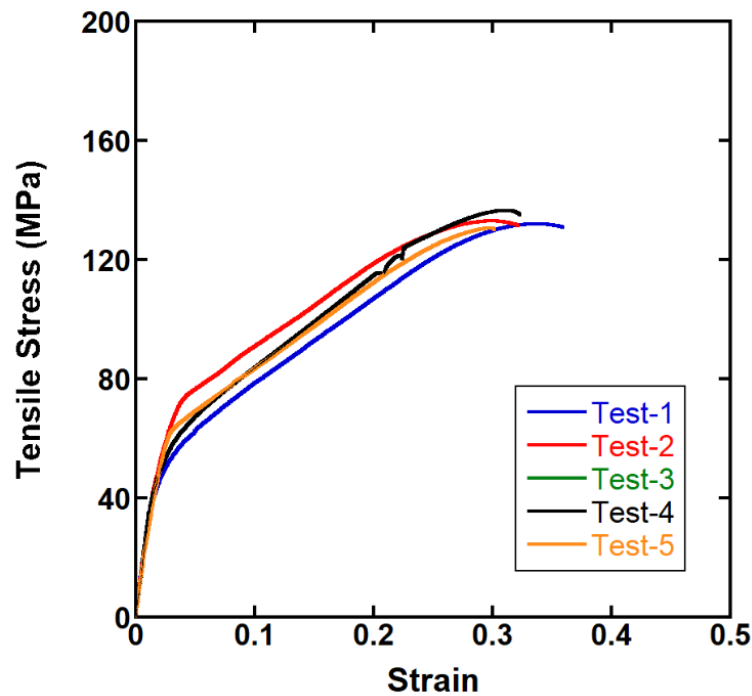


Figure 4.12. Standard quasi-static in-plane shear test curves

The results of the in-plane shear tests are tabulated in Table 4.9. The mean shear modulus of elasticity is found 3200 MPa and the mean failure strain and peak failure stress are sequentially 0.315 and 133 MPa.

Table 4.9. Standard in-plane shear test results

| <u>In-plane shear test results</u> | | | |
|---|----------------------------|-----------------------|--------------------------|
| TEST_ID | Shear Modulus (MPa) | Failure Strain | Peak Stress (MPa) |
| 1 | 3198 | 0.3589 | 132 |
| 2 | 3329 | 0.3219 | 133 |
| 3 | 3348 | 0.2716 | 132 |
| 4 | 3016 | 0.3233 | 137 |
| 5 | 3105 | 0.3017 | 131 |
| Mean | 3200 | 0.3155 | 133 |
| Std. Dev. | 143 | 0.0320 | 2 |

The pictures of the fractured in-plane shear test coupons at the front and back faces are shown in Figure 4.13(a-b), respectively. It is seen in the same pictures that considerable deformation occurs on the specimen by shear testing. The specimens fractured at the upper-middle region and the strain gauges attached to the test coupons were detached from its surface due to the extensive deformation.

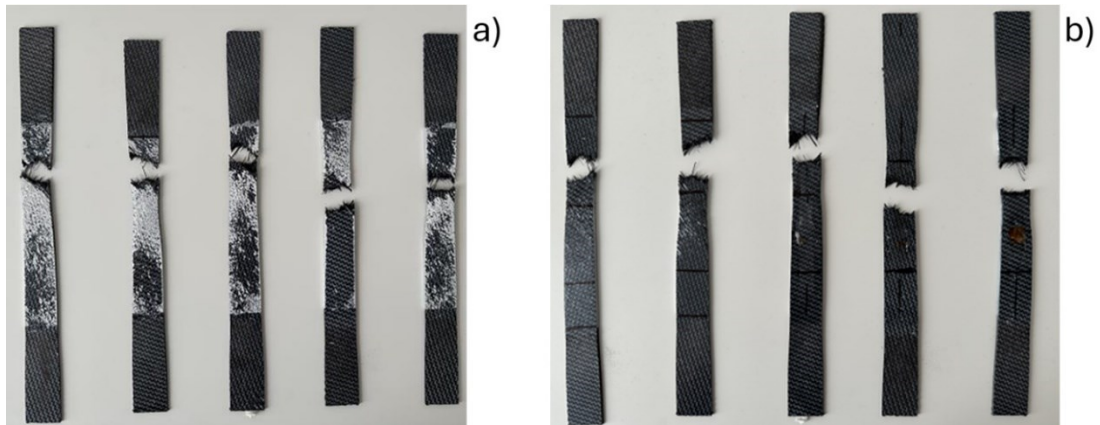


Figure 4.13. Failed shear test specimens a) front face and b) back face

4.2. Low Velocity Impact Tests

All LVI tests were performed using an instrumented drop tower (drop weight) impact test apparatus following the ASTM D7136 test standard.⁹⁵ The results of LVI tests using the drop-weight impact test apparatus were divided into two categories according to the impactor types. The effect of impactor velocity and impact energy were investigated using a 16 mm hemispherical impactor, while the effect of projectile geometry was studied using a 38 mm hemispherical impactor. The stacking sequence of all samples was an 8-ply symmetric quasi-isotropic lay-up [45/0/-45/90]_s. Thermoplastic

composite laminates with dimensions of 150x100x 2.25 mm were used for all tests. For repeatability and using one specimen for CAI testing, at least two tests were performed for all impact energy levels except the tests performed with a 38 mm projectile. The summary of all LVI tests performed on CF/PPS thermoplastic composite laminates is given in Table 4.10. The impactor size, impact velocity, and kinetic energy are all input parameters while peak impact force and dent depth were measured after impact. The tests were also recorded using a high-speed camera from the bottom face of the specimen to see impact deformation.

Table 4.10. Summary of drop weight impact tests

| Impact Case | Test No | Impactor | Impact Weight (kg) | Impact Velocity (m/s) | Impact Kinetic Energy (J) | Peak Impact Force (N) | Dent Depth (mm) |
|-------------|---------|----------|--------------------|-----------------------|---------------------------|-----------------------|------------------|
| 1 m/s | 1 | 16 mm | 2.8 | 0.99 | 1.372 | 1133.3 | - |
| 1 m/s | 2 | 16 mm | 2.8 | 0.99 | 1.372 | 991.6 | - |
| 2 m/s | 1 | 16 mm | 2.8 | 2 | 5.600 | 2215.9 | 0.21 |
| 2 m/s | 2 | 16 mm | 2.8 | 2 | 5.600 | 2185.6 | 0.2 |
| 3 m/s | 1 | 16 mm | 2.8 | 2.99 | 12.516 | 2893.9 | 0.76 |
| 3 m/s | 2 | 16 mm | 2.8 | 2.99 | 12.516 | 3086.1 | 0.77 |
| 4 m/s | 1 | 16 mm | 2.8 | 3.98 | 22.177 | 3126.6 | 2.77 |
| 4 m/s | 2 | 16 mm | 2.8 | 3.99 | 22.288 | 3096.3 | 2.75 |
| 4 m/s | 3 | 16 mm | 2.8 | 3.98 | 22.177 | 3045.7 | 2.75 |
| 5 m/s | 1 | 16 mm | 2.8 | 4.76 | 31.721 | 3086.1 | Full Penetration |
| 5 m/s | 2 | 16 mm | 2.8 | 4.75 | 31.588 | 3207.6 | Full Penetration |
| 6 m/s | 1 | 16 mm | 2.8 | 5.68 | 45.167 | 2914.1 | Full Penetration |
| 6 m/s | 2 | 16 mm | 2.8 | 5.7 | 45.486 | 3379.6 | Full Penetration |
| 6 m/s | 3 | 16 mm | 2.8 | 5.7 | 45.486 | 2924.2 | Full Penetration |
| CAI Test1 | 1 | 16 mm | 2.8 | 3.27 | 14.970 | 3227.8 | 0.95 |
| CAI Test2 | 2 | 16 mm | 2.8 | 3.27 | 14.970 | 3237.9 | 0.94 |
| CAI Test3 | 3 | 16 mm | 2.8 | 3.27 | 14.970 | 3126.6 | 0.92 |
| 35J | 1 | 38 mm | 1.986 | 5.6 | 31.140 | 5959.5 | 1.77 |
| 50J | 1 | 38 mm | 1.986 | 6.67 | 44.177 | 6173.7 | 3 |

4.2.1. The Effect of Impact Velocity

The LVI tests using drop weight impact apparatus were performed under seven different impact velocities and corresponding impact energies. The impacted weight was constant for all tests which was 2.8 kg in total. It has been aimed that the impact velocity is increased from 1 m/s to 6 m/s within 1 m/s increment and one additional impact energy level according to the ASTM D7136 standard using $E = C_E h$ where, E is the potential energy of the impactor, C_E is the specified ratio of impact energy to specimen thickness, and h is the nominal thickness of the composite laminate. Taking C_E is equal to 6.7 J/mm

and 2.25 mm total thickness of laminates resulted in 15 Joule of impact energy according to the ASTM standard. Because of the accuracy of the test apparatus, there were some discrepancies between the aimed and measured impact velocity as shown in Table 4.10.

Force-energy versus time and force-energy versus displacement curves for all impact velocity levels are shown in Figure 4.14 through Figure 4.20. It is noticed that as the impact velocity is increased the magnitude of the oscillations in the force values are increased. This is mainly caused by the delamination type of damage that occurred in the specimen. It is observed that after 2 m/s of impact velocity, delamination is one of the types of failure mode that causes sudden load drops and increases in the force values. This is more emphasized especially after 4 m/s of impact velocity.

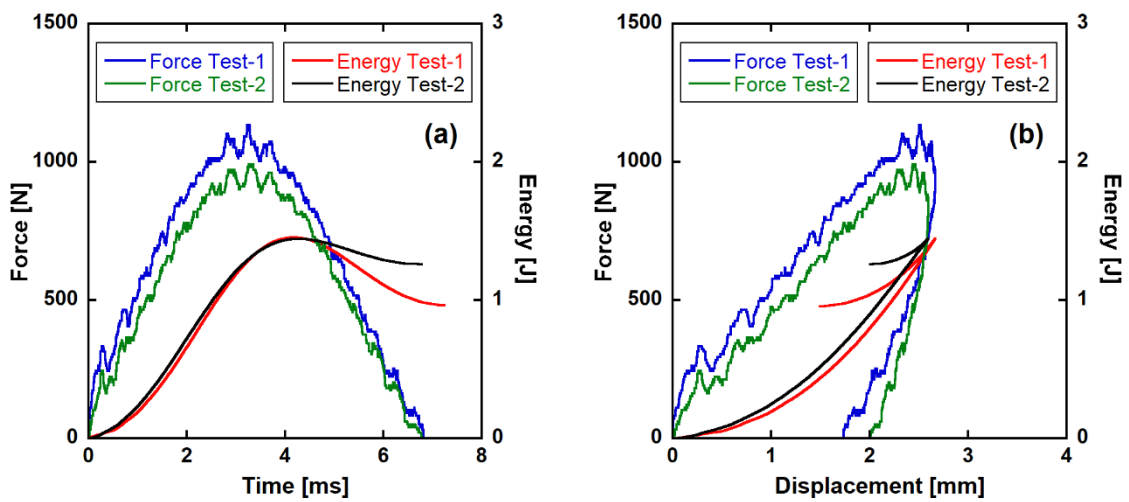


Figure 4.14. Force-Energy vs a) time and b) displacement curves at 1.37J impact energy (1 m/s)

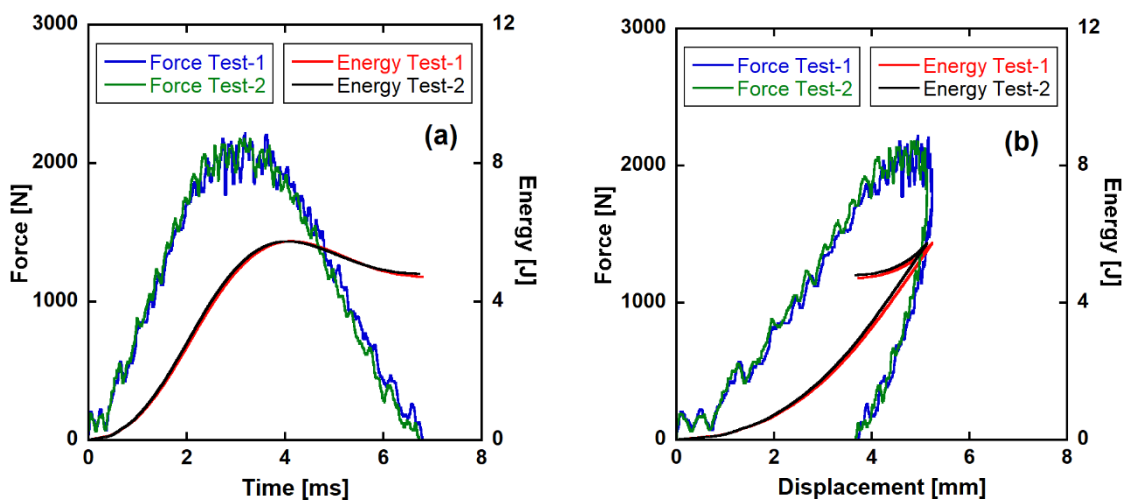


Figure 4.15. Force-Energy vs a) time and b) displacement curves at 5.60J impact energy (2 m/s)

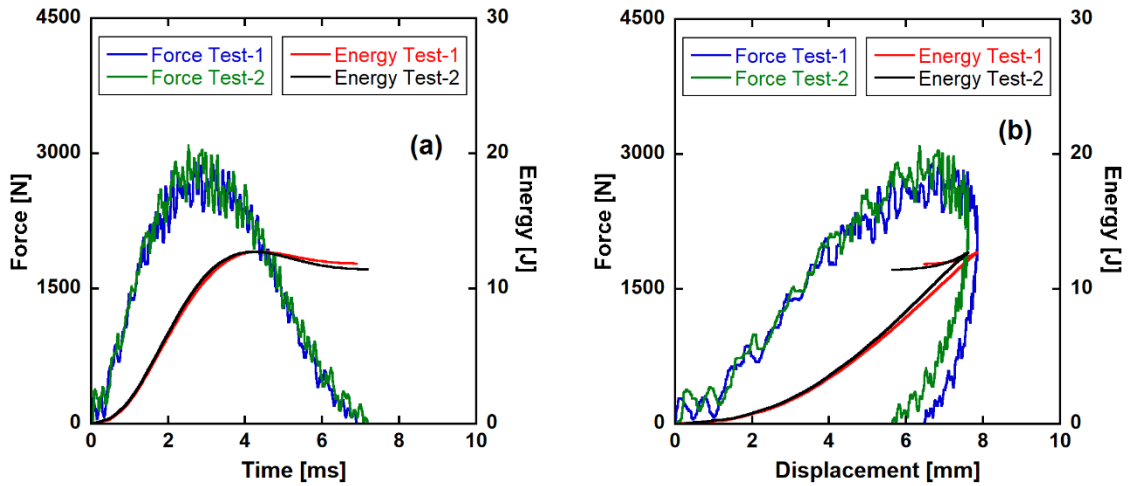


Figure 4.16. Force-Energy vs a) time and b) displacement curves at 12.51J impact energy (3 m/s)

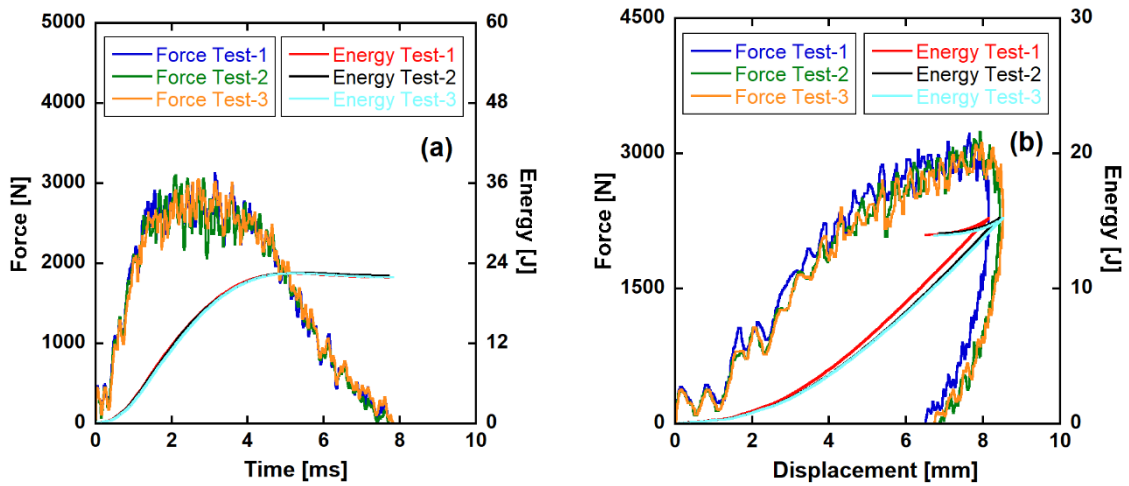


Figure 4.17. Force-Energy vs a) time and b) displacement curves at 14.97J impact energy (CAI m/s)

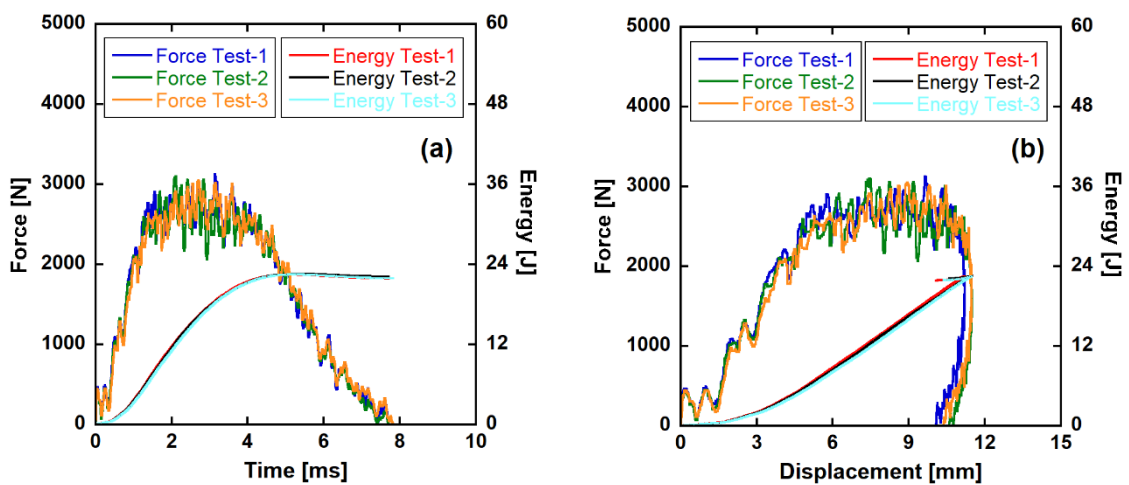


Figure 4.18. Force-Energy vs a) time and b) displacement curves at 22.23J impact energy (4 m/s)

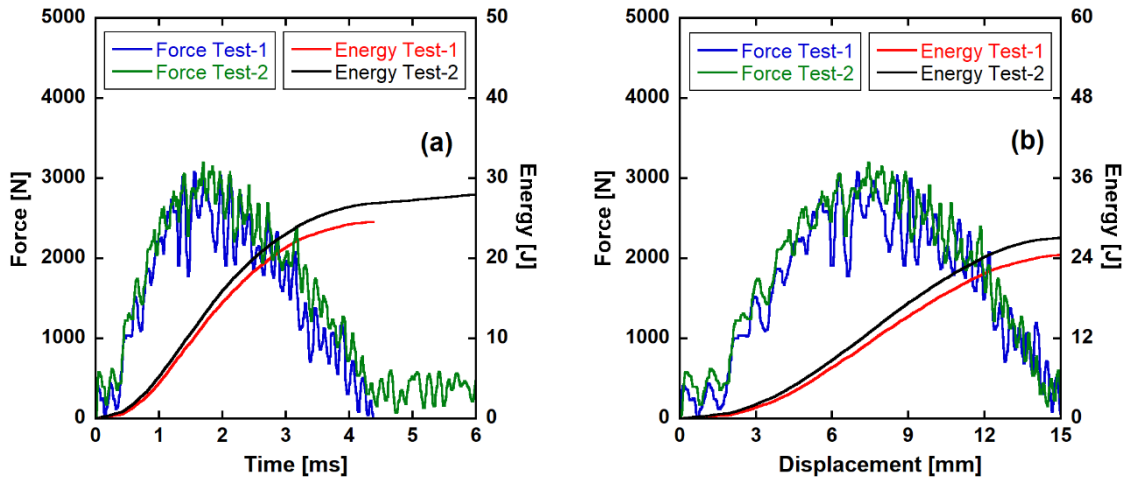


Figure 4.19. Force-Energy vs a) time and b) displacement curves at 31.65J impact energy (5 m/s)

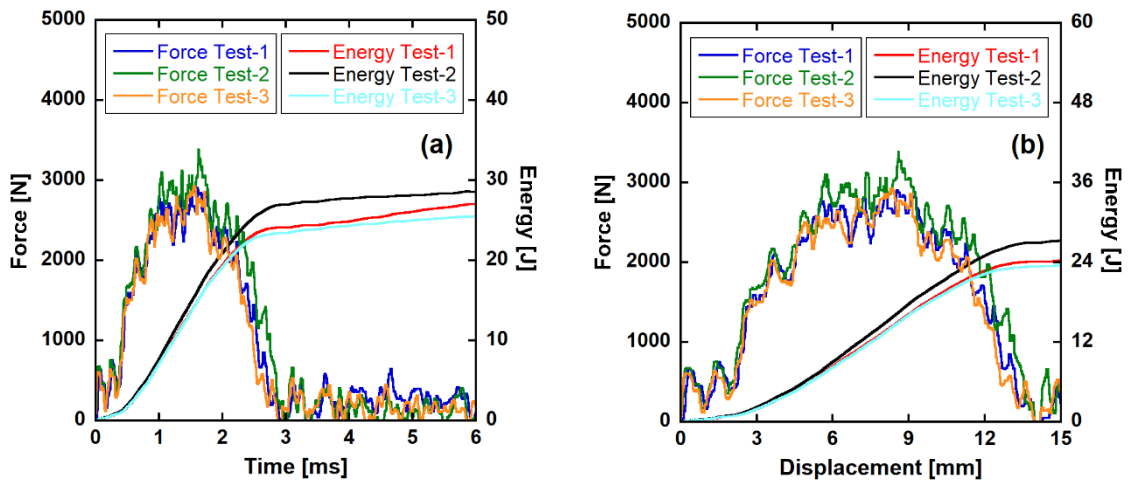


Figure 4.20. Force-Energy vs a) time and b) displacement curves at 45.48J impact energy (6 m/s)

The impact velocity versus contact time, peak force, absorbed energy, maximum displacement, dent depth, and damaged area are shown in Figure 4.21(a-f), respectively. The contact time between specimen and projectile is about 7 milliseconds for the impact speed between 1 m/s and 3 m/s. The most duration takes place in the impact at 4 m/s which is around 8 milliseconds. This is due to the maximum deformation without perforation happening at this impact velocity. Beyond 4 m/s of impact velocity, the contact time decreases gradually because of full penetration and perforation.

The peak force increases linearly with increasing impact velocity from 1 m/s to 3 m/s and then, it remains at around 3000 N up to 6 m/s (Figure 4.21(b)). The absorbed energy almost increases linearly from 1 J to 25 J in the range of 1-5 m/s impact (Figure

4.21(c)). The absorbed energy does not change after 5 m/s. The maximum absorbed energy is around 26 J for the impact at 6 m/s.

The maximum displacement of the tip of the projectile (Figure 4.21(d)) also increases linearly till 5 m/s which is around 15 mm maximum displacement was measured. After 5 m/s of impact, the maximum displacement does not increase anymore due to the perforation failure occurs on the specimen.

The dent depth shows an exponential growth behavior with increasing impact speed. The dent depth measurement results are presented in Figure 4.21(e). No dent is observed with the impacts with 1 m/s of impact velocity. The maximum dent depth is reached at 2.75 mm for an impact speed of 4 m/s. After 4 m/s of impact velocity, a full penetration occurs. Thus, dent depth is not measured beyond this impact velocity.

Damage areas are measured using a non-destructive ultrasonic C-Scan ultrasonic inspection. There is again a similar exponential increase in the damage areas like in the dent depth graph as shown in Figure 4.21(f). There is no damaged zone in the 1 m/s of impact speed conforming to the observation of no dent or visible damage. After an impact velocity of 4 m/s impact, the damaged area measurement is not changed greatly. For 4 m/s and 5 m/s of impact speeds the damage area is around 600 mm² while 630 mm² for the 6 m/s impact.

The non-destructive inspection of C-scan images and the impacted specimen photographs are shown in Figure 4.22. The C-Scan ultrasonic inspection images illustrate the damage caused by the impact. The red-colored areas in the same figure are the damage-affected areas. The total area of the specimen is 15000 mm². The tests at 0.99 m/s do not cause any internal or visible impact damage. This is also confirmed by measuring the dent depth which is zero for these tests. The test at 2 m/s show a smaller damaged area in the C-Scan ultrasonic inspection which is 58 mm². The damaged area increases gradually up to 4 m/s of impact velocity (587 mm² damage area) where penetration through specimen occurs. The transition from mainly fiber and matrix cracks to perforation through the specimen can be clearly seen at 4.76 m/s. As the perforation occurs at 4.76 m/s and 5.70 m/s impact velocities, the affected damage area on the specimen is slightly increased. The total damage area is measured as 594 mm² for the 4.76 m/s of impact velocity and 630 mm² for the 5.70 m/s impact velocity. This is also seen in the photographs of the tested specimen.

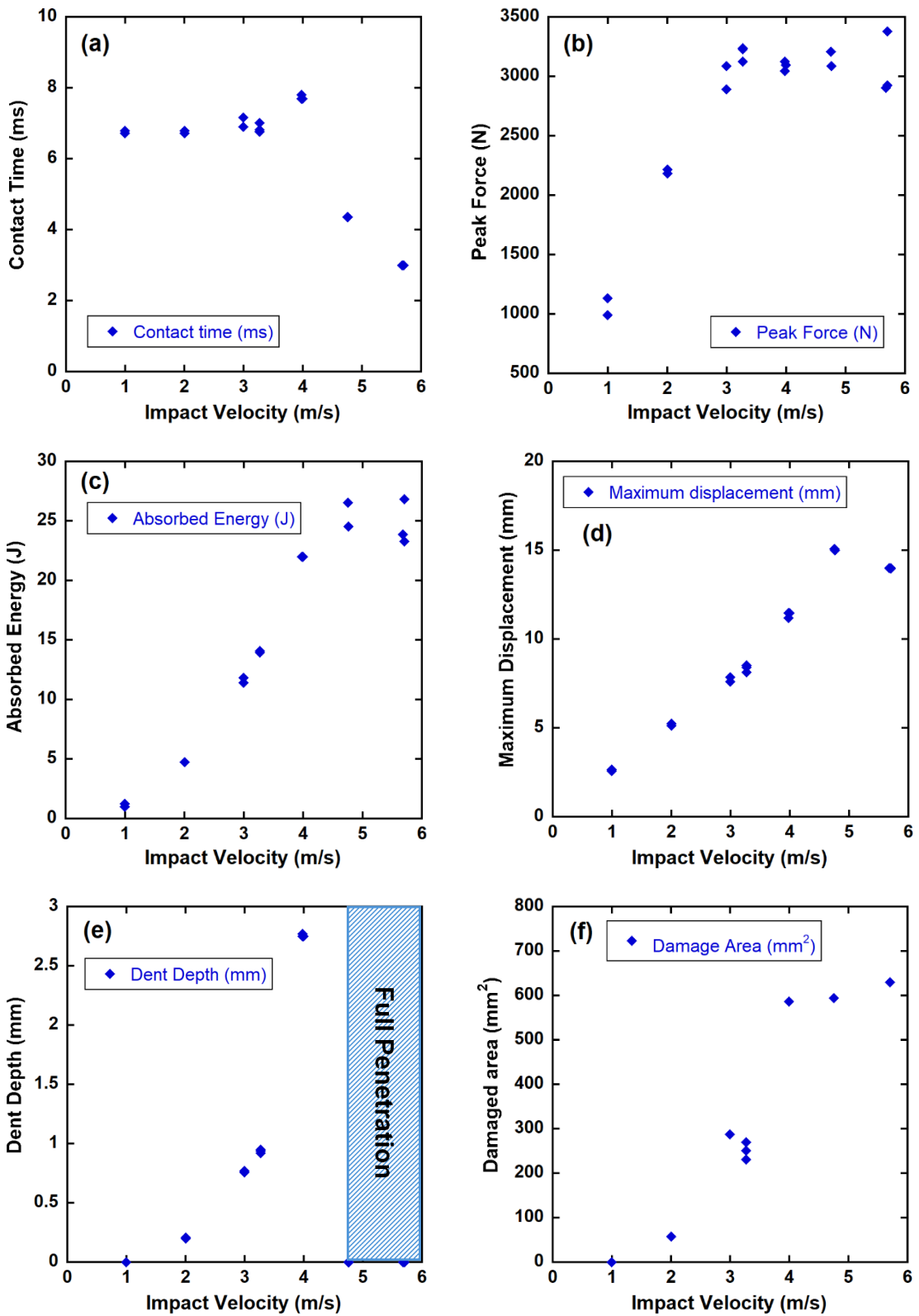


Figure 4.21. Impact velocity versus a) Contact time, b) Peak Force, c) Absorbed energy, d) Maximum displacement, e) Dent depth and f) Damaged Area

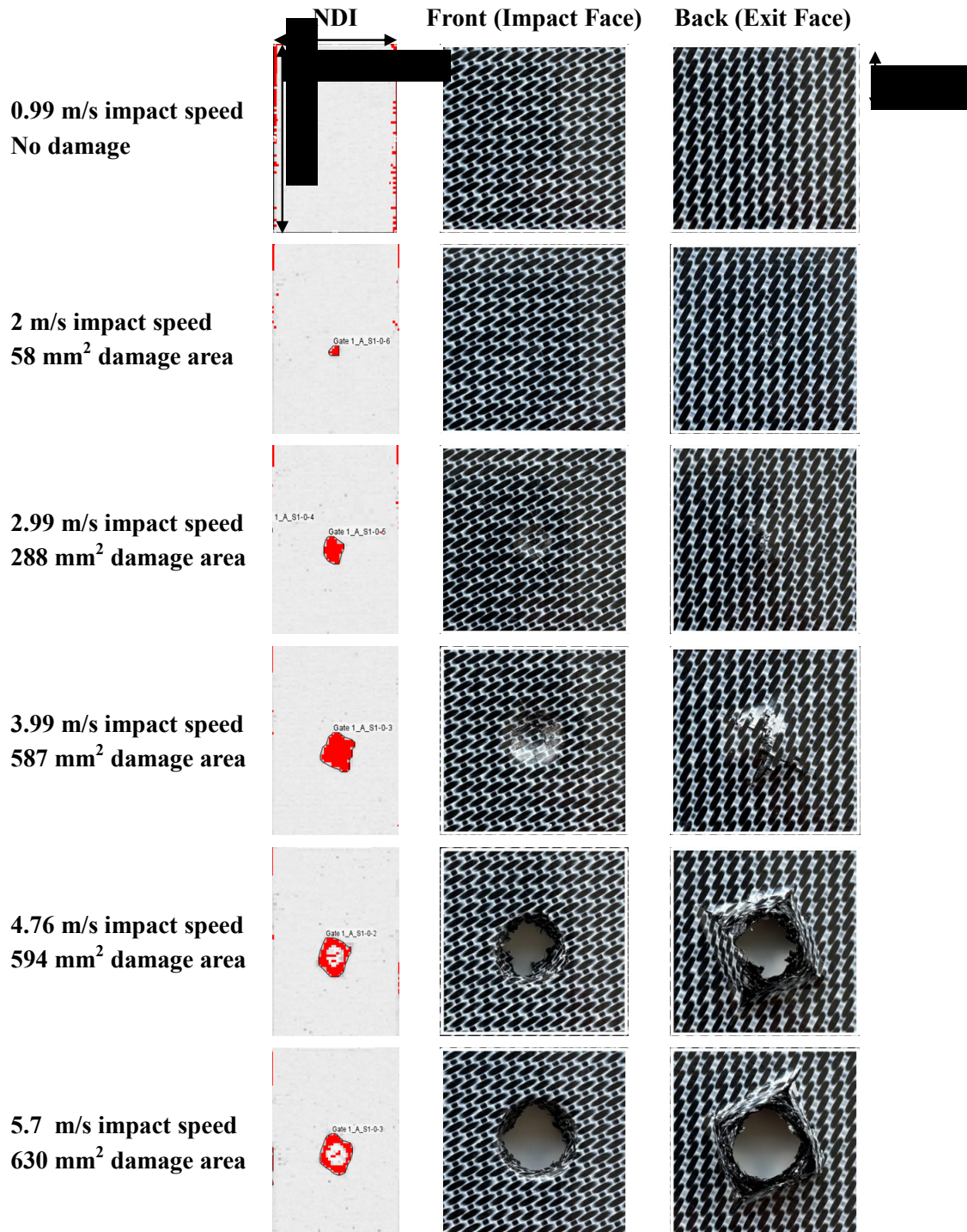


Figure 4.22. NDI and impacted specimen images at different impact velocities

4.2.2. The Effect of Impactor Geometry

To see the effect of impactor geometry, a 38 mm diameter hemispherical impactor tip made of steel was used. To eliminate other effects such as impact velocity, impact energy, impactor mass, and inertial effects, impact configuration was chosen to be similar to the impact cases of the 16 mm impactor. There are two impact configurations according to the impact speed and impact energy to make comparisons. The total mass of the impactor with the 38 mm diameter tip was 1.986 kg. Two impact speeds were chosen which were 5.6 m/s and 6.67 m/s, resulting in 31.14 and 44.18 J energy, respectively. Those corresponding energies within the 16 mm impactor tests are 31.65 J and 45.48 J, respectively. The reason for choosing these impact speeds and impact energy levels was that reaching similar impact energy levels for the 16 mm diameter impactor caused penetration on the composite laminates. Only one test was performed for each impact energy level with the 38 mm impactor since no CAI tests were performed. Impact test properties such as impactor mass, impact velocity and energy for the tests with both projectiles are given in Table 4.11.

Table 4.11. Impact energy levels for comparison of impactor geometry

| Impactor Diameter (mm) | Impactor Mass (kg) | Impact Velocity (m/s) | Impact Energy (J) |
|------------------------|--------------------|-----------------------|-------------------|
| 16 mm | 2.8 | 4.76 (Mean) | 31.65 (Mean) |
| 16 mm | 2.8 | 5.7 (Mean) | 45.48 (Mean) |
| 38 mm | 1.986 | 5.6 | 31.14 |
| 38 mm | 1.986 | 6.67 | 44.18 |

The force-energy vs. time and force-energy vs. displacement curves for the impact with a 38 mm diameter impactor are shown in Figure 4.23 (a) and (b) and Figure 4.23 (c) and (d), respectively. The peak force is measured around 6000 N for the 38 mm impactor and 3000 N for the 16 mm impactor. Absorbed energy is around 25 J for both tests of different energy levels of 16 mm impactor. Absorbed energy increases from 20 J to 34 J with increasing impact energy from 31 J to 44 J using a 38 mm impactor. The different behavior of the curves between 16 mm and 38 mm impactor test is reasoned because of the failure type of the specimen. There was perforation in the tests with 16 mm impactor while penetration occurred in the tests with 38 mm impactor.

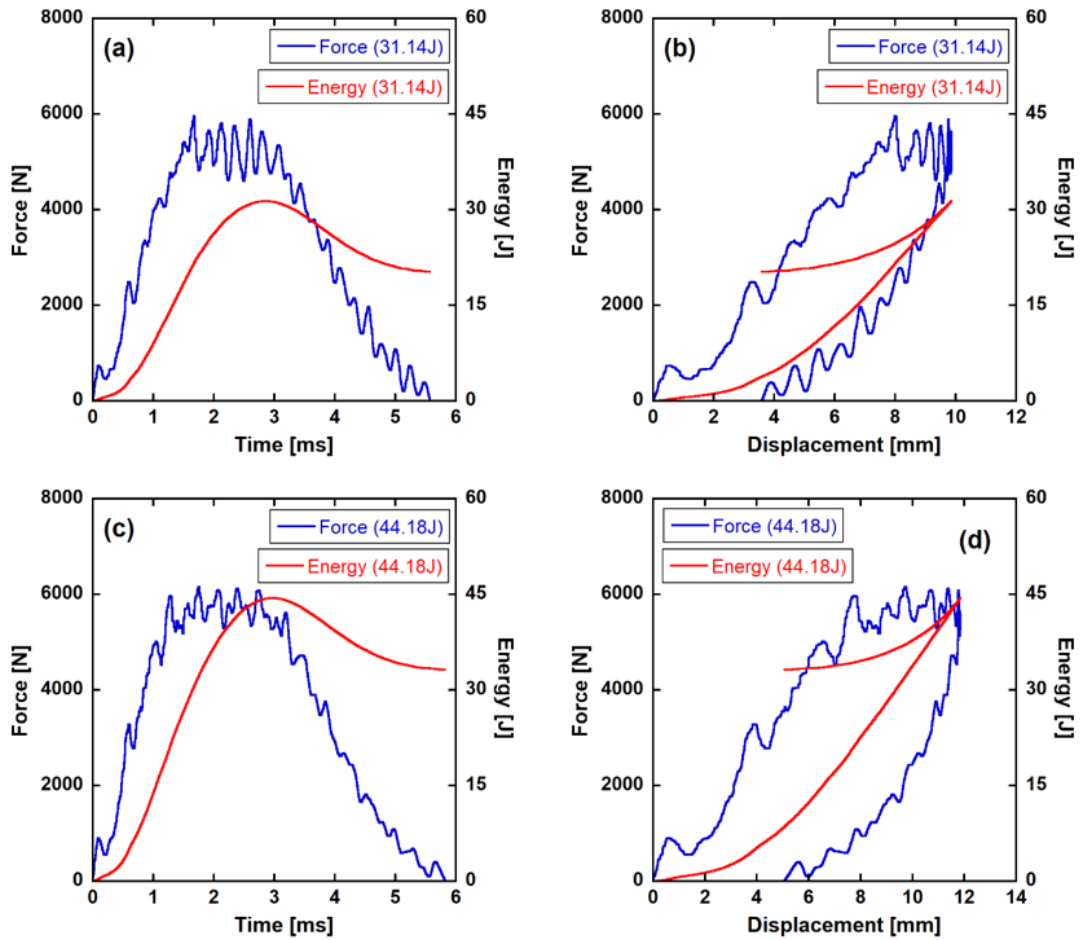


Figure 4.23. Force-Energy vs a) time (31.14J), b) displacement (31.14J) c) time (44.18J) and d) displacement (44.18J) curves for the 38 mm impactor

Non-destructive inspection of ultrasonic C-scan images and impacted test specimen photographs for the tests with a 16 mm and a 38 mm impactor are shown in Figure 4.24. Full penetration occurred with the 16 mm impactor while no penetration occurred with the 38 mm impactor. The damaged area increased for both impact energy levels for the 38 mm impactor compared to the 16 mm impactor. This might be caused by more deformation areas taking place in the 38 mm impactor tests. More energy-absorbing mechanisms become dominant due to the wider deformation area with the 38 mm impactor.

The impact energy versus contact time, peak force, absorbed energy, maximum displacement, dent depth, and damaged area for the 16 mm and the 38 mm impactor are shown in Figure 4.25(a-e). Although the impact energy is increased from 31.14 J to 44.18 J for the 38 mm impactor, the contact time durations are similar for both tests, 5.6 milliseconds and 5.8 milliseconds, respectively. Since there is a full penetration for the 16 mm impactor test, the contact time decreases at increasing impact velocity.

The peak force values for both impact energy levels are almost the same with changing impact energy. It is recorded as around 3000 N for the 16 mm impactor and 6000 N for the 38 mm impactor for both impact energy levels as shown in Figure 4.25(a). Absorbed energy levels remain stable with increasing impact energy for the 16 mm impactor. However, the absorbed energy increases from 20 J to 33 J with increasing impact energy (Figure 4.25(b)). This is also confirmed by the maximum displacement of the impactor. While there is no increase in the maximum displacement for the 16 mm impactor, the maximum displacement is increased from 10 mm to 12 mm with increasing impact energy for the 38 mm impactor tests (Figure 4.25(d)).

It is seen on the 16 mm impactor tests that the impactor creates a hole in the impact zone as it penetrates through the specimen beyond 5 m/s impact velocity. Thus, the damaged area is not changed greatly with increasing impact energy from 31.65 J to 45.48 J which is around 600 mm² for both impact energy levels. However, there is an obvious increase in the damaged area for the 38 mm impactor between the same energy levels (Figure 4.25(c)). The damaged area is increased from 830 mm² to 1280 mm² with increasing impact energy due to extensive delamination area and crack propagation as shown in Figure 4.24. Thus, it can be said that a higher diameter impactor causes a greater damage area than the smaller diameter impactor at the same level of impact energy at low velocity impacts.

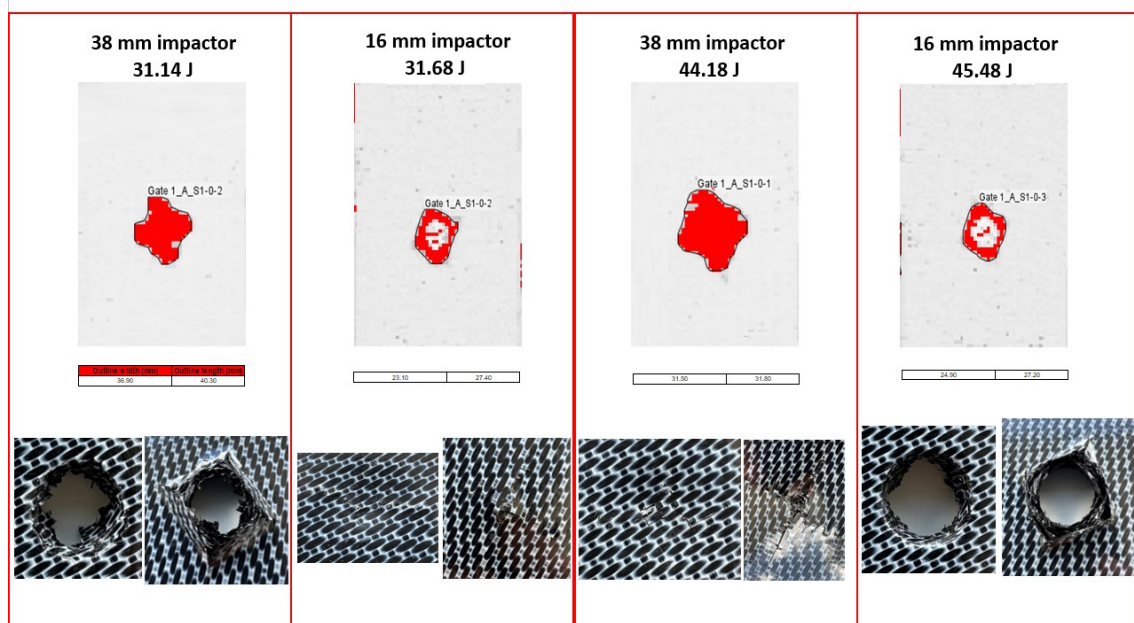


Figure 4.24. NDI images and impacted specimen images at two different impact energies and impactor

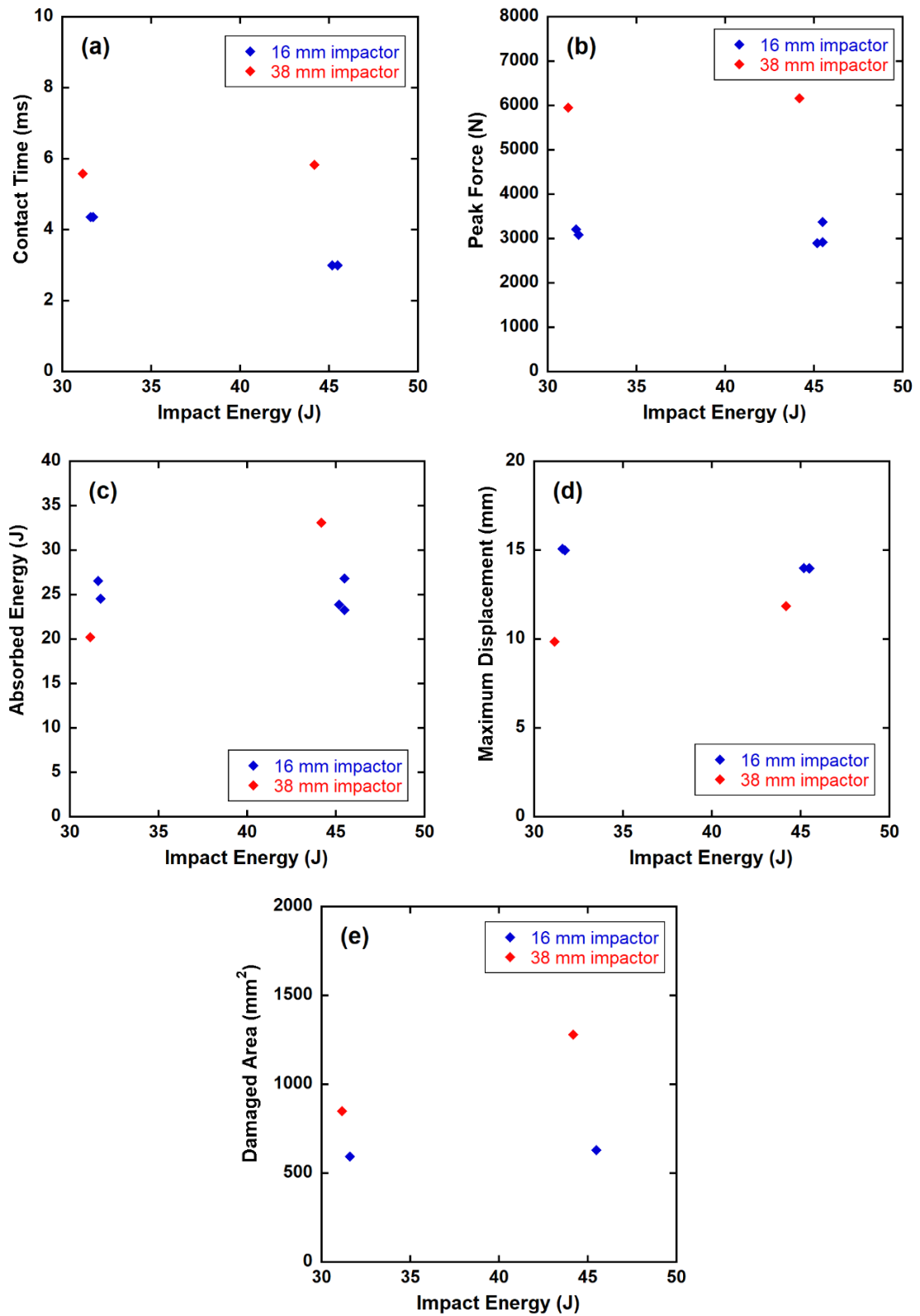


Figure 4.25. Impact Energy versus a) Contact time, b) Peak Force, c) Absorbed energy, d) Maximum displacement and e) Damaged Area for the 38 mm impactor

4.3. Compression After Impact Tests

The LVI tested specimens at seven different impact energies were exposed to the CAI tests. For each impact energy, one CAI test was performed based on the ASTM D7137⁹⁶ test standard. In all tests, the DIC was used to capture strain, damage and crack propagation as well as the overall damage zone. The test specimens of the CAI tests are listed in Table 4.12 along with the previously applied impact velocity and kinetic energy. The CAI test-7 which is the LVI test specimen impacted at 3.27 m/s and 14.97 J refers to the ASTM D7136 test standard⁹⁵ impact energy.

Table 4.12. Compression after impact test specimens and their impact scenario

| Impact Case | Impact Velocity (m/s) | Impact Kinetic Energy (J) |
|--------------------|------------------------------|----------------------------------|
| CAI Test-1 | 0.99 | 1.37 |
| CAI Test-2 | 2.00 | 5.60 |
| CAI Test-3 | 2.99 | 12.52 |
| CAI Test-4 | 3.98 | 22.18 |
| CAI Test-5 | 4.76 | 31.72 |
| CAI Test-6 | 5.70 | 45.49 |
| CAI Test-7 | 3.27 | 14.97 |

The stress-strain curves for all CAI tests are shown in Figure 4.26. The standard deviation for the average stress and strain at failure was 11.67 MPa and 0.0013, respectively. As a reference, the CAI strength was reported 209 MPa in the manufacturer product datasheet¹. This shows that the results obtained are at a similar level to the manufacturer data and vary with the extent of damage that existed. The experimental ultimate strength, failure strain, effective modulus, damage area, and failure modes of the CAI tests are tabulated in Table 4.13. The damaged areas are measured from the non-destructive inspection. Failure strain was recorded from both stroke displacement and DIC strain measurement. The characteristic failure mode was found to be LDM (lateral-trough damage-middle) according to the ASTM standard.⁹⁶

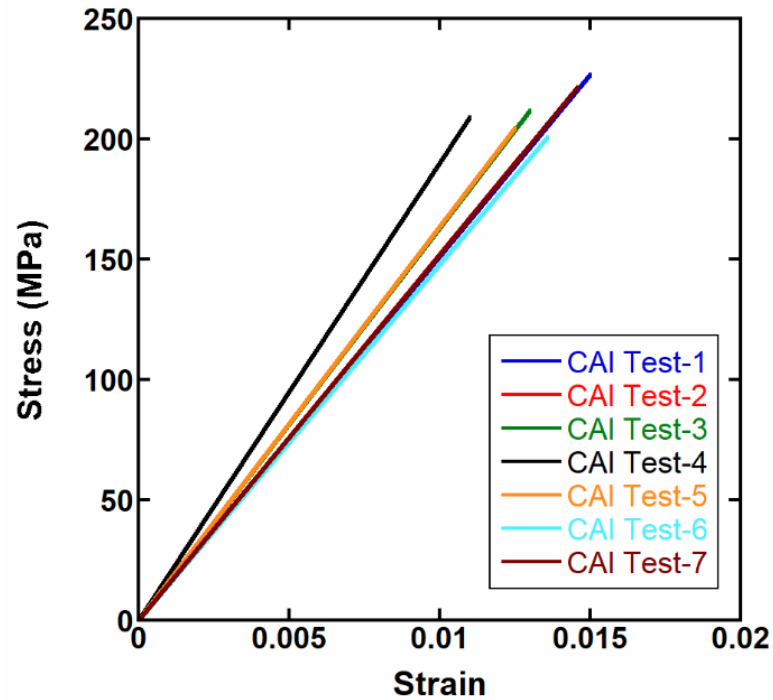


Figure 4.26. Stress-strain curve for CAI tests

Table 4.13. Compression after impact test results

| CAI Test ID | Ultimate Strength (MPa) | Failure Strain Stroke | Failure Strain DIC | Damage Area (mm ²) | Effective Modulus (MPa) | Failure Mode |
|-------------|-------------------------|-----------------------|--------------------|--------------------------------|-------------------------|--------------|
| CAI Test-1 | 227 | 0.0150 | 0.0102 | 2335 | 15129 | LDM |
| CAI Test-2 | 193 | 0.0127 | 0.0183 | 2453 | 16063 | LVV |
| CAI Test-3 | 212 | 0.0130 | 0.0155 | 2697 | 16296 | LDM |
| CAI Test-4 | 209 | 0.0110 | 0.0121 | 1422 | 19000 | LDM |
| CAI Test-5 | 205 | 0.0125 | 0.0130 | 1494 | 16376 | LDM |
| CAI Test-6 | 201 | 0.0136 | 0.0140 | 2576 | 14762 | LDM |
| CAI Test-7 | 222 | 0.0146 | 0.0128 | 1983 | 15137 | LGM |

L=Lateral, D=at/through Damage, M=Middle, V=Various, G=Gage, away from damage

The change in the ultimate strength, failure strain, effective modulus, and damage area with respect to impact energy are given in Figure 4.27(a-d). as seen in Figure 4.27(a), the ultimate strength values do not change with increasing impact energy. Another word, there is no clear trend of the ultimate strength within the studied impact energies. Furthermore, the failure strain and effective modulus values do not also change with increasing impact energy levels, Figure 4.27(b) and (c), respectively. The failure strain varies between 0.011 and 0.015 for all tests and the effective modulus between 15000 MPa and 20000 MPa. The damaged area has also no direct correlation with the impact energy levels as shown in Figure 4.27(d). In the low-impact energy levels, the damage area increases with increasing impact energy. At the intermediate impact energy level,

the damage area decreases, and the maximum damage area is reached at the highest impact energy level. However, it is hard to say that there is a clear trend about the damage area and impact energy.

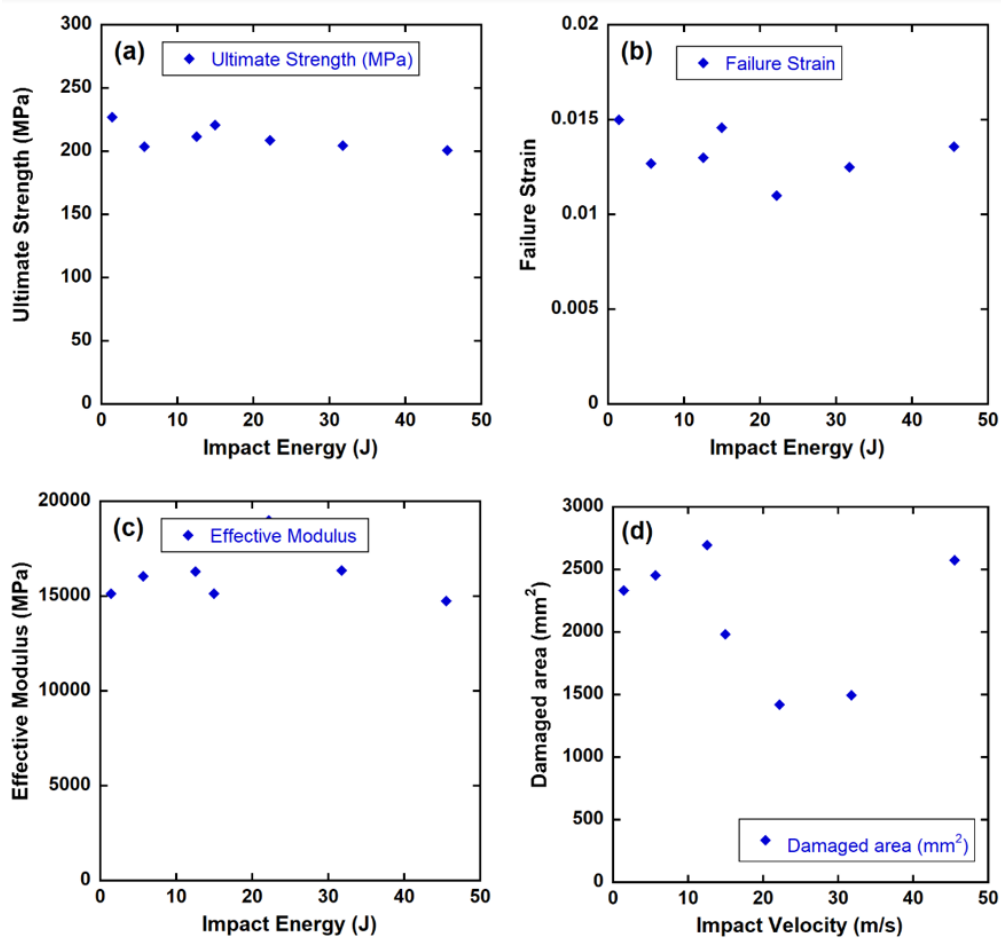


Figure 4.27. Impact Energy versus a) Ultimate strength, b) Failure strain, c) Effective modulus and d) Damaged Area

The full field 2D strain maps of all tests just before the failure are shown in Figure 4.28(a-f). Just before failure images give good idea about the deformation behavior and loading condition of the specimen which can be then comparable with numerical results. These figures show the regions where the compressive strain takes place up to 0.02. The blue region in the same figures is affected by the compressive loading and this region belongs to the impact zone in the range of ± 50 mm. After the damage is initiated at a certain location in this compressive zone where the impact take place, it spreads out through lateral transverse direction causing matrix cracking, fiber rupture, and delamination.

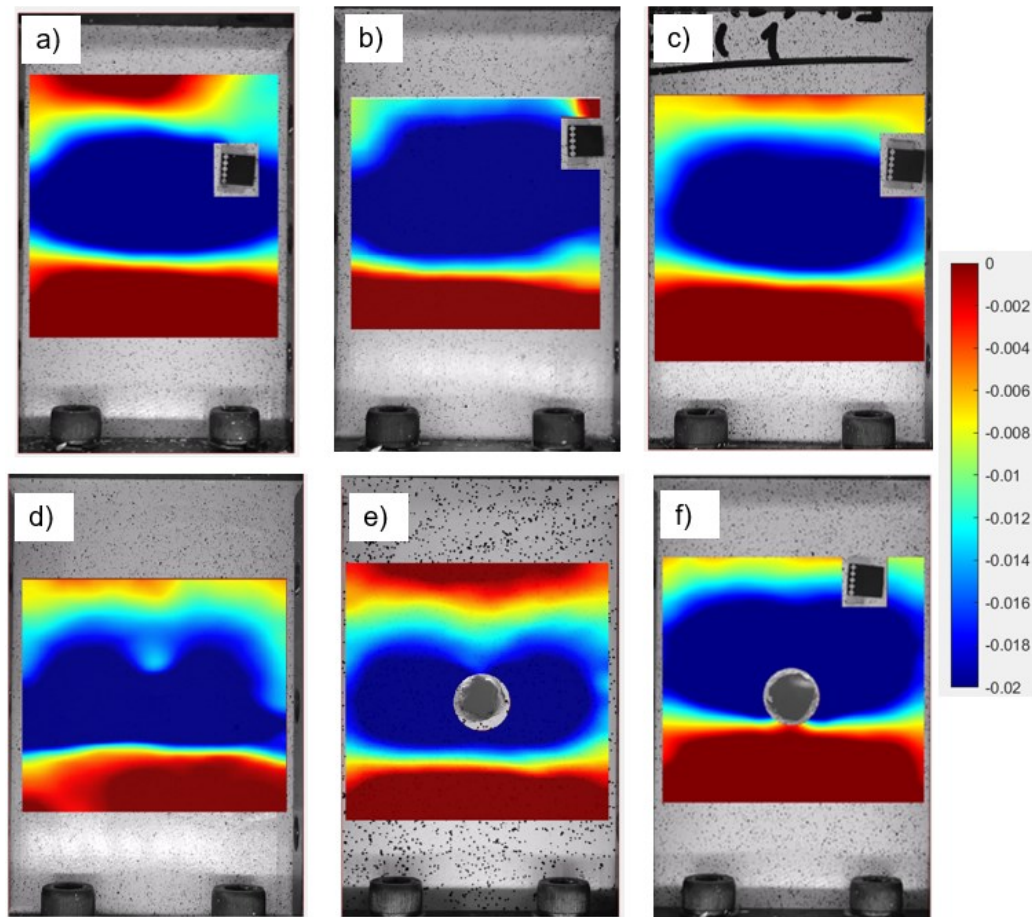


Figure 4.28. Full-field strain measurement just before failure for test specimen; a) CAI Test-1, b) CAI Test-2, c) CAI Test-3, d) CAI Test-4, e) CAI Test-5 and f) CAI Test-6

The front and back face deformation images, 2D full-field strain deformation view, and C-Scan images of the CAI test specimens after the failure are shown through Figure 4.29 and Figure 4.34. It is noted in the same figures that the DIC images correlate well with the C-scan images after failure. The DIC images show the y-axis strain values between 0 and 0.02 with the color changing from red to blue. The blue regions of the DIC images correspond to the regions having a strain than greater 0.02, corresponding to a complete failure. The assessment of effective damage areas is further seen in the same figures not possible just by looking at photographic images of test specimens. The photographic images just give an idea about the failure modes of the specimens. The actual effective damage area can be determined by ultrasonic C-Scan images which are tabulated in Table 4.13. All specimens exhibit lateral failure at the mid-section of the specimen. Only test specimen-4 shows lateral failure at the upper part of the impact zone. Double-sided crack propagation and failure are more pronounced in the CAI test-4, test-5, and test-6 where the impact is more severe.

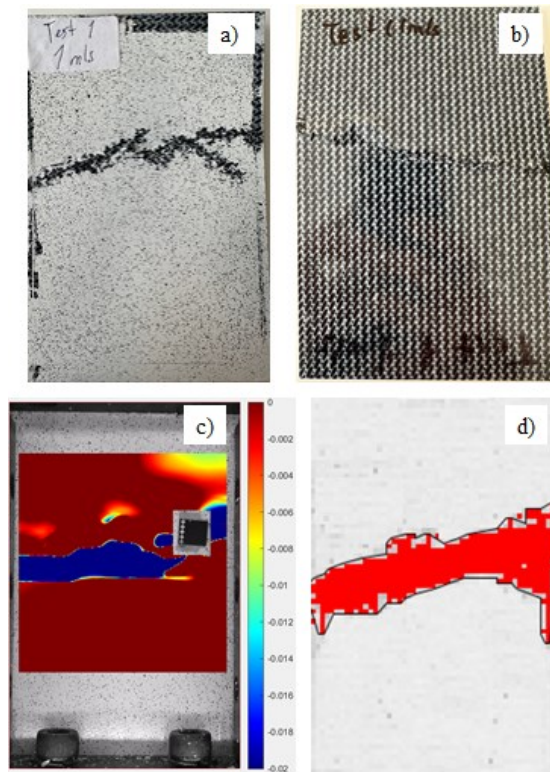


Figure 4.29. CAI test specimen-1 after failure a) front face, b) back face, c) DIC image, and d) C-Scan image

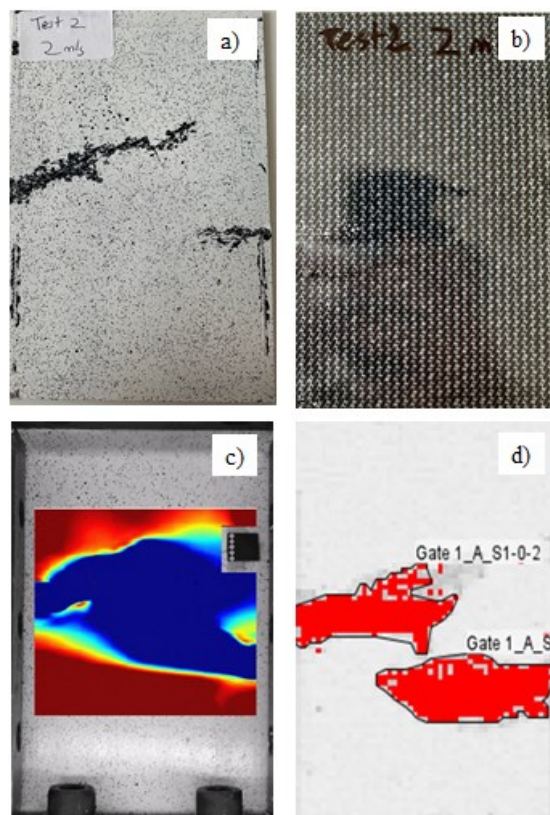


Figure 4.30. CAI test specimen-2 after failure a) front face, b) back face, c) DIC image, and d) C-Scan image

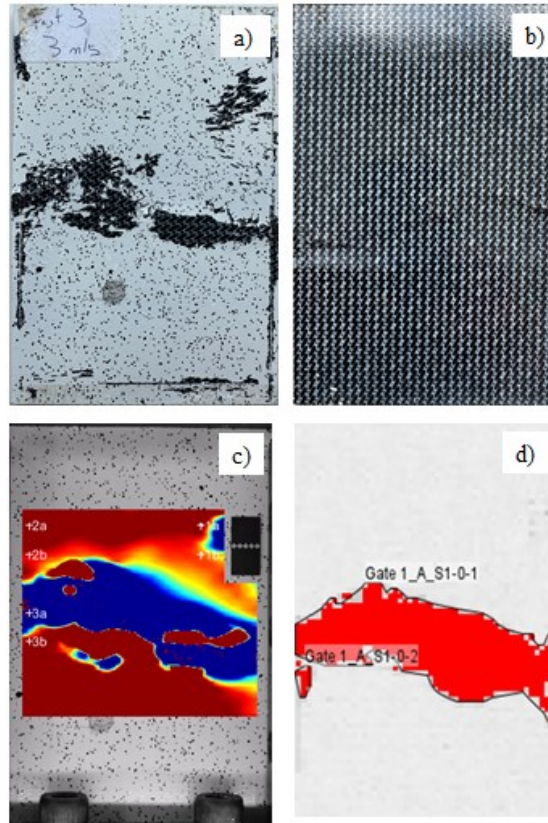


Figure 4.31. CAI test specimen-3 after failure a) front face, b) back face, c) DIC image, and d) C-Scan image

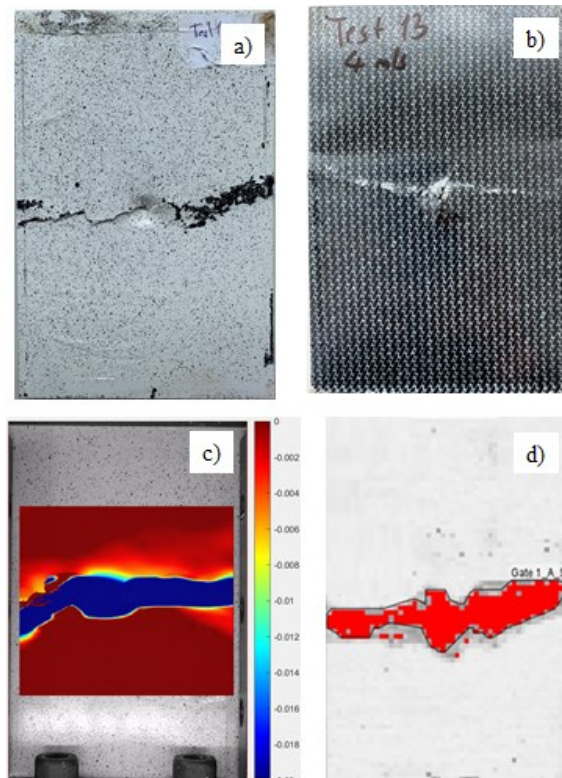


Figure 4.32. CAI test specimen-4 after failure a) front face, b) back face, c) DIC image, and d) C-Scan image

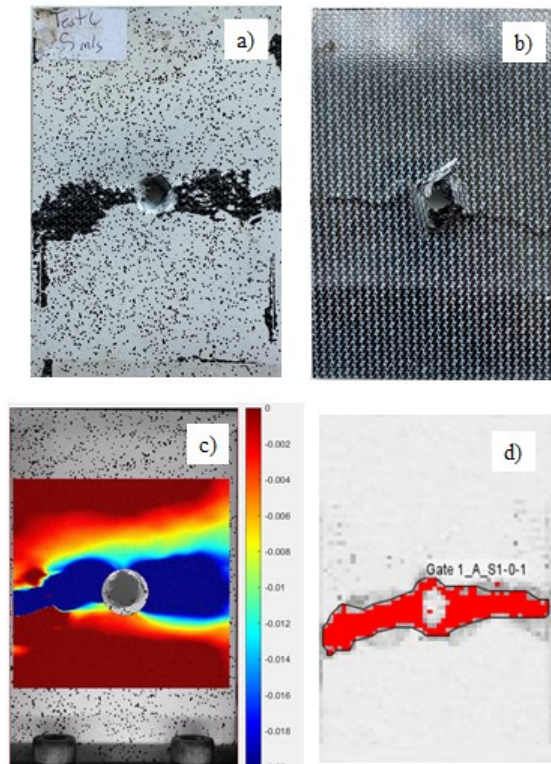


Figure 4.33. CAI test specimen-5 after failure a) front face, b) back face, c) DIC image, and d) C-Scan image

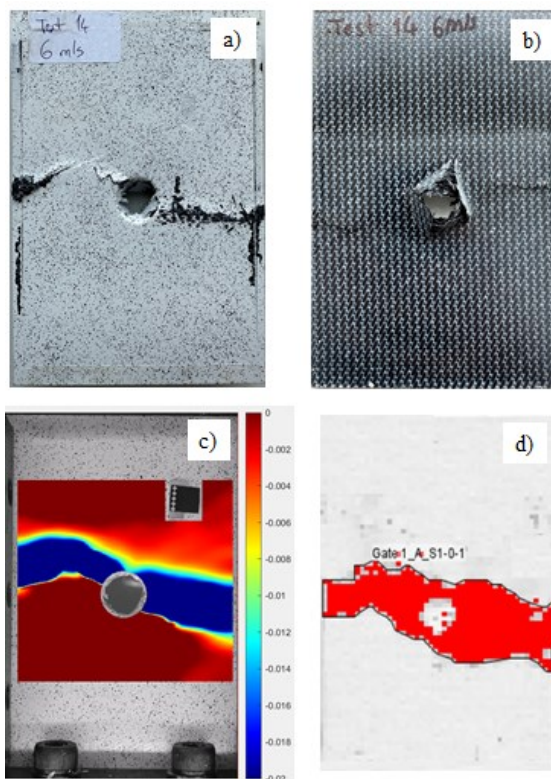


Figure 4.34. CAI test specimen-6 after failure a) front face, b) back face, c) DIC image, and d) C-Scan image

4.4. Gas Gun Impact Tests

The HVI tests were performed to measure the impact resistance behavior of CF/PPS thermoplastic composite at high-velocity impact. The results of the HVI tests are tabulated in Table 4.14. The impact and exit velocities of the projectiles were measured using a laser beam measurement system. Impact energy, exit energy, and absorbed energy were calculated as described in the experimental methodology. The initial aim was to impact at the center of the specimen with a 100 m/s of impact velocity. However, due to the inherent nature of experimental tests, there were minimal discrepancies in impact location and impact velocity. It is seen in the same table that as the impact velocity increases the exit velocity increases as well. Also, the exit energy of the projectile increases as the impact energy increases. However, absorbed energy does not correlate with impact velocity instead there is kind of correlation between the total damaged area and the absorbed energy. There is a higher absorbed energy within the impact velocity of 99.93 m/s compared to the 101.68 m/s impact velocity test. The maximum absorbed energy is seen in the test with 107.15 m/s impact velocity. Approximately 22-28% of the initial impact energy is absorbed through complex failure and deformation mechanisms. Correspondingly, the effective damage area results from ultrasonic C-scan inspections are well correlated with the absorbed energy. The higher absorbed energy generates a higher damage area in the specimen. The lowest damage area was measured as 3644 mm² while the maximum damaged area was measured as 8504 mm².

Table 4.14. Gas gun impact test results

| <i>Test Number</i> | <i>Impact Velocity (m/s)</i> | <i>Exit Velocity (m/s)</i> | <i>Impact energy (J)</i> | <i>Exit Energy (J)</i> | <i>Absorbed Energy (J)</i> | <i>Damage Area (mm²)</i> |
|--------------------|------------------------------|----------------------------|--------------------------|------------------------|----------------------------|-------------------------------------|
| Test 1 | 99.93 | 84.58 | 549.23 | 393.46 | 155.77 | 6708 |
| Test 2 | 101.68 | 89.73 | 568.64 | 442.83 | 125.80 | 3644 |
| Test 3 | 107.15 | 91.14 | 631.46 | 456.86 | 174.60 | 8504 |

High-speed video camera images during an HVI test are shown in Figure 4.35. The high-speed video camera images are given within 0.1 milliseconds of interval, and it took 1 milliseconds of the whole perforation and exit phase of the projectile. It can be seen from the figures that the projectile creates transverse and longitudinal cracks as it penetrates through the specimen.

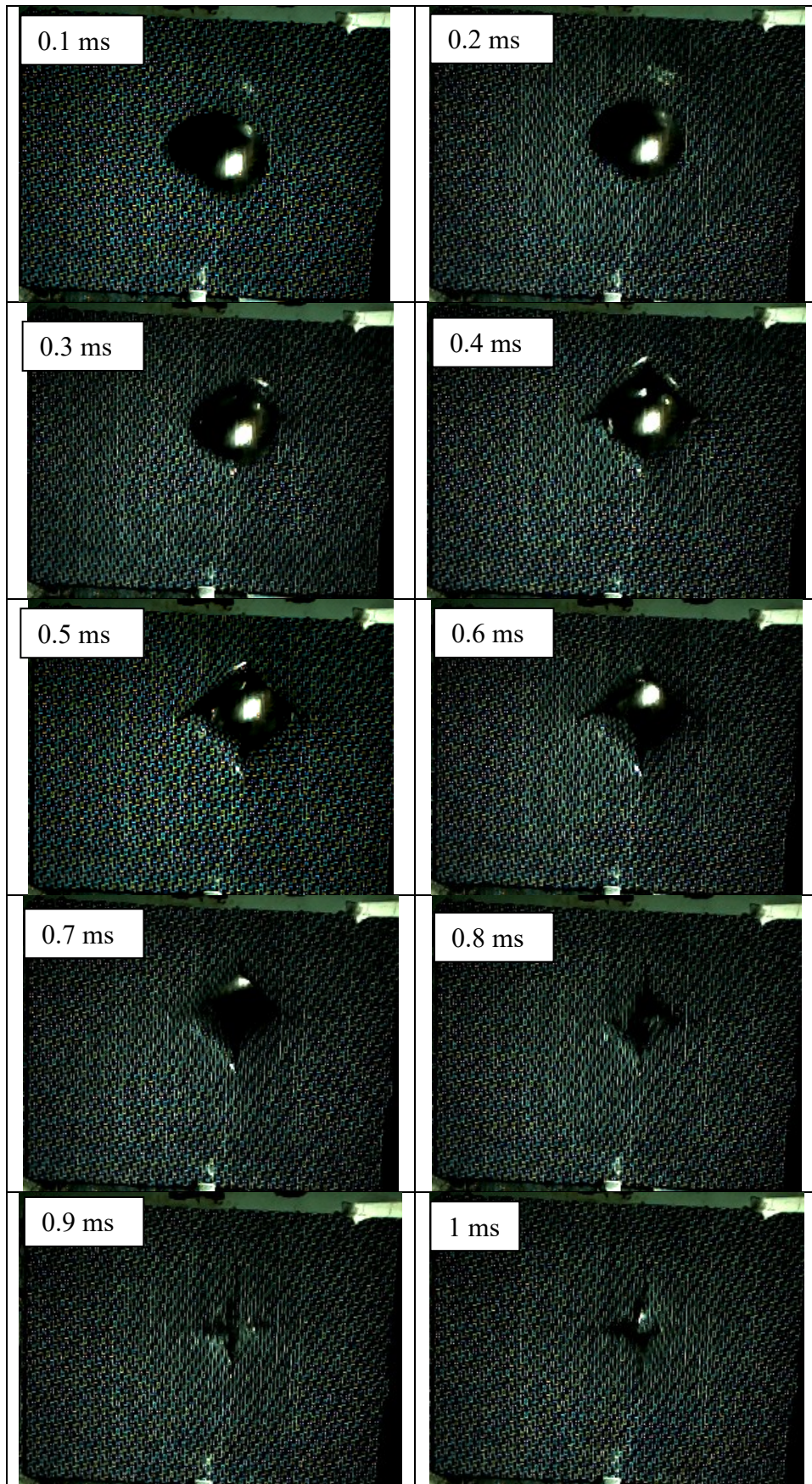


Figure 4.35. High-speed video camera images during impact

After impact images and C-scan inspection damage maps for all three tests are shown in Figure 4.36 (a-c), Figure 4.37 (a-c), and Figure 4.38 (a-c), respectively. It is clear from the figures that the damage is more obvious and extensive at the back face of the specimen. The main driving mechanisms for damage are fiber breakage, fiber-matrix debonding, and delamination. Long transverse and longitudinal cracks are formed at the impact zone. C-scan inspection shows the effective damage area on the whole composite plate, including delamination. The reason behind the distinguished damage area between the tested specimens might be the impact location. For the test-1 and test-3 the impact locations are slightly different than the midpoint of the specimen. This condition might affect the inhomogeneous stress distribution and corresponding delamination area. On the other hand, test-2 shows homogenous damage distribution and almost symmetric failure at the middle of the specimen where the projectile impacts. Because of this, test-2 is taken as a benchmark test for numerical analysis studies.

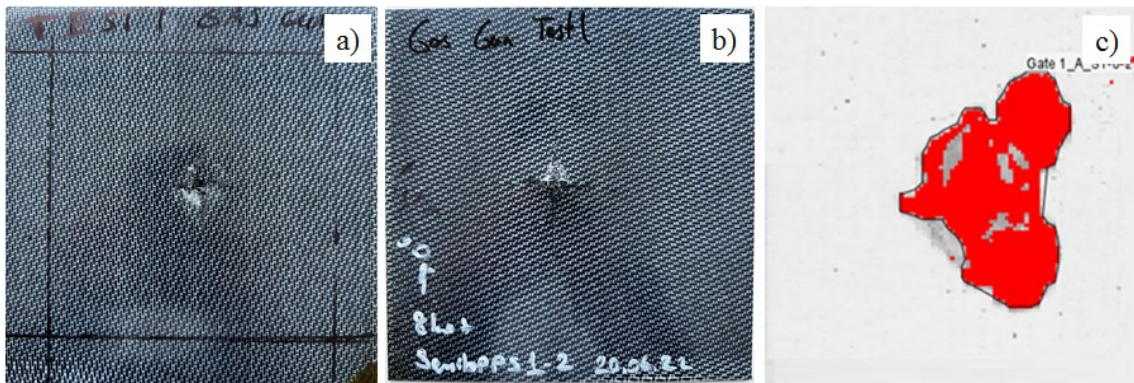


Figure 4.36. Gas gun impact test specimen-1 after impact; a) front face, b) back face, and c) C-scan image for damage assessment

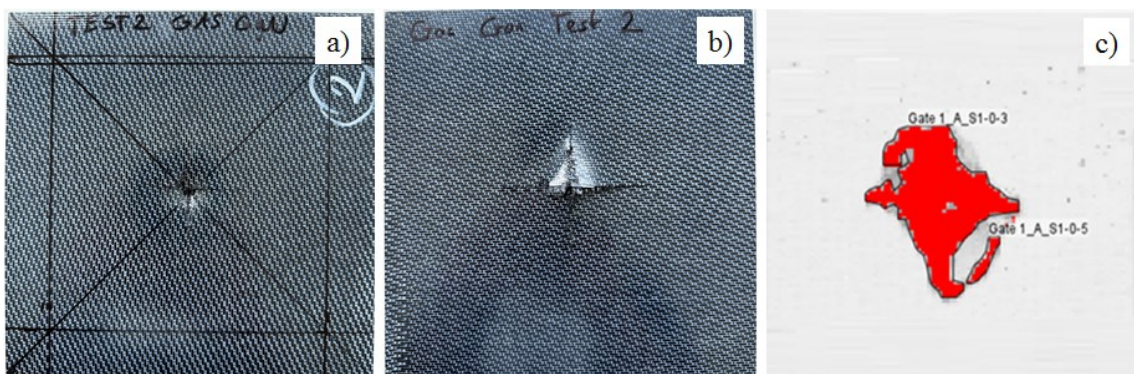


Figure 4.37. Gas gun impact test specimen-2 after impact; a) front face, b) back face, and c) C-scan image for damage assessment

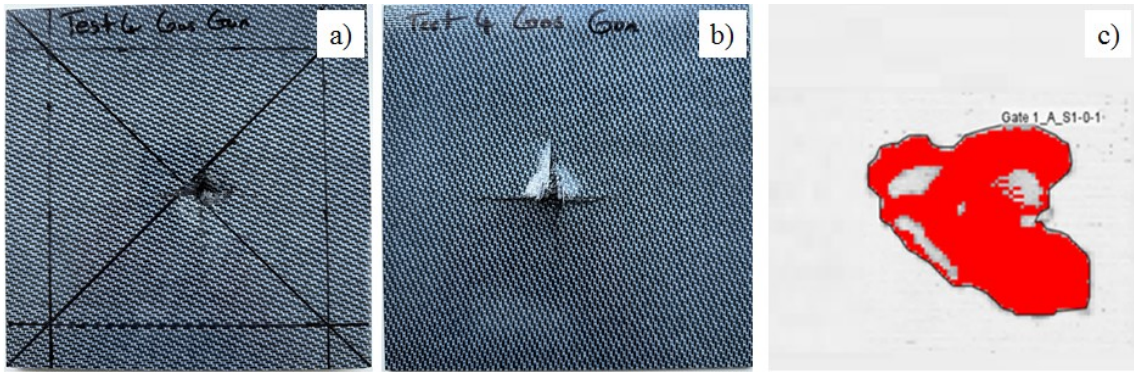


Figure 4.38. Gas gun impact test specimen-3 after impact; a) front face, b) back face, and c) C-scan image for damage assessment

CHAPTER 5

NUMERICAL ANALYSIS METHODOLOGY

5.1. Introduction

In this chapter, the numerical analysis methodologies of the accomplished experimental tests are presented. The constitutive material modeling and cohesive zone modeling techniques for CF/PPS thermoplastic composite laminate are discussed. Both implicit and explicit finite element analysis methods are implemented according to the analysis type. The quasi-static mechanical characterization and compression after impact analyses were executed using non-linear implicit solver of LS-DYNA. On the other hand, the impact analyses were conducted in the non-linear dynamic explicit FE code of LS-DYNA version R11 with double-precision solver. The details of the finite element modeling approaches used in this study are presented in the following sections.

5.2. Material Model Selection and Parameter Identification

Constitutive material modeling of FRP composites is a challenging task because FRP composites show highly non-linear deformation behavior. One can choose micromechanical, meso-scale or macro-scale approach according to the complexity of the problem. In this content, many material models have been developed so far, differing from each other according to their complexity including nonlinearity, failure, damage, strain rate, element type and modelling approach. In this study, only macro-scale level modelling approach is considered due to the scale of the tests conducted.

LS-DYNA material library offers different composite material models with different failure criteria and applicability according to the element type. These material models can be summarized as follows:

- MAT_2: Elastic-orthotropic behavior for shells, tshells and solids. Anisotropic behavior is only available for solid elements. Constitutive matrix has no plastic-like deformation, damage, erosion and the strain rate and temperature sensitivity.

- MAT_22: Shell, tshell and solid elements are applicable. The model is based on the Chang-Chang failure criteria with a linear elastic behavior in the longitudinal and transverse directions response up to failure. The model has no plastic-like deformation; damage, erosion and the strain rate and temperature sensitivity.
- MAT_54-55: Chang-Chang or Tsai-Wu failure model, selective property degradation using Matzenmiller in compression; shell or solids; no plastic-like deformation; no erosion; no rate sensitivity; no temperature sensitivity.
- MAT_58: Modified Hashin failure criteria is used, Matzenmiller continuum damage mechanics formulation with failure stress and strain-based curve fit; shells and tshells only; no plastic-like deformation; effective strain erosion; rate sensitivity; no temperature sensitivity; non-linear shear stress.
- MAT_158: Rate sensitive version of MAT_58, rate effects only limited to 15%. Rate dependence is based on the isotropic Maxwell model with viscoelastic Prony series. Applicable to shell and thick shell only; no plastic-like deformation; effective strain erosion; no temperature sensitivity.
- MAT_161-162: Suitable model for progressive failure analysis for UD or woven fabric composites with solid element. Progressive failure criteria is based on the Hashin stress-based initial failure with the Matzenmiller damage; no plastic-like deformation; volume strain erosion; modulus and strength scaled by strain rate; no temperature sensitivity; it requires additional license to use.
- MAT_219: CODAM model based on continuum damage mechanics and developed for progressive damage behavior of laminated fiber reinforced plastics. No plastic deformation or rate sensitivity exist, erosion is based on maximum principle strain. Applicable for shell or solid elements.
- MAT_221: Orthotropic damage model with the Marie damage model, failure is defined with 9 failure strains; no plastic deformation, applicable to solid elements only, no temperature or strain rate dependency.
- MAT_261: Pinho fracture model with separate damage evolution based on failure mode; shells or solids; no plastic-like deformation; no erosion; no rate sensitivity; no temperature sensitivity.
- MAT_262: Camanho fracture model with energy approach used to generate damage functions in various coordinate directions; shells or solids; no plastic-like deformation; no erosion; no rate sensitivity; no temperature sensitivity.

After evaluation of available material models in the literature, past experiences, and suitability for the current objective in this study, MAT_58 (MAT_LAMINATED_COMPOSITE_FABRIC) has been selected for the constitutive material model to represent CF/PPS thermoplastic composite mechanical behavior in the numerical analyses. A more detailed explanation about the selected material model and material model parameter identification study are given in the following section.

5.3. Material Model Theory and Parameter Identification

The material model Laminated_Composite_Fabric (MAT_58) was developed for modelling composite materials with unidirectional layers, laminates, and woven fabric. Material model parameters can be classified experimental and computational. There are also defined parameters of material orientation for local coordinate system. Experimental parameters can be extracted from the experimental tests including tension, compression, and shear. Computational parameters can be adjusted through numerical analysis results. Table 5.1 tabulates the MAT_58 material model parameters and Table 5.2 presents their categories and definitions. The material constitutive properties include elastic properties which can be determined through experimental tests. The failure and element deletion parameters are used for the element deletion in numerical analysis. The ply orientations and local axis can be arranged with material local axes determination parameters. The last group of parameters are the material strength and corresponding strain properties.

Table 5.1. MAT_58 material model parameter set

| *MAT_58 (LAMINATED_COMPOSITE_FABRIC) | | | | | | | |
|--|-------|-------|--------|--------|--------|--------|---------|
| MID | RO | EA | EB | EC | PRBA | TAU1 | GAMMA1 |
| GAB | GBC | GCA | SLIMT1 | SLIMC1 | SLIMT2 | SLIMC2 | SLIMS |
| AOPT | TSIZE | ERODS | SOFT | FS | EPSF | EPSR | TSMD |
| XP | YP | ZP | A1 | A2 | A3 | PRCA | PRCB |
| V1 | V2 | V3 | D1 | D2 | D3 | BETA | LCDFAIL |
| E11C | E11T | E22C | E22T | GMS | | | |
| XC | XT | YC | YT | SC | | | |
| Material constitutive properties; EA, EB, EC, PRBA, PRCA, PRCB, TAU1, GAMMA1, GAB, GBC, GCA | | | | | | | |
| Failure and element deletion parameters; SLIMT1, SLIMC1, SLIMT2, SLIMC2, SLIMS, TSIZE, ERODS, SOFT, FS, EPSF, EPSR, TSMD, BETA, LCDFAIL | | | | | | | |
| Material local axes determination parameters; AOPT, XP, YP, ZP, A1, A2, A3, V1, V2, V3, D1, D2, D3 | | | | | | | |
| Material strength and corresponding strain properties; E11C, E11T, E22C, E22T, GMS, XC, XT, YC, YT, SC | | | | | | | |

Table 5.2. Material model parameter definitions

| Variable | Description | Type | Measurement |
|---|---|---------------|---|
| MID | Material identification number | - | N/A |
| RO | Density | Experimental | Density Test |
| Ea | Axial Young's Modulus | Experimental | 0-degree tension test |
| Eb | Transverse Young's Modulus | Experimental | 90-degree tension test |
| Ec | Through-thickness Young's Modulus | Inactive | - |
| PRBA | Minor Poisson's ratio ν_{21} | Experimental | 0-degree tension test with biaxial strain measurement |
| PRCA | Minor Poisson's ratio ν_{31} | Experimental | May be assumed equal to ν_{21} |
| PRCB | Major Poisson's ratio ν_{32} | Experimental | May be assumed equal to ν_{21} |
| Gab,Gbc,Gca | Shear Modulus | Experimental | Shear Test |
| AOPT XP,YP,ZP A1,A2,A3 V1,V2,V3 D1,D2,D3 | Material Axis Option and parameters to determine local material axis | Computational | N/A |
| TSIZE | Time step for automatic element deletion | Computational | Derived from numeric time step |
| ERODS | Maximum effective strain for element layer failure | Computational | |
| SOFT | Softening factor for strength | Computational | |
| SLIMT1 | Stress limit factor for fiber tension | Computational | Stress-strain curve |
| SLIMC1 | Stress limit factor for fiber compression | | |
| SLIMT2 | Stress limit factor for matrix tension | | |
| SLIMC2 | Stress limit factor for matrix compression | | |
| SLIMS | Stress limit factor for shear stress | | |
| FS | Flag for failure surface type | | |
| TAU1 | Stress limit of the first slightly nonlinear part of the shear stress versus shear strain curve | Experimental | Shear stress versus shear strain curve |
| GAMMA1 | Strain limit of the first slightly nonlinear part of the shear stress versus shear strain curve | Experimental | |
| EPSF | Damage initiation transverse shear strain | | |
| EPSR | Final rupture transverse shear strain | | |
| E11C | Strain at longitudinal compressive strength | Experimental | 0-degree compressive test |
| E11T | Strain at longitudinal tensile strength | Experimental | 0-degree tension test |
| E22C | Strain at transverse compressive strength | Experimental | 90-degree compressive test |
| E22T | Strain at transverse tensile strength | Experimental | 90-degree tension test |
| GMS | Shear strain at shear strength | Experimental | Shear test |
| XC | Longitudinal compressive strength | Experimental | 0-degree compressive test |
| XT | Longitudinal tensile strength | Experimental | 0-degree tension test |
| YC | Transverse compressive strength | Experimental | 90-degree compressive test |
| YT | Transverse tensile strength | Experimental | 90-degree tension test |
| SC | Shear strength | Experimental | Shear test |
| BETA | Material angle for axis option | Computational | |

Material constitutive parameters (EA, EB, EC, PRBA, PRCA, PRCB, TAU1, GAMMA1, GAB, GBC, GCA) and material strength and corresponding strain properties (E11C, E11T, E22C, E22T, GMS, XC, XT, YC, YT, SC) are directly obtained from the standard quasi-static compression, tension, and shear tests. For those parameters mean resultant values for all tests are chosen.

The SOFT parameter is a softening reduction factor for the strength of elements at the crash front. It is a reduction factor for strength and correspondingly stiffness of the crash front elements. This degradation is applied to four strength parameters namely, XC, XT, YC and YT. The relation material strength and crash front element strength as follows:

$$\{XC, XT, YC, YT\}^* = \{XC, XT, YC, YT\} \times SOFT \quad (5-1)$$

where the asterisk shows the reduced strength. SOFT parameter is generally used to increase the stability of the crushing analysis and defined within the range of 0-1 after a trial-and-error calibration procedure. When the SOFT parameter is equal to 1, the elements in the crash front preserve their original strength and no softening occurs.

The stress limiting parameters are defined to limit the stress reduction in the softening part of the stress-strain curve. There are five stress limiting parameters: SLIMT1, SLIMC1, SLIMT2, SLIMC2 and SLIMS. These reduction factors determine the post-failure residual strength of every layer of laminate after elastic damage. So, elastoplastic behavior can be obtained by specifying SLIMxx parameters. SLIMT1 and SLIMC1 are the stress limiting factors of fiber, sequentially for tension and compression, and SLIMT2 and SLIMC2 are the stress limiting factors of matrix, sequentially for tension and compression and SLIMS is the factor for shear. Generalized equation for limiting stress after maximum stress in the softening part is given as follows:

$$\sigma_{min} = SLIMxx \times strength \quad (5-2)$$

The value of SLIMxx varies between 0 and 1. Material shows perfectly elastoplastic behavior when the value is 1. A very small value for SLIMTx is usually preferred for tensile failure and 1 is acceptable for SLIMCx for compressive failure. A value of 1 for SLIMS is also preferred for the elastoplastic shear behavior.

If the failure surface type (FS) parameter is set to -1, then nonlinear shear stress-strain curve is activated as seen in Figure 5.1. By setting FS equals to -1, two additional material model parameters are required as input to activate nonlinearity in shear stress strain curve which are $GAMMA1$ and $TAU1$. Elastic portion of the shear stress-strain curve is defined by the shear modulus, G_{AB} . $TAU1$ and $GAMMA1$ are the corresponding stress and strain value of the initial part of the nonlinear portion of the stress-strain curve, respectively. These parameters cannot be experimentally determined but can be obtained by optimizing numerical shear stress-strain curve with the experimental curve. However, the maximum shear strain (GMS) and maximum shear strength (SC) can be directly determined from the experiments. SLIMS parameter is used for reducing the stress when the maximum shear strength (SC) is obtained. The value of SLIMS is in between 0 to 1. The reduced stress is calculated as $SLIMS \times SC$ and this stress level is maintained until the strain parameter ERODS is reached.

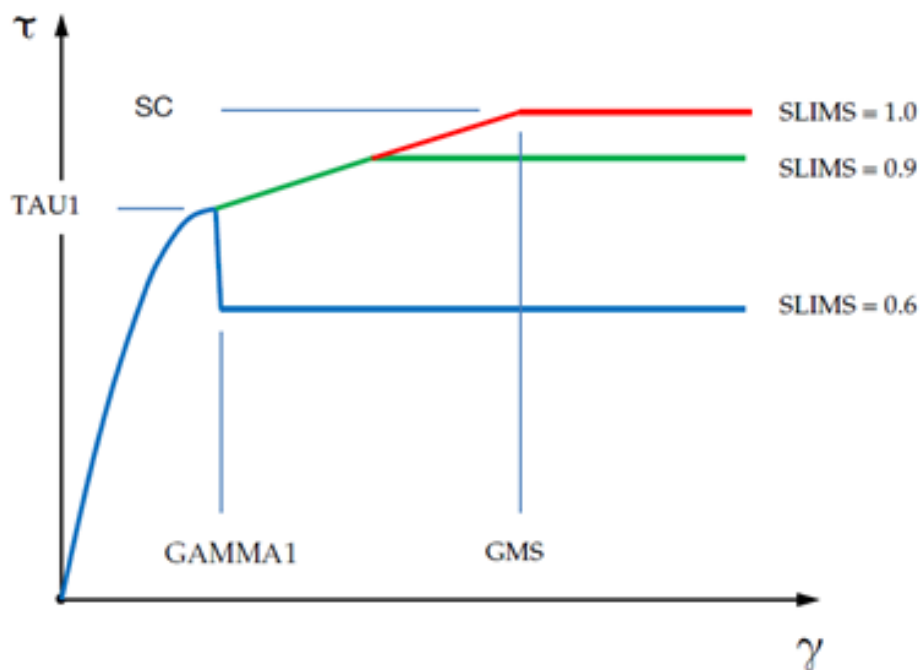


Figure 5.1. Shear stress-strain curve when the value of FS is set to -1
(Source: LS-DYNA Manual⁹⁹)

The ERODS is the failure and element deletion parameter, also called the maximum effective strain and includes the longitudinal and transverse strains as well as the shear strain. The element is deleted and removed after the ERODS reaches the maximum value. The equation for ERODS parameter is formulated as;

$$ERODS = \frac{2}{\sqrt{3}} \sqrt{3 \cdot \left(\frac{\varepsilon_x + \varepsilon_y}{2}\right)^2 + \left(\frac{\varepsilon_x - \varepsilon_y}{2}\right)^2 + \gamma_{xy}^2} \quad (5-3)$$

The Hashin failure criteria, the failure criteria in MAT_58, include four failure modes namely longitudinal fiber tension, longitudinal fiber compression, transverse matrix tension and transverse matrix compression. One additional failure mode becomes active when the value of FS (Failure Surface) parameter equals to -1. These failure modes and the corresponding failure criterion are shown in Figure 5.2. FS can be -1, 0, or 1 depending on the composite material investigated. The failure surface types according to their use can be listed as the following.

- FS = 1 is the smooth failure surface with a quadratic criterion for both fiber and matrix directions. This type of mode is convenient for laminates and fabrics. Nonlinear shear behavior and shear failure mode are not included in this form.
- FS = 0 is the smooth failure surface in transverse direction with a limiting value in the fiber direction. This option is suitable for unidirectional composites only.
- FS=-1 is the faceted failure surface. Damage propagates in tension and compression for both transverse and fiber direction when the strength values are reached. Shear failure mode is included. Only compatible with fabric composites.

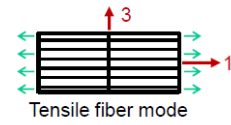
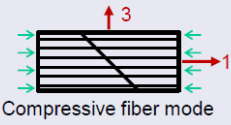
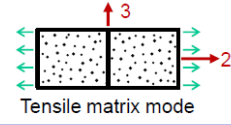
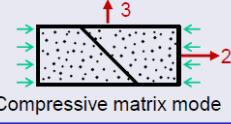
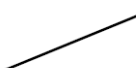
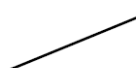
| Failure mode | FS=0.0 | FS=1.0 | FS=-1.0 |
|--|---|--|--|
|  Tensile fiber mode | $e_m^2 = \left(\frac{\sigma_{11}}{X_T}\right)^2 - 1$ | Failure is assumed whenever $e_m^2 > 0$ $e_m^2 = \left(\frac{\sigma_{11}}{X_T}\right)^2 + \left(\frac{\sigma_{12}}{S_C}\right)^2 - 1$ | $e_m^2 = \left(\frac{\sigma_{11}}{X_T}\right)^2 - 1$ |
|  Compressive fiber mode | $e_d^2 = \left(\frac{\sigma_{11}}{X_C}\right)^2 - 1$ | Failure is assumed whenever $e_d^2 > 0$ $e_d^2 = \left(\frac{\sigma_{11}}{X_C}\right)^2 + \left(\frac{\sigma_{12}}{S_C}\right)^2 - 1$ | $e_d^2 = \left(\frac{\sigma_{11}}{X_C}\right)^2 - 1$ |
|  Tensile matrix mode | $\varepsilon_m^2 = \left(\frac{\sigma_{22}}{Y_T}\right)^2 + \left(\frac{\sigma_{12}}{S_C}\right)^2 - 1$ | Failure is assumed whenever $\varepsilon_m^2 > 0$ $\varepsilon_m^2 = \left(\frac{\sigma_{22}}{Y_T}\right)^2 + \left(\frac{\sigma_{12}}{S_C}\right)^2 - 1$ | $\varepsilon_m^2 = \left(\frac{\sigma_{22}}{Y_T}\right)^2 - 1$ |
|  Compressive matrix mode | $\varepsilon_d^2 = \left(\frac{\sigma_{22}}{Y_C}\right)^2 + \left(\frac{\sigma_{12}}{S_C}\right)^2 - 1$ | Failure is assumed whenever $\varepsilon_d^2 > 0$ $\varepsilon_d^2 = \left(\frac{\sigma_{22}}{Y_C}\right)^2 + \left(\frac{\sigma_{12}}{S_C}\right)^2 - 1$ | $\varepsilon_d^2 = \left(\frac{\sigma_{22}}{Y_C}\right)^2 - 1$ |
| |  |  | $\varepsilon_s^2 = \left(\frac{\sigma_{12}}{S_C}\right)^2 - 1$ |

Figure 5.2. Failure modes of MAT_58 according to the failure surface
(Source: Dynamore⁹⁷)

The failure criteria for matrix and fibers are further divided into tensile and compressive modes. Shear failure mode is activated, when FS=-1. The coefficients of the quadratic polynomials are linked to five strength parameters: XC, XT, YC, YT and SC, which are obtained from uniaxial tension, compression and shear tests. With a plane stress assumption, the following simplified form of failure criteria are obtained:

$$\text{Tensile fiber failure mode } \sigma_{11} > 0: \quad e_m^2 = \left(\frac{\hat{\sigma}_{11}}{X_T} \right)^2 - 1 \Big\} > 0 \quad (5-4)$$

$$\text{Compressive fiber failure mode } \sigma_{11} < 0: \quad e_d^2 = \left(\frac{\hat{\sigma}_{11}}{X_C} \right)^2 - 1 \Big\} > 0 \quad (5-5)$$

$$\text{Tensile matrix failure mode } \sigma_{22} > 0: \quad e_m^2 = \left(\frac{\hat{\sigma}_{22}}{Y_T} \right)^2 - 1 \Big\} > 0 \quad (5-6)$$

$$\text{Compressive matrix failure mode } \sigma_{22} < 0: \quad e_d^2 = \left(\frac{\hat{\sigma}_{22}}{Y_C} \right)^2 - 1 \Big\} > 0 \quad (5-7)$$

$$\text{Shear failure mode:} \quad e_s^2 = \left(\frac{\hat{\tau}_{12}}{S_C} \right)^2 - 1 \Big\} > 0 \quad (5-8)$$

The stresses ($\hat{\sigma}_{ij}$) in above are the effective stresses and related to true stresses (σ_{ij}) with the damage parameters (ω_{ij}) as:

$$\hat{\sigma} = \begin{bmatrix} \hat{\sigma}_{11} \\ \hat{\sigma}_{22} \\ \hat{\tau}_{12} \end{bmatrix} = \begin{bmatrix} \frac{1}{1 - \omega_{11}} & 0 & 0 \\ 0 & \frac{1}{1 - \omega_{22}} & 0 \\ 0 & 0 & \frac{1}{1 - \omega_{12}} \end{bmatrix} \begin{bmatrix} \sigma_{11} \\ \sigma_{22} \\ \tau_{12} \end{bmatrix} \quad (5-9)$$

The damage parameter is expressed as:

$$\omega = 1 - \exp \frac{1}{m} \left(\frac{\varepsilon}{\varepsilon_f} \right)^m \quad (5-10)$$

The damage parameter takes the values between 0 and 1 and it equals to 0 for elastic deformation and to 1 for full damaged. In above equation, ε is the current strain in the respective damage direction and ε_f is the failure strain which is calculated by dividing strength (σ_f) by the Young's modulus. The parameters e and m are calculated as:

$$m = \frac{1}{\ln\left(\frac{\varepsilon_q}{\varepsilon_f}\right)} \quad \text{and} \quad e = \frac{\varepsilon_1}{(X_T/E)} \quad (5-11)$$

The constitutive tensor $C(w_{ij})$ can be expressed as a function of damage parameters and the properties of undamaged layer as:

$$\hat{\sigma} = C(w_{ij})\varepsilon$$

$$C(w_{ij}) = \frac{1}{D} \begin{bmatrix} (1 - \omega_{11})E_{11} & (1 - \omega_{11})(1 - \omega_{22})v_{21}E_{22} & 0 \\ (1 - \omega_{11})(1 - \omega_{22})v_{21}E_{11} & (1 - \omega_{22})E_{22} & 0 \\ 0 & 0 & D(1 - \omega_{12})G_{12} \end{bmatrix} \begin{bmatrix} \sigma_{11} \\ \sigma_{22} \\ \sigma_{12} \end{bmatrix} \quad (5-12)$$

where $D = 1 - (1 - w_{11})(1 - w_{22})v_{12}v_{21} > 0$.

The continuous damage mechanics based (CDM) formulation ensures a gradual increase in damage, preventing a sudden decrease in stresses when failure initiates in the element. Additionally, it is important to highlight that the two damage parameters, ω_{11} and ω_{22} , take on distinct values for tension and compression.

5.4. Modeling Composite Laminates using Tiebreak Contacts

Delamination is one of the major failure and energy absorption damage mechanisms of composites under impact loading. It is modeled using different techniques. Tiebreak contacts or cohesive elements between each sub-laminates or plies are used with solid elements. Tiebreak contacts can also be used with thin shell elements. Moreover, there are some drawbacks of composite modelling using solid elements. Solid elements require the through-thickness material parameters, more complex material models obtained through additional experimental tests and an additional layer for each interface between composite plies with cohesive zone elements, increasing the computational cost. On the other side, the use of thin shell elements is far more computationally effective.

Tiebreak contact refers to a technique used to model the behavior of two contacting surfaces, e.g., adjacent layer of composite plies. In this technique, the nodes of contacting surfaces are bonded to each other within a certain threshold value or criteria. When the threshold value is exceeded or the failure criteria are fulfilled, the tiebreak contact releases, resulting in a delamination on the released area of composite laminates. Damage initiation and propagation in the interlaminar surface are defined using the discrete crack model with the power law and B-K (Benzeggagh-Kenane) damage models. There are three delamination failure modes, namely Mode I, Mode II, and Mode III (see Figure 5.3). Mode I refers to the fracture due to tensile loading normal to the failure plane. Mode II and Mode III fractures are resulted from shear loading in the fracture plane as shown in Figure 5.3.

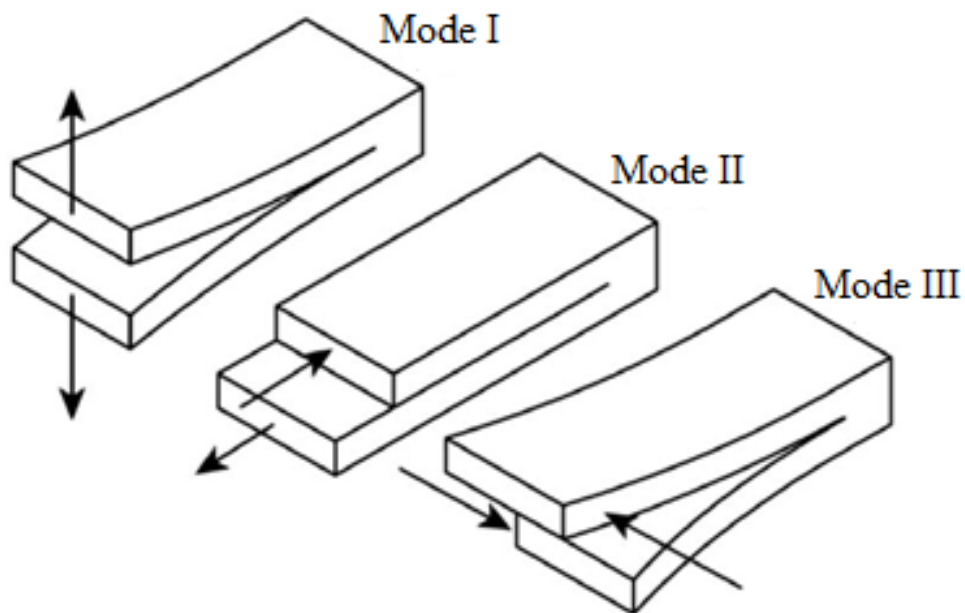


Figure 5.3. Failure modes of matrix

Figure 5.4 shows the bilinear constitutive model of the Mode I delamination in pure tension (elastic stiffness, the slope of the curve between the points 0 and 2, and the peak stress are used as bilinear law parameters). Note in the same figure that, the material response is elastic with no damage until point 2. The loading and unloading between the point 1 and point 2 are elastic. The point 2 is called the onset of damage and beyond this point damage grows. For example, at the point 3, the material exhibits a certain damage, but the damage parameter is less than one but greater than zero. Hence, the plies have not

separated at the point 3. Unloading from this point is not recovered and the area under the 0, 2 and 3 points shows how much energy is dissipated by the partial damage. When loading continues until the point 4, plies are separated permanently, that is the damage parameter is equal to 1. The total energy under the area under the 0, 2 and 4 points is called the fracture energy for the delamination between two plies. The fracture energy is also called the fracture toughness or energy release rate in LS-DYNA.

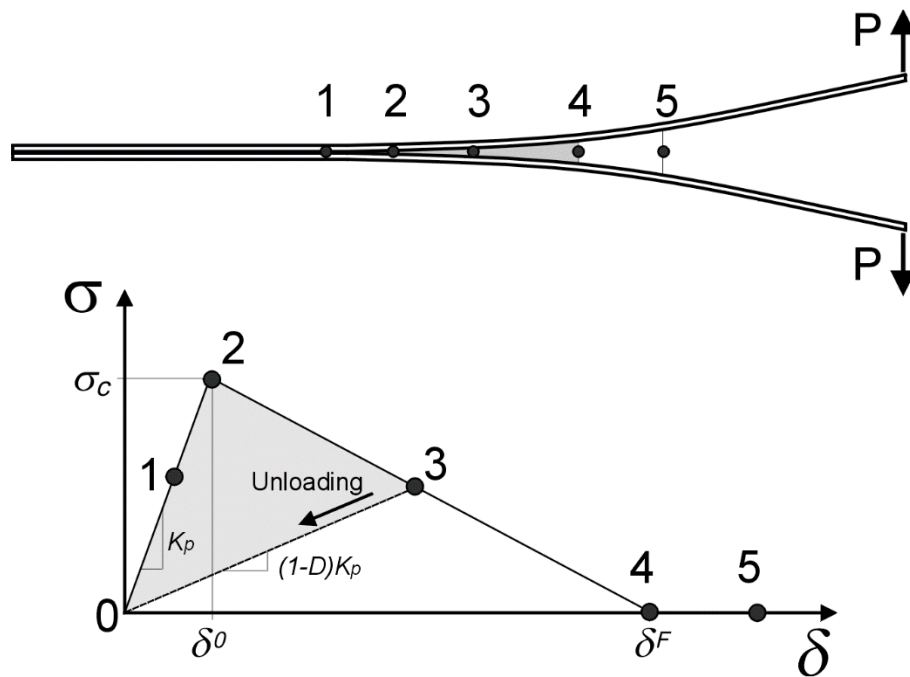


Figure 5.4. Bilinear constitutive law
Source: (Aerospace Working Group⁹⁸)

At the point 4 of Figure 5.4, ultimate displacements in the normal and tangential directions are reached when the separation is completed, that is the tractions are zero. There is a simple relationship between the peak traction stresses, ultimate displacements, and energy release rates (fracture toughness). The ultimate normal (*UND*) and tangential (*UTD*) displacements can be determined sequentially from the following basic equations,

$$G_{IC} = \frac{TxUND}{2} \quad (5-13)$$

$$G_{IIC} = \frac{SxUTD}{2} \quad (5-14)$$

where G_{IC} and G_{IIC} are the Mode I and Mode II energy release rates and T and S are the normal and tangential stresses, respectively. Since there may be both tangential and normal relative motion between plies, the total mixed mode displacement (δ_m) is defined as;

$$\delta_m = \sqrt{\delta_I^2 + \delta_{II}^2}, \quad (5-15)$$

where $\delta_I = \delta_3$ is separation in normal direction (Mode I) and $\delta_{II} = \sqrt{\delta_1^2 + \delta_2^2}$ is the separation in tangential direction (Mode II). Then the mixed mode damage initiation displacement (δ^0) is given by

$$\delta^0 = \delta_I^0 \delta_{II}^0 \sqrt{\frac{1 + \beta^2}{\beta(\delta_I^0)^2 + (\delta_{II}^0)^2}} \quad (5-16)$$

where $\delta_I^0 = \frac{T}{K_N}$ and $\delta_{II}^0 = \frac{S}{K_T}$, are single mode damage initiation parameters in which K_N is normal stiffness and K_T is defined as tangential stiffness of the cohesive zone. The parameter of mode mixity is defined as $\beta = \delta_{II}/\delta_I$. The mixed mode separation for the power law is invoked if $\alpha > 0$ and for Benzeggagh-Kenane law $\alpha < 0$ which are given as

$$\delta^f = \frac{2(1 + \beta)^2}{\delta^0} \left[\left(\frac{K_N}{G_{IC}} \right)^\alpha + \left(\frac{K_T \beta^2}{G_{IIC}} \right)^\alpha \right]^{-\frac{1}{\alpha}} \quad \text{for } \alpha > 0 \quad (5-17)$$

$$\delta^f = \frac{2}{\delta^0 \left(\frac{1}{1 + \beta^2} K_N + \frac{\beta^2}{1 + \beta^2} K_T \right)} \left[G_{IC} + (G_{IIC} - G_{IC}) \left(\frac{\beta^2 K_T}{K_N + \beta^2 K_T} \right)^{|\alpha|} \right] \quad \text{for } \alpha < 0 \quad (5-18)$$

Mixed-mode traction separation law which is a combination of traction-separation of Mode I and Mode II is shown in Figure 5.5. The peak tractions in tension and shear loading are represented by T and S, respectively. The damage initiation δ^0 , and the mode mixity, β can be found. The shaded triangle represents the damage initiation, damage growth and separation under three-dimensional loading.

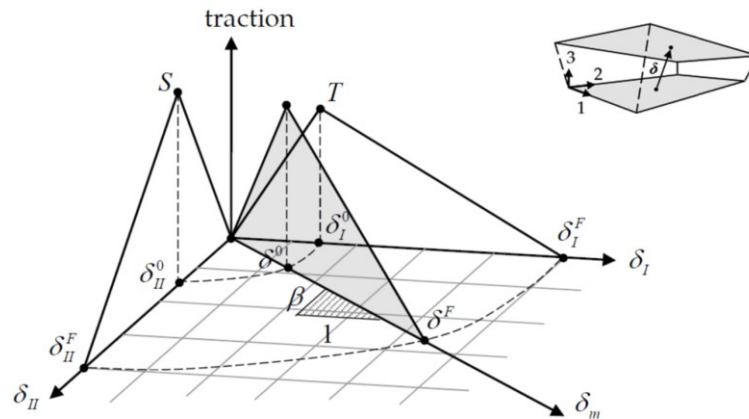


Figure 5.5. Mixed-mode traction-separation law
Source: (LS-DYNA User Manual⁹⁹)

In LS-DYNA, mixed mode failure can be defined with the cohesive interface elements and MAT_138 (MAT_COHESIVE_MIXED_MODE) material model. Similarly, Contact_Automatic_One_Way_Surface_To_Surface_Tiebreak with Option 9 and 11 can be used. Option 9 is used for the solid and thick shell elements only while Option 11 can only be used for shell elements. Since only shell elements were used to model the investigated thermoplastic composite coupons in this thesis, Contact_Automatic_One_Way_Surface_To_Surface_Tiebreak with Option 11 was used to simulate the contact and cohesive zone between plies. The parameters used to fully define the tiebreak contact are tabulated in the Table 5.3. After the interlaminar failure of the surfaces between plies occurred, the automatic contact algorithm became active.

Table 5.3. Tiebreak contact parameters used to model CF/PPS thermoplastic composite

| Tiebreak Parameter | Physical Description | Experimental Test | Definition |
|--------------------|---|---------------------------|--|
| NFLS, T | Interlaminar tensile strength (ILT) | Curved beam strength test | Normal failure stress/Peak traction in normal direction |
| SFLS, S | Interlaminar shear strength (ILSS) | Short beam shear test | Shear failure stress/Peak traction in tangential direction |
| PARAM | Failure mode | - | Exponent of mixed-mode criteria |
| ERATEN | Mode I Interlaminar Fracture Toughness | Double Cantilever Beam | Energy release rate for Mode I |
| ERATES | Mode II Interlaminar Fracture Toughness | End-notched flexure test | Energy release rate for Mode II |
| CT2CN | $CT/CN = G_{epoxy}/E_{epoxy}$ | - | Ratio of tangential stiffness to normal stiffness |
| CN | $CN = E_{epoxy}/\delta_{RRR}$ | - | Normal stiffness |

The delamination damage model input parameters used in the models are further given in Table 5.4. Fracture toughness, interlaminar tensile and shear strength values of the investigated CF/PPS thermoplastic composite were taken from the available test data in the literature. Other numerical parameters such as PARAM, CT2CN and CN were either determined numerically, trial and error method, or taken from the literature. *PARAM* is the damage model exponent in OPTION=11. Assigning a positive value activates the power law and a negative value invokes the B-K model. The parameter NFLS or T (Interlaminar tensile strength) can be determined from the curved beam test, which can be performed in accordance with the ASTM D6415 and AITM 1-0069. The examples of the determination of the curved beam strengths of carbon fiber reinforced PPS, PEEK and PAEK thermoplastic composites can be found in the study of Hron et al.³⁴ The parameter SFSL or S is extracted can from the interlaminar shear strength (ILSS) called the short beam shear test. Hamdan et al.¹⁰⁰ had performed short beam shear test for CF/PPS thermoplastic composite laminates with 6 ply and 8 ply to investigate layering effect. EN2563 test standard has been used to determine interlaminar shear strength property. Baere et al.¹⁰¹ and Ivanov et al.¹⁹ investigated the Mode I and Mode II fracture toughness of CF/PPS thermoplastic composites. The Mode I crack propagation and toughness (G_{IC}) were investigated with Double Cantilever Beam (DCB) test setup. The Mode II fracture toughness (G_{IIC}) was determined with End Notch Flexural (ENF) test setup.

Table 5.4. Delamination damage model input parameters

| <i>Tiebreak Option</i> | <i>T (MPa)</i> | <i>S (MPa)</i> | <i>G_{IC} (N/mm)</i> | <i>G_{IIC} (N/mm)</i> | <i>PARAM</i> | <i>CN</i> | <i>CT2CN</i> |
|----------------------------|--------------------|--------------------|----------------------------------|-----------------------------------|--------------|-----------|--------------|
| 11 | 81.4 ³⁴ | 79 ¹⁰⁰ | 0.97 ^{19, 101} | 3.287 ^{19, 101} | 1.0 | 1.0 | 100000 |

5.5. Material Characterization Modeling Studies

Material modeling for characterization tests is divided into two sections: single element level and coupon level analyses. Although the aim is the same for both methods, which is the constitution of the numerical material model parameters by validating numerical analysis results of the material characterization tests, the complexity of the numerical model constituted in each method is different.

5.5.1. Single Element Level Analysis

The single element analysis loading and boundary conditions for tension, compression and shear tests are shown in Figure 5.6. These analyses include only one single element having boundary conditions according to the loading type. Since CF/PPS thermoplastic composite material is classified as an elasto-brittle material in which an insignificant amount of plastification takes place, this type of modelling provides elasto-brittle material properties.

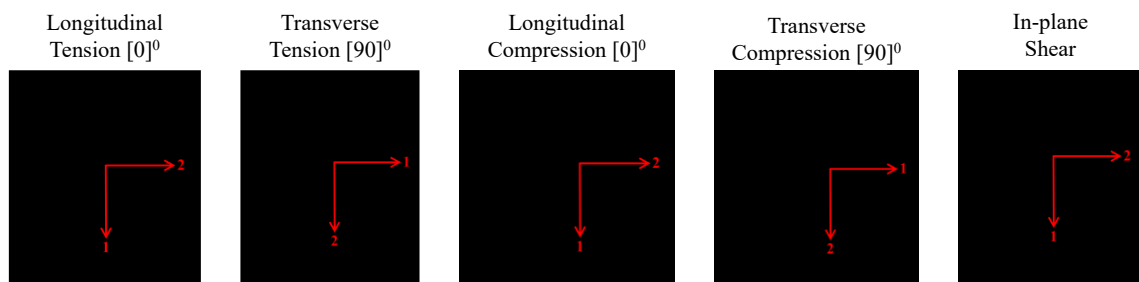


Figure 5.6. Single element analysis loading and boundary conditions

In the model, the composite laminates were represented using only one single element. PART_COMPOSITE input card with ply number, ply thickness and orientation angle was used for the composite definition. Element formulation 16 (ELFORM16), fully integrated shell element, was used for all single element analyses. The displacement of the moving nodes was provided using DEFINE_CURVE card as velocity input. Since this modeling technique required only one element, explicit non-linear solver of LS_DYNA was used in the analyses.

5.5.2. Coupon-level Material Characterization Analysis

Coupon-level numerical studies included the finite element full models of ASTM standard tension, compression, and shear test coupons. The coupon level characterization analyses were performed using non-linear implicit solver in LS-DYNA using the MAT_58 (LAMINATED COMPOSITE FABRIC) as the material model for 5HS fabric CF/PPS thermoplastic composite coupons. To replicate experimental tests, the nodes at one of the end of the specimen were fixed and the nodes at other end region were moving nodes. The remaining nodes were free of moving and rotating, 6-DOF (degree of

freedom). The movement of the moving nodes of the specimen was provided by applying constant velocity using DEFINE_CURVE card. The composite laminate properties were defined using PART_COMPOSITE input in which ply numbers, ply sequence, and thickness were defined. Similar to single element analyses, fully integrated shell elements (ELFORM16) was used for element formulation. The results obtained within the coupon level analyses are then compared with the single element level analyses to show efficiency and accuracy of the both numerical techniques.

5.5.2.1. Standard Tensile Test Numerical Model

Numerical tension test model is shown in Figure 5.7. Four-node quad-shell square elements were used in all models. The dimensions of the numerical sample were 250 x 25 x 2.25 mm (LxWxH), the same as the experiments. A total number of 1000 four-node quad elements within 2.5 mm element size are used to represent specimen in tension test analyses. PART_COMPOSITE definition was used for modelling plies in which eight stacks of plies were represented in a single ply of shell with eight integration points. Boundary condition was applied using BOUNDARY_SPC_SET card set. Two sets of nodes were created using SET_NODE definition for the gripped surfaces of the test specimen. The first node set was defined for the fixation of the nodes in the grip area in which all the nodes in this area were fixed in 6-DOF. The second node set was selected for the moving grips. Moving nodes are fixed in all translational and rotational directions excluding x-direction translation to provide tension loading in the x-direction. A constant velocity of 2 mm/min was applied to the moving nodes using the BOUNDARY_PRESCRIBED_MOTION_SET card. To obtain material properties in both longitudinal and transverse direction, two numerical test sample models were created by aligning all plies in 0° and 90° directions in the x-direction.

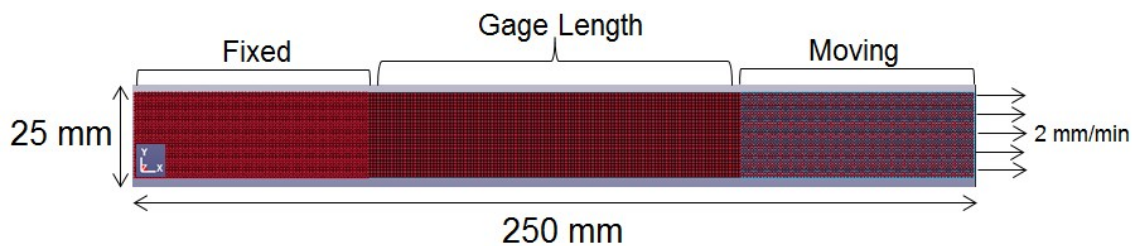


Figure 5.7. Numerical Model of Standard Tensile Test

5.5.2.2. Standard Compression Test Numerical Model

The numerical model of standard compression test is shown in Figure 5.8. The numerical model was constituted using the quadratic shell elements as with the tension model. MAT_58 (LAMINATED COMPOSITE FABRIC) constitutive material model was used with single ply shell elements using PART_COMPOSITE keyword. The dimensions of numerical model sample were 140 x 13 x 2.25 mm (LxWxH), the same as the experiment. A total number of 1344 four-node quad elements with 1.08 mm minimum element size were used to represent the whole compression test specimen. Boundary conditions and LS-DYNA card definitions were the same as the tension model, except a constant velocity of 1.3 mm/min was applied in the negative x-direction. To obtain material properties in both longitudinal and transverse direction, two numerical models were created by aligning all plies in 0° and 90° directions in the x-direction.

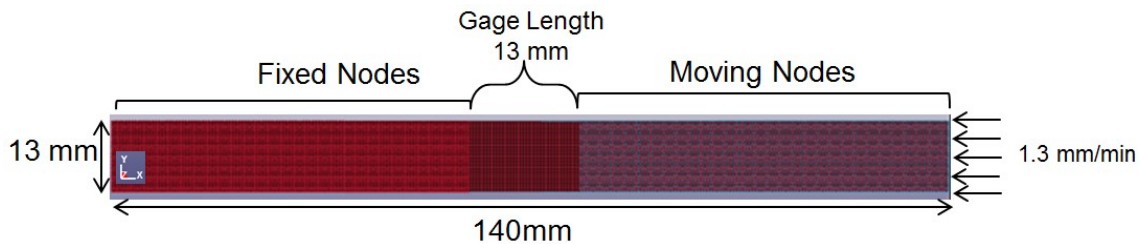


Figure 5.8. Numerical Model of Standard Compression Test

5.5.2.3. Standard In-plane Shear Test Numerical Model

The numerical model of the standard in-plane shear test is shown in Figure 5.9. The same numerical model as in the tensile numerical model was used for in-plane shear test simulations. The only difference was that the fibers were aligned $\pm 45^{\circ}$ direction to the loading axis. A total number of 1000 four-noded quad elements within 2.5 mm minimum element size were used and fiber alignment was made by using PART_COMPOSITE keyword and entering all plies aligned in $+45^{\circ}$ direction. Shear strain was calculated using the two nodes at the middle of gage length ends with DATABASE_HISTORY_NODE card. Force history was read using the keyword DATABASE_CROSS_SECTION_PLANE by defining a cross section in the middle of sample.

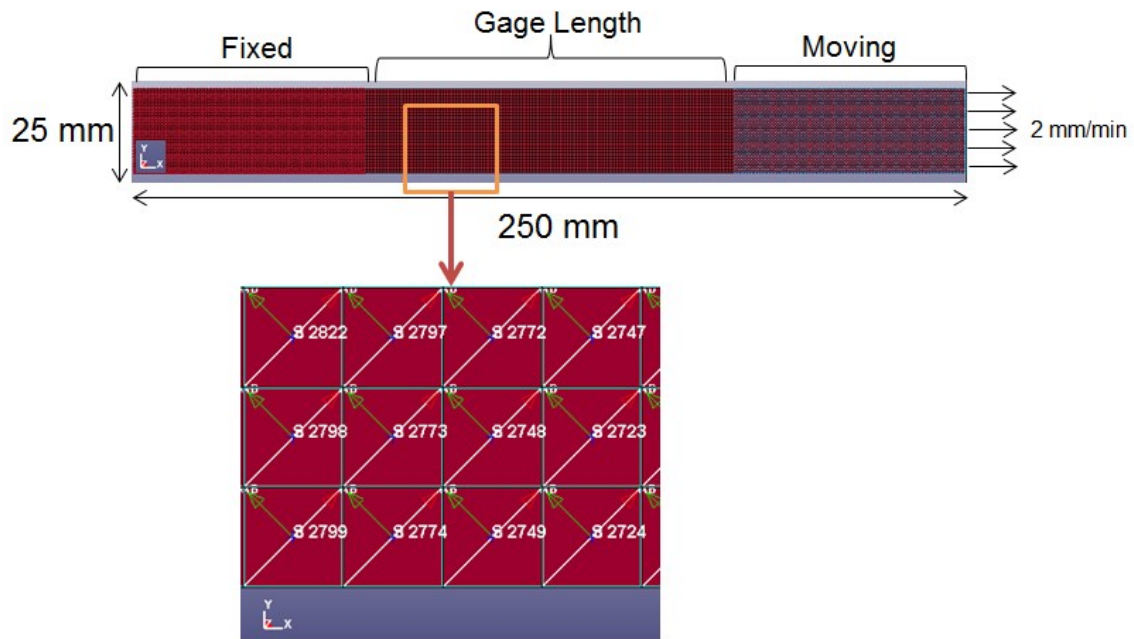


Figure 5.9. Numerical Model of Standard In-plane Shear Test

5.6. Drop-Weight Impact Test Modeling

The numerical model of drop weight impact tests consisted of the specimen, impactor and bottom specimen support as shown in Figure 5.10 and constituted using quad-shell elements and hexagonal solid elements. The clamps were modeled as the constrained boundary condition at their specified location. The thermoplastic composite specimen was modeled in both the single shell model and stacked shell element layer with tiebreak contact. The composite laminate specimen was composed of 8 plies that were stacked up in a sequence of $[45/0/-45/90]_s$. The dimension of the test specimen was 150 x 100 x 2.25 mm (LxWxH) with a 0.28125 mm cured ply thickness. The test specimen was modeled using only four-node quadratic shell elements in both single shell model and stacked shell element layer model. The specimen was placed at the middle of steel support fixture having a dimension of 300 x 300 mm and a 125 x 75 mm cut-out. The specimen support fixture was fixed from its bottom of the elements in all degrees of freedom. The support fixture was modeled using eight-node solid elements. As the specimen was constrained by the rubber tip clamps in the experiment, the locations of the clamps were fixed in 6-DOF. Only the impact end was modeled and the rest was defined as the artificial mass in order to reduce the computational time as depicted in Figure 5.10. The impactor was constrained in all directions and rotations, except the z-direction. Impact velocity was defined using VELOCITY_GENERATION card as a translational

velocity in global z-direction. The steel support fixture and the hemispherical impactor was modeled using the rigid material model, MAT_RIGID, having the same densities of 7850 kg/m^3 , the Young's modulus of 210 GPa and the Poisson's ratio of 0.3.

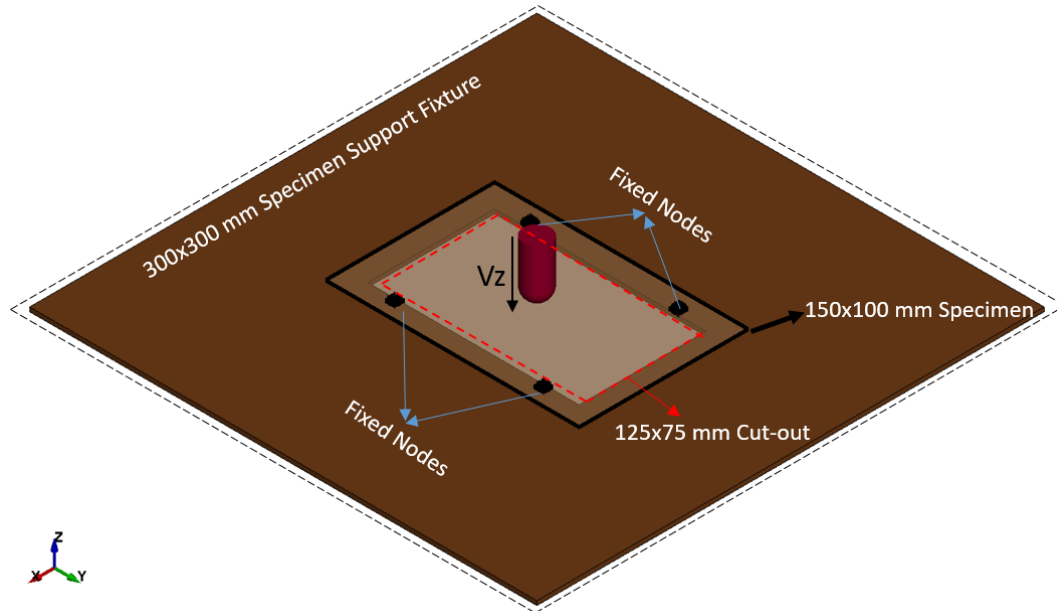


Figure 5.10. Finite Element Model of Drop Weight Impact Test

5.6.1. Single Shell Technique of the Low Velocity Impact Modeling

In this technique, the composite laminate shown in Figure 5.11 was modeled using one layer of four-node quadratic shell elements. PART_COMPOSITE keyword in LS-DYNA was used to create composite laminate composing of 8 plies of $[45/0/-45/90]_s$ and having a 2.25 mm thickness and an area of 150 x 100 mm. The composite plies were modeled as the integration points in one layer of shell elements and each integration point corresponded to the individual plies of 0.28125 mm thick. A total of 15000 four-node square shell elements having 1 mm mesh size was used to create composite specimen. ELFORM=16 was used as an element formulation option. Automatic_Single_Surface type contact algorithm by introducing all parts into a PART_SET to the slave side of the contact card was defined with the soft constraint formulation (SOFT=1). The layer sequence of the laminate is shown in Figure 5.12. Note that this technique provides computationally cost-effective way as it requires less time and effort to build models. Hence, the technique is much more suitable for modelling large structures. However, the delamination and individual behavior of each ply cannot be predicted using this method.

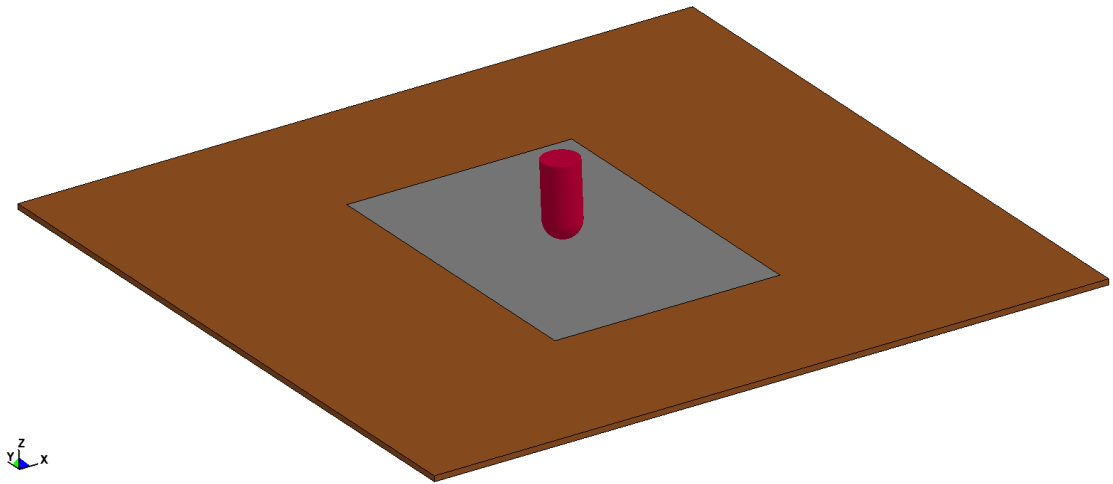


Figure 5.11. Finite element model of single shell drop weight impact testing

| | | |
|------------|---------|------------------|
| 0.28125 mm | IP #1 ● | 1st ply – (45°) |
| 0.28125 mm | IP #2 ● | 2nd ply – (0°) |
| 0.28125 mm | IP #3 ● | 3rd ply – (-45°) |
| 0.28125 mm | IP #4 ● | 4th ply – (90°) |
| 0.28125 mm | IP #5 ● | 5th ply – (90°) |
| 0.28125 mm | IP #6 ● | 6th ply – (-45°) |
| 0.28125 mm | IP #7 ● | 7th ply – (0°) |
| 0.28125 mm | IP #8 ● | 8th ply – (45°) |

Single Layer
Finite Element
Laminate Model

Figure 5.12. Finite element representation of the composite laminate using single shell layer technique

5.6.2. Stacked Shell Technique of Low Velocity Impact Modeling

As stated earlier, the stacked shell method is applicable to shells, thick shell and solid elements and the interface between plies can be modeled either using the tiebreak contact or thin solid elements depending on the element type. In this thesis, the composite laminate was constituted using the shell elements and the tiebreak contact was implemented as the cohesive zone between plies. The finite element representation of the composite specimen and orientation using the stacked shell method is shown in Figure 5.13. There are 8 plies, stacked in a $[45/0/-45/90]_s$ sequence. Each ply was individually modeled using four-node shell elements. A unique part identification was defined for each individual ply and SECTION_SHELL card definition was to define element formulation and thickness. ELFORM=16 and thickness of 0.28125 mm was given as input. The same

element size as in the single shell technique was used to model the test specimen. Since each individual ply was modeled separately in this method, the total number of the elements were eight times greater than those of single shell technique. To define cohesive zone for contact and delamination, seven tiebreak contacts were defined for each interface between composite plies. The finite element model of the stacked shell drop weight test is given in Figure 5.14.

LS-DYNA `Contact_Automatic_One_Way_Surface_To_Surface_Tiebreak` with Option 11 contact definition was used as the interlaminar contact definition. Two contact definitions using `Automatic_Surface_to_Surface` contact algorithm with `SOFT=1` option were used to create contact between the impactor and laminate and between the laminate and support fixture. For the contact between the impactor and laminate, `PART_SET` was defined for the specimen in the slave side and part definition was used for the support fixture in the master side. Part to Part contact definition on both slave and master side was used between the bottom ply of the laminate and the support fixture using `Automatic_Surface_to_Surface` contact algorithm. To extract force versus time curve between the specimen and impactor, `FORCE_TRANSDUCER_PENALTY` contact definition was introduced.

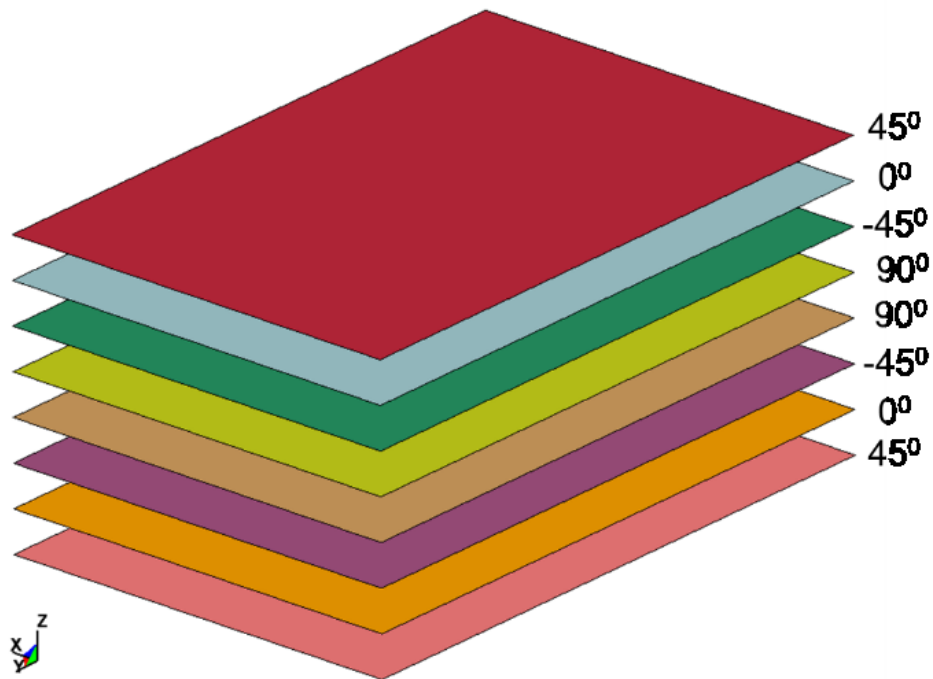


Figure 5.13. Finite element representation of the composite laminate using stacked shell technique



Figure 5.14. Finite element model of stacked shell drop weight impact testing

5.7. Compression After Impact Modeling

The finite element model of the compression after impact tests were created using the impacted specimens that were subjected to low velocity impact tests. The impacted specimens in the FE model of low velocity impact tests were extracted from the post processing analysis. To do this, an LS-DYNA keyword card called `INTERFACE_SPRINGBACK_LSDYNA` was used. This card provides the final form of impacted specimen geometry with all the information of post processing data such as residual stress, residual strain, and history variables. Two LS-DYNA files were obtained after low velocity impact analysis using springback card. The first one is the impacted geometry shape which is the final damaged geometry information of the impacted specimen. The second file includes LS-DYNA keywords which are `INITIAL_STRESS_SHELL` and `INITIAL_STRAIN_SHELL`. These keywords provide all the necessary residual stress and strain state of the impacted specimen as well as damage history variables. Both files are combined to constitute compression after impact test specimen numerically.

After getting the FE model of the impacted specimen, the boundary conditions and loading for the compression after impact tests were applied. Velocity controlled displacement was applied to the top moving boundary condition as 1.25 mm per minute as shown in Figure 5.15. Top nodes were the nodes where compression loading was applied and fixed in all DOFs except translational constraint in global y-direction. Side edges were also fixed except translational constraint in global x- and y-direction. Bottom nodes were constrained in all DOFs.

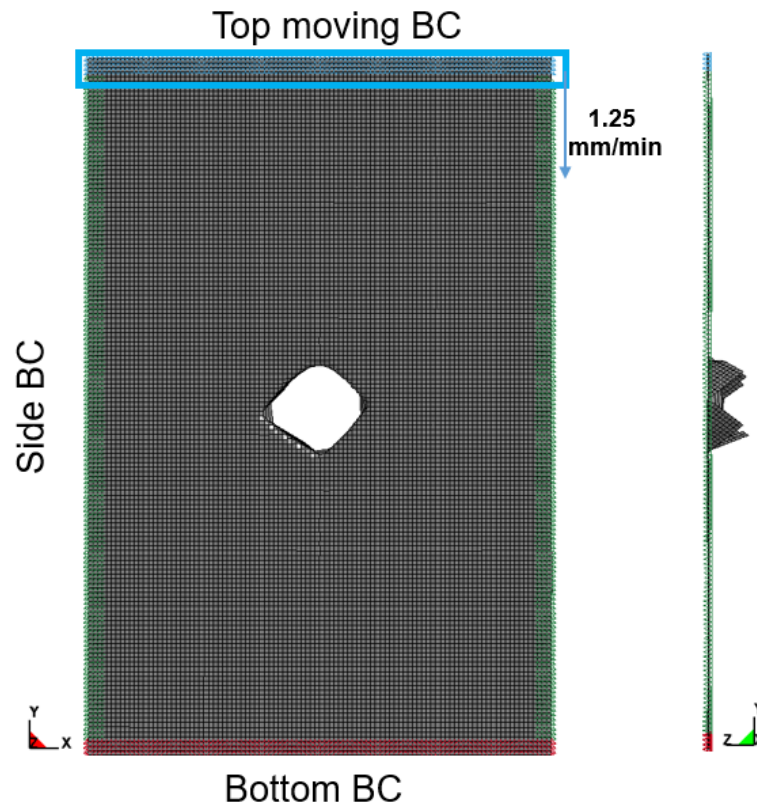


Figure 5.15. Finite element model of the compression after impact analysis

5.8. High Velocity Impact Tests and Modeling Studies

High velocity impact tests were also modeled numerically. Again, the efficiency of the two methods, the single shell modeling and stacked shell element technique, were implemented in these tests like the previous modelling approach. The 30 mm-diameter steel ball projectile, having a 7700 kg/m^3 density and a 110-gram total mass was modeled using the solid hex elements. The shell elements were only used in modelling the composite test specimen. The projectile velocity (101.68 m/s) was defined using the INITIAL_VELOCITY_GENERATION card in LS-DYNA in the negative z-direction. Clamping boundary condition was set by defining node set at the 50 mm outer edge zone of the specimen by fixing those nodes in 6-DOF.

5.8.1. Single Shell Technique Gas Gun Impact Analysis

The high velocity numerical impact test is shown in Figure 5.16. Only one thin shell element layer with eight integration points was used to represent eight ply 200 x 200 x 2.25 mm fabric thermoplastic composite laminate test specimen. The stacking sequence

of the laminate was $[0]_8$ and all the plies were stacked up in the warp direction (x-direction) in the finite element model. PART_COMPOSITE keyword in LS-DYNA was used to constitute full laminate model. The test specimen mesh size was chosen 1 mm. The specimen was modeled using 40000 four-node square shell elements. The edge distance for clamping was 50 mm from the specimen edge and the nodes in the clamping area were fixed in 6 degree-of-freedom as shown in Figure 5.16 with red color. The contact between the specimen and the projectile was defined using the Automatic_Single_Surface contact. In this contact type, all parts were defined into a part set and this part set was used in the slave side of the contact algorithm.

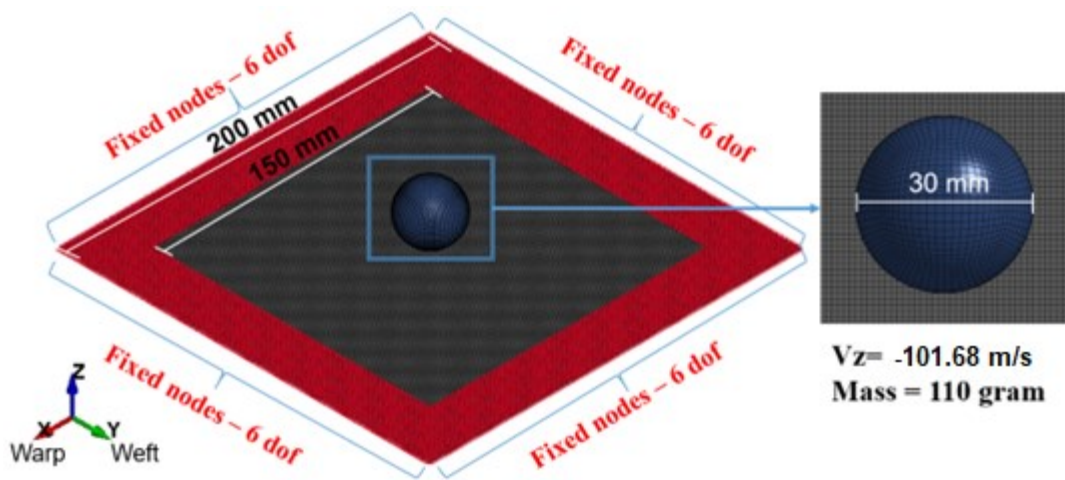


Figure 5.16. High velocity impact test model using single shell technique

5.8.2. Stacked Shell Element Technique Gas Gun Impact Analysis

The stacked shell element modeling technique in this thesis was utilized to get more information about the high velocity impact behavior of composite laminates made of CF/PPS thermoplastic. The stacked shell element numerical model of the gas gun impact test is shown in Figure 5.17. Each ply in the model was given with a unique part and section identification using the SECTION_SHELL input. Element formulation 16, fully integrated shell elements, were used with a 0.28125 mm-shell thickness for each ply. The four-node square shell elements were 1.25 mm in size. The interlaminar behavior between each ply was modeled using the tiebreak contact, Contact_Automatic_One_Way_Surface_To_Surface_Tiebreak with Option 11. Since there were seven interlaminar zones in between 8-ply laminate, there were seven tiebreak contact definitions in total.

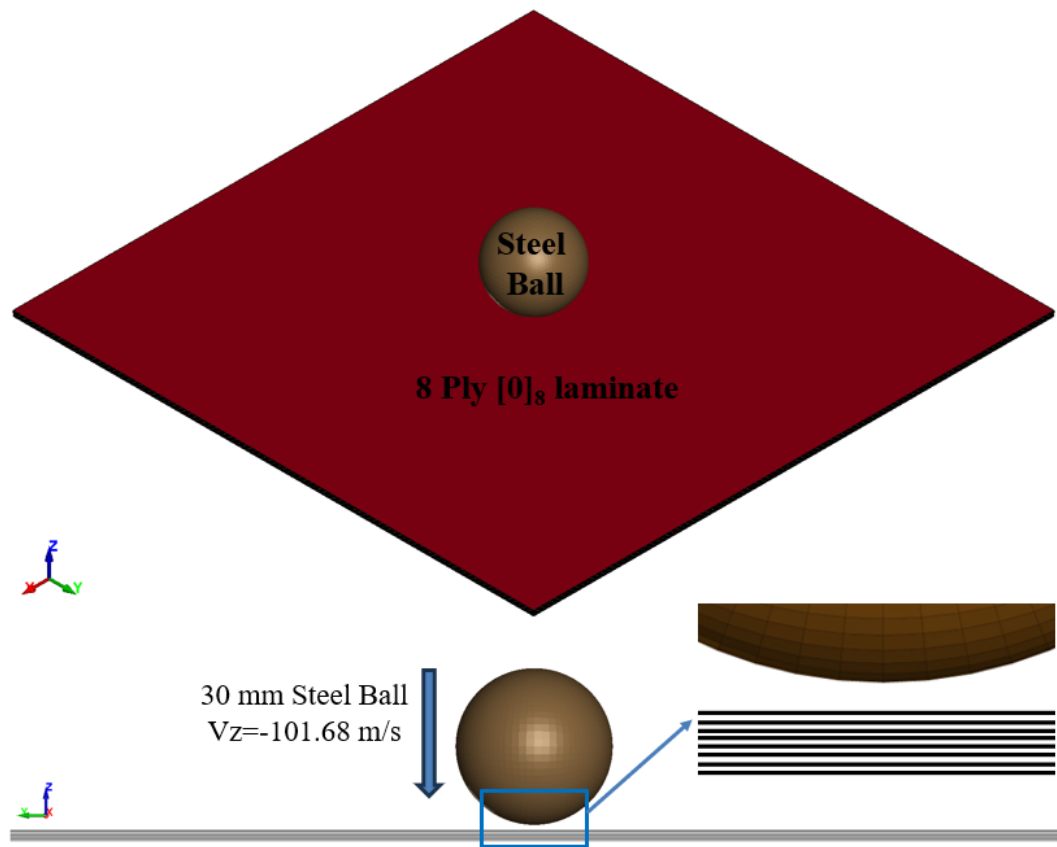


Figure 5.17. Finite element model of the stacked shell element gas gun impact test

CHAPTER 6

NUMERICAL ANALYSIS RESULTS AND DISCUSSION

6.1. Introduction

The numerical analyses of the experimental tests of quasi-static tension, compression and shear, low velocity impact, compression after impact and gas gun impact are presented in this chapter. A validation procedure was further performed by numerical modeling the mechanical tests. Then, validated parameters of the constituted material model were implemented to the numerical analyses. The results obtained from numerical analyses were compared with those of the experiments and the results were discussed. Lastly, the finite element analysis results were used to interpret the mechanical behavior of CF/PPS thermoplastic composites under different loading conditions. The post-processing numerical analyses was performed using LS-PrePost software, which is used both as the pre-processor and post-processor developed by LSTC company.

6.2. Material Model and Tiebreak Contact Parameters

The used parameters in the LS-DYNA material model MAT-58 are tabulated in Table 6.1. Material model parameters as described in Chapter 5 were determined using experimental tests and numerical calibrations. The parameters determined from the experimental tests and from the numerical calibrations are also identified in a separate column in the same table. These parameters were further used in all types of numerical analyses, including the numerical modelling the quasi-static, LVI, HVI and CAI tests. Some parameters in the numerical models was taken as default to make them inactive such as TSIZE, EPSF, EPSR, and BETA. The second parameter set given in Table 6.2 is used for modeling the composite delamination using the tiebreak contact. The tiebreak contact (Contact_Automatic_One_Way_Surface_To_Surface_Tiebreak with Option 11) requires Mode I and Mode II energy release rates (G_{IC} and G_{IIC}) and normal and tangential stresses (T and S).

Table 6.1. Material model parameter set for MAT-58

| Parameter Type | Parameter | Value | Definiton |
|---|-----------|---------------------------------------|--|
| Experimental Parameters (Material constitutive properties) | RO | 1570 kg/m ³ | Material Property |
| | Ea | 55000 Mpa | Taken as equal, average elastic modulus of longitudinal and transverse tests |
| | Eb | 55000 Mpa | |
| | PRBA | 0.5 | Strain gauge value |
| | Gab | 3200 MPa | In-plane shear tests |
| | Gbc | 3200 MPa | |
| | Gca | 3200 MPa | |
| | TAU1 | 56 MPa | |
| | GAMMA1 | 0.02 | |
| | E11C | 0.0111 | Compression tests in longitudinal direction |
| | E11T | 0.0121 | Compression tests in transverse direction |
| | E22C | 0.01136 | Tension tests in longitudinal direction |
| | E22T | 0.013 | Tension tests in transverse direction |
| | GMS | 0.315 | In-plane shear tests |
| | XC | 588 Mpa | Compression tests in longitudinal direction |
| | XT | 707 Mpa | Compression tests in transverse direction |
| | YC | 602 Mpa | Tension tests in longitudinal direction |
| YT | 762 Mpa | Tension tests in transverse direction | |
| SC | 133 Mpa | In-plane shear tests | |
| Failure and element deletion parameters | FS | -1 | Applicable for woven weave fabric, including nonlinear shear behavior |
| | SLIMT1 | 0.1 | Numerically calibrated parameter |
| | SLIMC1 | 0.4 | Numerically calibrated parameter |
| | SLIMT2 | 0.1 | Numerically calibrated parameter |
| | SLIMC2 | 0.4 | Numerically calibrated parameter |
| | SLIMS | 1 | Numerically calibrated parameter |
| | ERODS | 0.4 | Calculated and calibrated for impact analysis |
| | SOFT | 1 | No crasfront is applied |

Table 6.2. Delamination damage model input parameters

| Tiebreak Option | T (MPa) | S (MPa) | G _{IC} (N/mm) | G _{IIC} (N/mm) | PARAM | CN | CT2CN |
|--------------------|--------------------|-------------------|---------------------------|----------------------------|-------|-----|--------|
| 11 | 81.4 ³⁴ | 79 ¹⁰⁰ | 0.97 ^{19, 101} | 3.287 ^{19, 101} | 1.0 | 1.0 | 100000 |

6.3. Mechanical Characterization Analysis Results

This section includes numerical analyses studies of the standard quasi-static tensile, compression and in-plane shear tests. The numerical results include the single element and coupon level 2D shell modeling as described in detail in Chapter 5. The purpose of using two different methods is to investigate the effectivity of different methods for modeling FRP composite laminates and validation of material model within different modeling techniques.

6.3.1. Tensile Analysis

The experimental and numerical tension test elastic modulus, failure strain and peak stress are tabulated in Table 6.3 for the warp (0° longitudinal) and weft (90° transverse) directions. In the warp direction, the test mean elastic modulus is 56029 MPa while the elastic modulus of the single element and coupon level analyses are 54800 MPa and 55070 MPa, respectively. The percent differences between the experimental and the single element and coupon level test elastic modulus values are 2.2% and 1.7%, respectively. The percent differences between the experimental test and numerical analysis failure strains of the warp direction are however comparatively larger as compared with the modulus and are 15.7% for the single element analysis and 13.4% for the coupon level analysis.

The mean experimental peak stress and numerical peak stress, on the other hand are very similar and are experimentally 707 MPa and numerically 705 and 704 MPa for the single element and coupon level models. Similar results are also seen in the modelling of the weft direction. The experimental mean modulus is 54943 MPa and the numerical modulus values are 54800 MPa for the single element model and 55090 MPa for the coupon level model. The percent differences between the experimental and the single

element and coupon level test elastic modulus values are less than 0.5%. As with the warp direction larger deviations are found in the failure strains between experiment and models. The numerical failure strains in the weft direction deviate from the experimental test by 7.7% for the single element analysis and by 13.11% for the coupon level analysis. The mean experimental peak stress and numerical peak stress, on the other hand, are very similar and are experimentally 762 MPa and numerically 762 and 759 MPa for the single element and coupon level models. These results clearly indicated that both the elastic modulus and peak stress values of the experimental tests are well predicted using both the single element and coupon level models. On the other side, the percent deviations between the failure strains of the experiments and models are relatively higher, ranging between 7.7% and 15.7%.

The experimental and numerical tensile stress-strain curves of the composite are sequentially shown in Figure 6.1(a) and (b) for the warp and weft directions. The agreement between the experimental and numerical tensile stress-strain curves is seen in the same curves. The numerical model stress-strain curves represent an average of the experimental tests in both directions. The experimental and numerical stress-strain curves shown in Figure 6.1(a) and (b) are seen to show a linear relation between stress and strain until about the failure/fracture. While a nonlinearity between stress and strain is seen in the numerical curves in a narrow strain region near the failure strain for both the warp and weft directions. The numerical non-linear behavior indicates a more gradual failure in the model as compared with the experiments in which the specimen fractures suddenly when a critical strain is reached.

The FEA -x direction strain distributions before and after the failure for both the warp (0° longitudinal) and weft (90° transverse) coupons are shown in Figure 6.2, together with a picture of experimentally tested and failed specimen. The numerical strain measurements show uniform strain distributions in the gage sections as seen in the same figure. Similar to experimental results of failure strain which is about 0.012-0.015, the failure strain measured in coupon level analyses are almost the same. Moreover, numerical failure is also seen to occur at the near bottom of the gage section for both longitudinal and transverse axes, as the same as the experiments. While there is no such information like failure or deformation of the test specimen in the single element level analysis, the deformation and failure location can be observed and measured numerically using coupon level analysis.

Table 6.3. Experimental tests and numerical analyses results for tension

| Tension results in warp (0⁰) direction | | | |
|---|----------------------------------|-----------------------|------------------------------|
| | Elastic Modulus (MPa) | Failure Strain | Peak Stress (MPa) |
| Experimental Mean | 56029 | 0.0121 | 707 |
| Single Element Analysis | 54800 | 0.014 | 705 |
| Error % | 2.2 | 15.7 | 0.3 |
| Coupon Level Analysis | 55070 | 0.0136 | 704 |
| Error % | 1.7 | 12.4 | 0.4 |
| Tension results in weft (90⁰) direction | | | |
| | Elastic Modulus (MPa) | Failure Strain | Peak Stress (MPa) |
| Experimental Mean | 54943 | 0.013 | 762 |
| Single Element Analysis | 54800 | 0.014 | 762 |
| Error % | 0.3 | 7.7 | 0.0 |
| Coupon Level Analysis | 55090 | 0.0147 | 759 |
| Error % | 0.3 | 13.1 | 0.4 |

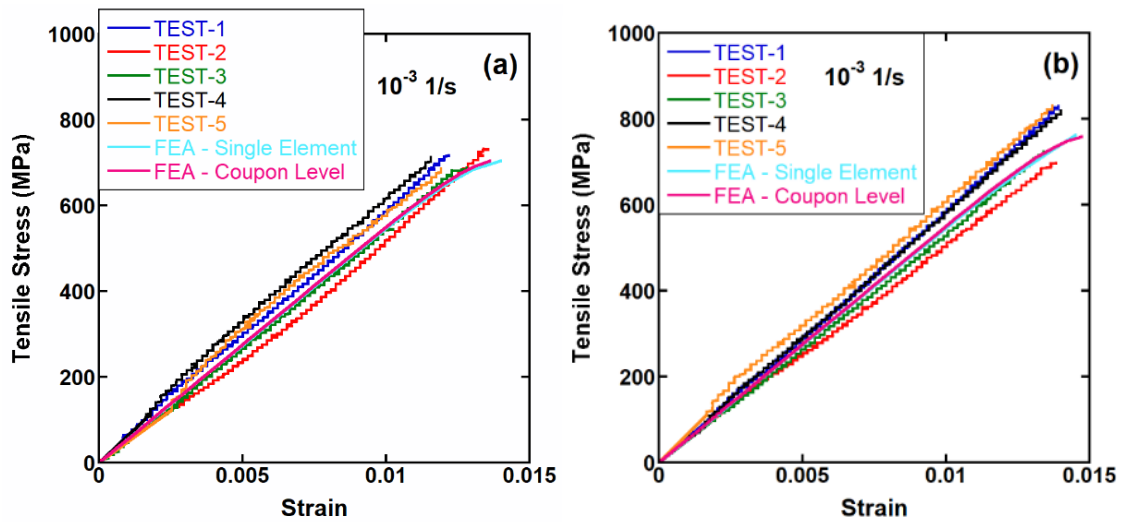


Figure 6.1. Experimental and numerical standard quasi-static tension test stress-strain curves of the a) warp and b) weft direction

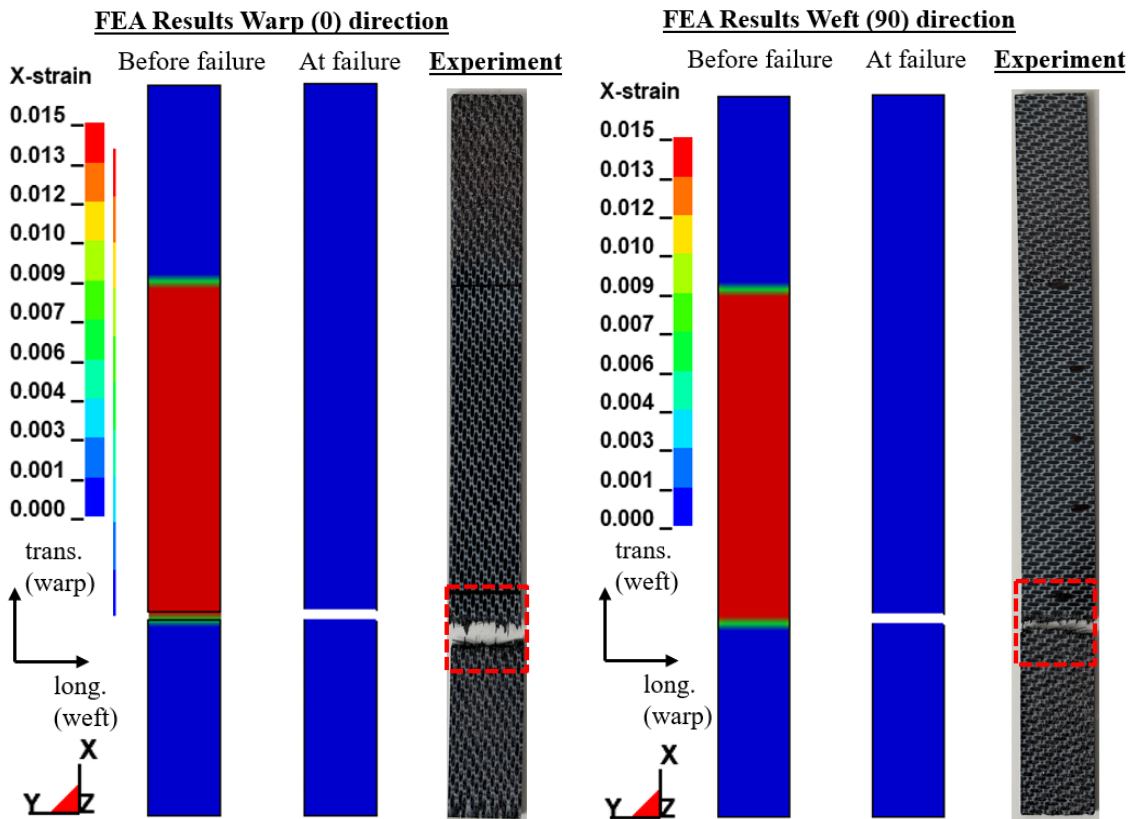


Figure 6.2. Tension -x strain FEA results and experimental failure

6.3.2. Compression Analysis

The experimental and numerical compression test elastic modulus, failure strain and peak stress are tabulated in Table 6.4 for the warp (0° longitudinal) and weft (90°

transverse) directions. The average experimental modulus, failure strain and peak stress values are sequentially 53039 MPa, 0.0111 and 588 MPa in the warp and 53065 MPa, 0.0113 and 598 MPa in the weft direction. The single element and coupon level analyses results of modulus, failure strain and peak stress values are further well agreed with those experimental values as tabulated in Table 6.4. The single element analysis modulus, failure strain and peak stress values are sequentially 55200 MPa, 0.0115 and 583 MPa in the warp and 55190 MPa, 0.012 and 600 MPa in the weft direction. The modulus and failure strain and peak stress values of the coupon level finite element analysis are sequentially 54230 MPa, 0.0116 and 579 MPa and for the warp direction and 54360 MPa, 0.012 and 565 MPa for the weft direction. The maximum percent difference between the experimental and the single element and coupon level test is 4.1% for the elastic modulus, 6.2% for the failure strain and 1.5% for the peak stress. With these numbers, the compression mechanical response is more precisely predicted than the tensile mechanical response of experimental tests by the numerical models. The experimental and numerical stress-strain compression curves of both warp and weft directions are shown together in Figure 6.3(a) and (b), respectively. As with the tension test, a good agreement between the experimental and numerical stress-strain curves and a non-linear numerical stress-strain behavior near the failure are noted in the same figures.

The FEA-x direction strain distribution of both warp and weft direction before and after the failure and a picture of the tested specimen after the failure are shown in Figure 6.4. As with the tensile test, there is a uniform strain distribution in the gage section of the coupons in the numerical compression tests just before the failure. The failure in both directions takes place inside of the gage section. The -x strain failure strain values (~ 0.012) for both directions coincides well with the failure strain in the stress-strain curves shown in Figure 6.3(a) and (b). The coupon level compression test 2D modeling FRP composite laminates is also useful for macro level failure and strain distribution prediction of the specimen itself. However, there is no such failure information in the single element modeling technique. Although it is a powerful, simple, and efficient technique for determining stress-strain response in a quick way, it does not provide information about failure and damage. It should also be noted that both of these methods do not give information on the interlaminar behavior, fiber-matrix interaction and fiber failure or matrix debonding. To get these further predictions in numerical FEA, one has to use a meso-scale level finite element modeling technique.

Table 6.4. Experimental tests and numerical analyses results for compression

| <u>Compression results in warp (0⁰) direction</u> | | | |
|--|----------------------------------|-----------------------|------------------------------|
| | Elastic Modulus (MPa) | Failure Strain | Peak Stress (MPa) |
| Experimental Mean | 53039 | 0.0111 | 588 |
| Single Element Analysis | 55200 | 0.0115 | 583 |
| Error % | 4.1 | 3.6 | 0.9 |
| Coupon Level Analysis | 54230 | 0.0116 | 579 |
| Error % | 2.2 | 4.5 | 1.5 |
| <u>Compression results in weft (90⁰) direction</u> | | | |
| | Elastic Modulus (MPa) | Failure Strain | Peak Stress (MPa) |
| Experimental Mean | 53065 | 0.0113 | 598 |
| Single Element Analysis | 55190 | 0.012 | 600 |
| Error % | 4.0 | 6.2 | 0.3 |
| Coupon Level Analysis | 54360 | 0.012 | 595 |
| Error % | 2.4 | 6.2 | 0.5 |

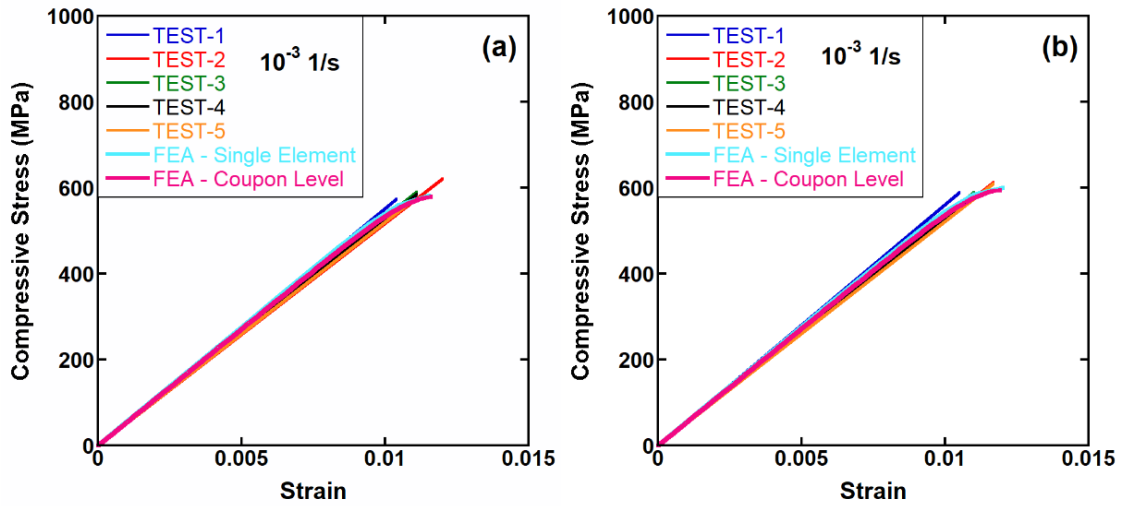


Figure 6.3. Experimental and numerical standard quasi-static compression test stress-strain curves of the a) warp and b) weft direction

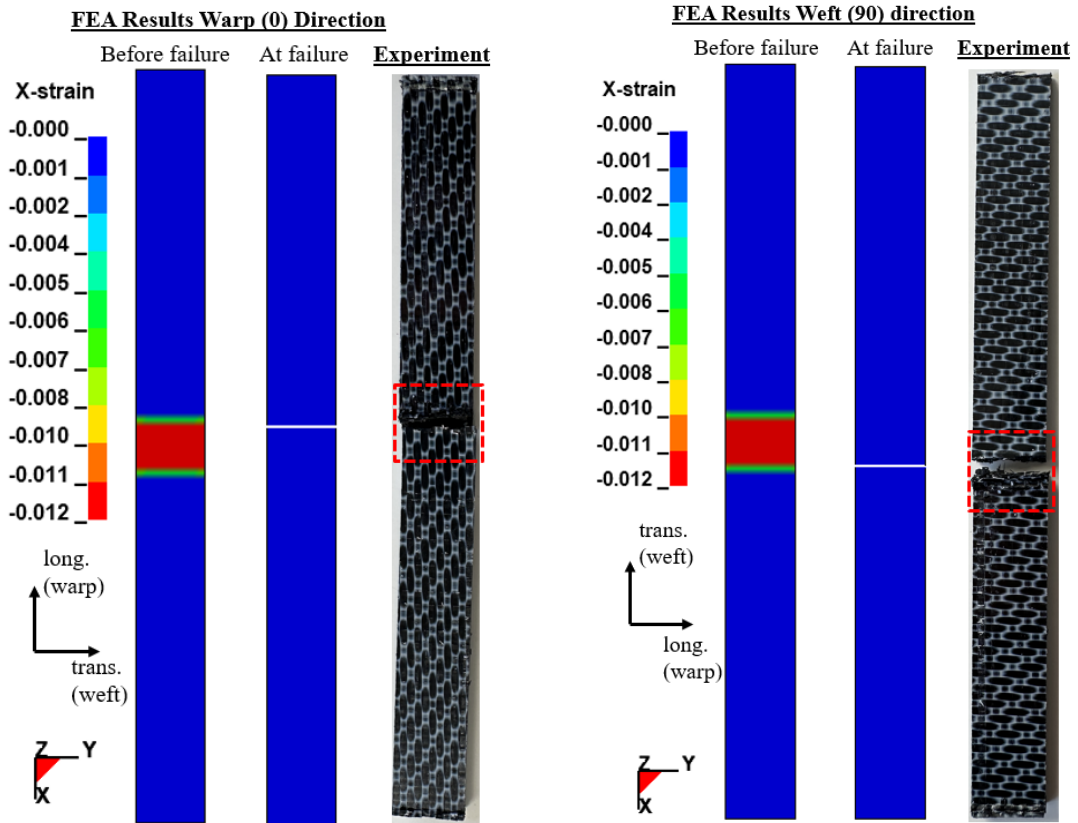


Figure 6.4. Compression -x strain FEA results and experimental failure

6.3.3. In-plane Shear Analysis

The experimental and numerical shear modulus, failure strain and peak shear stress values are tabulated in Table 6.5. The experimental shear modulus, failure strain

and peak shear stress values are sequentially 3200 MPa, 0.3155 and 133 MPa. These values are sequentially 2900 MPa, 0.357 and 133 MPa for the single element analysis model and 3165 MPa, 0.314 and 133 MPa for the coupon level analysis. There is a 9.4% difference in the shear modulus values between the single element analysis and experimental test while the difference decreases to 1.1% between the coupon level analysis and experimental test. The difference between the failure strain of the coupon level analysis and experimental test is as low as 0.5% while the difference increases to 13.2% between the single element analysis and experimental test. Note also that experimental test and two numerical modeling approach, the single element analysis and coupon level analysis, result in the same peak stress value of 133 MPa. Although both techniques predict the experimental values in an expectable level, the coupon level analysis predicts the experimental test values better than the single element level model in the in-plane shear test.

Table 6.5. Experimental tests and numerical analyses results for shear tests

| <u>In-plane shear results in warp (0⁰) direction</u> | | | |
|--|--------------------------------|-----------------------|------------------------------|
| | Shear Modulus (MPa) | Failure Strain | Peak Stress (MPa) |
| Experimental Mean | 3200 | 0.3155 | 133 |
| Single Element Analysis | 2900 | 0.357 | 133 |
| Error % | 9.4 | 13.2 | 0.0 |
| Coupon Level Analysis | 3165 | 0.314 | 133 |
| Error % | 1.1 | 0.5 | 0.0 |

For comparison, the experimental and numerical shear stress-shear strain curves are shown together in Figure 6.5. As it seen in the same curves, the numerical shear stresses are slightly below the experimental stresses while the trends of the numerical an experimental stress-strain curves are very much similar to each other as seen in Figure 6.5.

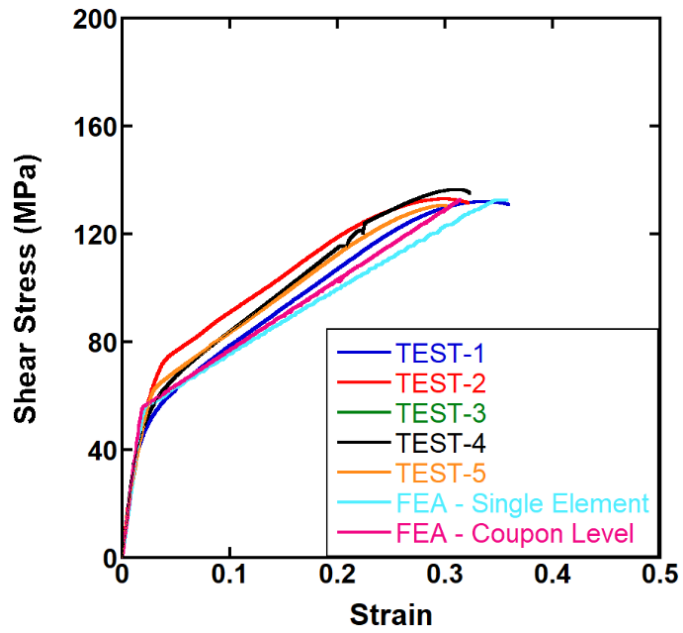


Figure 6.5. Shear stress-strain test-analysis comparison

The FEA -x strain distributions just before and after the failure and a picture of the tested specimen after the failure in the in-plane shear test are shown in Figure 6.6. The failure strain is the combination of -x strain and -y strain which is approximately two times that of -x strain and coincides with the experimental one. Necking is also observed (see Figure 6.6) in the numerically tested coupon as with the experimentally tested specimen. The test specimen fracture occurs at the lower section of the test coupon for both numerical models and also for experimental test.

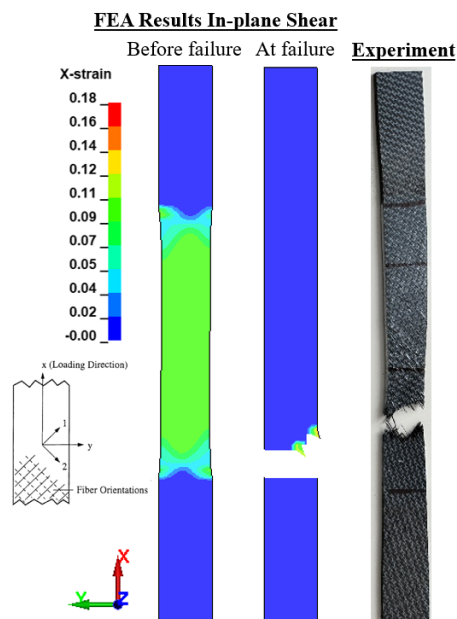


Figure 6.6. In-plane shear -x strain FEA results and experimental failure

6.4. Mesh Sensitivity Analysis

A mesh sensitivity analysis was performed for the numerical impact analyses. A LVI test at 5.7 m/s velocity was chosen as a benchmark to compare the results of the single shell element analysis. Four different mesh sizes which are 0.5 mm, 1 mm, 2 mm, and 4 mm, were implemented by using 2 CPU and 16 GB Ram capacity. The resulting force-time curves of LVI numerical tests are shown sequentially for 0.5 mm, 1 mm, 2 mm, and 4 mm mesh sizes in Figure 6(a-d), together with that of the experimental test. As is noted in Figure 6.7(a), 0.5 mm mesh size underpredicts the experimental test force values near the peak force. On the other hand, the 2 mm and 4 mm mesh sizes (Figure 6.7 (c) and Figure 6.7 (d)) over predict the experimental force values. The best agreement between the numerical and experimental LVI test force values is seen for the 1 mm mesh size as seen in Figure 6.7(b). Both rising and descending portions of the 1 mm mesh size model curve are well agreed with the experimental curve.

The peak force, absorbed energy, damaged area, and CPU time of the mesh sensitivity analyses are further tabulated in Table 6.6. As tabulated in the same table, the experimental peak force and the absorbed energy are best matched with those of the 1 mm mesh size model. Although the coarser mesh sizes, 2 and 4 mm, require less computational time, the differences between the model and experimental results are higher than those of the 1 mm mesh size. Moreover, the use of finer mesh size of 0.5 mm do not lead to better results in terms of peak force and damaged area while it takes the longest solution time, ~25 hours. Thus, a mesh size of 1 mm is selected for all finite element impact analyses by considering both the accuracy of the results and computational time.

The experimental top and bottom images of a LVI test specimen are shown in Figure 6.8 together with the top images of the numerical models using different sizes of the meshes. In the model images, the damage parameter (a damage parameter value of 1.0 shows the fully damaged areas) in the longitudinal direction is shown. The 0.5 mm mesh size analysis shows a diamond shaped damage at the top view and all other mesh size analysis exhibits a rounded hole damage at the top view as similar with the experimental test. As seen in Figure 6.8, increasing the mesh size from 1 to 4 mm decreases the resolution of the fracture pattern. The best match failure with the experimental one is the analysis with having mesh size of 1 mm as shown in Figure 6.8(b).

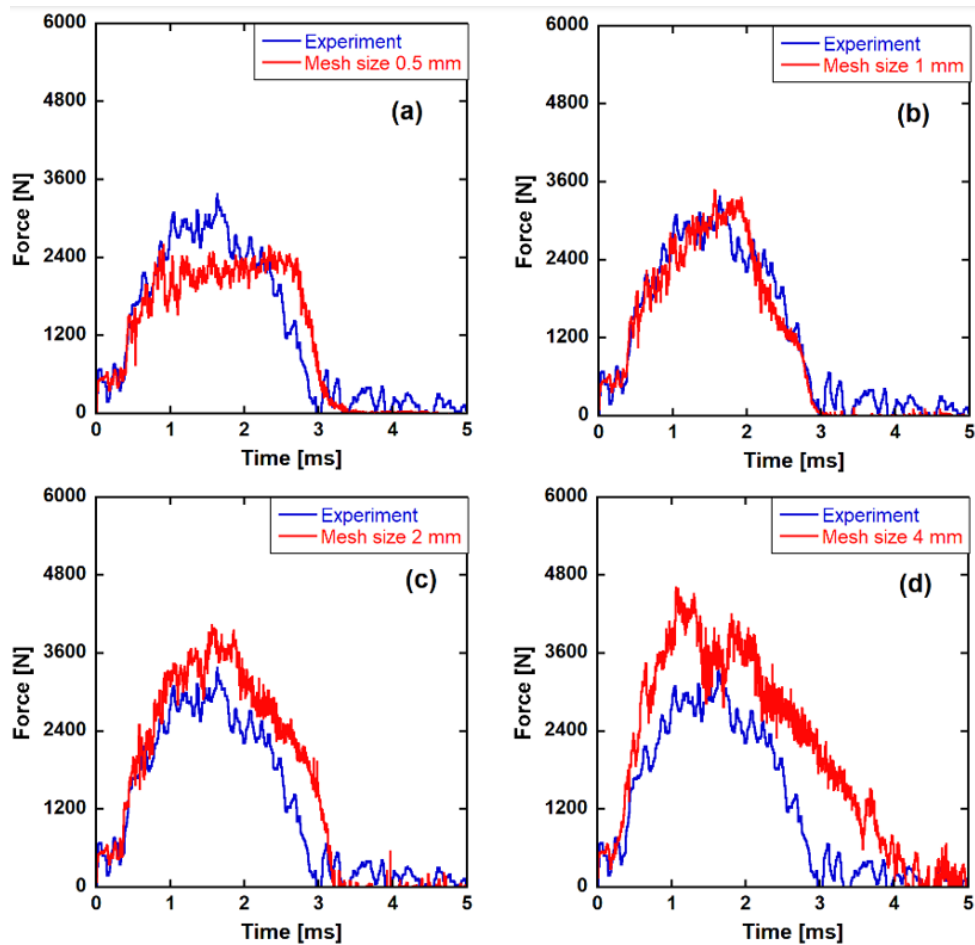


Figure 6.7. Experimental and numerical force-time comparisons for different mesh sizes; a) 0.5 mm, b) 1 mm, c) 2 mm and d) 4 mm

Table 6.6. Mesh sensitivity analysis results

| Mesh Sensitivity Analysis | | | | |
|----------------------------------|--------------------------------|----------------------------|-------------------------------------|-------------------------|
| | Peak Impact Force (MPa) | Absorbed Energy (J) | Damage Area (mm²) | CPU Time (hours) |
| Experiment | 3380 | 425.0 | 630 | - |
| 0.5 mm mesh size | 2513 (-26%) | 25.5 (3%) | 824 (31%) | 25 hours |
| 1 mm mesh size | 3471 (3%) | 25.6 (4%) | 453 (-28%) | 4 hours |
| 2 mm mesh size | 4037 (19%) | 35.3 (43%) | 481 (-24%) | 2 hours |
| 4 mm mesh size | 4610 (36%) | 40.2 (63%) | 603 (-4%) | 9 min |

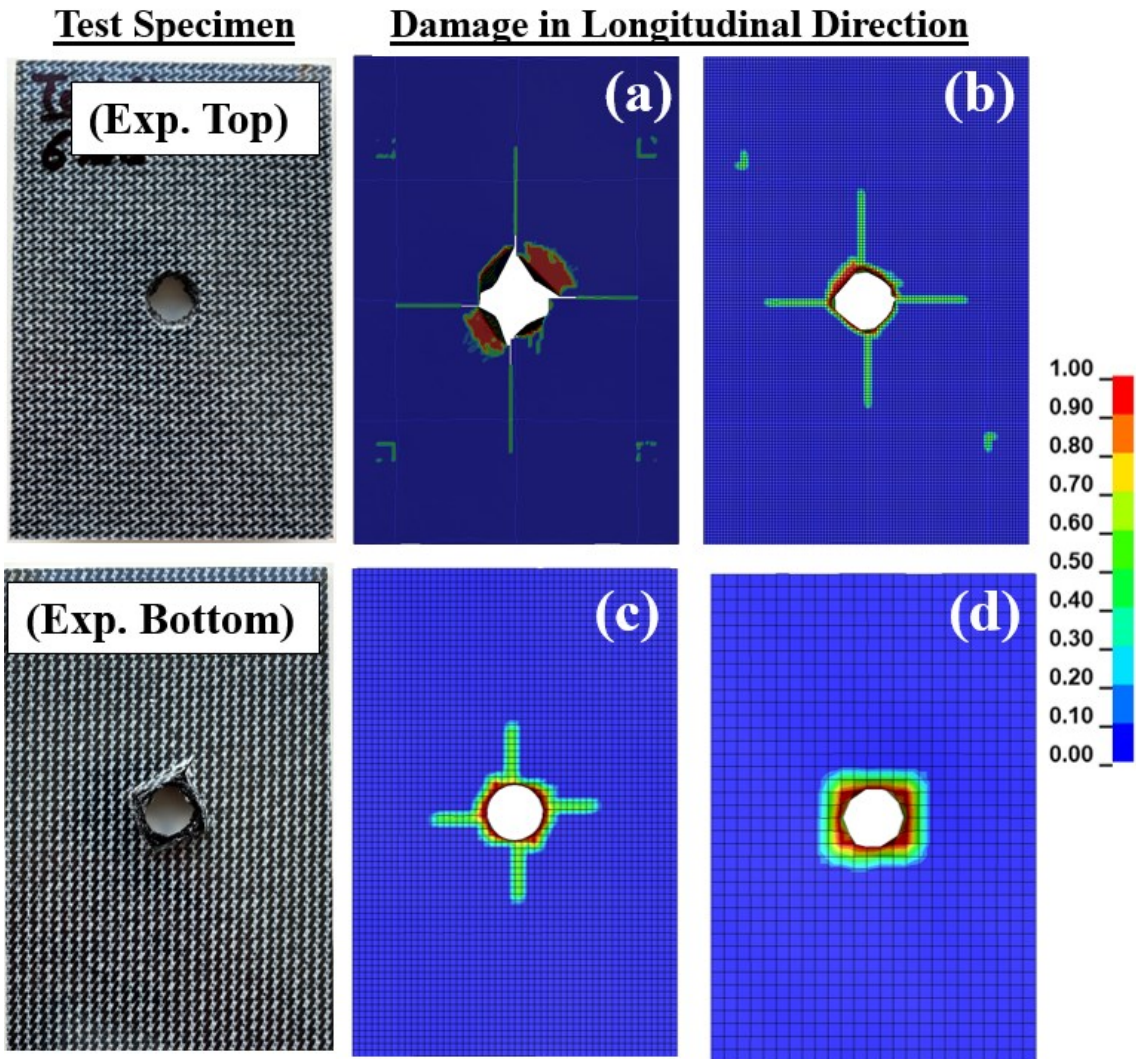


Figure 6.8. Experimental and numerical after impact images with different mesh sizes; a) 0.5 mm, b) 1 mm, c) 2 mm and d) 4 mm

6.5. Low Velocity Impact Analysis Results

The peak force, absorbed energy, damage area, delamination area and the maximum displacement value of the impactor results of experimental and numerical model LVI tests of CF/PPS thermoplastic (16 mm and 38 mm diameter hemispherical impactor) are listed in Table 6.7.

6.5.1. Numerical Investigation of the Effect of Impactor Velocity

The effect of impactor velocity is investigated by plotting the force-time, force-displacement, energy-time and energy-displacement curves. The force-time, force-displacement, absorbed energy-time and absorbed energy-displacement curves of the experimental test and single and stacked shell models are shown sequentially in Figure 6.9(a-f), Figure 6.10(a-f), Figure 6.11(a-f) and Figure 6.12 (a-f) for 1, 2, 3, 4 5 and 6 m/s impact tests.

As seen in Figure 6.9(a-f), the experimental maximum force values increases as the impact velocity increases up to 3 m/s. Beyond 3 m/s impact velocity, the experimental maximum force reaches a plateau value of ~3200N. It is further noted that the contact time decreases as the impact velocity increases. The contact time is near and above 7 milliseconds between 1-4 m/s of impact velocity and decreases to 3-4 milliseconds for the impact velocities of 5 m/s and 6 m/s. Above trends in the maximum force and contact time are also seen in the numerical force-time curves in Figure 6.9(a-f). As is seen in the same curves, the experimental maximum force values are slightly over predicted by the numerical models. Furthermore, higher contact times are found for the single shell model while the contact times of the stacked shell model is much closer to those of the experimental tests. Moreover, the curve similarities between the experimental and numerical tests results increases as the impact velocity increases. For example, there are an almost 20% difference between the experimental and numerical maximum force values at lower impact velocities such as 1 m/s impact velocity. This difference reduces to 1.3% for the stacked shell model at 6 m/s. As a conclusion, both the single shell and stacked shell models predict the experimental force-time curves with acceptable accuracies.

Table 6.7. Experimental and numerical LVI results summary

| Experimental and Numerical LVI Results Summary | | | | | | |
|---|--------------------|--------------------------------|----------------------------|-------------------------------------|---|----------------------------------|
| Impact Case | Result Type | Peak Impact Force (MPa) | Absorbed Energy (J) | Damage Area (mm²) | Delamination Area (mm²) | Maximum Displacement (mm) |
| 16 mm Impactor 1 m/s - 1.37 J | Experiment | 1133 | 0.95 | 0 | 0 | 2.67 |
| | Single Shell | 1446 | 1.17 | 0 | N/A | 1.61 |
| | Stacked Shell | 1370 | 1.04 | 8 | 6 | 1.77 |
| 16 mm Impactor 2 m/s - 5.60 J | Experiment | 2215 | 4.71 | 58 | 58 | 5.24 |
| | Single Shell | 2352 | 4.15 | 31 | N/A | 4.25 |
| | Stacked Shell | 2652 | 3.65 | 93 | 59 | 3.80 |
| 16 mm Impactor 2.99 m/s - 12.52 J | Experiment | 3086 | 11.41 | 288 | 288 | 7.85 |
| | Single Shell | 3057 | 8.45 | 45 | N/A | 7.62 |
| | Stacked Shell | 3229 | 8.77 | 273 | 205 | 7.24 |
| 16 mm Impactor 3.98 m/s - 22.18 J | Experiment | 3126 | 22.00 | 587 | 587 | 11.20 |
| | Single Shell | 3256 | 16.08 | 427 | N/A | 10.41 |
| | Stacked Shell | 3418 | 17.33 | 510 | 498 | 10.95 |
| 16 mm Impactor 4.76 m/s - 31.59 J | Experiment | 3207 | 26.56 | 594 | 594 | 15.10 |
| | Single Shell | 3258 | 25.73 | 571 | N/A | 15.20 |
| | Stacked Shell | 3291 | 24.44 | 580 | 573 | 13.70 |
| 16 mm Impactor 5.7 m/s - 45.49 J | Experiment | 3379 | 26.96 | 630 | 630 | 13.99 |
| | Single Shell | 3470 | 27.45 | 393 | N/A | 14.95 |
| | Stacked Shell | 3472 | 26.97 | 651 | 564 | 13.71 |
| 38 mm Impactor 5.6 m/s - 31.14 J | Experiment | 5959 | 20.22 | 849 | 849 | 9.60 |
| | Single Shell | 6100 | 16.04 | 238 | N/A | 10.54 |
| | Stacked Shell | 5855 | 18.15 | 755 | 587 | 10.04 |
| 38 mm Impactor 6.67 m/s - 44.18 J | Experiment | 6173 | 33.11 | 1281 | 1281 | 11.86 |
| | Single Shell | 6079 | 31.72 | 1179 | N/A | 14.25 |
| | Stacked Shell | 6095 | 31.11 | 1159 | 963 | 12.33 |

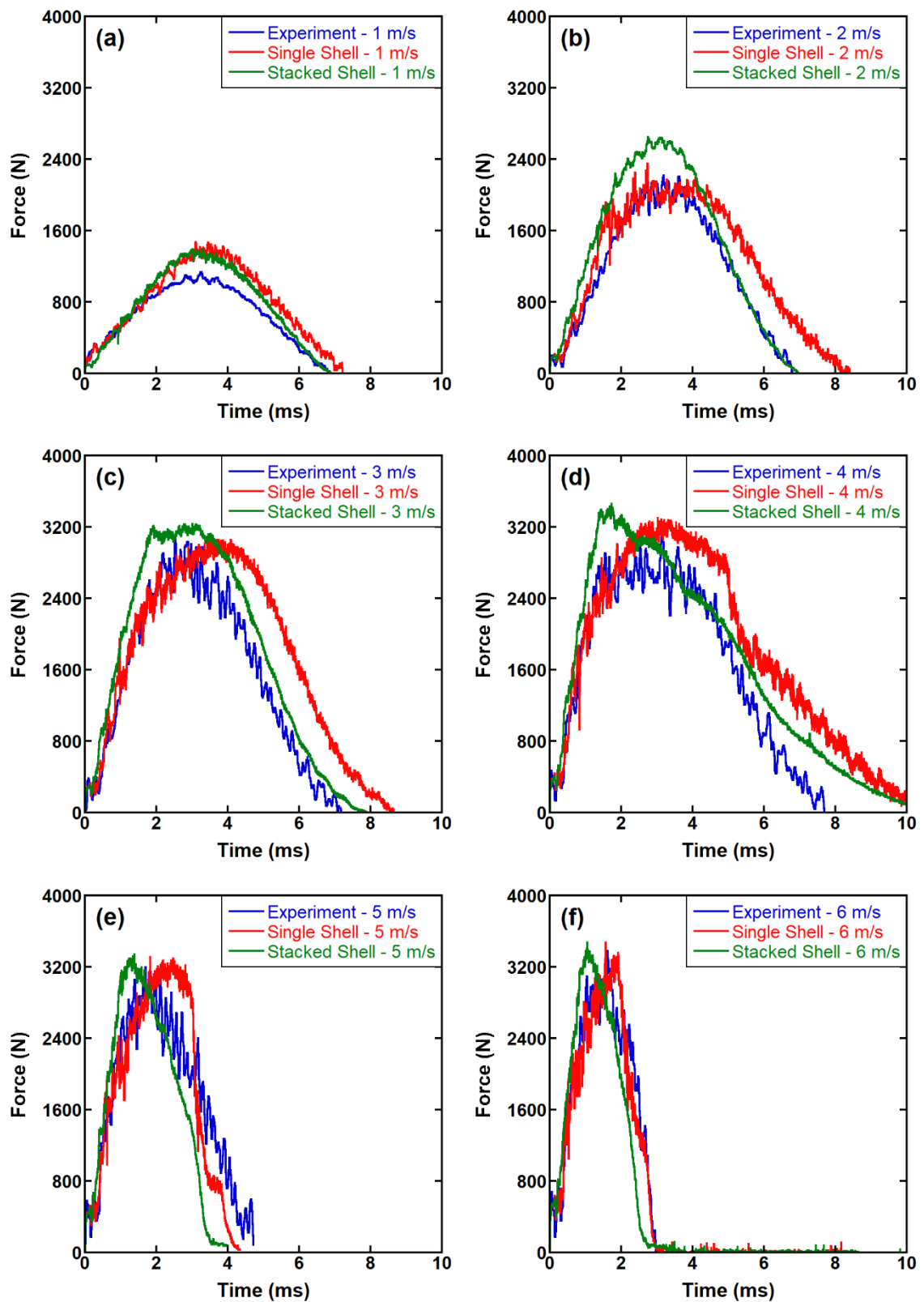


Figure 6.9. Experimental and numerical force-time curve comparison for different velocities; a) 1 m/s, b) 2 m/s, c) 3 m/s, d) 4 m/s, e) 5 m/s, f) 6 m/s

The numerical force-displacement curve at 1 m/s differs significantly from the experimental curves (Figure 6.10(a)). The difference is however decreases as the velocity increases to 2, 3,4, 5 and 6 m/s (Figure 6.10(b-f)). The numerical force-displacement curves at 5 m/s and 6 m/s show very much similarities with the experimental force-displacement curves at the same velocities as seen Figure 6.10(e-f). The difference between the curves mainly resulted from the difference in the maximum displacement and the residual displacement values. For the 1 m/s and 2 m/s impact velocities, both the numerical maximum and residual displacements show significant deviations from those of the experimental tests (Figure 6.10(a-b)). On the other side, the numerical maximum displacements are very similar while the numerical residual displacements are slightly different from the experimental tests at 3 m/s and 4 m/s impact velocities. A good agreement is seen in Figure 6.10(e-f) between the numerical and experimental maximum and residual displacements at 5 and 6 m/s impact velocities.

In the energy-displacement curves shown in Figure 6.12(a-f), the peak energy values correspond to the total energy and the last points in the curve correspond to the absorbed energy and the difference between them was referred to as the elastic energy. The resultant energy-time and displacement curves of the stacked and single shell models are very similar to each other and the discrepancy between the numerical and experimental test results decrease as the impact velocity increases. As is seen in Figure 6.12 (a-d), the majority of the energy is absorbed by the composite laminates up to 4 m/s and a small portion of the initial kinetic energy is dissipated as the elastic energy. The elastic energy also results in a spring back of the projectile. The spring of the projectile is seen up to 3 m/s of impact velocity for experimental tests and up to 4 m/s impact velocity for numerical analysis. The absorbed energy is the area under the force-displacement curve. At the impact velocity of 4 m/s, almost all energy is absorbed by the specimen itself. Since there is a full perforation of the impactor at 5 m/s (Figure 6.11(e)) and 6 m/s (Figure 6.11(f)), there is no elastic energy. Although the impact energy increases from 31 to 45 J when the impact velocity increases from 5 to 6 m/s, the absorbed energy almost remain unchanged at 26.56 J and 26.96 J, respectively. This shows that energy absorbing mechanisms are similar at these velocities or impact energies and the specimen reaches its maximum energy absorption capacity. For every test, the total energy is reached when the displacement is maximum. In the test with no damage, partial damage, and penetration, some of the energy is stored as elastic energy which is then related to the spring back of the impactor.

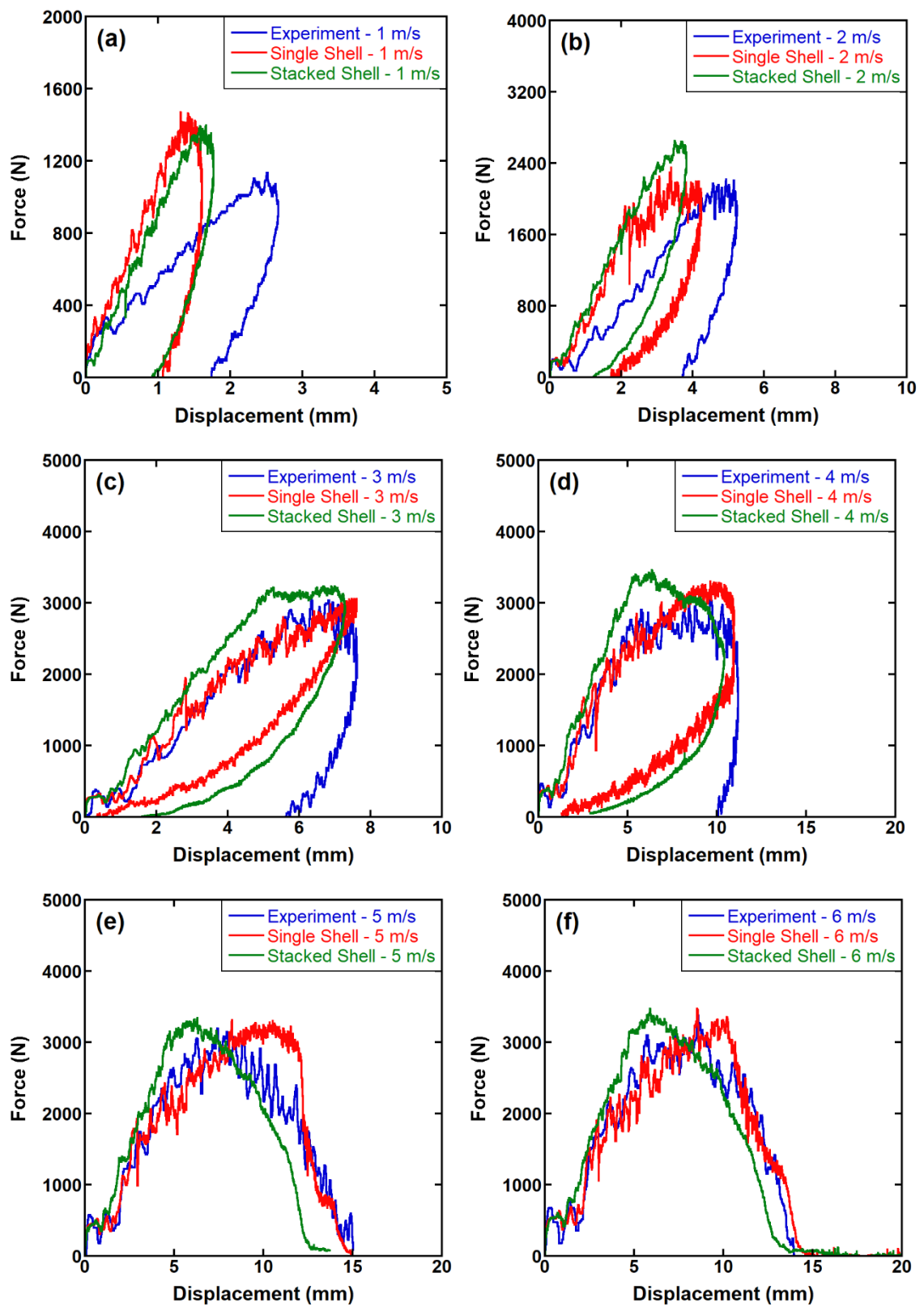


Figure 6.10. Experimental and numerical force-displacement curve comparison for different velocities; a) 1 m/s, b) 2 m/s, c) 3 m/s, d) 4 m/s, e) 5 m/s and f) 6 m/s

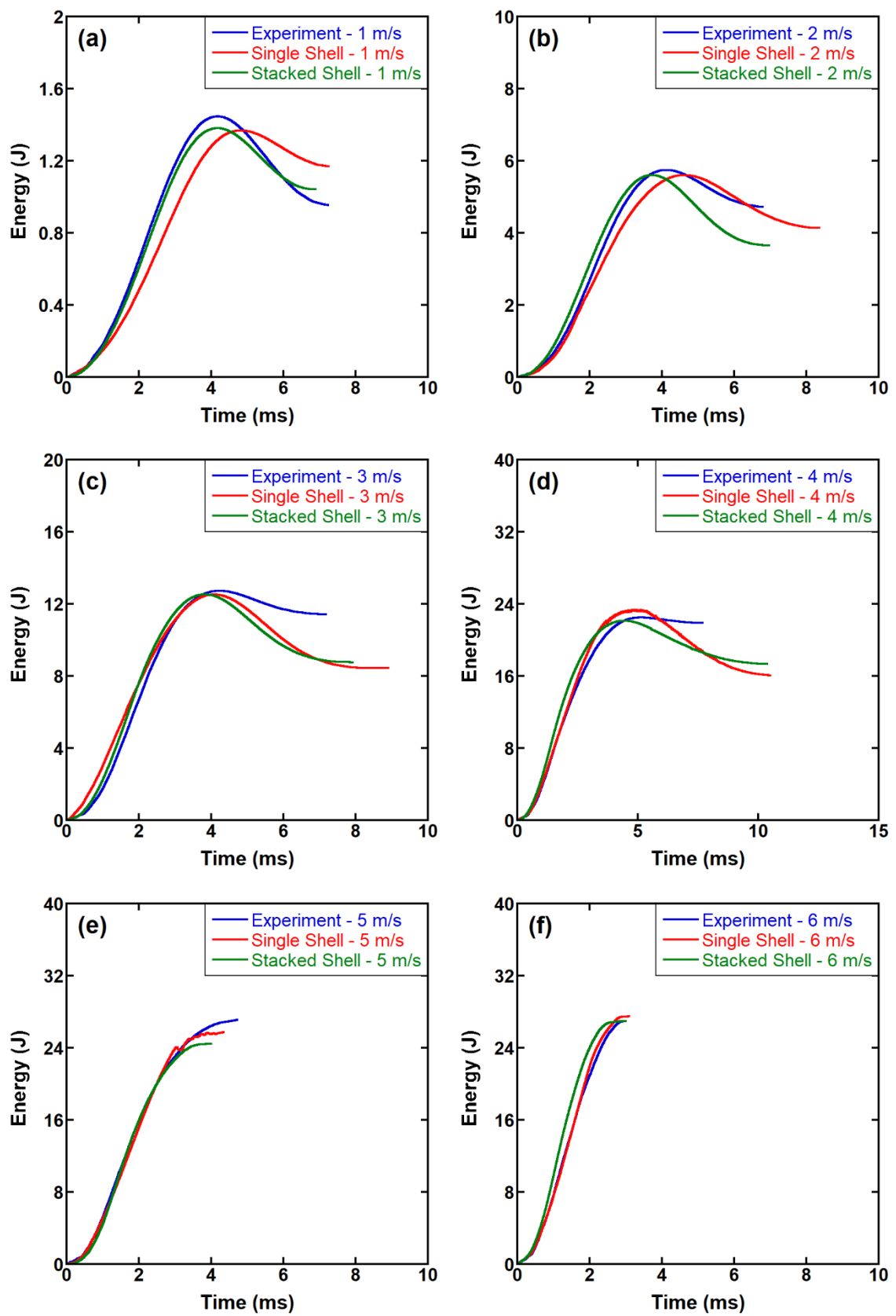


Figure 6.11. Experimental and numerical energy-time curve comparison for different velocities; a) 1 m/s, b) 2 m/s, c) 3 m/s, d) 4 m/s, e) 5 m/s and f) 6 m/s

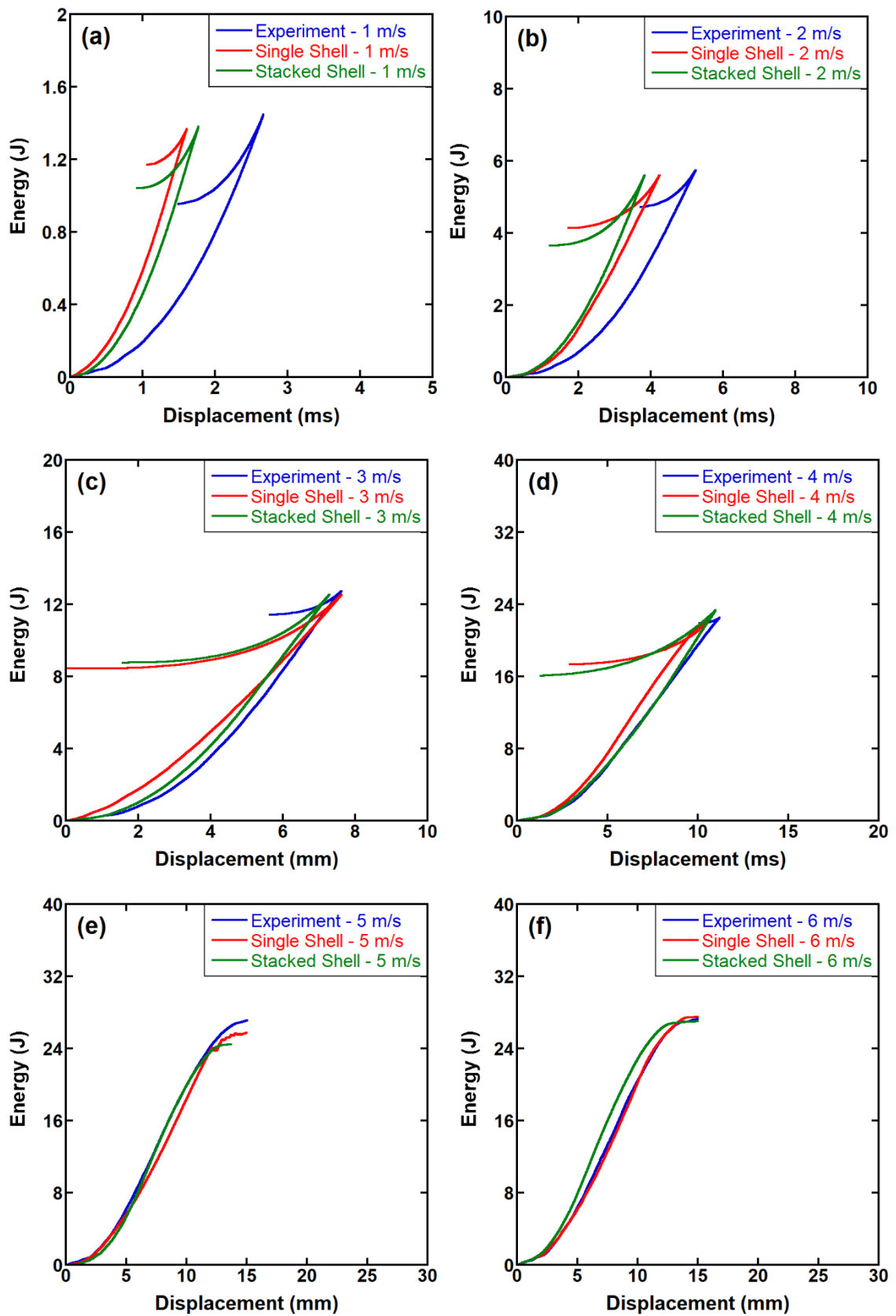


Figure 6.12. Experimental and numerical energy-displacement curve comparison for different velocities; a) 1 m/s, b) 2 m/s, c) 3 m/s, d) 4 m/s, e) 5 m/s and f) 6 m/s

Delamination is an important energy absorption mechanism for FRP composite laminates. The delamination is numerically determined as the effective delamination area using the tiebreak contact definition in the stacked shell model. The “CGAP” damage parameter in the stacked shell model shows the delaminated area as the red color and the intact area as the blue color. After getting the damage maps, the net effective delamination area is calculated using the ImageJ software.

The experimental NDI and numerical damage maps of the LVI tests at different impact velocities are shown in Figure 6.13(a-f). As seen in the same Figure 6.13(a), there is no delamination in the experimental test and numerical delamination area is 6 mm². When the impact velocity increases to 2 m/s, the experimental and numerical delamination area increases to 5 and 59 mm², respectively. This impact velocity, 2 m/s, and the corresponding energy level, 5.60 J, may be considered as the threshold for delamination damage initiation. Increasing the impact velocity from 2 m/s to 3 m/s, 2.25 times increase in the impact energy, increases the experimental delaminated area nearly 5 times (288 mm²) (Figure 6.13(c)).

The numerical model also predicts a similar but slightly increase in the delaminated area at the same velocity, 205 mm². At the 4 m/s of impact velocity, the impactor penetration occurs, resulting in almost a maximum delamination damage area for the 16 mm hemispherical tip the impactor. A delamination area of 587 mm² and 498 mm² are sequentially measured experimentally and numerically at 4 m/s as shown in Figure 6.13(d). At 5 m/s (4.76 m/s measured) and 6 m/s (5.7 m/s measured), perforation occurs, causing a circular hole-shaped perforation as seen in Figure 6.13(e) and Figure 6.13(f), respectively. Compared to test at 4 m/s of impact velocity, the delaminated area at 5 and 6 m/s do not change much even though the impact energy increased more than twice. The experimental and numerical damage geometries are very much similar, and the damage areas are 594 mm² and 573 mm² at 5 m/s and 630 mm² and 564 mm² at 6 m/s, respectively. As the single shell method do not model interlaminar failure, there is no information available for delamination. However, the method of stacked shell method is a very powerful and accurate technique to detect delamination type failure, thanks to applying proper tiebreak contact definitions for interlaminar zone.

Another way of assigning damages on the composite laminate numerically is to map history variables available for certain material models in LS-DYNA. MAT-58 material model can estimate damage in the longitudinal, transverse and shear directions. Figure 6.14 shows the first history variable (the damage in the longitudinal direction)

effective damage area map as function of impact velocity for both the single shell and stacked shell model. The measured damaged areas are further tabulated in Table 6.7.

As seen in Figure 6.14(a-f) no damage occurs in the single shell analysis at 1 m/s while a very small damage is seen in the stacked shell model at the same velocity. The single shell model predicts lower damage areas than the stacked shell model and the ultrasonic C-Scan of the experimentally tested specimen at 2 m/s and 3 m/s. The discrepancy is more emphasized at the 3 m/s impacted specimen. At and above 4 m/s at which penetration and perforation occur, both numerical model damage areas and the experimental damage areas approach each other. Especially, there is a good agreement in the damage history variables at 5 m/s and 6 m/s impact velocities. However, the stacked shell model damage areas converge better to the experimental damage areas than the single shell model damage areas. By considering lesser CPU time, the single shell method can also be used to predict the damage with an expense of accuracy.

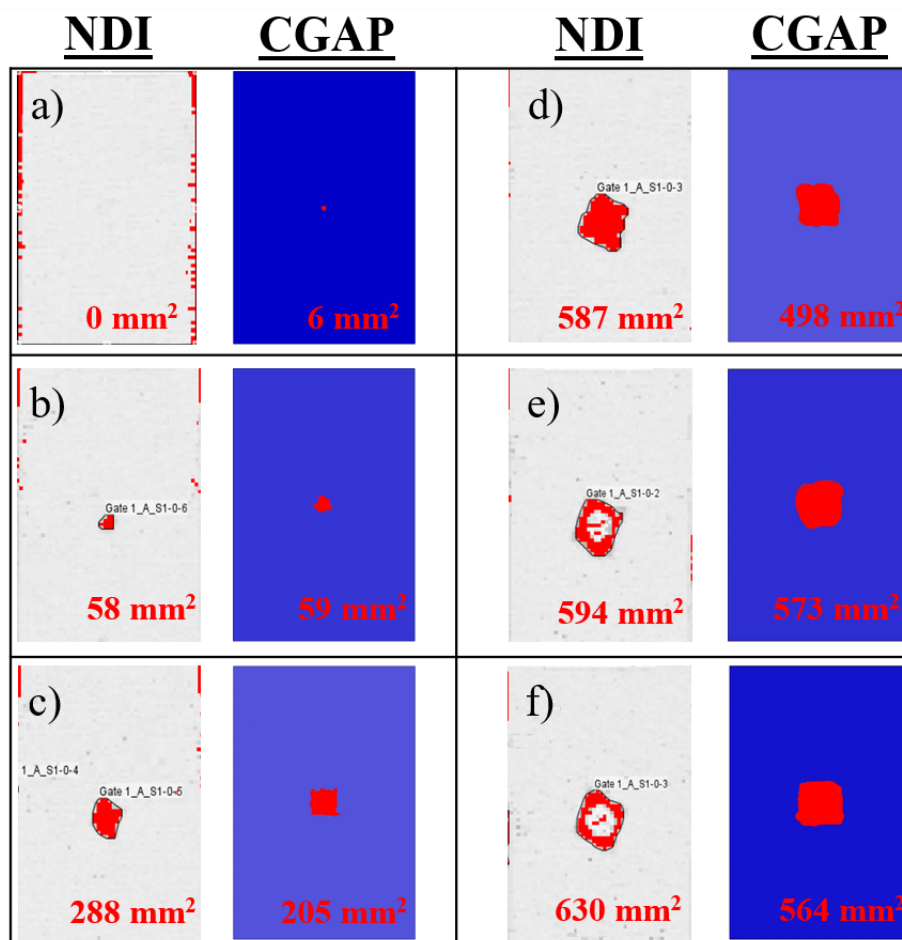


Figure 6.13. Experimental NDI images and numerical delamination parameter results at different impact velocities; a) 1 m/s, b) 2 m/s, c) 3 m/s, d) 4 m/s, e) 5 m/s and f) 6 m/s

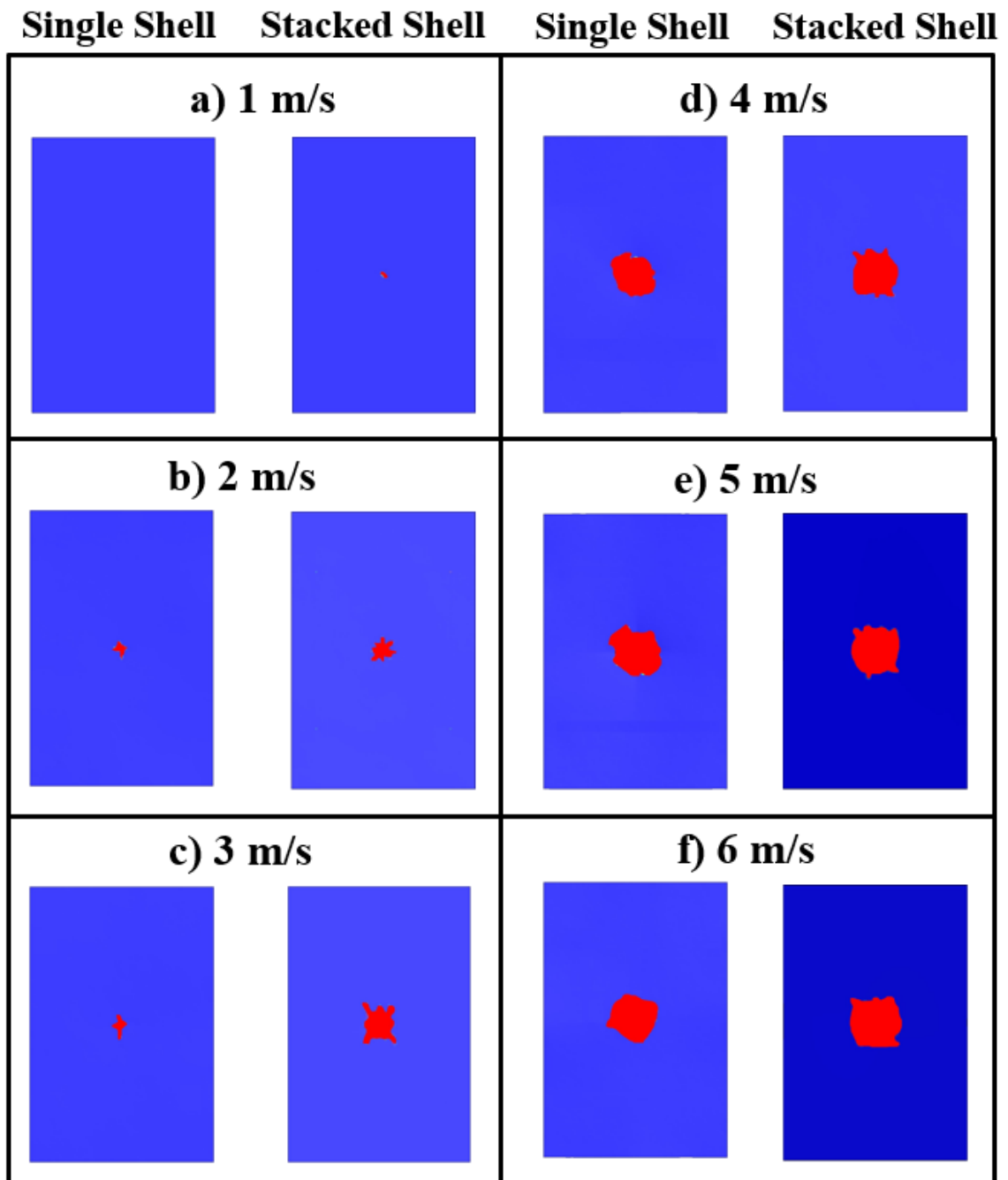


Figure 6.14. Damage history variable mapping for single shell and stacked shell method at different impact velocities, a) 1 m/s, b) 2 m/s, c) 3 m/s, d) 4 m/s, e) 5 m/s and f) 6 m/s

6.5.2. Numerical Investigation of the Effect of Impactor Geometry

The effect of the impactor geometry on the LVI test response was investigated both experimentally and numerically using a 38 mm diameter hemispherical tip projectile at two different impact energies, similar to the impact energies in the 16 mm diameter impactor tests. The test using the 16 mm impactor at 4.76 m/s impact velocity and 2.8 kg total impact weight had an impact energy of 31,59 J impact energy. Almost the same energy level, 31.14 J, was reached at 5.6 m/s impact velocity and 1.986 kg total impact weight using the 38 mm impactor. Similarly, the test using the 16 mm impactor at 5.7 m/s impact and the same impactor weight had an impact energy of 45.49 J and a similar energy level, 44.18 J, was reached at 6.67 m/s impact velocity using the 38 mm diameter impactor.

The experimental and numerical force-time, force-displacement, energy-time and energy-displacement curves of the LVI tests using the 38 mm diameter hemispherical tip projectile at 31 J are shown in Figure 6.15 (a-d), respectively. As noted in Figure 6.15(a-b), higher force fluctuations are seen in the experimental test force values than the numerical force values. Furthermore, the stacked shell model results in lesser force fluctuations than the single shell model results. The experimental and numerical maximum peak forces are also noted to be very much close to each other as shown in Figure 6.15 (a).

The maximum peak forces are 5919 N experimentally, 6100 N for the single shell model and 5855 N for the stacked shell model. The contact duration of the impactor to the specimen is almost the same for experimentally and numerically and approximately 6 milliseconds. The maximum displacement values shown in Figure 6.15 (b) are also very similar in the experimental test (9.6 mm), and numerical tests (10.54 mm for the single shell and 10.04 mm for the stacked shell model).

The experimental absorbed energy by the composite is slightly higher than the numerical absorbed energies as shown in Figure 6.15 (c-d). In the experimental test, the total absorbed energy is 20.22 J while the absorbed energy is 16.04 J in the single shell model and 18.15 J in the stacked shell model.

As a summary, the stacked shell model approximates the experimental tests nearer than the single shell model 31 J impact energy. The experimentally tested specimen picture and the experimental and numerical damage areas of the 16 mm and 38 mm

impactor tests at 31 J are shown in Figure 6.16. As seen in the same figure, the visible experimental damage type changes from perforation for the 16 mm impactor to large cracks with fiber breakage and matrix cracking for the 38 mm impactor at the same level of impact energy of 31J.

NDI images show that the length of lateral cracks increase from 23 mm to 31 mm and longitudinal cracks increases from 27 mm to 32 mm when the impactor diameter increases from 16 mm to 38 mm. The damage area is 594 mm² and 573 mm² in the experimental test and numerical analysis of 16 mm impactor test, respectively. For the test with 38 mm impactor, the numerical analysis predicts a delamination area of 587 mm² while it is 849 mm² in the experimental test. There is a better numerical analysis prediction of the damaged areas comparison of the test and analysis with 16 mm impactor compared to 38 mm impactor. This might be caused because of the specimen is perforated in the 16 mm impactor test for both experimentally and numerically.

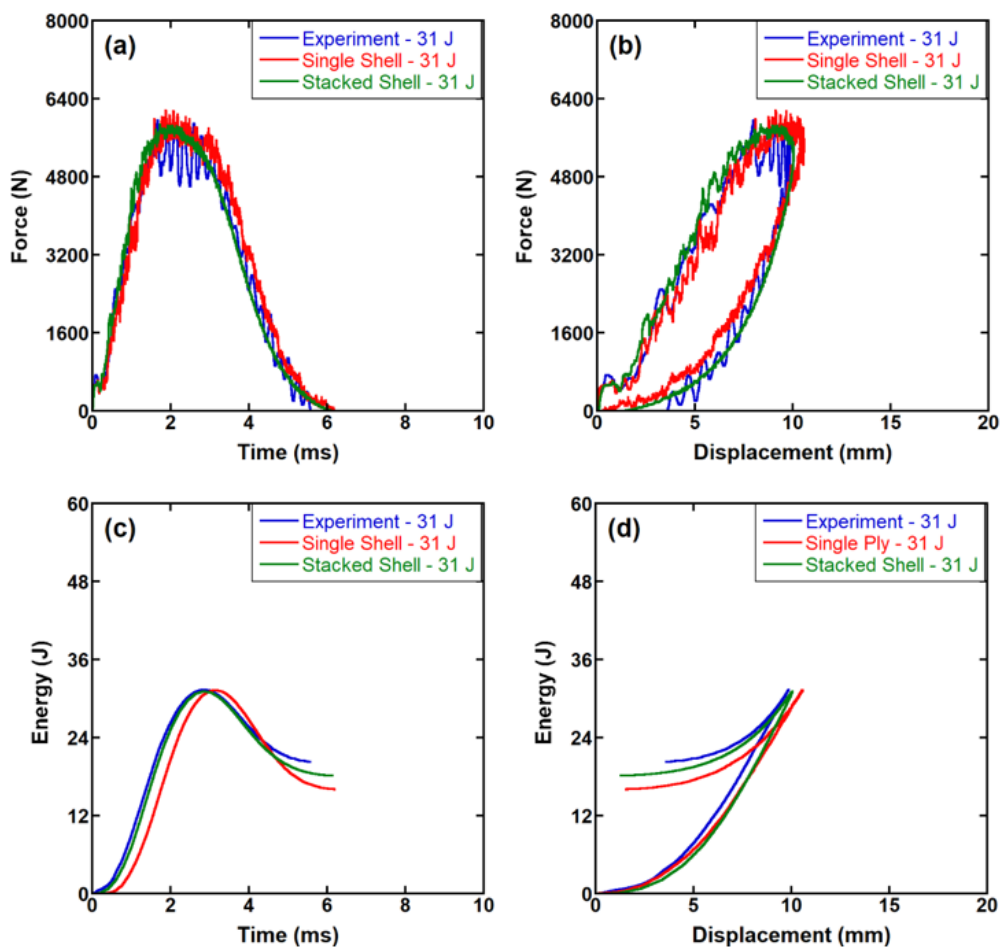


Figure 6.15. Experimental and numerical comparison for 31 J impact energy; a) Force-time, b) Force-displacement, c) Energy-time and d) Energy-displacement curves

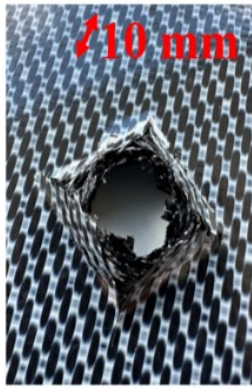
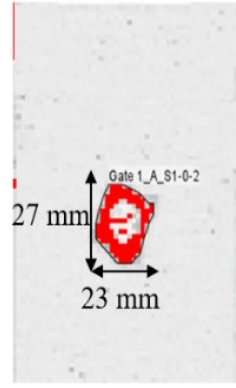
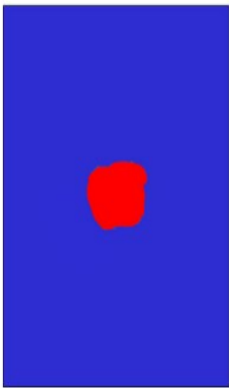

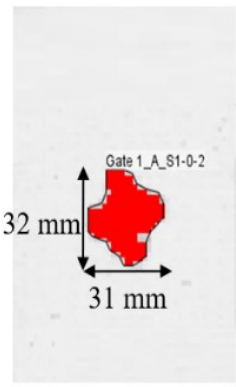
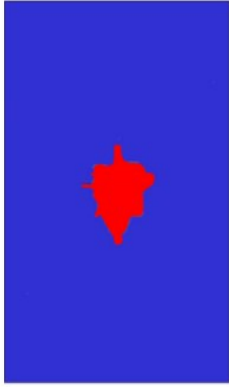
| | Exp. Specimen | Exp. NDI | Num. Delamination |
|--------------------------------------|--|---|--|
| 16 mm impactor 4.76 m/s – 31.59 J |  |  |  |
| 38 mm impactor 5.6 m/s – 31.14 J |  |  |  |

Figure 6.16. Comparison of two different impactor LVI tests results at 31 J impact energy

The experimental and numerical force-time, force-displacement, energy-time and energy-displacement curves of the LVI tests using the 38 mm diameter hemispherical tip projectile at 44 J are shown in Figure 6.17 (a-d), respectively. The peak force in the experimental test is 6173 N and the numerical single shell and the stacked shell model sequentially result in peak force 6079 N and 6095 N, respectively. The maximum displacement is measured as 11.86 mm in the experiment and 14.25 mm in the single shell and 12.33 mm in the stacked shell model as highlighted in Figure 6.17 (a-b). The total energy absorbed by the composite is very similar for the experimental (33.11 J) and the numerical models, 31.72 J in the stacked shell and 31.11 J in the single shell model. In general, a noisier force history is found in the single shell model and less force fluctuations are seen in the models than in the experiment test. Especially in the stacked shell model results, the smoothest curves are obtained. Although both numerical models well predict the LVI experimental test curve, the stacked shell model is more successful in approaching the experimental test curve.

The second comparable impact energy level (45.49J for the 16 mm impactor and 44.18 J for the 38 mm impactor) was used for the investigation of impactor geometry effect at a higher impact energy than the first one. The NDI images, macroscopic specimen images after test and numerical delamination results are shown in Figure 6.18. Similar to tests at lower impact energy, the failure mode in the 16 mm impactor test is perforation with hole creation and fiber breakage with long cracks in back side of the specimen. The damage dimensions increase from 25 mm width and 27 mm length to 37 mm width and 40 mm length with changing the impactor diameter from 16 mm to 38 mm at same level of impact energy. NDI images for the damage in the test and measured delamination area on the numerical analysis are very close for the 16 mm impactor (630 mm², 564 mm², respectively). While the delamination area is measured 1281 mm² for the 38 mm impactor test and 963 mm² in the numerical analysis having a similar damage shape.

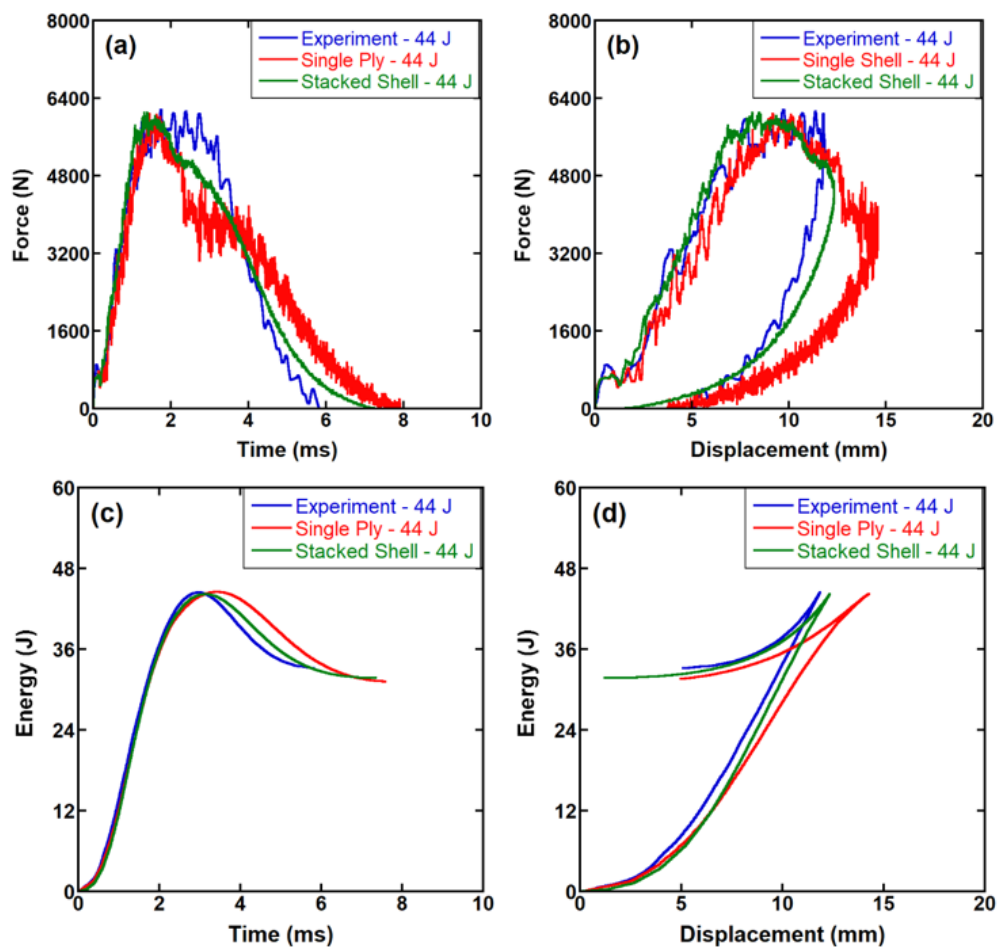


Figure 6.17. Experimental and numerical comparison for 44 J impact energy; a) Force-time, b) Force-displacement, c) Energy-time and d) Energy-displacement curves



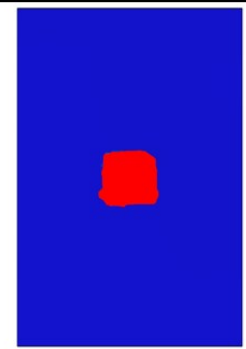
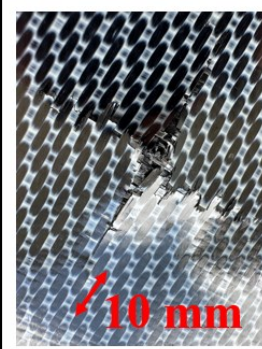
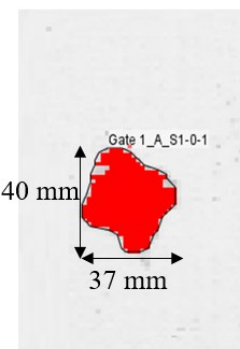
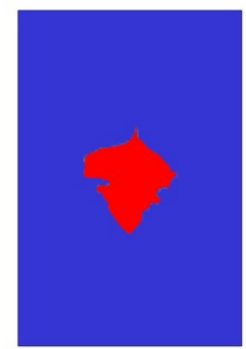
| | Exp. Specimen | Exp. NDI | Num. Delamination |
|--------------------------------------|---|--|---|
| 16 mm impactor 5.7 m/s – 45.49 J |  |  |  |
| 38 mm impactor 6.67 m/s – 44.18 J |  |  |  |

Figure 6.18. Comparison of two different impactor LVI tests results at 44 Joule impact energy

6.6. Compression After Impact Analysis Results

The CAI tests and numerical analyses were performed on the LVI test specimens impacted at six different impact velocities. The experimental and numerical ultimate strength and damages areas of the CAI tests are tabulated in Table 6.8. Although, the experimental delamination areas (ultrasonic C-Scan NDI) and numerical history variable-1 (the maximum effective damage in longitudinal direction) are not actually the same type of damage, they are very useful in assessing the damage occurred in the CAI specimen. As tabulated in Table 6.8, the experimental delamination area values obtained from NDI inspection vary between 1567 and 2697 mm² and the numerical damaged area between 1154 and 1879 mm². A larger damage variation is therefore found in the experimental damage values. For all CAI test cases including experimental and numerical, the ultimate strength did not show an increasing or decreasing trend with changing the impact case. The ultimate strength in experimental tests were measured between 193-227 MPa and 181-261 MPa in the numerical analysis. The higher discrepancy in the numerical analysis may be resulted because of greater effect of damage

existence in the numerical analysis. The percent differences between experimental test and numerical analysis varies between 2-15% depending on the test cases.

Table 6.8. CAI Experimental and numerical results comparison

| CAI Test Number | Impact Case | Result Type | Ultimate Strength (MPa) | | Experimental Delamination / Numerical Damaged Area (mm ²) |
|-----------------|---------------------|-------------|-------------------------|-----|---|
| CAI Test-1 | 0.99 m/s 1.37 J | Experiment | 227 | 15% | 2335 |
| | | Numerical | 261 | | 1879 |
| CAI Test-2 | 2 m/s 5.60 J | Experiment | 193 | 12% | 2453 |
| | | Numerical | 217 | | 1530 |
| CAI Test-3 | 2.99 m/s 12.52 J | Experiment | 212 | 2% | 2697 |
| | | Numerical | 216 | | 1154 |
| CAI Test-4 | 3.98 m/s 22.18 J | Experiment | 209 | 13% | 1422 |
| | | Numerical | 181 | | 1567 |
| CAI Test-5 | 4.76 m/s 31.76 J | Experiment | 205 | 12% | 1494 |
| | | Numerical | 181 | | 1599 |
| CAI Test-6 | 5.70 m/s 45.48 J | Experiment | 201 | 7% | 2576 |
| | | Numerical | 186 | | 1542 |

The experimental and numerical stress-time curves of the CAI test specimens impacted at 1, 2, 3, 4,5 and 6 m/s are shown Figure 6.19. As is noted in the same figures, the numerical stress values are slightly higher than those of the experiment in the 1 and 2 m/s impacted specimens, the numerical and experimental stresses are comparable with each other in the 3 and 4 m/s impacted specimens and the stresses are almost the same until about the ultimate strength in the 5 and 6 m/s impacted specimens. The 1 m/s and 2 m/s impacted test specimens do not numerically exhibit clear damage. This can result in higher discrepancy between the experimental and numerical CAI test results. On the other size, the differences between experimental and numerical ultimate strength values are in the range of 2-15%. The closest results are obtained for CAI Test-3, experimentally 212 MPa and numerically 216 MPa.

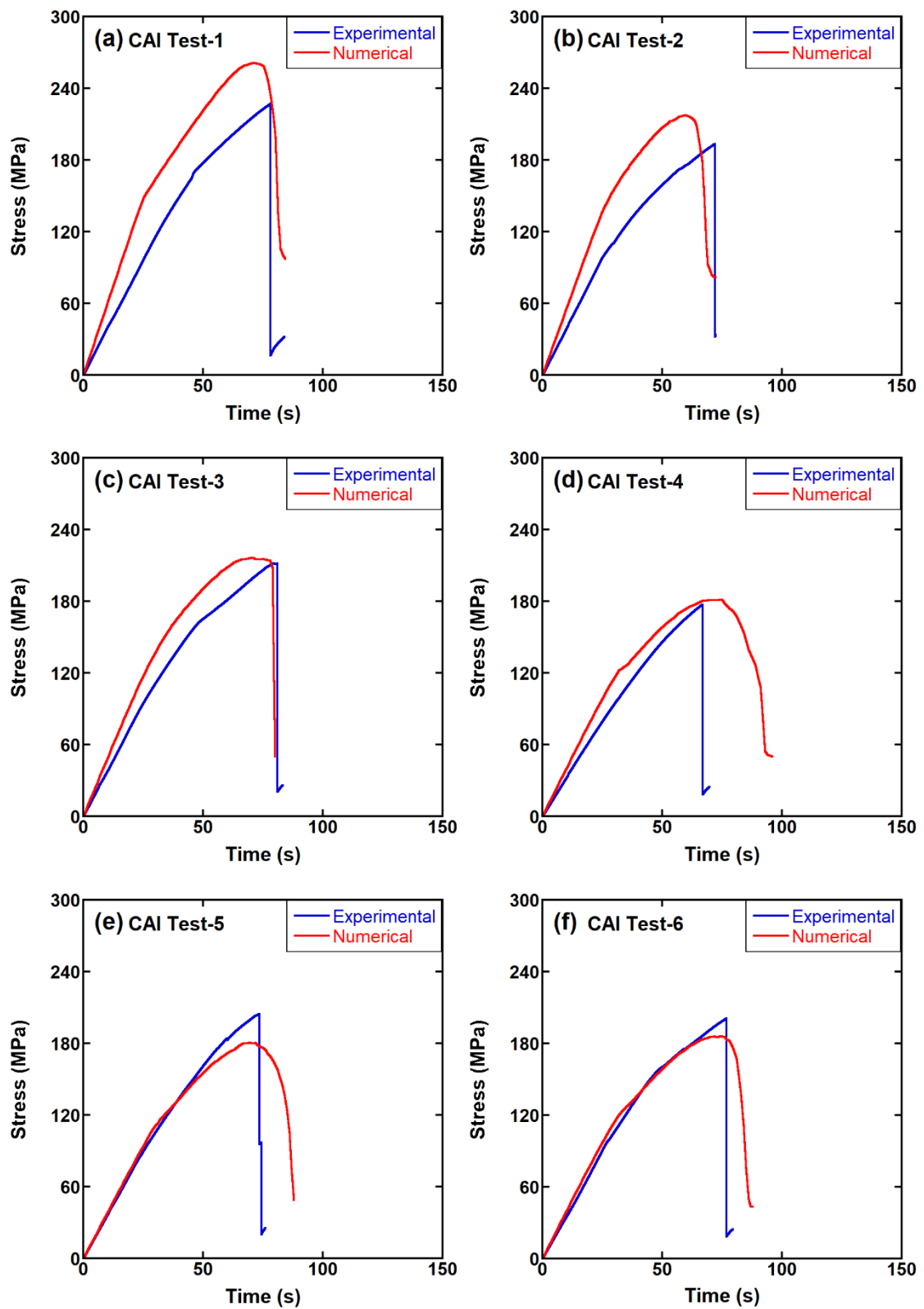


Figure 6.19. Time-Stress curve experimental and numerical results comparison; a) CAI Test-1, b) CAI Test-2, c) CAI Test-3, d) CAI Test-4, e) CAI Test-5 and f) CAI Test-6

The front and back pictures of the experimentally and numerically tested specimens, the numerical and experimental DIC y-axis displacement and the experimental and numerical damages of CAI tests are shown together in Figure 6.20. In every test specimen a lateral mid sectional failure is seen in Figure 6.20. An impact zone crossing failure is seen especially for the test specimen 3-4-5 and 6. Note that the -y direction is the loading direction of the test fixture. Experimental -y displacement measurement by DIC was made on a relatively smaller area than the specimen itself due to the test fixture. The scale is taken as from 0.0 to -2.0. Overall, a similar displacement map is observed for both experimental test and numerical analysis. The bottom half of the specimen exhibits very small or no displacement. The maximum -y displacement is about 2 mm and takes place upmost part of the upper half of the specimen. It can be said that there is good correlation between experimental and numerical results of the -y displacement map. It can also be said that the DIC system works consistently and effectively between tests which can be considered as a useful tool for displacement and strain measurement and mapping. The C-Scan images show that through thickness scanning of the composite laminates and total delamination area over the surface of the specimen. The red areas show the total delaminated area. Except CAI Test-2 in which the delamination take place in two distinct regions, the specimens exhibit laterals through damage middle section failure mode with different delamination sizes. It is also observed that in the CAI tests with the 3 m/s and above impacted tests specimens, the failure starts at the impact location where the impact damage occurs. However, failure can initiate at the edges of the specimen and more likely buckling type of failure can be observed in the specimen where the impacted specimen is intact or small damage. Numerical damage map showing the damage in longitudinal direction indicates the maximum damage occurs in the specimen in which the value of 1.0 is fully damaged and 0.0 is intact. Since the composite laminate is 5HS woven fabric, the damage in both longitudinal and transverse directions are very similar.

It is further seen from Figure 6.20, the damage propagates laterally through the middle section of the specimen at the impact zone. Since the damage in longitudinal direction is only the fiber failure mode and it does show matrix damage or debonding, it is expected to have a relatively smaller area than the delamination damage area obtained from NDI.

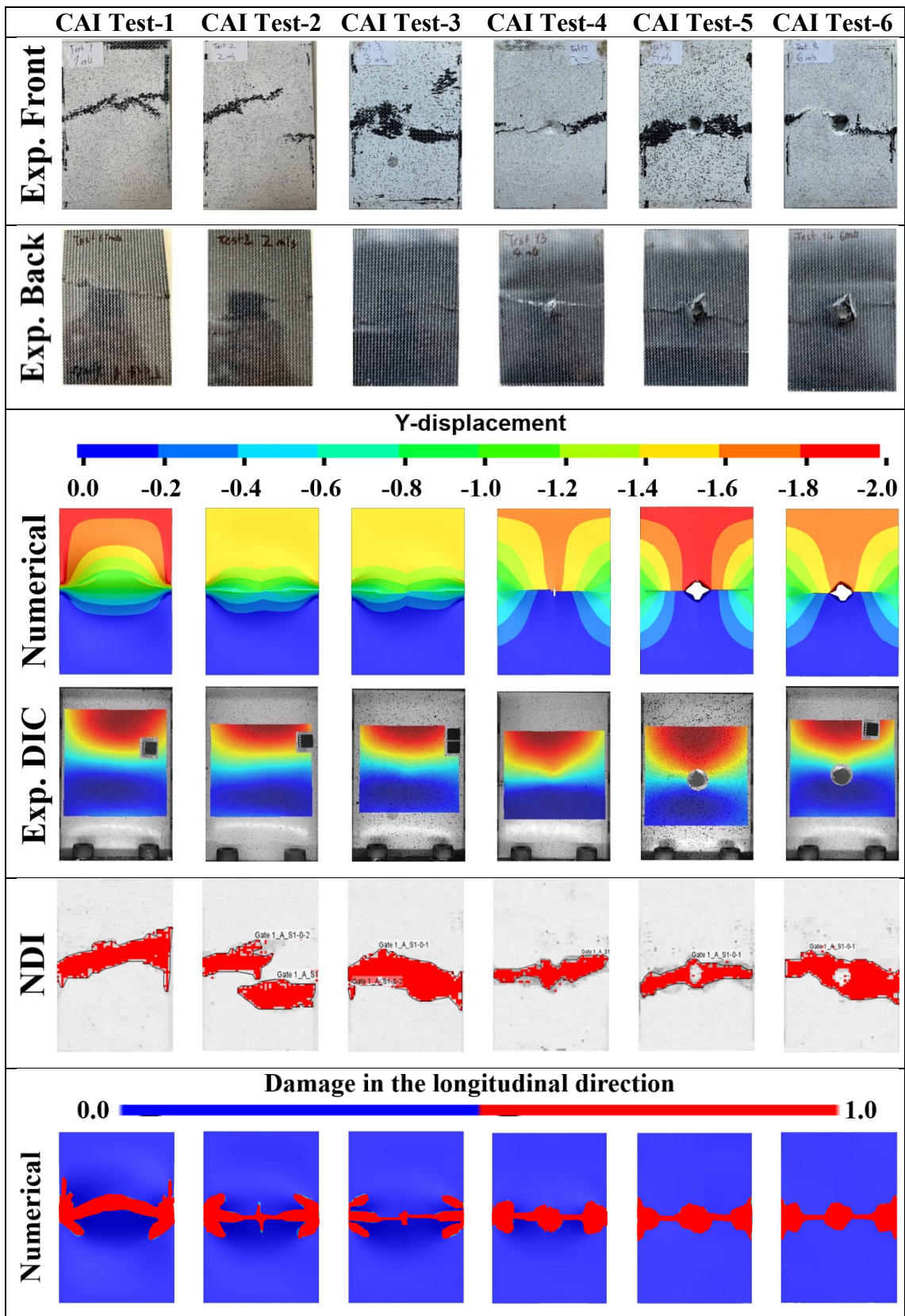


Figure 6.20. Experimental and numerical CAI test results comparison

6.7. Gas Gun Impact Analysis Results

The HVI gas gun impact tests were completed with three repetitive tests using 8 ply 200 mm x 200 mm x 2.25 mm composite laminates in which all plies were sequenced in 00 directions ($[0]_8$). The results of Test-2 were used for comparison with the numerical models. The numerical models were performed using the single shell layer model and stacked shell model with tiebreak contact. The impact velocities, exit velocities, impact energies, exit energies, absorbed energies, delamination areas and peak force values of the experimental and numerical Gas gun impact tests are tabulated in Table 6.9. Note that the force measurement in the experimental tests could not be possible. On the other side, numerical analyses allowed to measure the contact forces with respect to time. Also, the stacked shell model provided the delamination area, thanks to tiebreak contact which is interlaminar modeling technique between composite plies.

The numerical variations of the contact force, velocity, kinetic energy, and displacement with time are shown sequentially in Figure 6.21(a-d) for both single shell and stacked shell models. Both model result in similar force-time response as seen in Figure 6.21(a). The exit velocity of the projectile in the stacked shell model is 90.60 m/s, converging nearer the experimental exit velocity, 89.73 m/s, while the single shell model yield slightly a higher exit velocity 91.90 m/s as seen Figure 6.21(b). As it is seen in Figure 6.21(c), the final kinetic energy of the projectile in the stacked shell method is closer to that in the experiment while the single shell models results in a higher kinetic energy. The projectile lost 22% of its initial kinetic energy in the experimental test. The numerical energy absorption by the laminate is 18% and 21% of initial kinetic energy for the single shell and stacked shell model, respectively. Lastly, both models exhibit similar displacements and duration of the impact time 0.4-0.5 milliseconds as seen in Figure 6.21(d).

Table 6.9. Experimental and numerical gas gun test results comparison

| <i>Results</i> | <i>Impact Velocity (m/s)</i> | <i>Exit Velocity (m/s)</i> | <i>Impact Energy (J)</i> | <i>Exit Energy (J)</i> | <i>Absorbed Energy (J)</i> | <i>Delamination Area (mm²)</i> | <i>Peak Force (N)</i> |
|-------------------------------|------------------------------|----------------------------|--------------------------|------------------------|----------------------------|---|-----------------------|
| Experiment | 101.68 | 89.73 | 568.64 | 442.83 | 125.80 | 3644 | - |
| Single Shell Analysis | 101.68 | 91.90 | 568.64 | 464.51 | 104.13 | N/A | 9392 |
| Stacked Shell Analysis | 101.68 | 90.60 | 568.64 | 451.46 | 117.18 | 2535 | 7959 |

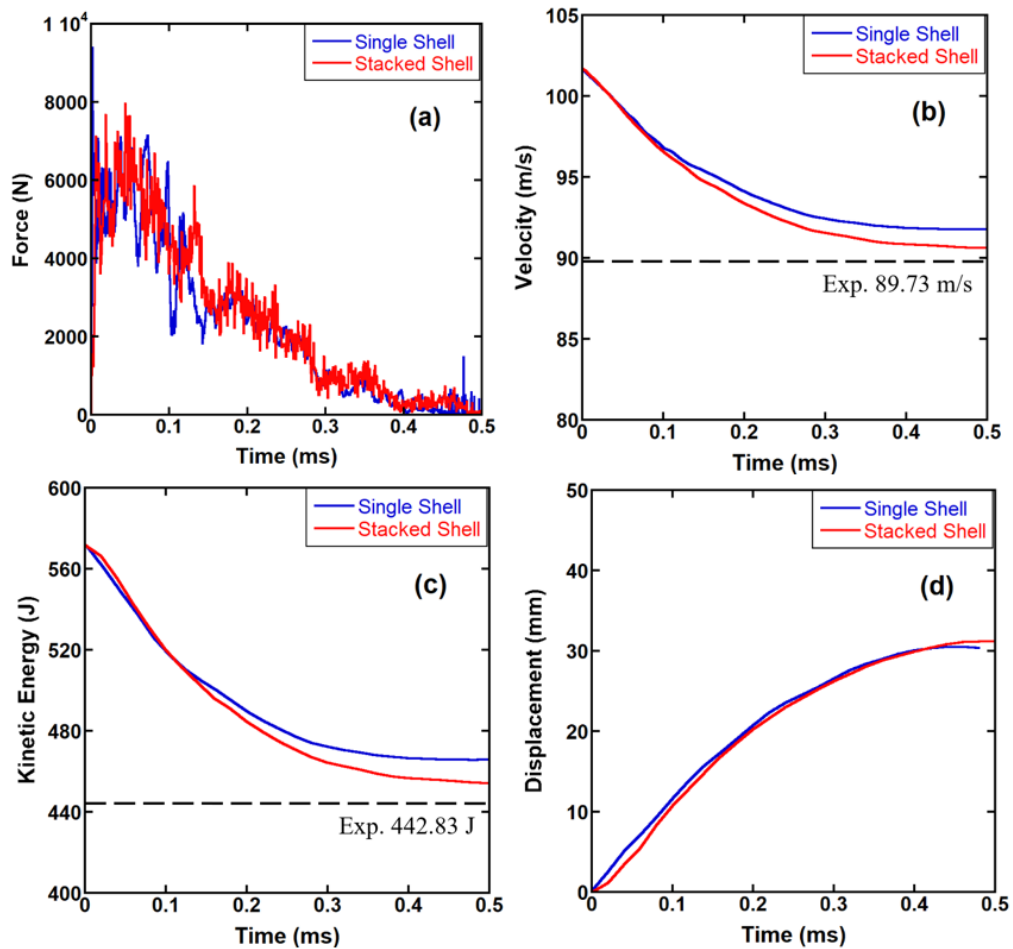


Figure 6.21. Numerical comparison curves; a) Force-time, b) Velocity-time, c) Kinetic energy-time and d) Displacement-time

The perforation of the steel ball projectile in the impact tests, the longitudinal and transverse cracks at the impact zone as shown in Figure 6.22(a-c) for the experimental test and for the single shell and stacked shell models, respectively. As the projectile completely perforates the laminate, the specimen springbacks to almost its initial position along with the two main longitudinal and transverse cracks. The formed impact crack dimensions are also shown in Figure 6.22(a-c). In the experimental test, the longitudinal and transverse crack dimensions are 79 mm and 73 mm, respectively as shown in Figure 6.22 (a). Whereas, the longitudinal and transverse cracks are 55 mm and 53 mm in the single shell model (Figure 6.22 (b)) and 80 mm and 76 mm in the stacked shell model Figure 6.22 (c), respectively. The stacked shell model predicts the experimental crack dimension nearer than the single shell model. Moreover, the longitudinal cracks observed in both experimental test and numerical analyses are bigger than the transverse cracks observed in every cases within minor difference.

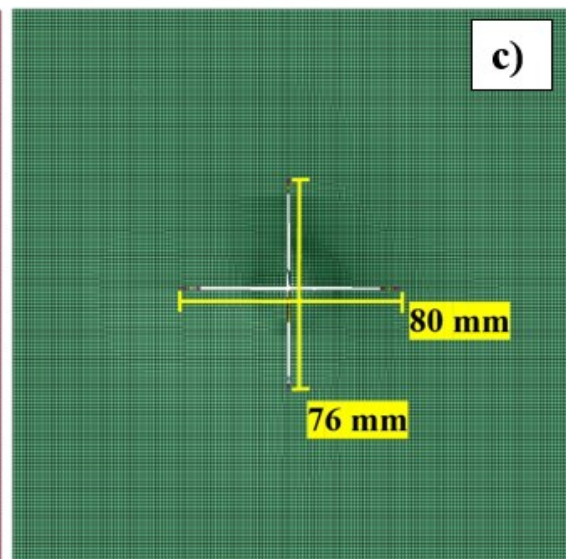
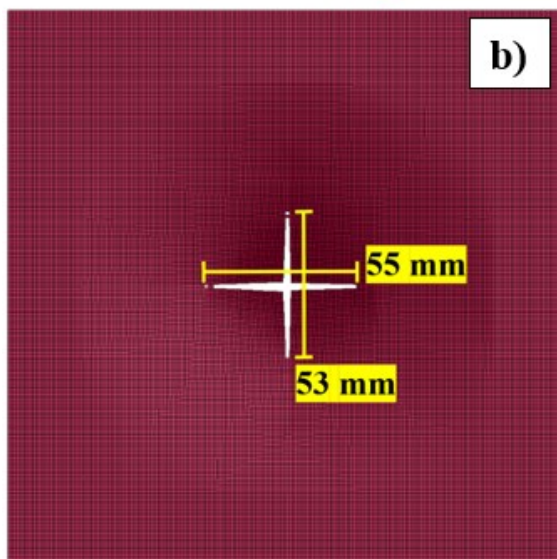
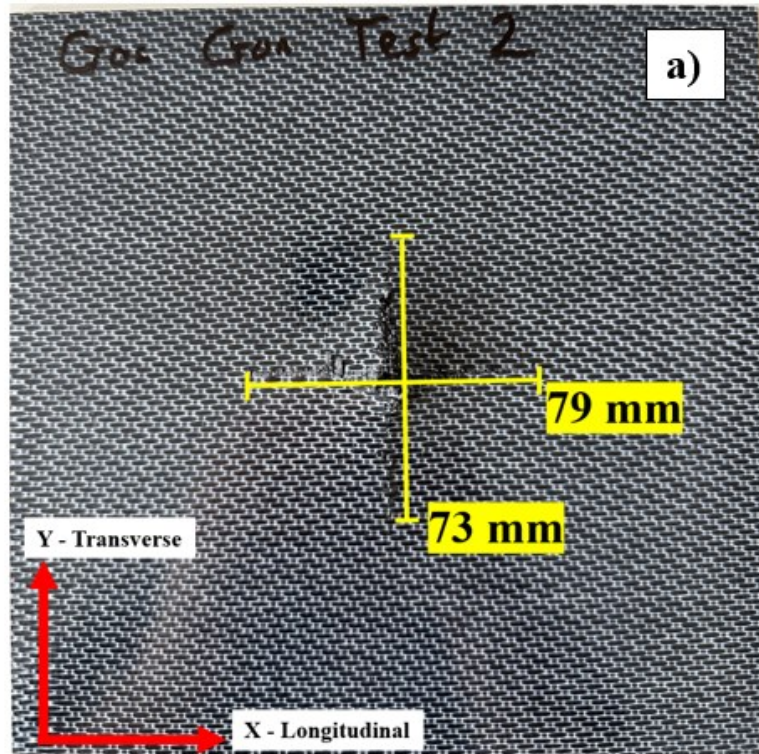


Figure 6.22. Longitudinal and transverse failure dimensions at the impact zone; a) Experiment, b) Single shell and c) Stacked shell

The numerical and experimental failure mode and damage mechanism of the composite laminate under HVI gas gun impact are shown in Figure 6.23 (a-b). There are two main cracks constituted in the composite laminate due to the perforation of the steel ball. Correspondingly, delamination is one of major damage and energy absorbing mechanisms which is seen in both the numerical and experimental test specimens. The delamination occurs on the several interlaminar sections which is detected using the tiebreak contact in the numerical analysis and the NDI techniques in experimental test coupons. The other two failure mechanisms are the fiber fracture and matrix cracking which is clearly seen in the experimental test coupon shown in Figure 6.23(b). Since the numerical model is macro, it is not possible to distinguish and observe the fiber breakage and matrix cracking.

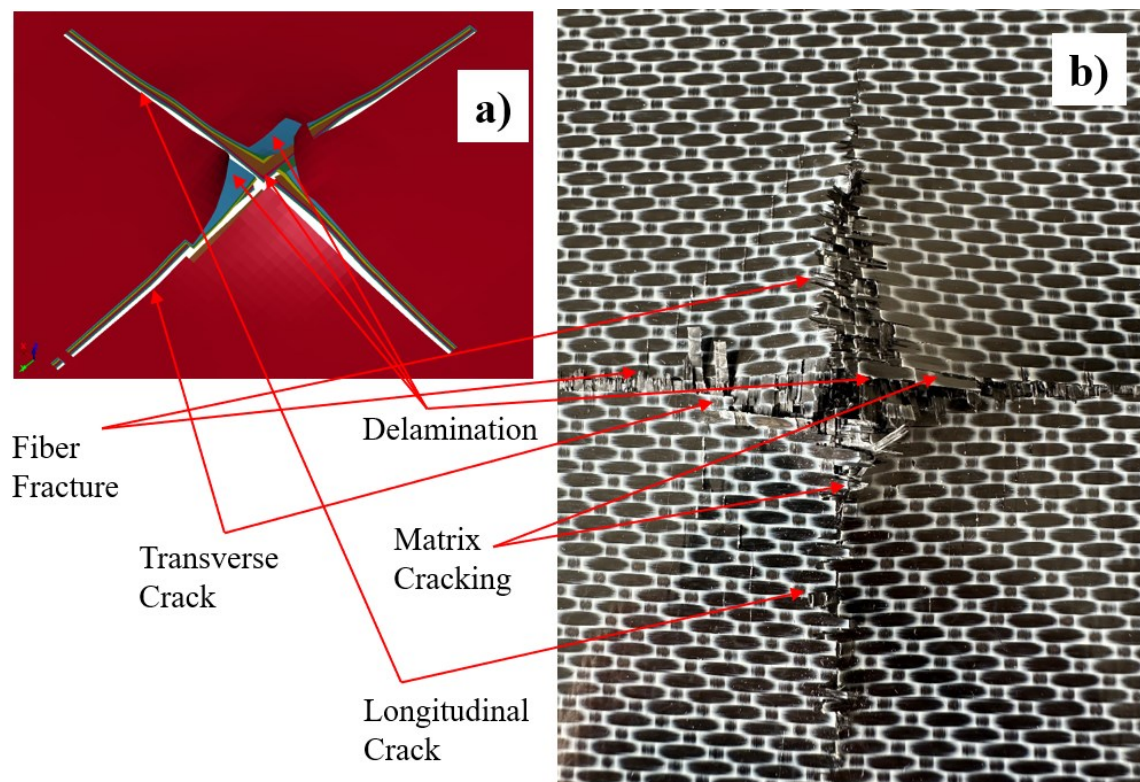


Figure 6.23. Failure modes; a) Stacked shell model and b) Experimental test

The contact gap parameter “CGAP” map in the stacked shell model is drawn for the composite laminate and shown in Figure 6.24(a). The CGAP parameter varies from 0.0 to 1.0 and the value higher than zero shows the delaminated area. The area is then measured using ImageJ software and the resultant measurement is shown in Figure 6.24(b). The total delaminated area is measured 2535 mm² for the numerical stacked model. The experimental damage areas measured using the NDI images is 3644 mm² as

shown in Figure 6.24(c). The experimental delamination area is higher than the numerical one. However, the experimental and numerical shape of the delamination and the boundaries are very close to each other. In this respect, the numerical stacked model is considered successful in capturing the delamination failure of the CF/PPS composite.

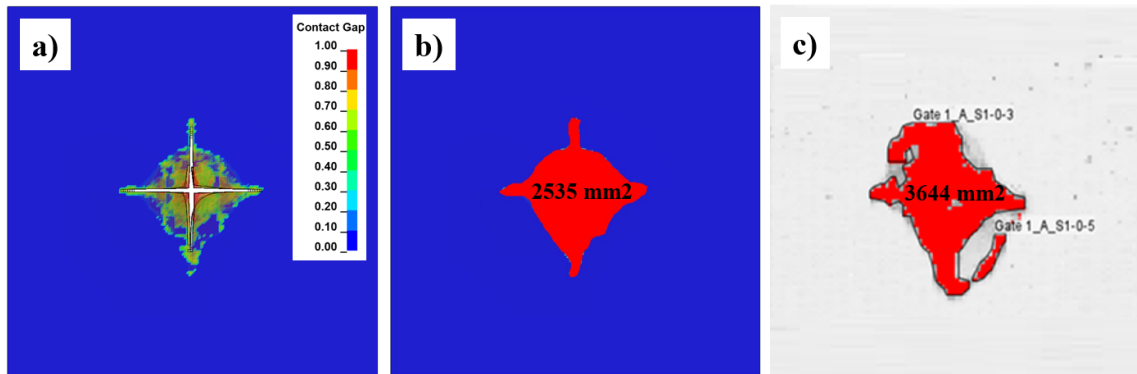


Figure 6.24. Delamination area comparison a) Stacked shell model CGAP, b) The resultant delamination area and c) C-Scan

CHAPTER 7

CONCLUSIONS

The impact resistance and impact damage tolerance of an aerospace grade high performance 5HS woven CF/PPS thermoplastic matrix composite was investigated experimentally and numerically. The initial experimental procedure was composed of mechanical and high strain rate sensitivity screening tests. The quasi-static uniaxial tension and compression tests in the warp and weft directions and the in-plane shear tests were performed in order to determine the material model parameters of the composite for the numerical models. Uniaxial tension and compression tests at 10^{-3} s^{-1} and 10^{-2} s^{-1} showed no strain rate sensitivity for the investigated CF/PPS thermoplastic matrix composite and the numerical models were constructed without rate sensitivity of the composite. The numerical modeling of the quasi-static tests was performed using the material model MAT-58 and Hashin failure criteria in LS-DYNA explicit solver. The numerical models of the mechanical tests were developed based on the single shell element and coupon level models. Single element model provided a quick and simple but effective method for analyzing the mechanical behavior of FRP composites. Coupon level analysis showed very good results for validating numerical analyses results with those the experimental results. It also allowed to determine the failure location and type numerically.

The LVI tests (1- 6 m/s) were performed at seven different impact energies and with two different impactors. The numerical models of the LVI tests were implemented using the single shell and stacked shell models. The repetitive LVI experimental tests showed similar results. The experimental contact duration of the LVI test impactor to the specimen did not change up to 4 m/s while the contact time decreased at 5 and 6 m/s due to the perforation of impactor to the test specimen. In accordance with above, the LVI test peak force increased as the velocity of the impactor increased from 1 to 3 m/s. The absorbed energy and maximum displacement of the composite increased as the velocity increased from 1 to 5 m/s. Since a full perforation was observed at and above 5 m/s, the absorbed energy and maximum displacement did not change after 5 m/s. The dent depth also increased with increasing the velocity up to 4 m/s. The damaged areas were further measured using the C-Scan NDI technique and found to increase till 4 m/s impact

velocity; thereafter, the damage area remained almost the same due to the impactor perforation. The increasing impactor diameter from 16 mm to 38 mm changed the deformation mode from a full perforation in the 16 mm impactor to an indentation on a larger damage area composing of long cracks and fiber breakage in the 38 mm impactor. The numerical models of the LVI tests showed good correlations with the experimental tests. Although the single shell model predicted acceptable results, the stacked shell model showed very similar results with the experimental tests. The stacked shell model with the tiebreak contact definition allowed to estimate the delamination area which was found to be comparable with the experimental damage areas measured by the NDI method. The LVI tested coupons were further subjected to the CAI tests in order to determine the damage tolerance of CF/PPS composite. The CAI tests were modeled using the single shell model. The experimental CAI strength values varied between 193 and 227 MPa and the failure strains between 0.010 to 0.015 without a direct relationship with the impact damage. The effective modulus values were measured around 15000 MPa. Good correlations were shown between the failure and damage of the test specimen and the NDI, and DIC measurements. The damage area showed no correlation with the LVI damage and increased up to 3 m/s impacted test specimen. However, no trend was observed beyond 3 m/s of impacted test specimen. The common failure mode was observed as “LDM” according to ASTM standard indication, which is lateral, through damage at the middle of the specimen. The numerical models of the CAI tests showed very similar trends with the experimental CAI tests. The trends were shown to be more converging at 3 m/s and above.

Lastly, three HVI tests were performed at around 100 m/s and the tests were modelled. The failure mode of the HVI tests was dramatically changed as compared with that of the LVI tests. The long longitudinal and transverse cracks formed in the HVI tests and matrix cracking, fiber breakage and delamination were shown to be main damage mechanisms. The delamination damage determined using the stacked shell model was found to be more comparable with the experimental delamination damage determined by the NDI.

REFERENCES

1. TC1100 PPS Product Data Sheet; Toray Advanced Composites, USA, 2021.
2. Zaaba, N. F.; Ismail, H.; Saeed, A. M. A Review: Metal Filled Thermoplastic Composites. *Polymer-Plastics Technology and Materials* 2021, 60 (10), 1033-1050. DOI: 10.1080/25740881.2021.1882489.
3. Yao, S.-S.; Jin, F.-L.; Rhee, K. Y.; Hui, D.; Park, S.-J. Recent advances in carbon-fiber-reinforced thermoplastic composites: A review. *Composites Part B: Engineering* 2018, 142, 241-250. DOI: 10.1016/j.compositesb.2017.12.007.
4. Morgan, P. *Carbon Fibers and Their Composites*; Taylor & Francis, 2005.
5. Gong, Y.; Song, Z.; Ning, H.; Hu, N.; Peng, X.; Wu, X.; Zou, R.; Liu, F.; Weng, S.; Liu, Q. A comprehensive review of characterization and simulation methods for thermo-stamping of 2D woven fabric reinforced thermoplastics. *Composites Part B: Engineering* 2020, 203. DOI: 10.1016/j.compositesb.2020.108462.
6. Stoeffler, K.; Andjelic, S.; Legros, N.; Roberge, J.; Schougaard, S. B. Polyphenylene sulfide (PPS) composites reinforced with recycled carbon fiber. *Composites Science and Technology* 2013, 84, 65-71. DOI: 10.1016/j.compscitech.2013.05.005.
7. Reis, J. P.; de Moura, M.; Samborski, S. Thermoplastic Composites and Their Promising Applications in Joining and Repair Composites Structures: A Review. *Materials (Basel)* 2020, 13 (24). DOI: 10.3390/ma13245832
8. Vodicka, R. *Thermoplastics for Airframe Applications A Review of the Properties and Repair Methods for Thermoplastic Composites*; Aeronautical and Maritime Research Laboratory, Melbourne, Defence Science and Technology Organisation, 2006.

9. Reyes, G.; Sharma, U. Modeling and damage repair of woven thermoplastic composites subjected to low velocity impact. *Composite Structures* 2010, 92 (2), 523-531. DOI: 10.1016/j.compstruct.2009.08.038.
10. Zhao, T.; Palardy, G.; Villegas, I. F.; Rans, C.; Martinez, M.; Benedictus, R. Mechanical behaviour of thermoplastic composites spot-welded and mechanically fastened joints: A preliminary comparison. *Composites Part B: Engineering* 2017, 112, 224-234. DOI: 10.1016/j.compositesb.2016.12.028.
11. Xavier, S. F. *Thermoplastic Polymer Composites - Processing, Properties, Performance, Applications and Recyclability*; Scrivener Publishing, 2023.
12. Zhang, J.; Chevali, V. S.; Wang, H.; Wang, C.-H. Current status of carbon fibre and carbon fibre composites recycling. *Composites Part B: Engineering* 2020, 193. DOI: 10.1016/j.compositesb.2020.108053.
13. Rybicka, J.; Tiwari, A.; Alvarez Del Campo, P.; Howarth, J. Capturing composites manufacturing waste flows through process mapping. *Journal of Cleaner Production* 2015, 91, 251-261. DOI: 10.1016/j.jclepro.2014.12.033.
14. Ning, H. *Thermoplastic Composites - Principles and Applications*; De Gruyter, 2021.
15. Montagna, L. S.; Kondo, M. Y.; Callisaya, E. S.; Mello, C.; Souza, B. R. d.; Lemes, A. P.; Botelho, E. C.; Costa, M. L.; Alves, M. C. d. S.; Ribeiro, M. V.; et al. A review on research, application, processing, and recycling of PPS based materials. *Polímeros* 2022, 32 (1). DOI: 10.1590/0104-1428.20210108.
16. Bengu Yildiz Zeyrek, B. A., Esra Dilekcan, Fahrettin Ozturk. Review of Thermoplastic Composites in Aerospace Industry. *International Journal on Engineering Technologies and Informatics* 2022, 3 (1). DOI: 10.51626/ijeti.2022.03.00031.

17. Valverde, M. A.; Belnoue, J. P. H.; Kupfer, R.; Kawashita, L. F.; Gude, M.; Hallett, S. R. Compaction behaviour of continuous fibre-reinforced thermoplastic composites under rapid processing conditions. *Composites Part A: Applied Science and Manufacturing* 2021, 149. DOI: 10.1016/j.compositesa.2021.106549.
18. Beland, S. *High Performance Thermoplastic Resins and their Composites*; Noyes Data Corp, 1990.
19. Ivanov, S. G.; Beyens, D.; Gorbatikh, L.; Lomov, S. V. Damage development in woven carbon fibre thermoplastic laminates with PPS and PEEK matrices: A comparative study. *Journal of Composite Materials* 2016, 51 (5), 637-647. DOI: 10.1177/0021998316653460.
20. Jebri, L.; Abbassi, F.; Demiral, M.; Soula, M.; Ahmad, F. Experimental and numerical analysis of progressive damage and failure behavior of carbon Woven-PPS. *Composite Structures* 2020, 243. DOI: 10.1016/j.compstruct.2020.112234.
21. Wang, Y.; Zhang, J.; Zhang, J.; Zhou, Z.; Fang, G.; Wang, S. Compressive behavior of notched and unnotched carbon woven-ply PPS thermoplastic laminates at different temperatures. *Composites Part B: Engineering* 2018, 133, 68-77. DOI: 10.1016/j.compositesb.2017.09.027.
22. Vieille, B.; Taleb, L. About the influence of temperature and matrix ductility on the behavior of carbon woven-ply PPS or epoxy laminates: Notched and unnotched laminates. *Composites Science and Technology* 2011, 71 (7), 998-1007. DOI: 10.1016/j.compscitech.2011.03.006.
23. Ali Kouka, M.; Abbassi, F.; Demiral, M.; Ahmad, F.; Soula, M.; Al Housni, F. Behaviour of woven-ply PPS thermoplastic laminates with interacting circular holes under tensile loading: An experimental and numerical study. *Engineering Fracture Mechanics* 2021, 251. DOI: 10.1016/j.engfracmech.2021.107802.

24. Brown, K. A. Finite Element Modelling of The Static and Dynamic Impact Behavior of Thermoplastic Composite Sandwich Structures. The University of Nottingham, 2007.
25. Viorel, I. FEM Modeling of Delamination in AS4/PEEK Thermoplastic Composites under Mixed – Mode Bending Test. *Mechanics* 2020, 26 (2), 120-125. DOI: 10.5755/j01.mech.26.2.24183.
26. Kang, C. S.; Shin, H. K.; Chung, Y. S.; Seo, M. K.; Choi, B. K. Manufacturing of Carbon Fibers/Polyphenylene Sulfide Composites via Induction-Heating Molding: Morphology, Mechanical Properties, and Flammability. *Polymers (Basel)* 2022, 14 (21). DOI: 10.3390/polym14214587.
27. Alshammari, B. A.; Alsuhybani, M. S.; Almushaikeh, A. M.; Alotaibi, B. M.; Alenad, A. M.; Alqahtani, N. B.; Alharbi, A. G. Comprehensive Review of the Properties and Modifications of Carbon Fiber-Reinforced Thermoplastic Composites. *Polymers* 2021, 13 (15). DOI: 10.3390/polym13152474.
28. Abbassi, F.; Elfaleh, I.; Mistou, S.; Zghal, A.; Fazzini, M.; Djilali, T. Experimental and numerical investigations of a thermoplastic composite (carbon/PPS) thermoforming. *Structural Control and Health Monitoring* 2011, 18 (7), 769-780. DOI: 10.1002/stc.491.
29. Sacchetti, F.; Groupe, W. J. B.; Warnet, L. L.; Villegas, I. F. Effect of cooling rate on the interlaminar fracture toughness of unidirectional Carbon/PPS laminates. *Engineering Fracture Mechanics* 2018, 203, 126-136. DOI: 10.1016/j.engfracmech.2018.02.022.
30. Oshima, S.; Higuchi, R.; Kato, M.; Minakuchi, S.; Yokozeki, T.; Aoki, T. Cooling rate-dependent mechanical properties of polyphenylene sulfide (PPS) and carbon fiber reinforced PPS (CF/PPS). *Composites Part A: Applied Science and Manufacturing* 2023, 164. DOI: 10.1016/j.compositesa.2022.107250.

31. Rao, P. S.; Hardiman, M.; O'Dowd, N. P.; Sebaey, T. A. Comparison of progressive damage between thermoset and thermoplastic CFRP composites under in-situ tensile loading. *Journal of Composite Materials* 2020, 55 (11), 1473-1484. DOI: 10.1177/0021998320972471.
32. Mohsin, M. A. A. Manufacturing, Testing, Modelling and Fractography of Thermoplastic Composites for the Automotive Industry. Imperial College London, United Kingdom, 2018.
33. Tan, W.; Falzon, B. G. Modelling the crush behaviour of thermoplastic composites. *Composites Science and Technology* 2016, 134, 57-71. DOI: 10.1016/j.compscitech.2016.07.015.
34. Hron, R.; Kadlec, M.; Ruzek, R. Effect of the Test Procedure and Thermoplastic Composite Resin Type on the Curved Beam Strength. *Materials (Basel)* 2021, 14 (2). DOI: 10.3390/ma14020352.
35. Zou, H.; Yin, W.; Cai, C.; Wang, B.; Liu, A.; Yang, Z.; Li, Y.; He, X. The Out-of-Plane Compression Behavior of Cross-Ply AS4/PEEK Thermoplastic Composite Laminates at High Strain Rates. *Materials (Basel)* 2018, 11 (11). DOI: 10.3390/ma11112312.
36. Carolina Ramírez Montes, V. L. R., Carlos Vinicios Opelt, Rafael Celeghini Santiago, Maribel C Rezende, Citlalli Gaona Tiburcio, Maurício Vicente Donadon. High Strain-Rate Behavior Of Fiber-Reinforced Thermoplastic Composites Under Compressive Loadings. In 24th ABCM International Congress of Mechanical Engineering, Curitiba, PR, Brazil; 2017.
37. Wang, S.; Wen, L.; Xiao, J.; Lei, M.; Liang, J. Influence of strain rate and temperature on mechanical properties of carbon woven-ply PPS thermoplastic laminates under dynamic compression. *Polymer Testing* 2020, 89. DOI: 10.1016/j.polymertesting.2020.106725.

38. Mohsin, M. A. A.; Iannucci, L.; Greenhalgh, E. S. On the Dynamic Tensile Behaviour of Thermoplastic Composite Carbon/Polyamide 6.6 Using Split Hopkinson Pressure Bar. *Materials (Basel)* 2021, 14 (7). DOI: 10.3390/ma14071653.
39. Wang, S.; Wen, L.; Xiao, J.; Lei, M.; Hou, X.; Liang, J. The Out-of-Plane Compression Response of Woven Thermoplastic Composites: Effects of Strain Rates and Temperature. *Polymers (Basel)* 2021, 13 (2). DOI: 10.3390/polym13020264.
40. Morton, W. J. C. a. J. The impact resistance of composite materials-a review. *COMPOSITES* 1991, 22.
41. Sjoblom, P. O.; Hartness, J. T.; Cordell, T. M. On Low-Velocity Impact Testing of Composite Materials. *Journal of Composite Materials* 1988, 22 (1), 30-52. DOI: 10.1177/002199838802200103.
42. Bartus, S. D.; Vaidya, U. K. Performance of long fiber reinforced thermoplastics subjected to transverse intermediate velocity blunt object impact. *Composite Structures* 2005, 67 (3), 263-277. DOI: 10.1016/j.compstruct.2004.07.023.
43. Jogur, G.; Nawaz Khan, A.; Das, A.; Mahajan, P.; Alagirusamy, R. Impact properties of thermoplastic composites. *Textile Progress* 2019, 50 (3), 109-183. DOI: 10.1080/00405167.2018.1563369.
44. Richardson, M. O. W.; Wisheart, M. J. Review of low-velocity impact properties of composite materials. *Composites Part A: Applied Science and Manufacturing* 1996, 27 (12), 1123-1131. DOI: 10.1016/1359-835x(96)00074-7.
45. Feraboli, P. Some Recommendations for Characterization of Composite Panels by Means of Drop Tower Impact Testing. *Journal of Aircraft* 2006, 43 (6), 1710-1718. DOI: 10.2514/1.19251.

46. Ahmad, F.; Hong, J.-W.; Choi, H. S.; Park, S.-J.; Park, M. K. The effects of stacking sequence on the penetration-resistant behaviors of T800 carbon fiber composite plates under low-velocity impact loading. *Carbon letters* 2015, 16 (2), 107-115. DOI: 10.5714/cl.2015.16.2.107.
47. Shah, S. Z. H.; Karuppanan, S.; Megat-Yusoff, P. S. M.; Sajid, Z. Impact resistance and damage tolerance of fiber reinforced composites: A review. *Composite Structures* 2019, 217, 100-121. DOI: 10.1016/j.compstruct.2019.03.021.
48. Strait, L. H.; Karasek, M. L.; Amateau, M. F. Effects of Stacking Sequence on the Impact Resistance of Carbon Fiber Reinforced Thermoplastic Toughened Epoxy Laminates. *Journal of Composite Materials* 1992, 26 (12), 1725-1740. DOI: 10.1177/002199839202601202.
49. Vaidya, U. K. Impact Response of Laminated and Sandwich Composites. In *Impact Engineering of Composite Structures*, Abrate, S. Ed.; Springer Vienna, 2011; pp 97-191.
50. Cartié, D. D. R.; Irving, P. E. Effect of resin and fibre properties on impact and compression after impact performance of CFRP. *Composites Part A: Applied Science and Manufacturing* 2002, 33 (4), 483-493. DOI: [https://doi.org/10.1016/S1359-835X\(01\)00141-5](https://doi.org/10.1016/S1359-835X(01)00141-5).
51. Aktaş, M.; Karakuzu, R.; Arman, Y. Compression-after impact behavior of laminated composite plates subjected to low velocity impact in high temperatures. *Composite Structures* 2009, 89 (1), 77-82. DOI: 10.1016/j.compstruct.2008.07.002.
52. Agrawal, S.; Singh, K. K.; Sarkar, P. K. Impact damage on fibre-reinforced polymer matrix composite – A review. *Journal of Composite Materials* 2013, 48 (3), 317-332. DOI: 10.1177/0021998312472217.

53. G.A. Schoeppner, S. A. Delamination threshold loads for low velocity impact on composite laminates. *Composites: Part A* 2000, 31.
54. Bajurko, P. Comparison of damage resistance of thermoplastic and thermoset carbon fibre-reinforced composites. *Journal of Thermoplastic Composite Materials* 2019, 34 (3), 303-315. DOI: 10.1177/0892705719844550.
55. Dubary, N.; Taconet, G.; Bouvet, C.; Vieille, B. Influence of temperature on the impact behavior and damage tolerance of hybrid woven-ply thermoplastic laminates for aeronautical applications. *Composite Structures* 2017, 168, 663-674. DOI: 10.1016/j.compstruct.2017.02.040.
56. Sorrentino, L.; de Vasconcellos, D. S.; D'Auria, M.; Sarasini, F.; Tirillò, J. Effect of temperature on static and low velocity impact properties of thermoplastic composites. *Composites Part B: Engineering* 2017, 113, 100-110. DOI: 10.1016/j.compositesb.2017.01.010.
57. Liu, H.; Liu, J.; Ding, Y.; Zheng, J.; Kong, X.; Zhou, J.; Harper, L.; Blackman, B. R. K.; Kinloch, A. J.; Dear, J. P. The behaviour of thermoplastic and thermoset carbon fibre composites subjected to low-velocity and high-velocity impact. *Journal of Materials Science* 2020, 55 (33), 15741-15768. DOI: 10.1007/s10853-020-05133-0.
58. Mohsin, M. A. A.; Iannucci, L.; Greenhalgh, E. S. Experimental and Numerical Analysis of Low-Velocity Impact of Carbon Fibre-Based Non-Crimp Fabric Reinforced Thermoplastic Composites. *Polymers (Basel)* 2021, 13 (21). DOI: 10.3390/polym13213642.
59. Parvizi-Majidi, A.; Ghasemi Nejhad M. N. Impact behaviour and damage tolerance of woven carbon fibre reinforced thermoplastic composites. *COMPOSITES* 1990, 21 (2).

60. Vieille, B.; Casado, V. M.; Bouvet, C. About the impact behavior of woven-ply carbon fiber-reinforced thermoplastic- and thermosetting-composites: A comparative study. *Composite Structures* 2013, *101*, 9-21. DOI: 10.1016/j.compstruct.2013.01.025.
61. Schimmer, F.; Ladewig, S.; Motsch, N.; Hausmann, J. M.; Ehrlich, I. Comparison of Low-Velocity Impact Damage Behavior of Unidirectional Carbon Fiber-Reinforced Thermoset and Thermoplastic Composites. *Key Engineering Materials* 2019, *809*, 9-14. DOI: 10.4028/www.scientific.net/KEM.809.9.
62. J. Liu, H. L., H. Chai, L.T. Harper, B.G. Falzon,; B.R.K. Blackman, A. J. K. a. J. P. D. The performance of Thermoplastic and Thermoset Composites Subjected to Low-Velocity and High-Velocity Impact Loading. Twenty-Second International Conference on Composite Materials, Melbourne Australia; 2022.
63. M. A. A. Mohsin, L. I. a. E. G. Numerical and Experimental Analysis of High-velocity Impact Behaviour of Carbon Fibre Reinforced Thermoplastic Composites. In 18th European Conference on Composite Materials, Athens, Greece; 2018.
64. Liu, J.; Liu, H.; Kaboglu, C.; Kong, X.; Ding, Y.; Chai, H.; Blackman, B. R. K.; Kinloch, A. J.; Dear, J. P. The Impact Performance of Woven-Fabric Thermoplastic and Thermoset Composites Subjected to High-Velocity Soft- and Hard-Impact Loading. *Applied Composite Materials* 2019, *26* (5-6), 1389-1410. DOI: 10.1007/s10443-019-09786-2.
65. Liu, A.; Chen, Y.; Hu, J.; Wang, B.; Ma, L. Low-velocity impact damage and compression after impact behavior of CF/PEEK thermoplastic composite laminates. *Polymer Composites* 2022, *43* (11), 8136-8151. DOI: 10.1002/pc.26983.

66. Vieille, B.; Casado, V. M.; Bouvet, C. Influence of matrix toughness and ductility on the compression-after-impact behavior of woven-ply thermoplastic- and thermosetting-composites: A comparative study. *Composite Structures* 2014, *110*, 207-218. DOI: 10.1016/j.compstruct.2013.12.008.
67. Ong, C. L.; Liou, Y. Y. Characterization of mechanical behaviors of advanced thermoplastic composite after impact. *Acta Astronautica* 1993, *29* (2), 99-108. DOI: [https://doi.org/10.1016/0094-5765\(93\)90027-T](https://doi.org/10.1016/0094-5765(93)90027-T).
68. Olsson, R. 3 - Low- and medium-velocity impact as a cause of failure in polymer matrix composites. In *Failure Mechanisms in Polymer Matrix Composites*, Robinson, P., Greenhalgh, E., Pinho, S. Eds.; Woodhead Publishing, 2012; pp 53-78.
69. Limaye, M.; Pradeep, S. A.; Kothari, A.; Savla, S.; Agha, A.; Pilla, S.; Li, G. Thermoforming process effects on structural performance of carbon fiber reinforced thermoplastic composite parts through a manufacturing to response pathway. *Composites Part B: Engineering* 2022, *235*. DOI: 10.1016/j.compositesb.2022.109728.
70. Striewe, J.; Reuter, C.; Sauerland, K. H.; Tröster, T. Manufacturing and crashworthiness of fabric-reinforced thermoplastic composites. *Thin-Walled Structures* 2018, *123*, 501-508. DOI: 10.1016/j.tws.2017.11.011.
71. Bogenfeld, R.; Kreikemeier, J.; Wille, T. Review and benchmark study on the analysis of low-velocity impact on composite laminates. *Engineering Failure Analysis* 2018, *86*, 72-99. DOI: 10.1016/j.engfailanal.2017.12.019.
72. Rajaneesh, A.; Bruyneel, M. Low-velocity impact and compression after impact modeling of composites using modified mesoscale model. *Composite Structures* 2023, *311*. DOI: 10.1016/j.compstruct.2023.116821.

73. Rabiee, A.; Ghasemnejad, H. Finite Element Modelling Approach for Progressive Crushing of Composite Tubular Absorbers in LS-DYNA: Review and Findings. *Journal of Composites Science* 2021, 6 (1). DOI: 10.3390/jcs6010011.
74. Zeleniakiene, D.; Griskevicius, P.; Aniskevich, A.; Jankauskaite, V.; Zukiene, K. A Numerical and Experimental Study on the Impact Behavior of a Carbon-Fiber-Reinforced Thermoplastic Poly (Methyl Methacrylate) Composite. *Mechanics of Composite Materials* 2019, 55 (3), 393-404. DOI: 10.1007/s11029-019-09820-1.
75. Matzenmiller, A.; Lubliner, J.; Taylor, R. L. A constitutive model for anisotropic damage in fiber-composites. *Mechanics of Materials* 1995, 20 (2), 125-152. DOI: [https://doi.org/10.1016/0167-6636\(94\)00053-0](https://doi.org/10.1016/0167-6636(94)00053-0).
76. Xing, J.; Du, C.; He, X.; Zhao, Z.; Zhang, C.; Li, Y. Finite Element Study on the Impact Resistance of Laminated and Textile Composites. *Polymers (Basel)* 2019, 11 (11). DOI: 10.3390/polym11111798 From NLM PubMed-not-MEDLINE.
77. Giannaros, E.; Kotzakolios, A.; Sotiriadis, G.; Kostopoulos, V. A multi-stage material model calibration procedure for enhancing numerical solution fidelity in the case of impact loading of composites. *Journal of Composite Materials* 2021, 55 (1), 39-56. DOI: 10.1177/0021998320944992.
78. González, E. V.; Maimí, P.; Martín-Santos, E.; Soto, A.; Cruz, P.; Martín de la Escalera, F.; Sainz de Aja, J. R. Simulating drop-weight impact and compression after impact tests on composite laminates using conventional shell finite elements. *International Journal of Solids and Structures* 2018, 144-145, 230-247. DOI: 10.1016/j.ijsolstr.2018.05.005.
79. Chatla, P. LS-Dyna for Crashworthiness of Composite Structures. University of Cincinnati, 2012.

80. Ghasemnejad, A. R. a. H. Lightweight Design to Improve Crushing Behaviour of Multi-stitched Composite Tubular Structures under Impact Loading. *Thin-Walled Structures* 2019, *Volume 135*, 109-122.
81. Dávila, C.; Camanho, P.; Turon, A. Effective Simulation of Delamination in Aeronautical Structures Using Shells and Cohesive Elements. *Journal of Aircraft* 2008, *45*. DOI: 10.2514/1.32832.
82. Tuo, H.; Lu, Z.; Ma, X.; Zhang, C.; Chen, S. An experimental and numerical investigation on low-velocity impact damage and compression-after-impact behavior of composite laminates. *Composites Part B: Engineering* 2019, *167*, 329-341. DOI: 10.1016/j.compositesb.2018.12.043.
83. Dogan, F.; Hadavinia, H.; Donchev, T.; Bhonge, P. Delamination of impacted composite structures by cohesive zone interface elements and tiebreak contact. *Open Engineering* 2012, *2* (4), 612-626. DOI: 10.2478/s13531-012-0018-0.
84. Ahmad, F.; Abbassi, F.; Park, M. K.; Hong, J.-W. Numerical investigation to evaluate effect of fiber orientation on penetration-resistance of an aircraft composite material. *Mechanics of Advanced Materials and Structures* 2018, *26* (19), 1613-1621. DOI: 10.1080/15376494.2018.1444226.
85. Kim, Y. C.; Yoon, S. H.; Joo, G.; Jang, H. K.; Kim, J. H.; Jeong, M.; Kim, J. H. Crash Analysis of Aluminum/CFRP Hybrid Adhesive Joint Parts Using Adhesive Modeling Technique Based on the Fracture Mechanics. *Polymers (Basel)* 2021, *13* (19). DOI: 10.3390/polym13193364 From NLM PubMed-not-MEDLINE.
86. Maamar, D. B.; Ramdane, Z. Characterization of the Mechanical Behaviour of Carbon Fiber Composite Laminate under Low Velocity Impact. *Periodica Polytechnica Mechanical Engineering* 2016, *60* (3), 142-151. DOI: 10.3311/PPme.8633.

87. Borrelli, R.; Franchitti, S.; Di Caprio, F.; Romano, F.; Mercurio, U. A Numerical Procedure for the Virtual Compression after Impact Analysis. *Advanced Composites Letters* 2015, 24 (4), 096369351502400401. DOI: 10.1177/096369351502400401.
88. Mendes, P. A. A. E.; Donadon, M. V. Numerical prediction of compression after impact behavior of woven composite laminates. *Composite Structures* 2014, 113, 476-491. DOI: 10.1016/j.compstruct.2014.03.051.
89. Rozylo, P.; Debski, H.; Kubiak, T. A model of low-velocity impact damage of composite plates subjected to Compression-After-Impact (CAI) testing. *Composite Structures* 2017, 181, 158-170. DOI: 10.1016/j.compstruct.2017.08.097.
90. Suemasu, H. Analytical approaches to compression after impact (CAI) behavior of carbon fiber-reinforced composite materials. *Advanced Composite Materials* 2016, 25 (1), 1-18. DOI: 10.1080/09243046.2015.1122416.
91. Reiner, J.; Zobeiry, N.; Vaziri, R. Efficient finite element simulation of compression after impact behaviour in quasi-isotropic composite laminates. *Composites Communications* 2021, 28. DOI: 10.1016/j.coco.2021.100967.
92. ASTM. *D3039/D3039M - 14 "Standard Test Method for Tensile Properties of Polymer Matrix Composite Materials"*; 2014. DOI: 10.1520/d3039_d3039m-14.
93. ASTM. *D6641/D6641M - 14 "Standard Test Method for Compressive Properties of Polymer Matrix Composite Materials Using a Combined Loading Compression (CLC) Test Fixture"*; 2014. DOI: 10.1520/d6641_d6641m-14.
94. ASTM. *D3518/D3518M - 13 "Standard Test Method for In-Plane Shear Response of Polymer Matrix Composite Materials by Tensile Test of a $\pm 45^\circ$ Laminate"*; 2013. DOI: 10.1520/d3518_d3518m-13.

95. ASTM. *D7136/D7136M - 15 "Standard Test Method for Measuring the Damage Resistance of a Fiber-Reinforced Polymer Matrix Composite to a Drop-Weight Impact Event"*; 2015. DOI: 10.1520/d7136_d7136m-15.
96. ASTM. *D7137/D7137M - 17 "Standard Test Method for Compressive Residual Strength Properties of Damaged Polymer Matrix Composite Plates I"*; 2017. DOI: 10.1520/d7137_d7137m-17.
97. Dynamore. *Introduction to Composite Material Modeling with LS-DYNA*.
98. Group, L.-D. A. W. *Modeling Guidelines Document*; Aerospace Working Group, awg.lstc.com, 2022.
99. TECHNOLOGY, L. S. *LS-DYNA KEYWORD USER'S MANUAL*; 2021.
100. Hasanudin, H.; Nadlene, R.; Anita Akmar, K.; Nurfaizey Abdul, H.; Siti Hajar Sheikh Md, F.; Emy Aqillah, S.; Syazwan Ahmad, R.; Sarah, O. Characterization of Carbon Fibre Reinforced Polyphenylene Sulfide Composite Under Interlaminar Shear Strength. *Journal of Advanced Research in Applied Mechanics* 2023, 102 (1), 1-9. DOI: 10.37934/aram.102.1.19.
101. De Baere, I.; Jacques, S.; Van Paepegem, W.; Degrieck, J. Study of the Mode I and Mode II interlaminar behaviour of a carbon fabric reinforced thermoplastic. *Polymer Testing* 2012, 31 (2), 322-332. DOI: 10.1016/j.polymertesting.2011.12.009.

VITA

Semih Berk SEVEN completed his undergraduate degree in mechanical engineering as an honor student in 2015. He started his master's degree in the same year and took part in a TUBITAK supported research project. He continued his academic career as a research assistant in 2017 and successfully completed his master's degree in 2018 and started his doctoral studies. He started working as a structural design engineer in the Turkish Aerospace company in 2019 and continues to work as a lead engineer in the same company.

Publications

- Constitutive equation determination and dynamic numerical modelling of the compression deformation of concrete, *Strain*, Vol.57, Issue 2, January 2021.
- Experimental and numerical investigation of quasi-static and high strain rate compression behavior of a (0/90) cross-ply e-glass/polyester composite, September 2018, IV. International Ege Composite Materials Symposium.
- The investigation of low-velocity drop weight impact on concrete plates, November 2018, International Symposium on Advanced Manufacturing of Advanced Materials and Structures with Sustainable Industrial Applications, Rio de Janeiro, Brazil.
- The damage formation of an E/glass fiber reinforced polyester composite plate under multi-impact loadings, SAVTEK 2018, 9th Defence Technologies Congress, 27-29 Haziran 2018, ODTÜ, Ankara
- The investigation of dynamic stress equilibrium of concrete at high strain rates, September 2018, IV. International Ege Composite Materials Symposium.
- Dynamic compressive behavior of an e-glass/polyester composite material subjected to repeated loads, November 2018, International Symposium on Advanced Manufacturing of Advanced Materials and Structures with Sustainable Industrial Applications, Rio de Janeiro, Brazil.
- The effect of pulse shaping on the dynamic mechanical behavior of concrete, 22nd DYMAT Technical Meeting, October 2016, Grenoble, France.